University of Cyprus

Faculty of Engineering

Department of Mechanical and Manufacturing Engineering

Three-Dimensional Direct Numerical Simulations of Hydrodynamic and Magnetohydrodynamic Flows Over an Obstacle in a Confined Geometry

Doctoral Dissertation

Nicolas Kanaris

2012

University of Cyprus

Department of Mechanical and Manufacturing Engineering

Three-Dimensional Direct Numerical Simulations of Hydrodynamic and Magnetohydrodynamic Flows Over an Obstacle in a Confined Geometry

Nicolas Kanaris

A thesis submitted in partial fulfillment of the University's requirements for the
Degree of Doctor of Philosophy

September 2012

APPROVAL PAGE

Candidate:
Nicolas Kanaris

Title:
Three-Dimensional Direct Numerical Simulations of Hydrodynamic and Magnetohydrodynamic Flows Over an Obstacle in a Confined Geometry

The present Doctorate Dissertation was submitted in partial fulfillment of the requirements of the Degree of Doctor of Philosophy at the Department of of Mechanical and Manufacturing Engineering and approved on the 7th of September of 2012 by the members of the Doctoral Committee.

Research Advisor: Stavros Kassinos, Associate Professor

Committee Member: Andreas Alexandrou, Professor

Committee Member: Michalis Averkiou, Associate Professor

Committee Member: Michael A. Leschziner, Professor

Committee Member: Bertrand Aupoix, Research Director

This thesis is dedicated to
Elena

Περίληψη

Στην παρούσα διατριβή παρουσιάζεται η υδροδυναμική και μαγνητο-υδροδυναμική ροή που αναπτύσσεται γύρω από ένα κύλινδρο κυκλικής διατομής, σε γεωμετρίες περιορισμένες από σταθερά τοιχώματα. Η επίδραση του περιορισμού της ροής στα ποιοτικά χαρακτηριστικά της ροής, μελετήθηκε λεπτομερώς με απευθείας αριθμητική επίλυση των εξισώσεων Navier-Stokes (DNS).

Συγκεκριμένα, μελετήσαμε δύο διαφορετικές περιπτώσεις: τη ροή γύρω από κύλινδρο συμμετρικά τοποθετημένο σε κανάλι και τη μαγνητο-υδροδυναμική ροή υγρού μετάλλου πάνω από κύλινδρο, τοποθετημένο σε αγωγό ορθογώνιας διατομής, κάτω από την επίδραση εξωτερικού μαγνητικού πεδίου.

Στην πρώτη περίπτωση υδροδυναμικής ροής γύρω από κύλινδρο, δίνεται έμφαση σε μια περιοχή χαμηλών αριθμών Reynolds, $10 < Re < 390$, στην οποία η ροή μεταπίπτει απο τη στρωτή σε μια ασταθή μεταβατική κατάσταση η οποία χαρακτηρίζεται από πολύπλοκες τρισδιάστατες δομές. Η μετάβαση σε τρισδιάστατη ροή και η δημιουργία τρισδιάστατων διαταραχών πίσω από τον κύλινδρο, εξετάζονται με λεπτομέρεια. Τα αποτελέσματα καταδεικνύουν για πρώτη φορά σε μια τέτοια γεωμετρία, την παρουσία ασταθειών τύπου A και B (mode A and mode B instabilities) καθώς και την παρουσία δινών εξάρθρωσης (vortex dislocations), στην περιοχή μεταβατικής ροής. Επιπλέον, δίνεται εξήγηση για την αλλαγή στη μορφή και διάδοση των διαταραχών αυτών, εξαιτίας της παρουσίας των τοιχωμάτων του καναλιού.

Στη δεύτερη περίπτωση, η μελέτη της μαγνητο-υδροδυναμικής ροής γύρω από κύλινδρο σε ορθογώνιο αγωγό καλύπτει αριθμούς Reynolds μεταξύ $0 < Re \leq 5000$, κάτω από την επίδραση μεγάλου εύρους μαγνητικών πεδίων μεταξύ $0 \leq Ha \leq 1120$. Η εργασία αυτή, αποτελεί μια πρώτη προσπάθεια για να καλύψει το κενό που υπάρχει στη βιβλιογραφία στην περιοχή χαμηλών αριθμών Hartmann, για αυτού του είδους τις ροές. Τα αποτελέσματα αποκαλύπτουν μια μη-γραμμική εξάρτηση του κρίσιμου αριθμού Reynolds για την έναρξη περιοδικής αποκόλησης δινών (vortex shedding),σε σχέση με τον αριθμό Hartmann. Επιπρόσθετα, τα αποτελέσματα δείχνουν μια απροσδόκητη αύξηση του τρισδιάστατου χαρακτήρα της κατανομής των επιφανειακών δυνάμεων που ασκούνται κατά μήκος του κυλίνδρου, αυξάνοντας τον αριθμό Hartmann. Τέλος, μέσα από απεικονίσεις και ανάλυση των χαρακτηριστικών που σχετίζονται με τη δημιουργία και διάδοση των

δινὼν, προσφὲρουμε μια εξὴγηση για τη μη αναμενὸμενη αποσταθεροποὶηση της ροὴς, καθὼς αυξὰνεται ο αριθμὸς Hartmann.

Abstract

In this thesis, we are concerned with the hydrodynamic (HD) and magnetohydrodynamic (MHD) three-dimensional flow of incompressible fluids over a circular cylinder in confined geometries. Direct Numerical Simulations (DNS) are employed to investigate in detail the effect of confinement on the characteristics of the generated flow regimes and the evolution of force coefficients.

Two different cases are considered: the HD flow over a circular cylinder placed symmetrically in a plane channel, and the MHD flow of liquid metal past a cylinder placed symmetrically in a rectangular duct under the presence of an externally applied magnetic field.

In the first case of a purely HD flow past a cylinder in a channel, the focus is on a range of moderate Reynolds numbers, $10 < Re < 390$, where the flow transitions from a laminar flow regime to a highly complex three-dimensional tranistional-wake regime. The onset of three-dimensionality of the flow and the appearance of three-dimensional wake instabilities are studied in detail. For the first time for such a confined case, our results show the existence of vortex dislocations, mode A and mode B instabilities, along with a discontinuous change in the variation of the Strouhal number and base pressure coefficient, associated with the inception of this transitional flow regime. We also explain how the shape and evolution of instabilities is affected downstream by the confinement of the channel walls.

In the second case, the MHD flow around the circular cylinder in a duct is simulated for $0 < Re \leq 5000$, under low, moderate and strong magnetic fields, $0 \leq Ha \leq 1120$. This work is a first effort to try to fill the gap in the literature in the area of low Ha for this type of flows. Furthermore, we investigate the evolution and distribution of force coefficients, the enhancement or suppression of flow stability, as well as the induction of secondary flows. Results reveal a non-monotonic dependance of the critical Reynolds number for the onset of vortex shedding, with respect to the Hartmann number. Results also show an unexpected increasing three-dimensionality of the force distributions along the cylinder with increasing Ha. Finally, through visualizations and analysis of the characteristics of the formation and propagation of vortices, we offer an explanation for the surprising destabilization of the flow with increasing Ha.

Acknowledgements

First and foremost I would like to thank my advisor, professor Stavros Kassinos, whose patience and kindness have been invaluable to me all these years. His advise and guidance made possible the successful completion of this doctoral thesis.

I am especially grateful and owe a huge thank you to several co-workers who have become close friends over the years. In particular, I would like to thank Xavi Albets for putting up with me along the way, during the inevitable ups and downs, frustration and excitement. I know without a doubt that our fruitful conversations have influenced me greatly. I would also like to extend a sincere thanks to Hari Radhakrisnan for his meticulous advising, but more importantly, for making all computer related problems disappear with his voodoo magic. I consider my self fortunate to have worked alongside Dimokratis Grigoriadis, who has been amazing help all this time. I am also thankful to Konstantinos Panayiotou and Fotos Stylianou for their time, interest, helpful comments, and some good laughs.

Last but not the least, I would like to thank my family, Andreas, Sotiroulla and Alexis, for all their support and encouragement, and of course my wife Elena for her love, patience and unconditional understanding, throughout the years.

Contents

List of Symbols

Roman letters

$\mathbf{B}$	magnetic field
C_D	drag coefficient, Eq.(4.3)
C_L	lift coefficient, Eq.(4.3)
C_{pb}	base pressure coefficient, Eq.(4.6)
D	diameter of circular cylinder
$\mathbf{E}$	electric field, Eq.(3.22)
f	frequency of vortex shedding
$\mathbf{f}, \mathbf{F}$	force
G	minimal distance between the cylinder wall and the wall of the channel
H	height of channel
Ha	Hartmann number, Eq.(3.42)
i, j, k	integer numbers
$\mathbf{j}$	current density, Eq.(3.24)
L_r	recirculation length
N	interaction parameter, Eq.(3.41)
p	pressure (force per unit area)
q	electric charge
Re	Reynolds number, Eq.(5.7)
Re_{cr}	critical Reynolds number
St	Strouhal number, Eq.(4.5)
t	time
$\mathbf{u}$	velocity vector
U_b	bulk flow velocity
U_c	centerline inflow velocity
U_0	fluid typical velocity
W	width of rectangular duct
x, y, z	cartesian coordinates

Greek letters

α	aspect ratio, W/D
β	blockage ratio, D/H
γ	gap ratio, G/D
δ_{ij}	Kronecker's delta
δ_H	thickness of Hartmann layers
δ_S	thickness of Shercliff layers
ϵ_0	electric permettivity of conducting medium
λ_2	second eigenvalue of $\mathbf{S}^2 + \mathbf{X}^2$, where $\mathbf{S}$ and $\mathbf{X}$ denote the symmetric and antisymmetric part of the velocity gradient tensor
μ_0	magnetic permeability
μ	absolute viscosity
ν	kinematic viscosity
ρ	density (mass per unit volume)
σ	electrical conductivity
σ_{ij}	stress tensor
τ_{ij}	shear stress tensor
ϕ	electric potential field
$\boldsymbol{\omega}$	vorticity vector

List of Figures

List of Tables

Chapter 1

Introduction

1.1 Motivation/Objectives

While the flow over a circular cylinder represents one of the classical problems in fluid mechanics, the case of flow over a confined cylinder in a plane channel or a rectangular duct remains relatively unexplored. The extra confinement provided by the stationary no-slip walls affects the nature and stability of the flow. Understanding the wide variety of rich flow phenomena that ensue in this case is of intrinsic interest for the overall understanding of bluff body fluid dynamics. Even more importantly, the study of such a flow configuration is of considerable practical interest. It represents an idealization of several industrially important flows; typical examples include flow past dividers in polymer processing, tubular and compact heat exchangers, etc. On the other hand, liquid metal flow in confined arrangements under the presence of a magnetic field also plays a significant role in a wide range of applications in engineering and industrial processes, such as stirring of melts in the metallurgical industry and cooling of liquid metal blankets in fusion reactors. Introducing a cylindrical obstacle in the flow can induce vortices and enhance mixing and heat-transfer rates to favour these processes. Therefore, understanding the dynamics of a three-dimensional wake behind a confined cylinder, the enhancement or suppression of flow stability, and the induction of secondary flows, can provide valuable knowledge with practical importance.

The goal of this work is to produce Direct Numerical Simulation (DNS) results of the three-dimensional hydrodynamic (HD) and magnetohydrodynamic (MHD) flow over a confined cylinder in a channel and a rectangular duct, at low to moderate Reynolds number, using the Finite-Volume method. Understanding the flow behind a confined bluff body poses a great challenge, especially in the transitional regime where a large number of instabilities and physical phenomena take place. DNS simulations provide an accurate and reliable research tool to analyze the complicated physics of these instabilities. The main objective of this study is to enhance our understanding of these complex flow regimes through full three-dimensional Direct Numerical Simulations.

Two cases of flow have been studied. First, we have investigated in detail the flow around a circular cylinder placed symmetrically in a plane channel. Particularly, we describe the confinement effect due to the channel's stationary walls on the force coefficients and the associated Strouhal number, as well as on the generated flow regimes. Secondly, we have examined the flow of liquid metal around a circular cylinder placed symmetrically in a rectangular duct, under the influence of an externally applied magnetic field. Varying the intensity of the magnetic field, we have investigated the evolution of flow coefficients and the wake characteristics of the flow.

The design of the current thesis and the roadmap that has been used for its implementation, is shown in Figure 1.1

1.2 Thesis Structure

This thesis is structured as follows. In Chapter 2 we give a general overview of the current state of the art in the area of HD and MHD flows over a circular cylinder in confined and unconfined geometries. In the following chapter (Chapter 3) we briefly introduce the basic computational methods for fluid dynamics and describe the discretization methods used in our code for solving the governing equations of motion. In Chapter 4 we present the case of flow past a confined cylinder in a channel, while the case of liquid metal flow over a cylinder in a rectangular duct is presented in Chapter 5. Finally, in Chapter 6, we give a brief summary of the main results from this work, before discussing future work.

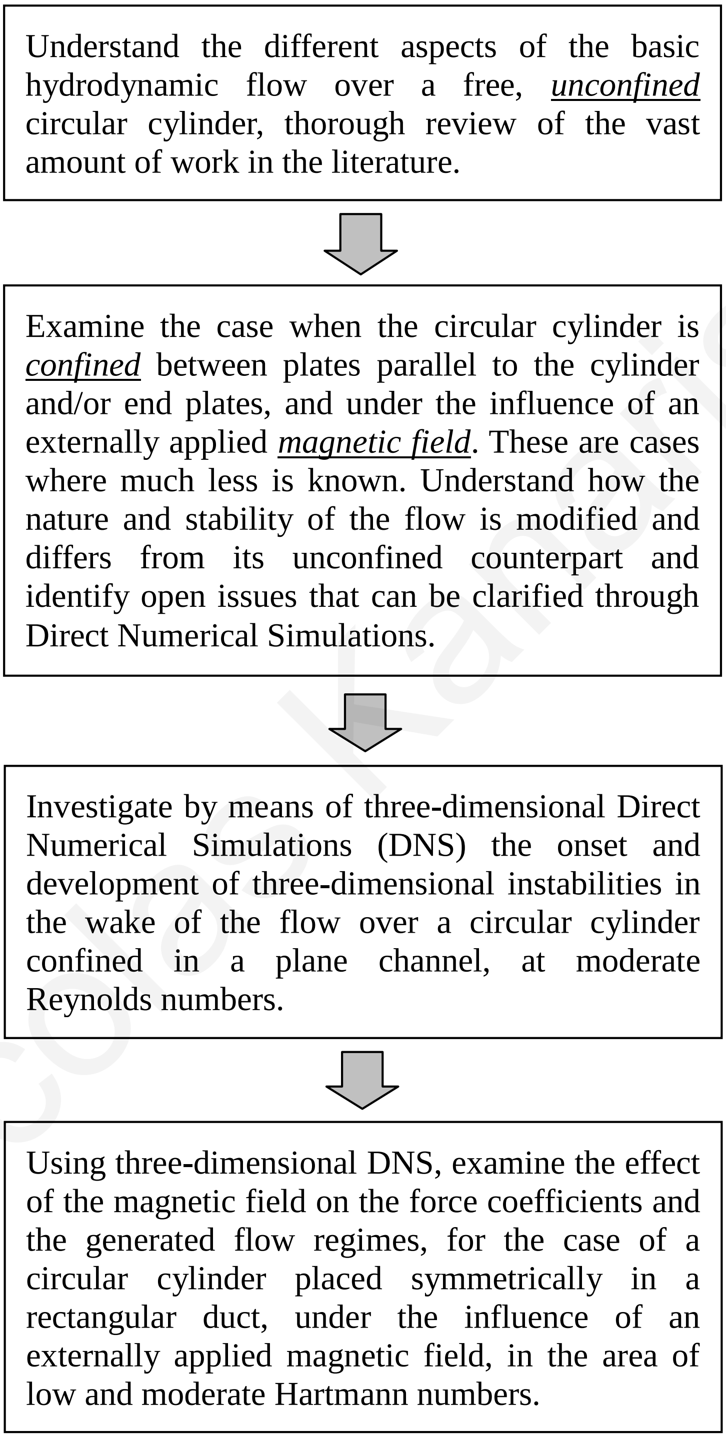

Understand the different aspects of the basic hydrodynamic flow over a free, *unconfined* circular cylinder, thorough review of the vast amount of work in the literature.

Examine the case when the circular cylinder is *confined* between plates parallel to the cylinder and/or end plates, and under the influence of an externally applied *magnetic field*. These are cases where much less is known. Understand how the nature and stability of the flow is modified and differs from its unconfined counterpart and identify open issues that can be clarified through Direct Numerical Simulations.

Investigate by means of three-dimensional Direct Numerical Simulations (DNS) the onset and development of three-dimensional instabilities in the wake of the flow over a circular cylinder confined in a plane channel, at moderate Reynolds numbers.

Using three-dimensional DNS, examine the effect of the magnetic field on the force coefficients and the generated flow regimes, for the case of a circular cylinder placed symmetrically in a rectangular duct, under the influence of an externally applied magnetic field, in the area of low and moderate Hartmann numbers.

Figure 1.1: Thesis roadmap.

Chapter 2

State of the art

A large amount of work in the literature is dedicated to the investigation of flow over an unconfined circular cylinder, both experimentally and numerically. On the other hand, the case of a circular cylinder confined in a channel has received much less attention. Even fewer studies have been done regarding the case of a cylinder confined in a duct. In the following subsections, a short review of the existing knowledge for both unconfined and confined cases is given. In this thesis, we are interested in the flow characteristics of incompressible, Newtonian fluids with density ρ and kinematic viscosity ν, ranging from laminar conditions up to the very early stages of turbulence. In this context, this review is limited to the corresponding flow regimes preceding turbulence. First, in Section 2.1, we present the fundamental features of flow over an unconfined cylinder. Special attention has been given in the flow regime where transition to turbulence occurs, and for this reason a more detailed description of transition is given in Section 2.2. Then in Sections 2.3 and 2.4, we investigate the effects of blockage and end-plates confinement, respectively. Finally in Section 2.5, we present the magnetohydrodynamic (MHD) case of flow over a cylinder in a rectangular duct.

2.1 Flow over an unconfined circular cylinder

Over the years, a significant amount of information dealing with different aspects of the basic hydrodynamic flow over a free, *unconfined* circular cylinder has been added to the literature. Several experimental and numerical studies have been performed to analyze the characteristics of the wake, the stability of the flow, the onset of the vortex shedding mechanism, as well as global flow parameters, such as the force coefficients. Extensive reviews of the accumulated knowledge can be found in the books of Zdravkovich [1, 2] and in the review paper of Williamson [3].

In this flow, non-dimensionalization of the Navier-Stokes equations leaves one governing dimensionless parameter. This is the Reynolds number, $Re = U_0 D/\nu$, where U_0 is the fluid typical velocity and D is the cylinder's diameter (or any other characteris-

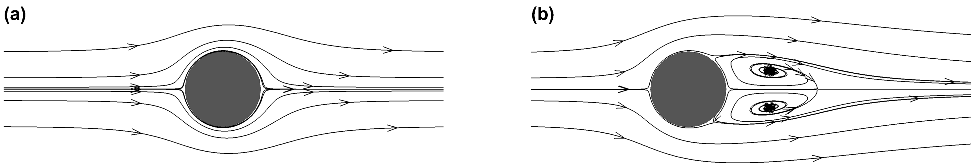

Figure 2.1: Visualization of laminar steady regime: (a) creaping flow, (b) steady recirculation regions.

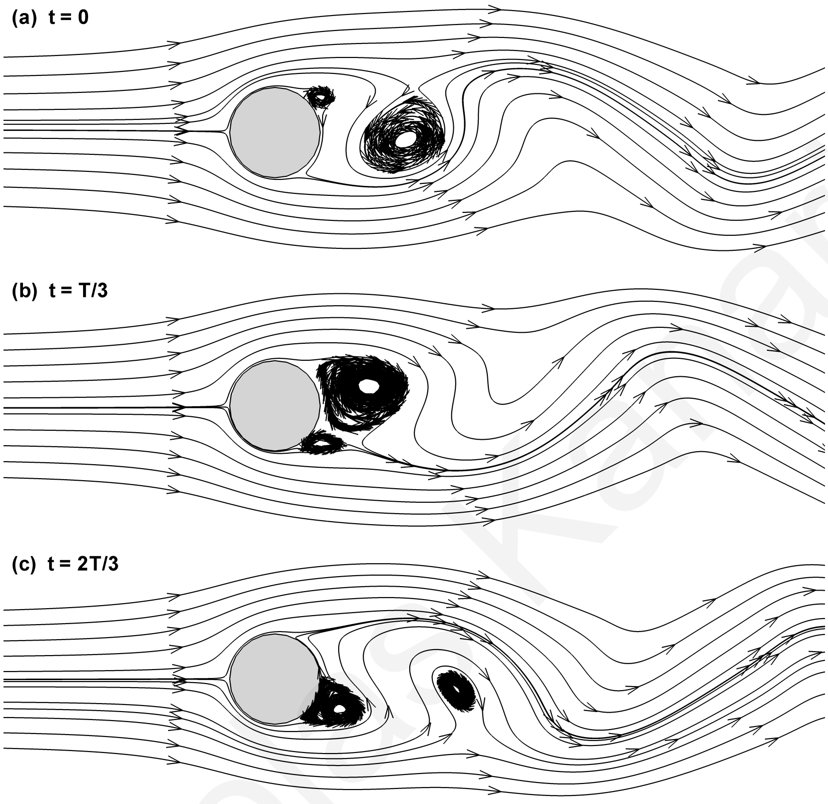

Figure 2.2: Sequence of snapshots illustrating the vortex shedding process in the unsteady flow regime.

tic length of the fluid domain). *Re* gives a measure for the ratio of the inertial to the viscous forces. Depending upon the value of *Re*, the properties of the flow differ and the flow may be divided into different regimes.

For Reynolds numbers up to approximately $Re \simeq 46$, the flow is laminar and steady [4, 5, 6]. At *Re* less than approximately 5, the flow is fore and aft symmetric, divides at the front stagnation point and reunites smoothly behind the cylinder as shown in Figure 2.1(a). For values of the Reynolds number in the range of $Re = 5$ to 46, the boundary layer on the cylinder surface separates, owing to the large friction forces in the thin viscous layer. Consequently two stable, well defined symmetric vortices are formed in the downstream direction of the flow, which remain attached to the cylinder as shown in Figure 2.1(b). The length of the recirculation zone behind the cylinder

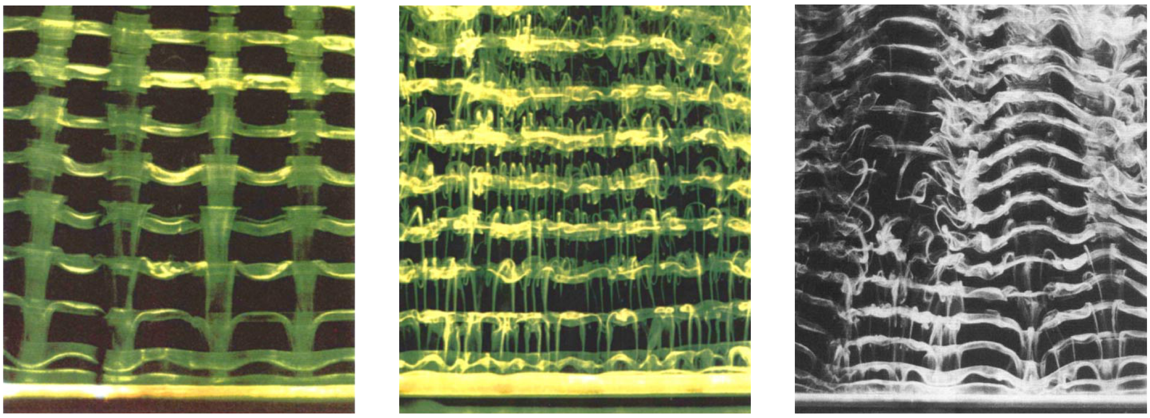

(a) Mode A **(b)** Mode B **(c)** Vortex dislocations

Figure 2.3: Experimental visualization of mode A and mode B three-dimensional instabilities along with vortex dislocations (Figure taken from Ref. [17]).

grows linearly with Re [4, 7, 8], while due to this increase, the base suction pressure (pressure exerted on the base of the cylinder) decreases with increasing Re [9].

In the range of $Re = 46$ to 189 the flow remains laminar, however the stability of the flow is lost [6, 10]. As a result of a supercritical Hopf bifurcation of the steady flow [11, 12], the recirculation region develops instabilities, that lead to a two-dimensional oscillatory flow. Vortices are shed from alternate sides of the cylinder, forming two rows of vortices that move alternately clockwise and anticlockwise, giving rise to the well-known von Kármán vortex street [13, 14]. The shed vortices, called primary vortices, are regularly placed behind the cylinder and decay as they convect downstream (see Figure 2.2). The wake is perfectly time-periodic, and the characteristic frequency of oscillation of the vortices is expressed in non-dimensional form as the Strouhal number, St. In this flow regime, St increases with Re [15] as shown in Figure 2.6(a). The base suction also increases with Re (see Figure 2.6(b)), due to the shrinking of the vortex formation region and the increase in the Reynolds stresses in the near wake region [16].

Beyond $Re \simeq 189$, the flow transitions to a three-dimensional wake-transition regime, consisting of complex three-dimensional flow structures in the wake of the cylinder. We shall discuss in more detail this regime in the following subsection.

2.2 Transition to three-dimensionality

Transition to three-dimensionality in the cylinder wake for the *unconfined* case is well understood, and much work has already been done in this area [6, 15, 16, 17, 18, 19]. For values of the Reynolds number above $Re \simeq 189$ [6], three-dimensional effects appear, and Roshko [10] was the first to observe a transition regime in the wake of an unconfined circular cylinder. In this transition regime, three physically different instabilities are observed, referred to by Williamson [20] as “mode A”, “mode B”, and

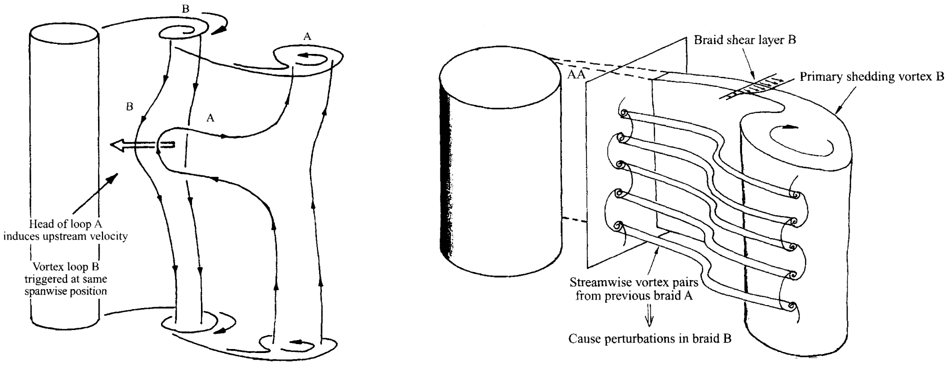

(a) Mode A **(b)** Mode B

Figure 2.4: Physical mechanism (a) in the primary vortex core to produce vortex loops, and (b) in the braid shear layer to produce mode B streamwise vortices (Figure taken from Ref. [20]).

"vortex dislocations" (see Figure 2.3).

Mode A is characterized by a discontinuous change in the wake formation, as the primary spanwise vortices become unstable and generate large-scale streamwise vortex loops (see Figure 2.3(a)), at a wavelength of around 3 to 4 cylinder diameters [6, 20, 21]. During the process of shedding, a spanwise waviness of the primary vortex cores appears. This initial small undulation grows until segments of the primary vortex are caught in the reverse flow and convected back upstream forming vortex loops, while the remaining segments of the roller travel downstream. A feedback mechanism between subsequent vortex cores, leads to a self-sustained tearing of the primary vortices occurring at fixed spanwise locations over time (see Figure 2.4(a)). The spanwise-periodic deformation of core vorticity during shedding is followed by the formation of streamwise vortices from the side of the vortex loops, in a process that gives an out-of-phase streamwise vortex pattern. Most of the streamwise vorticity is being pulled out of the vortex core and into the braid region [20].

Mode B corresponds to the appearance of small scale streamwise vortex structures, (see Figure 2.3(b)) with a wavelength of approximately one cylinder diameter [6, 20, 21]. This instability is not related with the waviness of the primary vortex core as in mode A, and scales on the smaller physical structure in the flow, the braid shear layer. The symmetries of mode B instability are linked with the presence of pre-existing streamwise vortices in the vicinity of newly forming streamwise vortices. The induced velocity from pairs of streamwise vortices formed in a previous half cycle, causes a spanwise waviness in the newly forming braid shear layer, which in turn will induce tilting and stretching of streamwise vorticity in the new braid shear layer (see Figure 2.4(b)). This imprint of one braid onto the next braid, generates an in-phase arrangement of streamwise vortices which reside in the successive braids [20]. The existence of both mode A and mode B of vortex shedding, has been confirmed by many three-dimensional numerical

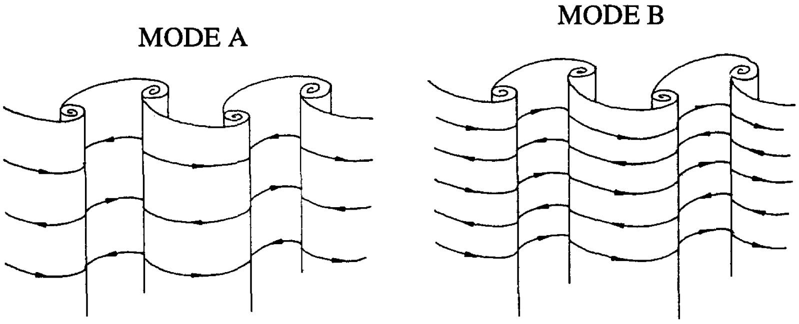

Figure 2.5: Out-of-phase and in-phase symmetry of mode A and mode B three-dimensional instabilities respectively (Figure taken from Ref. [20]).

simulations [22, 23, 24, 25].

Finally, large-scale spot-like three-dimensional structures called "vortex dislocations" represent another natural, fundamental feature of wake transition (see Figure 2.3(c)). At times, spontaneously along the span, shedding of vortices in neighboring cells in the near-wake falls out-of-phase with respect to each side [17]. This leads to a breakdown of the primary vortex core, modifying substantially the spanwise structures and causing the flow to become irregular. Williamson [17] suggests that this phenomenon is mostly responsible for the low-frequency fluctuations reported by Roshko [10] to characterize the transition regime, and the appearance of turbulent motion. However Williamson [20] places emphasis on the difference between these "two-sided" dislocations and the "one-sided" end-dislocations that are associated with the effects of end conditions, and which are only formed near the ends of the span between spanwise cells of different frequencies. Proper vortex dislocations are two-sided and are not an artifact of end conditions. They are triggered naturally, and their development is systematic and repetitive [19].

Wake transition is further characterized by velocity and pressure modifications. Various experimental and numerical investigations [15, 23, 24, 25] have shown the existence of two discontinuities in the evolution of Strouhal frequency with respect to Reynolds number, as shown in Figure 2.6(a). At the first discontinuity, the Strouhal frequency drops from the laminar curve to one corresponding to a mode A three-dimensional shedding plus vortex dislocations. Despite the debate among researchers about the role of large scale dislocations in the hysteretic behaviour of St–Re relationship, it is widely believed, and has been numerically confirmed [25], that the appearance of dislocations is responsible for this event. As the Reynolds number is increased further, another discontinuity is observed, this time related to mode B instabilities. This discontinuity is not hysteretic. Experiments have shown that the transition from mode A to mode B shedding takes place in the Re range 190 to 260.

According to Williamson [20] and Roshko [26] the presence of instabilities in the flow is also accompanied by variations of the base pressure coefficient, as shown in

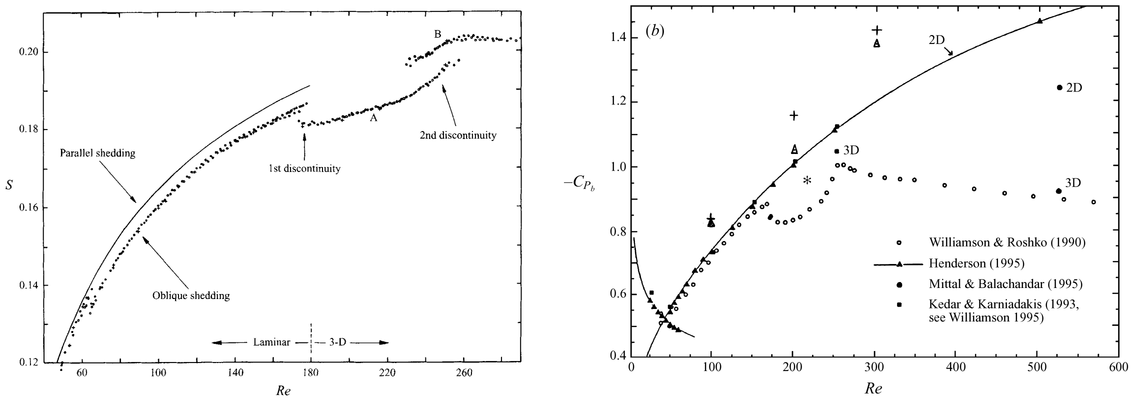

(a) **(b)**

Figure 2.6: (a) Strouhal number St, versus Re, and (b) base pressure coefficient C_{pb}, versus Re over the laminar and 3-D transition regimes, for the case of an unconfined circular cylinder (Figures taken from Refs. [17] and [24] respectively).

Figure 2.6(b). Around $Re = 180$ a drop in the pressure coefficient is observed which is associated with the presence of mode A instability and vortex dislocations. With increasing Re, the the pressure coefficient rises again until it reaches a local maximum around $Re = 260$. From that point on, the three-dimensional vortex pattern changes to one corresponding to mode B instability, and the base suction begins to decrease as the three-dimensional structures become more disordered.

2.3 Circular cylinder placed in a channel

When the circular cylinder is *confined* between plates parallel to the cylinder axis, the nature and the stability of the resulting flow is modified and differs from its unconfined counterpart due to the blockage effects induced by the stationary walls.

A typical confined geometrical configuration is shown in Figure 2.7. The geometry consists of an infinitely long circular cylinder, of diameter D, placed in a plane channel. In this case, two additional dimensionless parameters govern the flow, namely the blockage ratio, β, and the gap ratio, γ. The ratio of the cylinder diameter to the distance between the channel walls H, defines the blockage ratio, $\beta = D/H$, while the

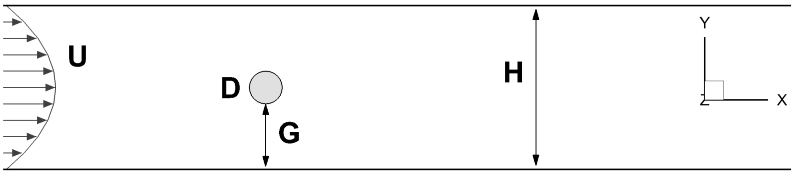

Figure 2.7: Geometrical configuration for the case of a circular cylinder confined in a plane channel.

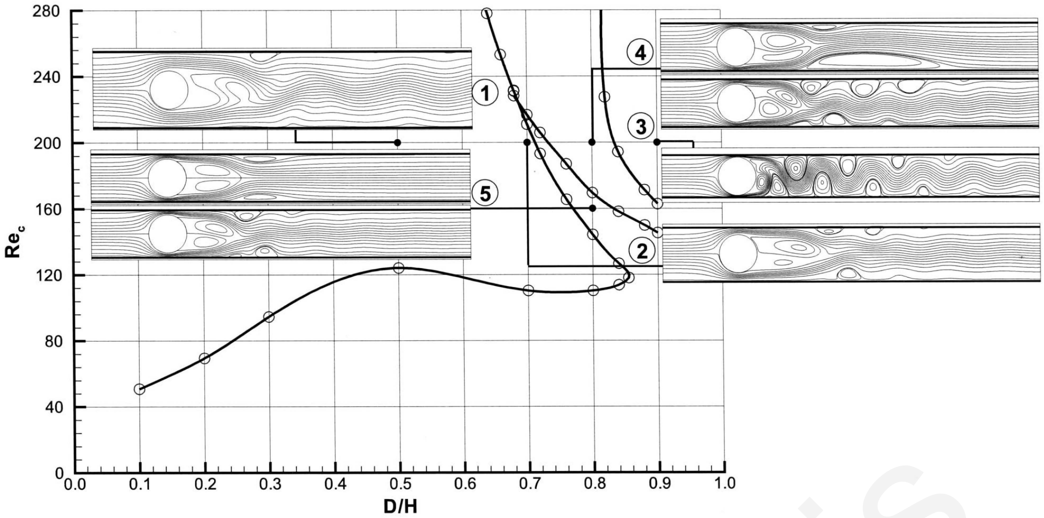

Figure 2.8: Change of critical Reynolds number for the onset of vertex shedding, with blockage ratio, β. Plots show change of time-dependent flow with Re and β (Figure taken from Ref. [27]).

ratio of the minimal distance between the cylinder wall and the wall of the channel G, over the cylinder diameter, defines the gap ratio, $\gamma = G/D$.

To analyze the influence of the blockage ratio on the wake of the flow, the case of a circular cylinder placed symmetrically in a channel is considered. At small blockage ratios, $\beta < 0.1$, the flow is quite similar to the unconfined case, and blockage effects may be ignored. In the range $0.1 < \beta < 0.6$, blockage ratio effects are more pronounced. In the laminar flow regime, for which the wake consists of a pair of standing vortices attached behind the cylinder, when the blockage ratio is increased, which is equivalent to moving the channel walls closer to the cylinder, the flow around the cylinder accelerates based on the continuity equation, and the flow carries locally higher momentum. As a result, with increasing β, the point where boundary layer separation occurs is pushed leeward, leading to a shorter and more narrow recirculation zone, compared with that of a lower β value [28, 29, 30, 31]. Furthermore, increasing β, enhances stability of the near wake, and transition from steady to unsteady flow in the laminar flow regime is delayed [27, 28, 32], with respect to the unconfined cylinder case, as seen in Figure 2.8. The onset of the instability is caused by the formation of gathers (spikes) along the shear layers, and the oscillation of the wake stagnation point in the transverse direction [4, 8]. The presence of the channel walls suppress such disturbances, hence transition occurs at higher Reynolds numbers [32]. Another interesting phenomenon related with blockage effects, is the inversion of the von Kármán vortex street, in the unsteady regime. Soon after a pair of vortices is shed from the top and bottom of the cylinder, they are repelled from the channel walls, and eventually their trajectories intersect with the vortices ending in opposite vertical positions with respect to the unconfined case [33]. Further increasing the blockage ratio, $\beta > 0.6$, alters the overall flow and

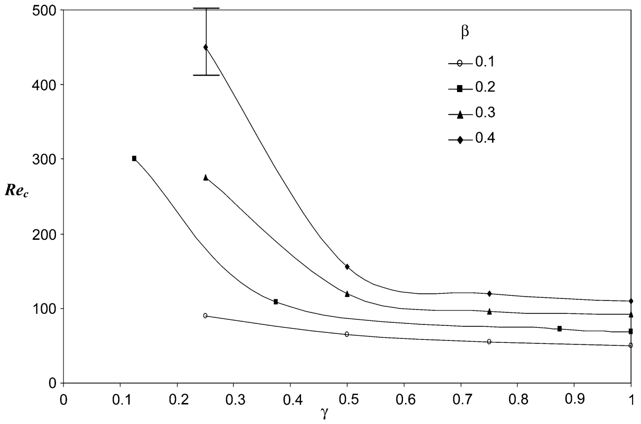

Figure 2.9: Variation of the critical Reynolds number with blockage, β, and gap ratio, γ (Figure taken from Ref. [34]).

vortex structure radically. In addition to the first critical Hopf bifurcation observed for values of β below 0.6, two more curves of neutral stability were found [27], and also vortices start to shed both from the cylinder and the channel walls the coupling of which modifies the wake flow and makes it much more complex (see Figure 2.8).

In the case where the cylinder is placed away from the channel axis of symmetry, an asymmetric blockage arises. In this kind of blockage, the influence of the wall nearest to the cylinder is dominant. For a given β, decreasing the gap ratio, i.e. moving the cylinder closer to one of the channel walls, the critical Reynolds number at which the flow becomes unsteady increases as shown in Figure 2.9. This delay of transition is attributed to the coupling of the boundary layer at the wall with that of the cylinders, which stabilizes the flow [33, 34]. Afterwards in the unsteady regime, with decreasing γ the once regular structure and symmetry of vortex shedding is distorted, and a single raw of like-signed vortices is observed.

All the aforementioned studies, where either two-dimensional numerical simulations or experiments restricted to Reynold numbers where the flow remained two-dimensional. Studies investigating three-dimensional effects at low Reynolds numbers, either experimentally or numerically, are relatively scarce. Almost all three-dimensional studies are at higher Reynolds numbers, in the range $O(10^4)$–$O(10^5)$ [35, 36, 37, 38]. These studies investigate the flow characteristics in the wake of a circular cylinder placed near a plane wall at various gap heights, G, with the further wall being at infinity. Their results show that, for small gap ratios, $\gamma \leq 0.3$, vortex shedding is suppressed. For larger gap ratios, some flow quantities, such as the Strouhal number, remain remarkably constant and independent of the gap ratio. Moreover, Wang and Tan [38] found that for the intermediate gap ratios $0.3 \leq \gamma \leq 0.6$ the influence of the wall is fairly strong, causing the flow to develop a distinct asymmetry about the cylinder centreline.

Only, two quite recent studies focused on the development of three-dimensional effects for a confined circular cylinder. Rehimi *et al.* [39], carried out experimental studies in the Reynolds number range 30–277 for a blockage ratio of 1/3. In their work, three-dimensional instabilities were observed having close similarities with mode A and mode B patterns of vortex shedding found in the unconfined case. However, in their experiments, mode A appeared at $Re = 159$, which is considered premature relative to the critical value of $Re \simeq 189$ for the onset of this instability in the unconfined case. They attributed this behavior to wall perturbations. The second study was that of Camarri and Giannetti [40] where a three-dimensional Floquet stability analysis was used to investigate the three-dimensional stability of the wake behind a symmetrically confined circular cylinder for a different blockage ratio of 1/5, for Re up to 300. Their results showed that the transition to a three-dimensional state has the same space-time symmetries as the unconfined case. They also found that the critical Reynolds numbers for the onset of instabilities, when based on the centerline velocity, are similar to the ones found in Barkley and Henderson [6] for the unconfined case. However, they observed that due to the inversion of the wake vortices, the linear unstable modes are significantly affected, leading to differences between the confined and the unconfined cases.

2.4 Effect of end plates

When the cylinder is further *confined* between end plates normal to the cylinder axis, in contrast to the infinitely long cylinder (unconfined case or channel flow), the wake flow is highly three-dimensional. End effects that occur at the junction of the cylinder with a wall, alter the flow structure in regions both upstream and downstream of the cylinder and very complex three-dimensional flow structures arise.

Figure 2.10, represents a typical geometrical configuration, that incorporates end effects. The geometry consists of a circular cylinder of finite height, with both ends of the cylinder being attached to side walls. When compared with the confined channel flow case, a different governing parameter appears. This is the aspect ratio, $\alpha = W/D$, which is defined by the ratio of the cylinder length over its diameter.

One important three-dimensional feature associated with the presence of a wall at

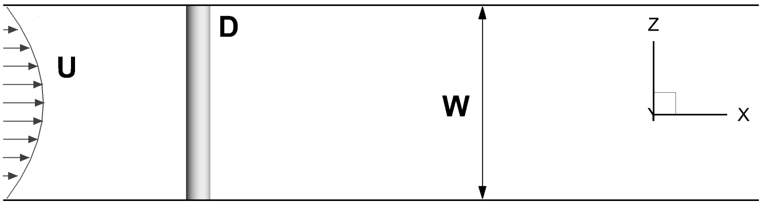

Figure 2.10: Geometrical configuration for the case of a circular cylinder confined by end plates.

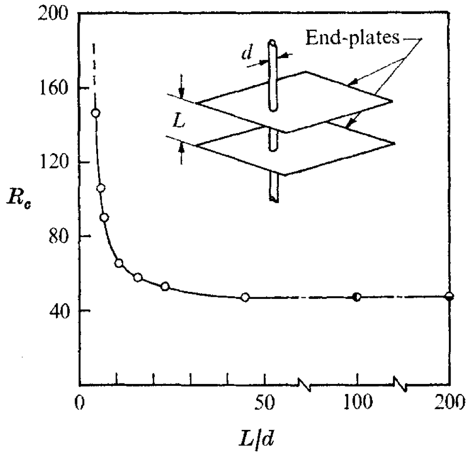

Figure 2.11: Change of critical Reynolds number, for the transition from steady to unsteady flow, with aspect ratio, α (Figure taken from Ref. [42]).

the end of the cylinder is the formation of a horseshoe vortex system [2, 41]. At the cylinder-wall juncture, the cylinder penetrates the wall boundary layer, creating a region of adverse pressure gradient. As a result, as the flow approaches the wall-mounted cylinder, a three-dimensional separation of this boundary layer occurs (upstream of the cylinder) producing a system of vortices that is swept symmetrically around the base of the cylinder. Due to its shape, it is usually referred as the horseshoe-vortex system. The characteristics of such a system depend upon the thickness of the wall boundary layer and the diameter of the cylinder.

Like the blockage and gap ratios, the aspect ratio is also a very important parameter when considering the stability of the steady wake [32, 42]. For large aspect ratios, $\alpha > 25$, the critical Reynolds number for the onset of vortex shedding remains relatively unaffected, as seen in Figure 2.11 [42]. However, for smaller aspect ratios, $\alpha < 25$, as α is decreased, the standing vortex behind the cylinder is stabilized and the formation of a vortex street is suppressed until larger Reynolds numbers, with an exponential increase.

End conditions also have a significant influence on the vortex shedding phenomenon. As soon as vortex shedding takes place, the vortices adjacent to the end walls begin to bend, due to the lower velocity with respect to the center of the span. This leads to an oblique shedding pattern, i.e. vortices are shed at an oblique angle with respect to cylinder axis, which can be observed even for cylinders with very large aspect ratios [43, 44]. In addition, cells with different frequencies and shedding angles, at different spanwise locations are formed [45, 46, 47]. This difference means that the number of vortices in neighbouring cells cannot be the same, causing the appearance of vortex dislocations [44] or vortex splitting [48] at the cell boundaries.

All these studies clearly show that the presence of the side walls substantially affects the forces and the vortex-shedding phenomena from the cylinder. Such changes in the flow patterns are also reflected in the values of the drag and lift coefficients, and Strouhal number. The situation becomes even more complex when blockage and end effects are combined, i.e. in the case of a cylinder placed in a rectangular duct with all walls being in close proximity. However even though such flows are common in many engineering systems (e.g., heat exchangers, cooling systems for electronic components etc.), only a handful of studies are available.

2.5 MHD duct flow over a cylinder

In the case where the flow is exposed to a uniform magnetic field, of amplitude B_0, and the fluid is electrically conducting with an electric conductivity σ, the wake-flow characteristics are dominated by magnetohydrodynamics (MHD) phenomena. A detailed overview of MHD can be found in the books of Davidson [49], and Müller and Bühler [50].

Including the magnetic field effects in the Navier-Stokes equations in dimensionless form, introduces a new governing parameter in addition to Re found in the hydrodynamic case. This is the interaction parameter, $N = \sigma W B_0^2/(\rho U_o)$, which represents the ratio of electromagnetic to inertial forces. The interaction parameter can be expressed in terms of the Reynolds number as $N = (DHa^2)/(WRe)$, where $Ha = WB_0\sqrt{\sigma/(\rho\nu)}$ is the Hartmann number, the square of whitch characterizes the ratio of electromagnetic to viscous forces.

This study is limited to the particular case of a circular cylinder placed symmetrically in a rectangular duct, under the influence of an external homogeneous magnetic field as shown in Figure 2.12. The magnetic field is applied along the spanwise direction z, aligned with the cylinder axis. Furthermore, the walls of the cylinder and the duct are assumed to be electrically insulating. The two dimensionless parameters characterizing the geometry, are the blockage $\beta = D/H$ and the aspect ratio $\alpha = W/D$, which were described in previous sections.

Any movement of a conducting fluid under the influence of a magnetic field, $\mathbf{B}_0$,

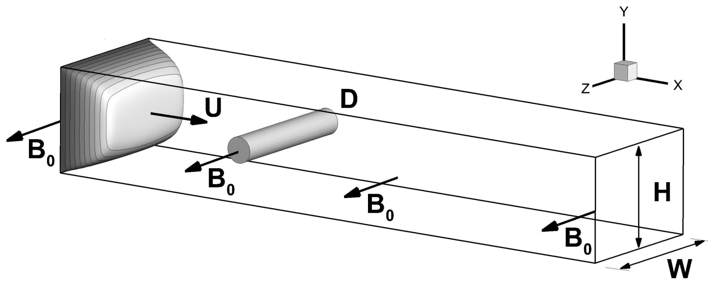

Figure 2.12: Geometrical configuration for the case of a circular cylinder confined in a rectangular duct under the influence of an externally applied magnetic field.

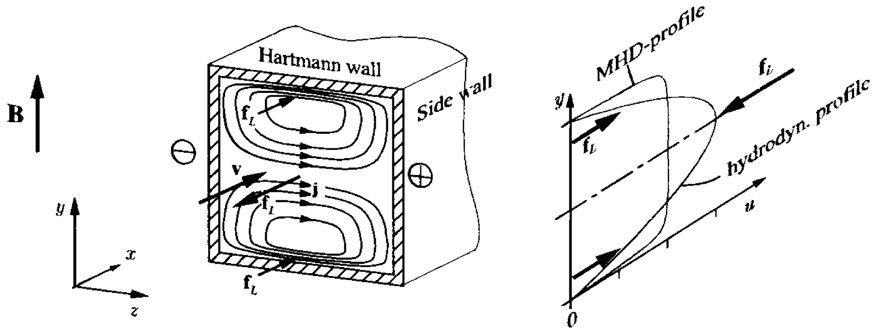

(a) (b)

Figure 2.13: (a) Sketch of current paths and corresponding Lorentz forces, f_L, at the cross section of a rectangular duct with insulating walls, and (b) influence of f_L on the velocity profile (Figure taken from Ref. [50]).

causes an electric field $\mathbf{u} \times \mathbf{B}_0$ to develop, and as a result electric currents, of density $\mathbf{j}$, are generated. In turn, these currents, induce a second magnetic field. The ratio of the induced magnetic field over the externally applied field is termed the magnetic Reynolds number, R_m [51]. However, for most cases of liquid metal flow encountered in industrial applications, the magnetic Reynolds number is generally very small, $R_m \ll 1$, hence the induced magnetic field is found to be negligible when compared to the imposed magnetic field. The interaction of the dominant imposed magnetic field with the induced currents gives rise to an MHD force, known as the Lorentz force, $\mathbf{j} \times \mathbf{B}_0$.

The Lorenz force acts in two ways; first it modifies the velocity distribution of the primary flow and, second due to its dissipative nature, it dampens the fluctuations of the unsteady flow [50, 49]. In the case of a rectangular duct with insulating walls considered here, the electric currents induced in the bulk flow are closed within the fluid, as shown in Figure 2.13. The magnitude of the resulting Lorentz forces depends linearly on the velocity, and tends to decelerate the fluid near the center of the duct. As a result, the flow exhibits a large, uniform core, where the velocity becomes nearly constant, and relatively thin boundary layers, where the velocity falls to zero. The boundary layers that develop at the walls parallel to the magnetic field, are called Shercliff layers, and have a thickness of $\delta_S \sim 1/\sqrt{Ha}$. At the walls perpendicular to the magnetic field, thinner boundary layers develop with sharp velocity gradients, called Hartmann layers [52]. Depending on the intensity of the magnetic field, these layers can be extremely thin ($\delta_H \sim 1/Ha$).

In such wall-bounded flows, if both the Hartmann number and the interaction parameter are very high, i.e. $Ha \gg 1$ and $N \gg 1$, any velocity variations parallel to the direction of the magnetic field are strongly suppressed by Joule dissipation, except in the viscous Hartmann layers [49, 53]. In these regions, because of the no-slip boundary condition, strong velocity gradients persist. Moreover, Lorenz forces diffuse momentum along the field lines and vortices whose axes are inclined to the magnetic field are

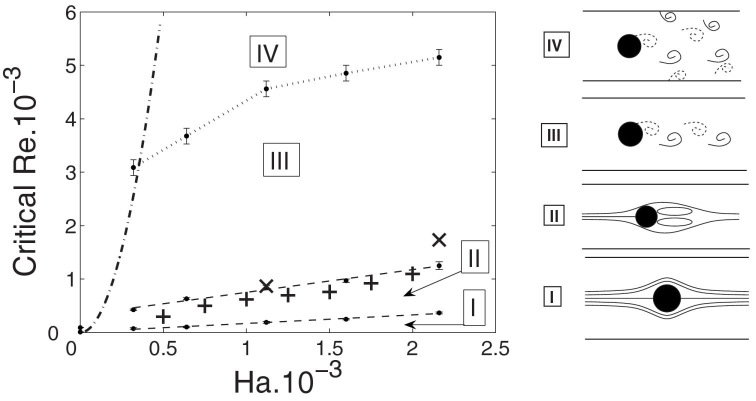

Figure 2.14: Variation of the critical Reynolds number for the appearance of different flow regimes, with Hartmann number, Ha (Figure taken from Ref. [56]).

strongly damped. On the other hand, vortices whose axes are parallel to the magnetic field are only influenced by friction in the Hartmann layer, which, however is significantly (Ha times) less efficient than Joule damping [49, 53]. These electromagnetic effects drive the flow toward a quasi-two-dimensional state, in which one can distinguish a core flow region, where both the gradient of the velocity and the velocity component in the direction of the magnetic field are negligible, and two thin Hartmann layers, where Lorentz forces are balanced by the viscous friction. Under these conditions, integrating the three-dimensional flow equations along the direction of the magnetic field, and adding a linear breaking term containing the net effect of the Lorentz forces, yields a model equation satisfying the two-dimensional hydrodynamic Navier-Stokes equation [54, 55]. An obvious advantage of this quasi-two-dimensional (Q2D) model is that it can reduce the computational cost of an initially three-dimensional problem by translating it to a two-dimensional one. Traditionally, most of the simulations of MHD flows in such geometrically complex domains, as the one considered in this study, rely on this model due to the high computational costs associated with full three-dimensional simulations.

While several studies in the literature deal with MHD flow passed a cylinder, only a few consider the case where the magnetic field is aligned with the axis of a confined cylinder. Thus, the only results previously reported in the literature for this case are from Refs. [56, 57, 51, 58, 59]. Results for $N \gg 1$, showed that the stability of the wake flow is significantly influenced by the magnetic field. References [51, 56, 57] showed that for moderate and high values of the Hartmann number, $Ha \geq 320$, the onset of vortex shedding is delayed till higher Reynolds numbers. For a given blockage ratio β, a quasi-linear dependence of the corresponding critical Reynolds number on Ha has been observed (e.g. dashed line separating regimes II and III in Figure 2.14) [51, 56, 57]. This behaviour was attributed to the damping of the fluctuations of the unsteady flow by the magnetic field. Hussam *et al.* [57], carrying out a parametric study based on the duct

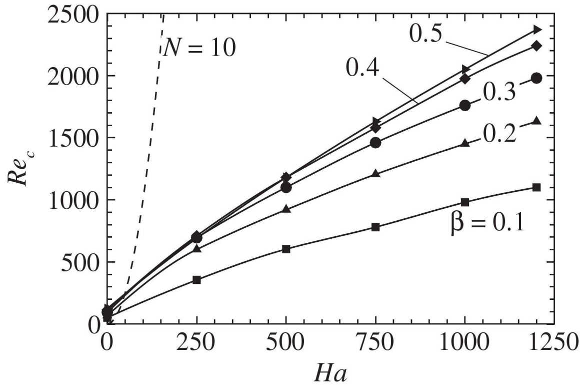

Figure 2.15: Variation of the critical Reynolds number for the onset of vortex shedding, with Hartmann number, Ha, and blockage ratio, β (Figure taken from Ref. [57]).

blockage ratio, observed furthermore that with increasing β, the slope of the critical Reynolds number curve is also found to increase (see Figure 2.15). This was associated with the interaction of the cylinder wake and the side walls, as already described in a previous section [57, 58]. By increasing further the Reynolds number, experiments from Frank *et al.* [51] and numerical simulations from Dousset and Pothérat [56] have revealed the presence of an additional flow regime that follows the laminar periodic vortex shedding, and which is not found in the purely hydrodynamic case (regime IV in Figure 2.14). In this regime, the flow is characterized by irregular vortex patterns, with secondary vortices being released from the side walls [56]. Again, as the imposed magnetic field is increased, transition to this regime is delayed. Mück *et al.* [59] showed that for interaction parameters in the range $2 \leq N \leq 10$ transition from a time-dependent three-dimensional flow to a two-dimensional state occurred. After the transition to a quasi-2D flow, cigar-shape vortices (larger diameter at the center, smaller diameter near the Hartmann walls) were observed (see Figure 2.16). They attributed the curvature of the vortices obtained near Hartmann walls not to the higher viscous damping in these regions, but rather to an inertial contribution to the electric potential in the core flow.

However, most of the aforementioned studies considering the case of a cylinder confined in a duct were not based on a fully three-dimensional analysis. Refs. [56, 57, 58] performed numerical simulations using a Q2D model. Even in the experimental study carried out by Frank *et al.* [51], a non intrusive measurement device was used to calculate the core flow quantities by measuring the electric potential only at one Hartmann wall. Only Mück *et al.* [59] performed 3-D simulations, however an analytical wall boundary model was again used, a fact that precluded the resolution of the Hartmann layers, therefore making impossible the complex analysis of the interaction between the vortices and the walls. In addition, due to the limited available computer resources at that time only two Reynolds numbers could be investigated ($Re = 200$ and 250), and

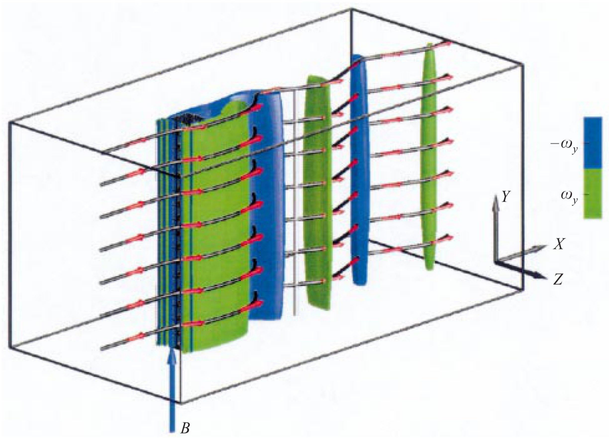

Figure 2.16: For $N \sim 1$, vortices aligned with the magnetic field are not strictly two-dimensional, but have a slight curvature along the direction of the magnetic field (Figure taken from Ref. [59]).

the Hartmann number was varied in the range of $63 < Ha < 850$.

Chapter 3

Important ingredients of numerical solution method

The equations describing fluid flow have been known for over 150 years. However, these equations are very complex and highly non-linear, making them extremely difficult to solve. In the range of practical problems, analytical solutions are known only for a few very simple cases. However, thanks to the availability and rapidly increasing speed of supercomputers, an alternative approach is to solve the governing equations numerically on a computer. This area of solving approximations to the governing fluid-flow equations using numerical methods is known as Computational Fluid Dynamics (CFD).

The field of CFD is as large as the field of fluid mechanics itself, and numerous books have been written regarding the mathematical modelling and numerical analysis employed in CFD for solving the partial differential equations that describe fluid flows and related phenomena [60, 61, 62, 63]. Therefore, in this chapter we shall focus our attention only in the techniques and methods implemented in the numerical code used in this study. All computations have been performed using the unstructured nodal-based finite-volume code CDP [1] as a general platform. The CDP code has been developed by the Center of Turbulence Research (CTR) at Stanford University. It should be noted here, that for the study of MHD fluid flow, we have complemented this code with a module to compute the additional force (Lorentz force) that appears in the governing equations. CDP is a highly scalable parallel code, capable of time-dependent simulations on fully unstructured grids with over 100 million control volumes.

This chapter is divided into five sections. In Section 3.1, we review the general governing equations of hydrodynamic and magnetohydrodynamic flow. In Section 3.2 we give a general outline of the finite-volume method used for the discretization of the partial differential equations describing the flow. In Sections 3.3 and 3.4 we discuss various grid-generation methods and mesh structures. Finally, in Section 3.5 we

---

[1] The code is named after the late Charles David Pierce (1969-2002)

introduce the methods for solving the discrete equations, focusing primarily on the finite-volume method. Special problems arising due to the numerical approximation of the flow equations are also discussed and methods to resolve them are also introduced in this section.

3.1 Mathematical model

The first step in any analysis is the derivation of the basic equations describing the behaviour of the flow These equations basically represent mathematical statements of fundamental conservation laws of physics: conservation of mass and momentum.

Before turning our attention to the derivation of the governing equations, we need to define the system on which the basic balances will be made. It is common practice in CFD to treat fluid as a continuum. This means that the molecular structure of matter can be ignored, and even in an infinitesimally small element of the fluid, macroscopic properties, such as velocity, pressure and density, are assumed not to be influenced by individual molecules. In this way, we can focus our attention on an infinitesimally small region in space through which matter is flowing and apply to it the basic conservation laws (see Figure 3.1). The defined space is sometimes called a control volume.

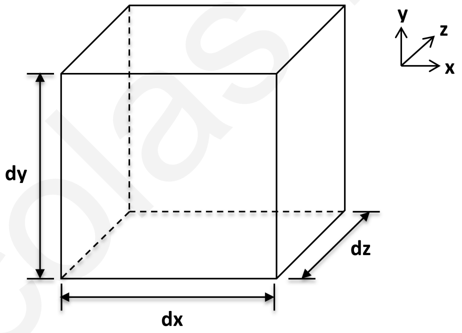

Figure 3.1: Illustration of a fluid element in cartesian coordinates.

The conservation of a certain flow quantity in a control volume analysis can be expressed in the following form:

$$\textbf{production rate} = \textbf{output rate} - \textbf{input rate} + \textbf{accumulation rate} \tag{3.1}$$

This equation states that the amount of a property created in the control volume per unit time, equals the rate of change of the property stored within the control volume plus the net flux of the property crossing the boundaries of the control volume. Applying the basic conservation laws to the control volume leads to the fluid flow equations.

3.1.1 Continuity equation

A basic principle of science and engineering is the conservation of mass. In particular, the law of conservation of mass states that, given an isolated system, the amount of matter present in the system remains constant over time. Alternatively, mass may be neither created nor destroyed.

Let us now consider an infinitesimal control volume (CV) of dimensions dx, dy and dz within a fluid flowfield in a cartesian coordinate system, as shown in Figure 3.1. The fluid velocity and density are respectively $\mathbf{u}$ and ρ, with the components of velocity being u, v, w. Following equation (3.1) and the definition of mass law, which states that mass may be neither created nor destroyed, mass conservation may be expressed verbally as:

$$\left\{\begin{array}{c}\text{rate of mass}\\ \text{accumulation in the CV}\end{array}\right\} = \left\{\begin{array}{c}\text{rate of mass entering minus}\\ \text{rate of mass leaving the CV faces}\end{array}\right\} \tag{3.2}$$

The time rate of change of mass within the CV is:

$$\frac{\partial}{\partial t}(\rho\, dx\, dy\, dz) = dx\, dy\, dz\, \frac{\partial \rho}{\partial t}\,. \tag{3.3}$$

Mass flow terms occur on all six faces. If the mass flux entering the volume through the left face is $\rho u\, dy\, dz$, the mass leaving the opposite side of the volume is:

$$\left[\rho u + \frac{\partial(\rho u)}{\partial x} dx\right] dy\, dz\,. \tag{3.4}$$

Summing up the contributions from all six faces of the elemental control volume leads to a partial differential equation, which in index notation reads:

$$\frac{\partial \rho}{\partial t} + \frac{\partial(\rho u_i)}{\partial x_i} = 0\,. \tag{3.5}$$

This equation is known as the continuity equation in cartesian coordinates. In the case of fluids that are incompressible, this equation reduces to:

$$\frac{\partial u_i}{\partial x_i} = 0\,. \tag{3.6}$$

3.1.2 Momentum equation

Another important principle is the conservation of momentum, also known as Newton's second law of motion. In the context of the control volume method, the law of momentum conservation states that:

$$\left\{\begin{matrix}\text{rate of increase}\\ \text{of momentum}\\ \text{in the CV}\end{matrix}\right\} = \left\{\begin{matrix}\text{net momentum influx}\\ \text{crossing the faces}\\ \text{of the CV}\end{matrix}\right\} + \left\{\begin{matrix}\text{any external forces}\\ \text{acting on the CV}\end{matrix}\right\} \tag{3.7}$$

Following an analogous analytical formulation as used above for deriving the continuity equation, a first expression for the conservation of momentum in differential form is:

$$\left[\frac{\partial(\rho u_i)}{\partial t} + \frac{\partial(\rho u_i u_j)}{\partial x_j}\right] dx\,dy\,dz = \sum F_i\,, \tag{3.8}$$

where $\sum F_i$ is the sum of externally applied forces on the control volume. On the left hand side of the equation, the first term represents the time rate of change of momentum within the CV, while the second term is associated with the momentum fluxes.

Let us turn our attention now on the forces acting on the control volume. These forces can be expressed as the sum of body forces, f_{bi}, and surface forces, f_{si} , per unit volume:

$$\frac{1}{dx\,dy\,dz}\sum F_i = f_{bi} + f_{si}\,. \tag{3.9}$$

Body forces act on the entire control volume, and include forces induced by external fields, such as gravity and magnetic fields. The only body force we shall consider in this study is the Lorentz force. Surface forces arise due to the stresses on the sides of the control surface. These stresses, σ_{ij}, are the sum of the hydrostatic pressure, p, plus viscous stresses τ_{ij} and can be defined by the equation:

$$\sigma_{ij} = -p\delta_{ij} + \tau_{ij}\,, \tag{3.10}$$

where δ_{ij} is the Kronecker's delta. Pressure is negative by convention. Stresses, σ_{ij} and τ_{ij}, are second-rank nine-component tensor quantities, unlike velocity which is a tree-component vector, and are identified by two subscripts. The first subscript i indicates the normal direction of the face on which the stress acts, while the second subscript j identifies the direction of the stress. The area of the element's face is denoted by the vector, A_i. Thus the force is really the inner product of $\mathbf{A}$ and $\boldsymbol{\tau}$, i.e. $F_i = A_j\tau_{ji}$.

Combining the contribution to the momentum balance coming from the fluid flow with the one coming from the stresses we get:

$$\frac{\partial(\rho u_i)}{\partial t} + \frac{\partial(\rho u_i u_j)}{\partial x_j} = -\frac{\partial p}{\partial x_i} + \frac{\partial \tau_{ik}}{\partial x_k} + f_{bi}\,. \tag{3.11}$$

Using the continuity equation (3.5) the above equation reduces to:

$$\rho \frac{\partial u_i}{\partial t} + \rho u_j \frac{\partial u_i}{\partial x_j} = -\frac{\partial p}{\partial x_i} + \frac{\partial \tau_{ik}}{\partial x_k} + f_{b_i} \, . \tag{3.12}$$

This equation is the differential momentum equation in its viscous stress approach, and it is valid for any fluid in general motion. However, despite the brief and compact form of the equation, we still need to write the viscous stresses in terms of velocity components. Otherwise the system of equations (continuity and momentum equation), can not be closed, i.e. there are fewer equations than the unknown dependent variables, and solution is not possible.

To do so, equation (3.12) must be coupled with a material constitutive equation. A constitutive equation is an empirical relation that can be applied to particular materials under limited circumstances. Under the assumption of a Newtonian fluid, i.e. an idealized fluid that approximates the behaviour of air, water and many other fluids, the following constitutive equation can be used.

$$\tau_{ij} = -\frac{2}{3}\mu S_{kk}\delta_{ij} + 2\mu S_{ij} \, , \tag{3.13}$$

where μ is the fluid viscosity and S_{ij} the rate of strain tensor given in terms of velocity gradients as:

$$S_{ij} = \frac{1}{2}\left(\frac{\partial u_i}{\partial x_j} + \frac{\partial u_j}{\partial x_i}\right) \, . \tag{3.14}$$

Equation (3.13) is called the Newton's Law of viscosity and linearly relates the stress to the rate of strain in a fluid medium.

For an incompressible fluid, with specified density and viscosity, which obeys the Newtonian constitutive equation, substitution of equation (3.13) in (3.12) yields the well known Navier-Stokes equations of motion:

$$\underbrace{\rho \frac{\partial u_i}{\partial t}}_{Transient\ term} + \underbrace{\rho u_j \frac{\partial u_i}{\partial x_j}}_{Convective\ term} = \underbrace{-\frac{\partial p}{\partial x_i}}_{Pressure\ term} + \underbrace{\mu \frac{\partial^2 u_i}{\partial x_j^2}}_{Diffusive\ term} + \underbrace{f_{b_i}}_{Body forces} \, . \tag{3.15}$$

All fluids under consideration in this work are assumed to obey equation (3.15).

3.1.3 Magnetohydrodynamics equations

In the case of electrically conducting fluids in the presence of a magnetic field magnetohydrodynamic (MHD) phenomena occur. An extensive introduction to MHD is available in references [49, 50]. Any movement of a conducting fluid in a magnetic field, **B**, causes an electric field, **E**, to develop, and as a result electric currents, of current density **j**, are generated. The interaction of the imposed magnetic field with the induced currents gives rise to an MHD force, known as the Lorentz force:

$$\mathbf{f}_L = \mathbf{j} \times \mathbf{B}\,. \tag{3.16}$$

The Lorentz force is explicitly added to the momentum balance which now, in more compact vector notation, takes the form:

$$\rho\frac{\partial \mathbf{u}}{\partial t} + \rho\mathbf{u}\cdot\nabla\mathbf{u} = -\nabla p + \mu\nabla^2\mathbf{u} + \mathbf{j}\times\mathbf{B}\,. \tag{3.17}$$

Having described, with the aforementioned equations, the motion of a conducting fluid interacting with a magnetic field, one needs to describe the evolution of the electric and magnetic field in the presence of electric charges or current. One of the most elegant and concise ways to state the laws of classical electromagnetism, is through the Maxwell's equations, which in differential form read:

$$\boldsymbol{\nabla}\cdot\mathbf{E} = \frac{q}{\epsilon_0} \tag{3.18}$$

$$\boldsymbol{\nabla}\cdot\mathbf{B} = 0 \tag{3.19}$$

$$\boldsymbol{\nabla}\times\mathbf{E} = \frac{\partial \mathbf{B}}{\partial t} \tag{3.20}$$

$$\boldsymbol{\nabla}\times\mathbf{B} = \mu_0\left(\mathbf{j} + \epsilon_0\frac{\partial \mathbf{E}}{\partial t}\right)\,. \tag{3.21}$$

Here μ_0 denotes the magnetic permeability and ϵ_0 denotes the electric permettivity of the conducting medium. Equation (3.18) means that the total flux of an electric field crossing a closed surface equals the charge density contained inside. Equation (3.19) tells us that the flux of a magnetic field through a closed surface is zero. Equation (3.20) describes how a magnetic field that is changing in time induces an electric field. Similarly, equation (3.21) describes how the current flow and a changing electric field, produces a magnetic field.

Following equations (3.18) and (3.19), the electric and magnetic field can be defined using a scalar, ϕ, and a vector potential, $\mathbf{A}$, as:

$$\mathbf{E} = -\boldsymbol{\nabla}\phi - \frac{\partial \mathbf{A}}{\partial t}\,, \tag{3.22}$$

$$\mathbf{B} = -\boldsymbol{\nabla}\times\mathbf{A}\,. \tag{3.23}$$

The electromagnetic potentials ϕ and $\mathbf{A}$ are defined as functions of space and time.

The current density is given by Ohm's law which reads as,

$$\mathbf{j} = \sigma(\mathbf{E} + \mathbf{u}\times\mathbf{B})\,, \tag{3.24}$$

where σ the electrical conductivity of the conducting medium.

The temporal evolution of the magnetic field, is linked with the advection of the magnetic field by the velocity field and the diffusion of the magnetic field within the domain, with the induction equation. We can derive the induction equation using equations (3.19), (3.20), and the curl of equations (3.21), (3.24):

$$\frac{\partial \mathbf{B}}{\partial t} = \frac{1}{\sigma \mu_0} \nabla^2 \mathbf{B} + \nabla \times (\mathbf{u} \times \mathbf{B}) . \tag{3.25}$$

At this point, we need to note that in this thesis we are interested in fields where the intensity of the magnetic field is assumed to be constant. Under this assumption the above equation is rendered unnecessary. Furthermore, using equation (3.22), for time-independent magnetic fields, Ohm's law becomes:

$$\mathbf{j} = \sigma(-\boldsymbol{\nabla}\phi + \mathbf{u} \times \mathbf{B}) . \tag{3.26}$$

To be able to solve the above equation we need to define the electric potential in terms of the velocity components and the magnetic field. For this we need Ampere's law (see equation (3.21)). For slowly varying electromagnetic processes, in which the occurring velocities and related time scales are much smaller compared to the speed of light, the last term in equation (3.21) is negligible and can be dropped [50], simplifying Ampere's law to:

$$\boldsymbol{\nabla} \times \mathbf{B} = \mu_0 \mathbf{j} . \tag{3.27}$$

Taking the divergence of (3.27), and noting that $\nabla \cdot \nabla \times \mathbf{B} = 0$, yields,

$$\boldsymbol{\nabla} \cdot \mathbf{j} = 0 . \tag{3.28}$$

That is to say, the current density lines are closed.

Combining now equations (3.28) and (3.26), gives a Poisson equation

$$\boldsymbol{\nabla}^2 \phi = \boldsymbol{\nabla} \cdot (\mathbf{u} \times \mathbf{B}) , \tag{3.29}$$

which can be used in to obtain the electric potential.

3.1.4 Dimensionless form of equations

Let us now briefly summarize the equations that describe the flow of an incompressible Newtonian fluid. These are the continuity and momentum equations:

$$\boldsymbol{\nabla} \cdot \mathbf{u} = 0 , \tag{3.30}$$

$$\frac{\partial \mathbf{u}}{\partial t} + \mathbf{u} \cdot \boldsymbol{\nabla} \mathbf{u} = -\frac{1}{\rho} \boldsymbol{\nabla} p + \nu \boldsymbol{\nabla}^2 \mathbf{u} + \frac{1}{\rho} (\mathbf{j} \times \mathbf{B}) . \tag{3.31}$$

with ν being the kinematic viscosity of the fluid. The last term in the momentum balance is the Lorentz force and appears only in the case of an electrically conducting fluid under the presence of a magnetic field. In that case, and under the assumption of a constant magnetic field, two additional equations are needed:

$$\mathbf{j} = \sigma(-\boldsymbol{\nabla}\phi + \mathbf{u} \times \mathbf{B})\,, \tag{3.32}$$

$$\boldsymbol{\nabla} \cdot \mathbf{j} = 0\,. \tag{3.33}$$

It is common practice to express the equations of motion in dimensionless form. Nondimensionalization of the governing equations reduces the number of variables making the equations simpler, and helps highlight those terms that are dominant. This way the generality of a numerical solution is extended.

The equations of motion (see equations (3.31)-(3.33)) can be written in dimensionless form by making the following scale transformations,

$$\begin{gathered} t \to \frac{L}{U_0}\,t\,, \quad \mathbf{u} \to U_0\mathbf{u}\,, \quad p \to \rho U_0^2\,p\,, \\ \mathbf{j} \to \sigma U_0 B_0\,\mathbf{j}\,, \quad \mathbf{B} \to B_0\,\mathbf{B}\,, \quad \phi \to L U_0 B_0\,\phi\,, \end{gathered} \tag{3.34}$$

where L, U_0 and B_0 are reference constants for length, velocity and magnetic field, that might be characteristic of the particular fluid flow. The resulting dimensionless equations of motion are:

$$\boldsymbol{\nabla} \cdot \mathbf{u} = 0\,, \tag{3.35}$$

$$\frac{\partial \mathbf{u}}{\partial t} + \mathbf{u} \cdot \boldsymbol{\nabla}\mathbf{u} = -\boldsymbol{\nabla}p + \frac{1}{Re}\boldsymbol{\nabla}^2\mathbf{u} + N(\mathbf{j} \times \mathbf{B})\,, \tag{3.36}$$

$$\mathbf{j} = -\boldsymbol{\nabla}\phi + \mathbf{u} \times \mathbf{B}\,, \tag{3.37}$$

$$\boldsymbol{\nabla} \cdot \mathbf{j} = 0\,. \tag{3.38}$$

Combining equations (3.37) and (3.38), we get the electrical potential Poisson equation which is used to obtain the electrical potential and remains the same as before,

$$\boldsymbol{\nabla}^2\phi = \boldsymbol{\nabla} \cdot (\mathbf{u} \times \mathbf{B})\,. \tag{3.39}$$

Two dimensionless parameters governing the problem appear in equation (3.31). The Reynolds number,

$$Re = U_0 D/\nu\,, \tag{3.40}$$

and the interaction parameter,

$$N = \frac{\sigma W B_0^2}{\rho U_0} = \frac{D}{W}\frac{Ha^2}{Re}, \tag{3.41}$$

where Ha is the Hartmann number, defined as:

$$Ha = WB_0\sqrt{\frac{\sigma}{\rho\nu}}. \tag{3.42}$$

Re represents the ratio of inertial to viscous forces, while Ha quantifies the ratio of electromagnetic to viscous forces and N the relationship between electromagnetic and inertial forces. It is important to note here that two different length scales D and W were chosen in calculating Ha and Re. This was driven by the fact that D characterizes the structure of the flow, while Ha and W govern the strength of the electromagnetic damping, as explained in the study of Frank *et al.* [51].

3.1.5 Analytical solution for flow in rectangular duct

Hydrodynamic case

Many approximate solutions were proposed in the past for the steady, laminar, fully developed fluid flow in a rectangular duct. In this study, we are using the analytical solution of the steady-state velocity profile, expressed as an eigenfunction expansion, described by Spiga and Morini [64].

We consider a laminar flow in a duct of rectangular cross section with width W and height H aligned in the z- and y-axis, respectively, as shown in Figure 3.2. The x-axis is aligned with the streamwise flow direction, and the flow is driven by a constant pressure gradient. For a fully developed flow the velocity is independent of the streamwise direction, $\mathbf{u} = u(y, z)\hat{x}$. Finally, for the presented formulation, the origin of the Cartesian coordinate system is located at the corner of the duct.

Under this conditions, using the following scale transformations,

$$x \to Wx\,, \quad y \to Wy\,, \quad z \to Wz\,, \quad u \to -\frac{\partial p}{\partial x}\frac{W^2}{\rho\nu}\,u\,, \tag{3.43}$$

the momentum equation (3.31) in dimensionless form becomes:

$$\frac{\partial^2 u}{\partial x^2} + \frac{\partial^2 u}{\partial y^2} + 1 = 0\,. \tag{3.44}$$

At the walls of the duct, $y = 0$, $y = \frac{H}{W}$, $z = 0$ and $z = 1$, no slip boundary condition is prescribed for the velocity field.

By taking Fourier's sine transform of (3.44) with respect to the variables x and y, and inverting the result by means of the inverse formula, we obtain the velocity field on $0 < y < \frac{H}{W}$ and $0 < z < 1$:

$$u(y, z) = \frac{16}{\pi^4}\sum_{n}^{\infty}\sum_{m}^{\infty}\frac{\sin(n\pi y)\,\sin(m\pi z)}{nm\left[n^2 + m^2\left(\frac{H^2}{W^2}\right)^{-1}\right]}\,, \tag{3.45}$$

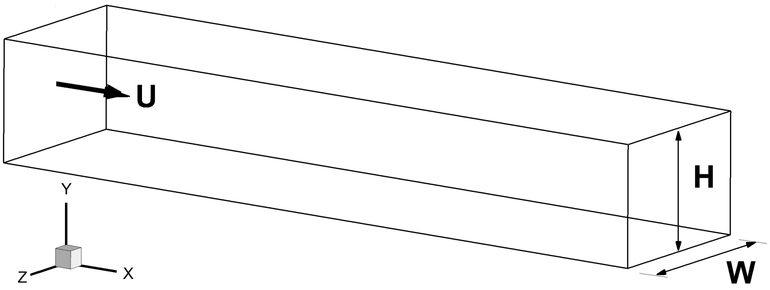

Figure 3.2: Geometrical configuration for the flow in a rectangular duct.

where

$$n, m = 1, 3, 5, 7... \, .$$

The series in the above equation are uniformly converging, hence the solution of the velocity profile can be obtained easily.

Magnetohydrodynamic case

The equations governing a similar flow, where the fluid is in addition subjected to an externally applied constant and uniform imposed magnetic field, are well known and are discussed by Shercliff [65], Dragos [66] and others.

In this case, the fluid is also driven by means of a constant pressure gradient, and the magnetic field is assumed to be parallel to the z-axis. Following from the induction equation (3.25), the only component of the induced magnetic field is $\mathbf{B}_i = B_i(y,z)\hat{x}$. This time, the origin of the Cartesian coordinate system is positioned at the geometrical center of the rectangular duct.

For this conditions, using the following scale transformation for the induced magnetic field in addition to the aforementioned transformations (3.43),

$$B_i \rightarrow -\frac{\partial p}{\partial x} W^2 \sqrt{\rho \nu \sigma}\, B_i \; , \tag{3.46}$$

the resulting dimensionless momentum (3.36) and induction equation (3.25) take the form:

$$\nabla^2 u + Ha \frac{\partial B_i}{\partial y} = -1 \; , \tag{3.47}$$

$$\nabla^2 B_i + Ha \frac{\partial u}{\partial y} = 0 \; . \tag{3.48}$$

Regarding the boundary conditions, without going into details (see, e.g., book of Müller and Bühler [50] for further details) at all walls, $y = \pm\frac{H}{W}$ and $z = \pm 1$, no slip is imposed for the velocity field and the walls are assumed to be electrically insulated with the induced magnetic field set to zero.

By the help of the so-called Elsasser variables, the above equations can be decoupled and the velocity field can be expanded into a Fourier series on $-\frac{H}{W} < y < \frac{H}{W}$ and $-1 < z < 1$ as:

$$u(y,z) = \sum_{n}^{\infty} u_n(z)\cos(\lambda_n y) \ , \tag{3.49}$$

where:

$$\begin{aligned}
n &= 1, 3, 5, 7... \\
u_n(z) &= \frac{\kappa_n}{\lambda_n^2}\left[1 - \frac{\sinh p_{n2}\,\cosh(p_{n1}z) - \sinh p_{n1}\,\cosh(p_{n2}z)}{\sinh(p_{n2} - p_{n1})}\right] \\
p_{n1} &= \frac{1}{2}\left(Ha - \sqrt{Ha^2 + 4\lambda_n^2}\right) \\
p_{n2} &= \frac{1}{2}\left(Ha + \sqrt{Ha^2 + 4\lambda_n^2}\right) \\
\lambda_n &= \frac{n\pi}{2\frac{H}{W}} \\
\kappa_n &= 2\frac{\sin\left(\lambda_n \frac{H}{W}\right)}{\lambda_n \frac{H}{W}}
\end{aligned}$$

3.2 Finite-volume Method

The next step in CFD, is to obtain the so-called discretized equations of motion. There are many available discretization methods for approximating the basic equations of motion (see equations (3.35)-(3.38)) by a system of algebraic equations at discrete locations within the calculation domain. Among the most often used methods are the *finite-difference*, *finite-volume* and *finite-element* methods. Here we will only concentrate our attention on the finite-volume method, which CDP (code developed at Stanford university) uses.

The finite-volume method is based on the discretization of the integral form of the governing equations, making it easier to comply with the conservation laws. The method starts by dividing the computational flow domain into a finite number of non-overlapping control volumes (CVs), defined by the computational mesh. The conservation equations are then integrated over each CV. At the center of each CV, a grid node is assigned where all the variable values are calculated. In order to approximate the resulting surface integrals, the variable values at the CV surfaces are needed. This can be done by interpolation in terms of the center values. This leads to an algebraic equation for every CV, in which neighbouring nodal values appear.

One of the principal advantages of this method is the build-in global conservation. Global conservation is ensured, since the discretization equations obtained in this manner are based on applying conservation principles over each small control volume.

Another advantage of the finite-volume method is its ability to be applied not only on structured meshes but also on unstructured meshes, making it suitable for complex geometries.

3.3 Numerical Grid

Before deriving the discrete approximations of the partial differential equations governing the flow we have to divide the physical space, i.e. the space where the flow is to be computed, into a large number of geometrical elements called grid cells. These make up the numerical grid, which essentially represents, in a discrete manner, the geometric domain on which the problem is to be solved. The numerical grid (also referred to as mesh) consists of a set of points, called nodes, which in turn form a set of volumes called cells or elements. Depending upon the way the solution domain is divided and the elements used, many grid types are available. Some of the most commonly used types are the *structured*, *block-structured* and *unstructured* grids.

A structured grid is one in which the elements have a regular topology. A single block structured grid may comprise of square elements (in 2-D) or hexahedral elements (in 3-D) which are uniquely identified by a set of two (e.g. i, j) or three (e.g. i, j, k) indices respectively. This implies that one can go to a neighbour node by increasing or reducing one of the indices by unity. This property directly corresponds to how the flow variables are stored in the computer memory. As a result, when solving the system of algebraic equations it is much easier to loop through neighbouring elements and this can be efficient with memory usage. On the other hand, for this type of grid, controlling the distribution of grid points in selected regions tends to be difficult. As a result, one is often forced to use more grid points than necessary in some parts of the domain in order to satisfy minimum resolution requirements in other parts. In addition, one is often forced to accept skewed grid elements. Another disadvantage of structured grids is that it is difficult to realize for complicated geometries, therefore can be used only for geometrically simple domains.

One way to avoid these difficulties is by allowing the mesh to be represented in multiple blocks. A block structured grid can be made up of arbitrary-connected blocks, which uses i, j, k indexing within each mesh block. This kind of grid allows the use of finer grids in selected regions, where greater resolution is required and yields high-quality elements. In general, block structured grids are more flexible than single block grids. However, they are usually more time consuming and still limited when compared with unstructured grids.

Unstructured grids are more flexible when it comes to meshing complex geometries and one can use different shape of elements or control volumes (like tetrahedra, prisms, pyramids, hexahedra) to address a problem. In such grids the cells have no particular ordering and are arranged in an arbitrary fashion lacking the i, j, k structure, thus

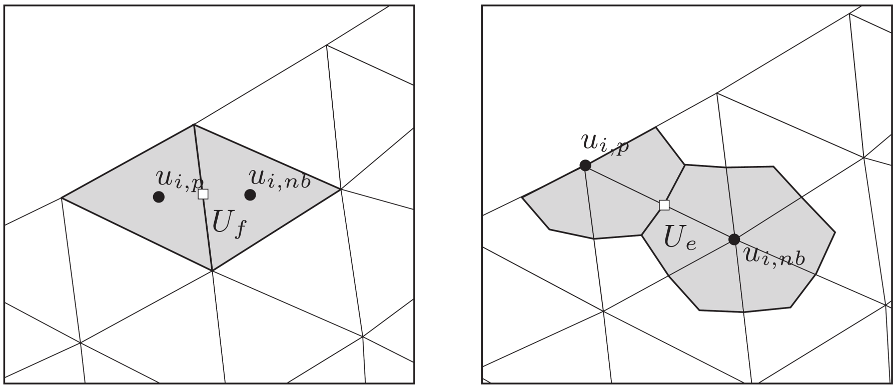

Figure 3.3: Schematic representation of CDP's collocated mesh. Lines belong to the grid, while the shaded area represents a face belonging to the dual mesh (Figure taken from Ref. [67]).

there are no restriction on the number of neighbour elements or nodes. Obviously, if desired, the grid may be easily locally refined. The advantage of increased flexibility is offset by the disadvantage of increased memory requirements, due to the irregularity of the data structure inside the flow solver. This means that for this kind of grid, solvers take longer to arrive at a solution than those for a structured grid. Also grid generation is usually much more difficult for unstructured grids.

3.4 Grid Arrangement and Flow Variables

Having generated the grid, we have to address two important questions: How do we define the control volumes and where do we locate the flow variables with respect to the computational grid.

With respect to the first question, among the many possibilities of defining the shape and position of the control volume (CV) with respect to the grid, two basic strategies are available. One of the most common approach is the *cell-centered* scheme, for which control volumes are identical with the grid cells and CV centers are located at their centroids, as shown in Figure 3.3(a), for a two-dimensional case. The other one is the *cell-vertex* scheme, also known as *dual based* scheme. Within this formulation, the control volumes are formed around each grid point by a median dual mesh construction, which connects the midpoints of the grid cells with surrounding midpoints of faces and edges, as shown in Figure 3.3(b). In such a case, we speak of dual control volumes.

In CFD both methods are successfully used in finite-volume codes, with each method having its own advantages and disadvantages [63]. Early implementations of CDP were based on a cell-centered CV approach, which proved very efficient and accurate, when used for high-quality hex-dominant meshes [68]. However, after reporting the results of a one-to-one comparison of the two methods on a variety of grids, Ham

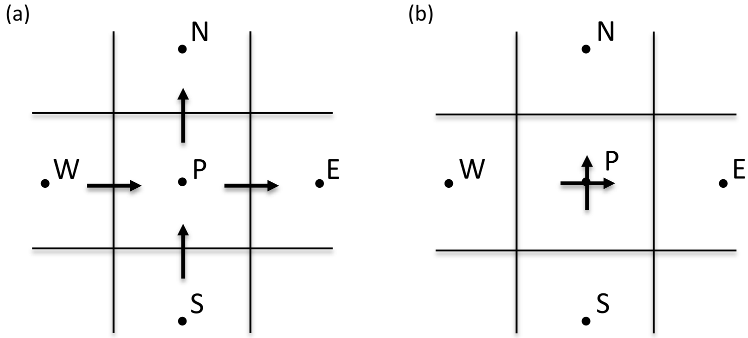

Figure 3.4: Staggered (a) and collocated (b) grid arrangements of velocity components and pressure on a finite-volume grid. Horizontal arrows indicate the locations for u velocities and vertical ones denote those for v velocity.

et al. [67] concluded that, with few exceptions, in truly complex geometries the nodal discretization was significantly more accurate. For this reason, CDP's discretization was modified to a node-based formulation.

With respect to the second question, regarding the locations within the domain at which the various variables are to be computed, several arrangements can be used. The two most popular are the staggered and collocated grid arrangement.

The staggered grid arrangement was introduced by Harlow and Welch [69]. On a staggered grid, pressure and other scalar variables are stored at the cell centers while the velocity components are stored at the cell face. A typical staggered arrangement is depicted in Figure 3.4(a) where the structure of the grid and the location of each variable is shown for a two-dimensional flow. As we will show in section 3.5, in the discretization of the N-S equations based on the finite-volume formulation velocities appear at the cell faces of the control volume. The staggered arrangement enable us to avoid further numerical approximations for obtaining velocities at the cell faces, therefore allowing a very natural and accurate discretization of equations. Another important advantage of staggered grids is the strong coupling they provide between the velocities and pressure, which helps to avoid non-physical oscillations in the pressure and velocity fields. We shall discuss this issue in greater detail further below. However, the staggered approach possesses serious drawbacks in terms of accuracy and stability, when applied in non-orthogonal three-dimensional grids employed to compute flow over complex geometries. Therefore the staggered arrangement is mainly used on structured grids.

The alternative grid arrangement is the collocated grid arrangement. Here, all the dependent variables are stored at the same nodal points, e.g. in the cell centers. Such arrangement is plotted in Figure 3.4(b) for a two-dimensional grid. The collocated arrangement offers significant advantages, especially when multigrid procedures and non-orthogonal grids are used. Although convenient, this method is related to major problems with respect to the pressure and velocity fields prediction. For example, when the gradient of pressure is approximated using the central difference scheme (CDS) on a collocated grid (see Figure 3.4), we obtain:

$$\left.\frac{\partial p}{\partial x_i}\right|_P = \frac{p_E - p_W}{x_E - x_W} + \frac{p_N - p_S}{x_N - x_S}\,. \tag{3.50}$$

This equation involves nodes which are a cell apart, and drops out the pressure at the point where the gradient is discretized. As a result, a pressure field that oscillates from node to node can appear as uniform to the discretized momentum equation, yielding clearly an unphysical solution. This effect is known as the pressure checkerboard effect. A similar result is obtained for the velocity field when the divergence of velocity is evaluated using CDS. To overcome this problem, Rhie and Chow [70] proposed a novel momentum interpolation technique to evaluate the cell face velocities.

In CDP the collocated arrangement is adopted for the location of flow variables. In order to avoid the checkerboard problem, CDP follows Rhie and Chow [70] methodology, but with a few differences in terms of the discretization details. For more detail on the methodology followed in CDP see reference [71].

3.5 Finite-volume approximations

Having generated the grid, we need to address the next question of how to actually discretize the governing equations. A considerable amount of information related to the discretization methods can be found in detail in the literature, e.g. in the books of Patankar [60], and Ferziger and Peric [62]. In this section some aspects of the discretization methods used in CDP, under finite-volume techniques, are briefly presented.

3.5.1 Spatial Discretization

As already mentioned, CDP uses a collocated finite-volume discretization in a nodal formulation. Figure 3.5 shows a typical grid element. For the dual mesh, in the node-based discretization, the velocity vector u_i, pressure p, electric current j_i, and electric potential ϕ are stored at the control volume center, while the the velocities normal to the faces U_f are treated as an independent variable which is stored at the centroid of each face.

With the finite-volume method all terms need to be computed inside the CV. Approximations of the terms that appear inside the volumetric integrals is needed. Most spatial derivatives can be obtained in an easier way at CV faces rather than at the mid-point. Hence, surface integrals are more easily addressed. In order to transform an integral over a volume V into a simpler surface integral over a closed surface S, the

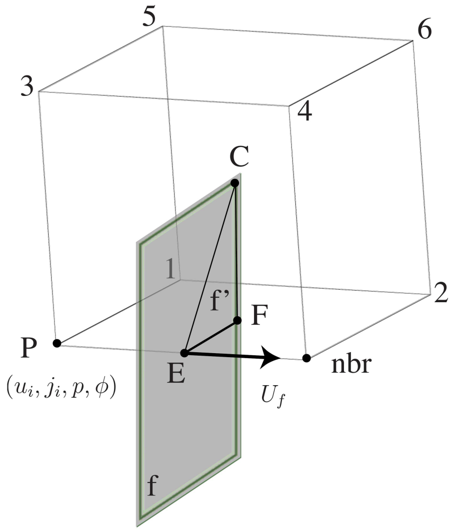

Figure 3.5: Schematic representation of CDP's collocated mesh. Lines belong to the grid, while the shaded area represents a face belonging to the dual mesh (Figure taken from Ref. [72]).

Gauss theorem (green theorem) is used:

$$\int_V \nabla \cdot \mathbb{G} dV = \oint_S \mathbb{G} \cdot \mathbf{n} dS \,, \tag{3.51}$$

where $\mathbb{G}$ is an arbitrary vector function.

The momentum equation (3.36) in integral form, after applying Gauss' theorem where ever possible, reads:

$$\begin{aligned} \int_V \frac{\partial u_i}{\partial t} dV = &- \oint_S u_i (u_j \cdot n_j) dS + \frac{1}{Re} \oint_S \frac{\partial u_i}{\partial x_j} \cdot n_j dS \\ &- \int_V \frac{\partial p}{\partial x_i} dV + \int_V N \left[\mathbf{j} \times \mathbf{B}\right]_i dV \,, \end{aligned} \tag{3.52}$$

where V and S are the volume and surface of the control volume, respectively. Approximation of integrals for an infinitesimal volume such as the control volume is, leads to a discrete equation:

$$\begin{aligned} \underbrace{\left.\frac{\partial u_i}{\partial t}\right|_P V_P}_{Transient} = &\underbrace{- \sum_f u_{i,f} U_f A_f}_{Convective} + \frac{1}{Re} \underbrace{\sum_f \left.\frac{\partial u_i}{\partial x_j}\right|_f \cdot n_{j,f} A_f}_{Diffusive} \\ &\underbrace{- \left.\frac{\partial p}{\partial x_i}\right|_P V_P}_{Pressure} + \underbrace{N \left[\mathbf{j}_P \times \mathbf{B}_P\right]_i V_P}_{Lorentz\ Force} \,. \end{aligned} \tag{3.53}$$

In the above equation, the subscript P denotes a value calculated at the control volume center, and f denotes a value evaluated at the common face, which lies between the control volume and a neighbour control volume. A_f denotes the face area and $n_{j,f}$ their unit normal vectors.

Focusing our attention on the convective and viscous terms, while assuming a linear profile between neighbour nodes we get:

$$u_{i,f} = \frac{u_{i,P} + u_{i,nbr}}{2}\,, \tag{3.54}$$

$$\left.\frac{\partial u_i}{\partial x_j}\right|_f \cdot n_{j,f} = \frac{u_{i,nbr} - u_{i,P}}{\|x_{j,nbr} - x_{j,P}\|}\,, \tag{3.55}$$

where $u_{i,nbr}$ indicates a component of the velocity evaluated at a neighbouring control volume.

The pressure term has been left in differential form, because a special treatment is needed to provide corrections for skewed or stretched elements. In this direction, the pressure gradient is computed using the discrete Gauss theorem which approximates the derivative of pressure with a summation-by-parts operator [73] as follows:

$$\left.\frac{\partial p}{\partial x_i}\right|_P V_P = \sum_f \sum_{f'} \frac{p_E + p_F + p_C}{3} n_{i,f'} A_{f'}\,. \tag{3.56}$$

p_E, p_F, and p_C are evaluated at different locations denoted by the corresponding subscripts as shown in Figure 3.5, and computed from simple averages over circumcenter values:

$$\begin{aligned} p_E &= (p_P + p_{nbr})/2 \\ p_F &= (p_P + p_{nbr} + p_1 + p_2)/4 \\ p_C &= (p_P + p_{nbr} + p_1 + p_2 + p_3 + p_4 + p_5 + p_6)/8\,. \end{aligned} \tag{3.57}$$

The accurate computation of the Lorentz force is the most challenging aspect in DNS calculations for moderate and high Hartmann numbers. Until recently a non-conservative method was used to calculate the Lorentz force on collocated meshes. Under this formulation the calculation of the Lorentz force depends on the current density at the cell center which can be directly calculated through equation (3.37) of the Ohm's law:

$$j_{i,P} = -\left.\frac{\partial \phi}{\partial x_i}\right|_P + [\mathbf{u}_P \times \mathbf{B}_P]_i\,. \tag{3.58}$$

The current density depends on the electrical potential gradient and the velocity at the cell center. The gradient of the electric potential at the cell center, can be evaluated by taking its integral over the volume of a CV and then applying the divergence theorem as follows:

$$\left.\frac{\partial \phi}{\partial x_i}\right|_P = \frac{1}{V_P}\int_V \frac{\partial \phi}{\partial x_i} dV = \frac{1}{V_P}\oint_S \phi n_i dS = \frac{1}{V_P}\sum_f \phi_f n_{i,f} A_f\,. \tag{3.59}$$

The value of the electric potential at the cell face, ϕ_f, can be calculated from linear interpolation between cell centers in a similarly way with velocity as shown in (3.54),

$$\phi_f = \frac{\phi_P + \phi_{nbr}}{2} \,. \tag{3.60}$$

Substituting equation (3.59) into (3.58), Ohm's law can then be rewritten in discrete form as follows:

$$j_{i,P} = -\frac{1}{V_P}\sum_f \phi_f n_{i,f} A_f + [\mathbf{u}_P \times \mathbf{B}_P]_i \,. \tag{3.61}$$

Therefore, the Lorentz force can be calculated based on the above equation as:

$$\mathbf{j}_P \times \mathbf{B}_P = \left(-\frac{1}{V_P}\sum_f \phi_f \mathbf{n}_f A_f + [\mathbf{u}_P \times \mathbf{B}_P]\right) \times \mathbf{B}_P \,. \tag{3.62}$$

However, this non-conservative scheme for the calculation of the Lorentz force, even though yielding smooth and numerically stable results, will introduce a numerical error for the calculation of the total momentum [74, 75], resulting in inaccurate predictions of the flow behaviour.

To get a more accurate result on the calculation of the Lorentz force, Ni *et. al.* [74, 75] proposed a conservative method. The basic idea of the method is to calculate the current density at the cell center from the current fluxes at the cell faces of a control volume. Ni *et. al.* [75] introduced the following equation for the current density:

$$\mathbf{j} = \nabla \cdot (\mathbf{j}\mathbf{r}) \,, \tag{3.63}$$

where $\mathbf{r}$ denotes the position vector. That is, $\nabla \cdot (\mathbf{j}\mathbf{r})$ can be regarded as an interpolation of the current density. The current density at the cell center can be written as:

$$\mathbf{j}_P = \frac{1}{V}\int_V \mathbf{j} dV \,. \tag{3.64}$$

Substituting equation (3.63) into (3.64) we therefore have:

$$\mathbf{j}_P = \frac{1}{V}\int_V \nabla \cdot (\mathbf{j}\mathbf{r}) dV \,. \tag{3.65}$$

Using Gauss' rule the detailed discretized formulation is:

$$\mathbf{j}_P = \frac{1}{V}\oint_S j_j \cdot n_j r_i dS = \frac{1}{V}\sum_f J_f r_{i,f} A_f \,, \tag{3.66}$$

where J_f represents the current densities normal to the faces. The current flux on the cell face can be calculated using Ohm's law:

$$J_f = j_{j,f} \cdot n_{j,f} = -\left.\frac{\partial \phi}{\partial x_j}\right|_f \cdot n_{j,f} + [\mathbf{u}_f \times \mathbf{B}_f]_j \cdot n_{j,f}\,. \tag{3.67}$$

Expanding the gradient of the electrical potential on the cell faces, in terms of the electric potential in the current cell and neighbouring cell, as in (3.55), we have:

$$J_f = -\sum_f \frac{\phi_{nbr} - \phi_P}{\|x_{j,nbr} - x_{j,P}\|} + [\mathbf{u}_f \times \mathbf{B}_f]_j \cdot n_{j,f}\,. \tag{3.68}$$

The main advantage of this method is that the information required for computing the current density at the cell center, and therefore the Lorentz force, is placed at the cell faces. Putting the current density fluxes on the cell faces is natural, and can effectively conserve the current density in the control volume, resulting in calculating the Lorentz force with higher accuracy [74, 75]. For this reason, we have adopted this formulation and implemented it in CDP.

In either scheme, conservative or non-conservative, we obtain the electric potential at the cell center through the discretization of the electric potential Poisson equation (3.39). The discretization of the Poisson equation includes the discretization of the Laplace and divergence operators. Integrating over a control volume and using Gauss' rule we obtain,

$$\nabla^2\phi = \int_V \nabla^2\phi dV = \oint_S \frac{\partial \phi}{\partial x_j} n_j dS = \sum_f \left.\frac{\partial \phi}{\partial x_j}\right|_f n_{j,f} A_f\,, \tag{3.69}$$

for the Laplace operator, and,

$$\nabla \cdot (\mathbf{u} \times \mathbf{B}) = \int_V \nabla \cdot (\mathbf{u} \times \mathbf{B}) dV = \oint_S [\mathbf{u} \times \mathbf{B}]_j n_j dS = \sum_f [\mathbf{u}_f \times \mathbf{B}]_j n_{j,f} A_f\,, \tag{3.70}$$

for the divergence operator. Combining equations (3.69) and (3.70), and then rewriting the electrical potential gradient on the cell faces in terms of cell center values, yields the discretized electric potential Poisson equation as follows:

$$\sum_f \frac{\phi_{nbr} - \phi_P}{\|x_{j,nbr} - x_{j,P}\|} A_f = \sum_f [\mathbf{u}_f \times \mathbf{B}]_j n_{j,f} A_f\,. \tag{3.71}$$

3.5.2 Time advancement

Time is also discretized by first integrating the equations of motion over the control volume, and then evaluating each integral using a numerical approximation method.

Taking the time integral of the discrete momentum equation (3.53) yields,

$$\int_{t^n}^{t^{n+1}} \left.\frac{\partial u_i}{\partial t}\right|_P V_P dt = \left(u_{i,P}^{n+1} - u_{i,P}^{n}\right) V_P = \int_{t^n}^{t^{n+1}} \left[(\text{Conv.}) + (\text{Diff.}) + (\text{Press.}) + (\text{LF})\right] dt\,, \tag{3.72}$$

where superscripts are used to indicate time level.

To evaluate the right hand side of this equation we need to make some assumptions regarding the variation of the different variables with time. We could estimate each integral using values at time t or at time $t + \Delta t$ or, alternatively, using a combination of values at time t and $t+\Delta t$. Depending on the approximation method used, different time-advancing schemes exist, each with different stability characteristics as we will briefly discuss later on.

Explicit, implicit and Crank-Nicolson schemes are some of the most commonly used schemes. In the explicit scheme the time integral is evaluated using the value of the integrand at the initial point of the integration interval where the solution is known (old time step). On the other hand, the implicit method uses the final point (new time step) to evaluate the integral. In the Crank-Nicolson scheme, the approximation of the integral is constructed by using a straight line interpolation between the initial and final points. For higher order approximations one must use information at more points, other than $t = t_n$ and t_{n+1}. Such methods are called multipoint methods. A very well known multipoint method is the Adams-Bashforth method, which is derived by fitting a polynomial to the derivatives at a number of points in time.

In the limit as the time step tends to zero, $\Delta t \rightarrow 0$, all methods produce good solutions. However, in practice we are concerned with finite steps. This raises the issue of stability. In the case where the time step becomes too large, many numerical methods become unstable, causing the solution to grow unboundedly. In order to establish the convergence of a numerical approximation of a partial differential equation, linear or nonlinear, it is necessary to imply limitations on the length of the time step. Generally two stability limits apply. The first is the viscous stability limit, which dictates that the largest time step size that allows convergence and numerical stability should be less than:

$$\Delta t_v = \frac{\text{VSL}\,(\Delta x)^2}{\nu}\,. \tag{3.73}$$

The VSL number depends on actual time advancement scheme. The viscous condition assures that for one time step, the distance a disturbance has propagated by diffusion is less than one grid length. The second is the famous Courant-Friedrichs-Lewy (or CFL) stability criterion [76], which requires that the time step should be less than:

$$\Delta t_c = \frac{\text{CFL}\,\Delta x}{u}\,, \tag{3.74}$$

The CFL condition also depends on the numerical discretization scheme used. The physical interpretation of this restriction, is that a fluid particle cannot travel more than the length of adjacent grid points, in a single time step.

Explicit schemes are known to be conditionally stable, usually requiring that the VSL number is roughly less than 0.5 and the CFL number less than or equal to 1. The exact time step, necessary for stability, differs between the various explicit schemes. Implicit, and semi implicit schemes are unconditionally stable allowing arbitrarily large time steps to be taken. An important drawback of these methods is that they need to solve a large coupled set of equations at each time step. Furthermore, when solving unsteady problems, there may be a limitation on the employed time step, since the solution can change a great deal in just one time step. In practice, implicit schemes allow a much larger time step than explicit schemes, with the limit being problem dependent.

CDP uses different time-advancement schemes for the various terms that appear in the Navier-Stokes equations. In CDP the nodal velocity is advanced in time using the Crank-Nicholson advancement scheme,

$$u_{i,f}^{n+1} = \frac{1}{2}\left(u_{i,f}^{n+1} + u_{i,f}^{n}\right) , \tag{3.75}$$

while the Adams-Bashforth scheme is used for the face normal velocity,

$$U_f^{n+1} = \frac{3}{2}U_f^n - \frac{1}{2}U_f^{n-1} . \tag{3.76}$$

Using equations (3.75) and (3.76), the time advancement of the convective term reads,

$$\begin{aligned} \int_{t^n}^{t^{n+1}} (Conv.)\, dt &\approx \sum_f u_{i,f}^{n+\frac{1}{2}} U_f^{n+\frac{1}{2}} A_f \Delta t \\ &= \sum_f \frac{1}{2}\left(u_{i,f}^{n+1} + u_{i,f}^{n}\right)\left(\frac{3}{2}U_f^n - \frac{1}{2}U_f^{n-1}\right) A_f \Delta t . \end{aligned} \tag{3.77}$$

The reasoning behind this blending of schemes is linked with the additional difficulties that arise when solving the convective terms. The non-linearity of the equations makes their solution using, the much more stable, implicit methods very difficult. In order to simplify the structure of the large system of equations to be solved, the best procedure is to combine direct and indirect methods, in the time-advancement of the velocity field.

For the diffusion term we have,

$$\begin{aligned}\int_{t^n}^{t^{n+1}} (Diff.)\, dt &\approx \sum_f \left.\frac{\partial u_i}{\partial x_j}\right|_f^{n+\frac{1}{2}} \cdot n_{j,f} A_f \Delta t \\ &= \sum_f \frac{1}{2}\left[\left(\left.\frac{\partial u_i}{\partial x_j}\right|_f^{n+1} \cdot n_{j,f}\right) + \left(\left.\frac{\partial u_i}{\partial x_j}\right|_f^{n} \cdot n_{j,f}\right)\right] A_f \Delta t\,.\end{aligned} \tag{3.78}$$

The Lorentz force is treated explicitly,

$$\int_{t^n}^{t^{n+1}} (LF)\, dt \approx \left[\mathbf{j}_P^n \times \mathbf{B}_P\right]_i V_P \Delta t\,. \tag{3.79}$$

Approximation of the pressure term involves a two-step, predictor-corrector time advancement scheme, due to the lack of an independent equation for pressure. This issue requires special attention and will be addressed in more detail in the next section.

In the CDP code, as there is no pure time-discretization implemented, the specific value of the maximum allowable CFL number is problem dependent. As a rule of thumb, to maintain convergence the dimensionless CFL number needs to be less than or equal to one.

3.5.3 Fractional Step Method

Solution of the Navier-Stokes (N-S) equations in incompressible flows is not a trivial task. The N-S equations suffer from a closure issue. Closure implies that there is a sufficient number of equations for all the unknowns. However, in the case of the N-S equations, there are more unknown variables than equations. Strictly speaking, this redundancy lies in the fact that there isn't an independent equation for obtaining pressure, whose gradient contributes to the momentum equation. Furthermore, for such a flow, the continuity equation is a kinematic constraint on the velocity field rather than a dynamic equation. Therefore, an additional equation is necessary to link the pressure with the velocity and provide closure. One possible way to overcome this difficulty is by constructing the pressure field through the continuity equation in such a way to guarantee conservation of the continuity equation.

An approach to solve the mass and momentum coupling of the N-S equations is the fractional step method (also known as time-splitting method) proposed by Chorin [77] and further developed later on by Kim and Moin [78]. The fractional step concept is a generic method for solving the incompressible Navier-Stokes equations, based on a pressure correction approach.

The fractional step method consists of a sequence of steps that solves for the velocity and pressure at each time level. A more detailed analysis of the methodology followed in CDP is given in Ref. [71]. In the first step of the method, the momentum equations are solved for an auxiliary velocity field, while the pressure gradient term is computed from the pressure in the previous time step:

$$\frac{\hat{u}_i - u_i^n}{\Delta t} = \mathcal{O}_i - \frac{\delta p^n}{\delta x_i}, \tag{3.80}$$

where $\mathcal{O}_i$ is a shorthand notation representing the discretized convective, diffusive and additional source terms (if present), whose treatment is of no importance here. $\delta p/\delta \mathbf{x}$ represents a discretized spatial derivative for pressure.

In the next step, the old pressure gradient is removed from the previous computation of $\hat{\mathbf{u}}$ using the following equation:

$$\frac{u_i^* - \hat{u}_i}{\Delta t} = +\frac{\delta p^n}{\delta x_i}\,. \tag{3.81}$$

Including the old pressure gradient in the momentum advancement is not necessary in the time-splitting method, however this numerical technique (of including and removing the old pressure gradient) is an additional feature which can improve the robustness and numerical behaviour of the code.

Once the intermediate velocity field $\mathbf{u}^*$ is computed, new velocities can be obtained, $\mathbf{u^{n+1}}$, through the new pressure field gradient:

$$\frac{u_i^{n+1} - u_i^*}{\Delta t} = -\frac{\delta p^{n+1}}{\delta x_i}\,. \tag{3.82}$$

Of course, at this step the new pressure is not available and is also important to note that the new velocity field does not satisfy the continuity equation. To circumvent the above mentioned issues, one can take the numerical divergence of the previous equation. Enforcing continuity to the unknown new velocity field, dependence on the unknown velocity field may be eliminated, resulting to a discrete Poisson system for pressure:

$$\frac{\delta}{\delta x_i}\left(\frac{\delta p^{n+1}}{\delta x_i}\right) = \frac{1}{\Delta t}\frac{\delta u_i^*}{\delta x_i}\,. \tag{3.83}$$

By solving the pressure Poisson equation the pressure field at the new time step can be obtained, hence the new velocity can be computed. At the same time, solving the Poisson equation, will also cause the velocity field to become divergence free satisfying the continuity equation.

Chapter 4

Three-dimensional DNS of the flow around a circular cylinder confined in a plane channel

This chapter presents two- and three-dimensional direct numerical simulations of the flow around a circular cylinder placed symmetrically in a plane channel. Results are presented in the Reynolds-number range (based on the cylinder diameter and centerline velocity) of 10 to 390, for a blockage ratio (ratio of the cylinder diameter to the channel height) of 0.2. To the best of our knowledge, no published direct numerical simulations of the three-dimensional flow in a channel exists in the Reynolds number range examined here. The main objective of this study is to investigate how the confinement provided by the channel walls affects the onset and development of three-dimensional instabilities in the wake of the flow at moderate Reynolds numbers. Comparisons are made with two-dimensional studies for the confined case, as well as with the extensive literature available for the unconfined case.

In the sections to follow, first the complete problem is formulated and presented together with a detailed grid-sensitivity analysis (Section 4.1). The main results from the 3-D simulations together with a discussion of confinement effects are presented in Sections 4.2, 4.3, followed by the conclusions of the present study.

Results of this work have been published in reference [79].

4.1 Problem statement and formulation

4.1.1 Flow configuration

The geometry considered in this study is shown in Figure 4.1. The geometry consists of a circular cylinder, of diameter D, symmetrically placed in a plane channel. The ratio of the cylinder diameter to the distance between the channel walls H, defines the blockage ratio, $\beta = D/H$. Results for $\beta = 1/5$ are presented in the present thesis, allowing for a direct comparison with the linear stability analysis of Camarri and

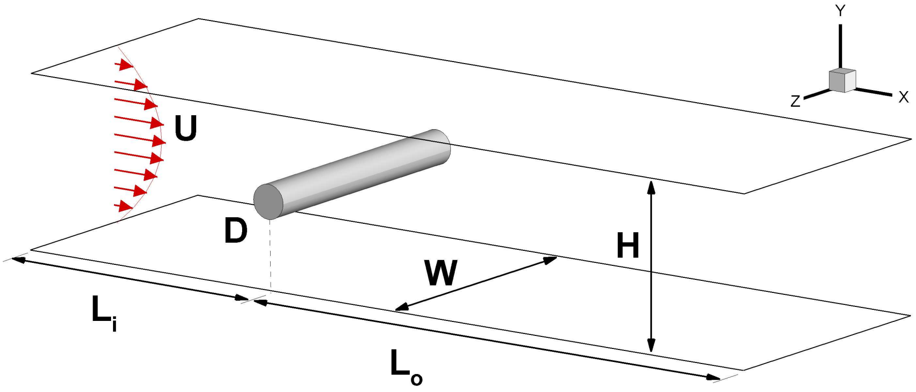

Figure 4.1: Schematic diagram of the flow configuration and related geometrical parameters.

Gianneti [40]. We decided not to use the higher blockage ratio ($\beta = 1/3$) that was used in the experiments of Rehimi *et al.* [39], even though that would have meant a smaller computational domain in favour of computational cost, "in order to avoid peculiar flow features related to a complex interaction between the wake and the confining walls," as mentioned in Camarri and Giannetti [40]. By choosing the lower blockage ratio, we can bring into focus the wall-blocking effects without these being obscured by the more complex interactions with the near-wall viscous regions.

The channel inlet is placed at a distance of $L_i = 12.5D$ upstream of the circular cylinder, while the outlet is located at $L_o = 35.5D$ behind the body. This choice of parameters ensures minimal distortion of the flow structure due to the boundary conditions [80], while maintaining a reasonable computational cost, and is in line with those used by others in the literature [33, 40]. Two spanwise lengths were considered, $W = 8D$ and $W = 12D$. Based on observations from the transitional wake of open uniform flow past a circular cylinder, the value of $8D$ was considered sufficient for the development of both mode B and the larger mode A three-dimensional wake instabilities. The relatively large spanwise length of $12D$ has been used only in the analysis of natural vortex dislocations. In this case, the use of such a large span was motivated by the need to provide a sufficiently wide domain for the development of such irregularities in the wake, and it is in agreement with the practice followed by Braza *et al.* [19].

4.1.2 Mathematical formulation

The flow is completely described by the set of Navier-Stokes equations for an incompressible Newtonian fluid, of density ρ, dynamic viscosity μ, and kinematic viscosity $\nu = \mu/\rho$. Using the cylinder's diameter, D, and the centerline inflow velocity, U_c, as the characteristic length and velocity scales respectively, the non-dimensional continuity and momentum equations in a Cartesian coordinate system are given by

$$\frac{\partial u_i}{\partial x_i} = 0 \tag{4.1}$$

$$\frac{\partial u_i}{\partial t} + \frac{\partial u_i u_j}{\partial x_j} = -\frac{\partial P}{\partial x_i} + \frac{1}{Re}\frac{\partial^2 u_i}{\partial x_j \partial x_i}\,, \tag{4.2}$$

where $Re = U_c D/\nu$ is the Reynolds number.

The drag and lift coefficients were both determined by considering the viscous and the pressure forces on the cylinder surface,

$$C_D = \frac{F_D}{\frac{1}{2}\rho U_c^2 D} \quad \text{and} \quad C_L = \frac{F_L}{\frac{1}{2}\rho U_c^2 D}\,, \tag{4.3}$$

where F_D and F_L are the drag and lift forces per unit length of the cylinder, defined as,

$$F_i = \left[-p\delta_{ij} + \nu\rho\left(\frac{\partial u_i}{\partial x_j} + \frac{\partial u_j}{\partial x_i}\right)\right] n_j\,. \tag{4.4}$$

Here, n_j denotes the unit normal vector pointing in the direction of x_j. The Strouhal number, characterizing the vortex shedding phenomenon, is based on the dominant frequency of the lift coefficient,

$$St = f\frac{D}{U_c}\,. \tag{4.5}$$

The base pressure coefficient is defined as,

$$C_{pb} = \frac{p_b - p_\infty}{\frac{1}{2}\rho U_c^2}\,, \tag{4.6}$$

where p_b is the spatiotemporal average, with respect to the time and the spanwise coordinate z, of pressure at the rear stagnation point of the cylinder (180 degrees from the front), and p_∞ is the free-stream pressure at the inlet boundary ($x = -12.5D$, $y = 0$).

4.1.3 Numerical method and boundary conditions

The current computations have been performed using an unstructured collocated nodal-based finite-volume code (CDP). Details of the discretization methods and the numerical techniques used by this code were provided in Chapter 3.

Boundary conditions are given at the domain's inlet by prescribing a Poiseuille, parabolic velocity profile,

$$u(-L_i, y) = U_c\left[1 - \left(\frac{y}{H/2}\right)^2\right]\,, \tag{4.7}$$

while a no-slip boundary condition is imposed on the cylinder surface, the top, and

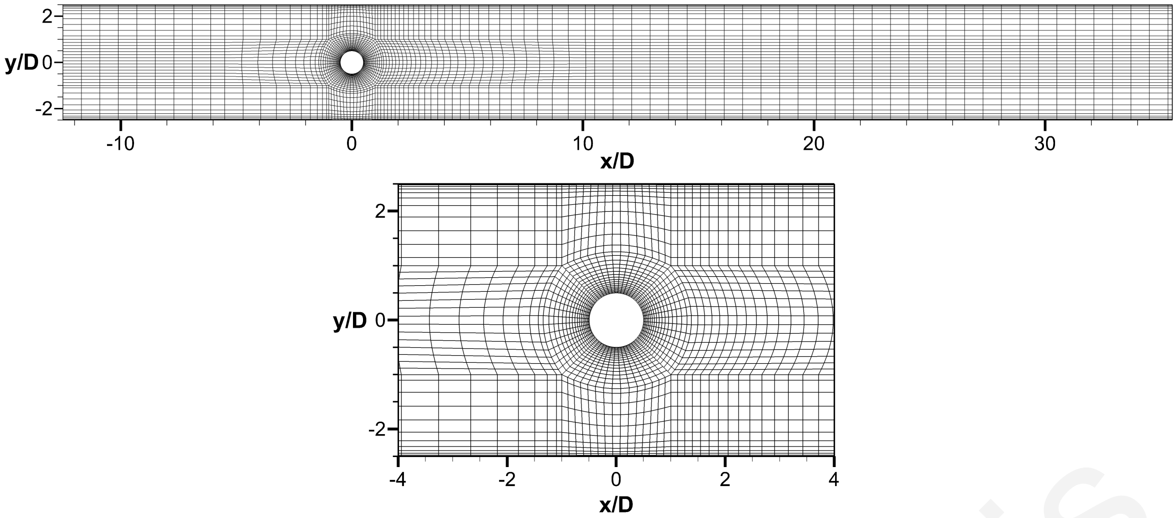

Figure 4.2: Computational grid G2. The picture on the top shows the whole domain, while the bottom picture shows an expanded view in the vicinity of the cylinder. Only every 4th node is plotted for clarity.

bottom walls. At the outlet, in order to minimize reflective effects and avoid the distortion of the flow structures leaving the domain, a convective boundary condition is applied,

$$\frac{\partial u_i}{\partial t} + U_{conv}\frac{\partial u_i}{\partial n} = 0\,, \tag{4.8}$$

where $U_{conv} \equiv \int \mathbf{u} ds / \int ds$. In order to assess the influence of this boundary condition on the computed physical characteristics of the flow, a domain dependance study is performed in Section 4.2.2. For the 3-D simulations, a Neumann boundary condition has been adopted for the velocity field in the spanwise direction,

$$\frac{\partial u_i}{\partial z} = 0\,, \tag{4.9}$$

which is considered appropriate and in accordance with experimental observations of the flow regime considered in the present study [24]. A series of simulations performed with periodic spanwise boundary conditions suggested that, even though numerical results where similar, not all of the critical physical mechanisms could be captured as accurately as with Neumann conditions.

4.2 Validation tests

4.2.1 Effect of grid resolution

The influence of the grid resolution on the computed physical characteristics of the flow was examined in detail in order to optimize the simulation in terms of accuracy and computational cost. For this reason, a series of two- and three-dimensional simulations

Table 4.1: Parameters used for the different grid configurations. N_{cyl}: nodes along cylinder circumference; Δn_{walls}: grid spacing normal to the cylinder surface and channel walls; Δz: grid spacing in spanwise direction; N_z: nodes along spanwise direction; W: channel width.

Grid		N_{cyl}	Δn_{walls}	Δz	N_z	W	Total Nodes
G1	2-D	120	0.020	–	–	–	25,531
G2	2-D	240	0.005	–	–	–	66,989
G3	2-D	320	0.002	–	–	–	112,657
G2C	3-D	240	0.005	0.4	21	8	1,406,769
G2M	3-D	240	0.005	0.2	41	8	2,726,109
G2F	3-D	240	0.005	0.1	81	8	5,426,109
G2W	3-D	240	0.005	0.12	101	12	6,765,889
G2FF	3-D	240	0.005	0.1	81	8	7,247,880
G2FS	3-D	240	0.005	0.1	81	8	4,533,084

were carried out at $Re = 300$. The parameters of the different grid configurations tested are summarized in Table 4.1.

First, a series of two-dimensional simulations were performed using three non-uniform grids (G1, G2, G3), mainly differing in the spatial resolution in the vicinity of the cylinder and the channel walls. The hyperbolic tangent function was used for stretching the cell sizes in a clustered region close to the cylinder, and linear grid stretching was applied in the direction normal to the channel walls, as shown in Figure 4.2. Further upstream and downstream of the cylinder a uniform grid was used. The discrepancy between the values of mean drag coefficient $\bar{C}_D$, rms value of the lift coefficient C'_L, Strouhal number St, and the base pressure coefficient C_{pb} resulting from the use of different grids is shown in Table 4.2. Results show that a grid independent solution can be achieved with the grids considered. For example, the percentage difference between the values predicted on the coarsest grid with respect to the ones obtained on the finest grid is below 2.1%. This discrepancy is further reduced to less than 0.5% when the two finest grids are compared. Hence, one can conclude that the intermediate grid G2 is sufficiently fine to resolve the flow.

To study the effect of the spanwise grid spacing in the numerical solution for the 3-D cases, several three-dimensional grids were generated by repeating the grid G2 along the spanwise direction. Three grids differing in the spanwise resolution were tested, namely G2C, G2M, and G2F with Δz grid spacings of $0.4D$, $0.2D$, and $0.1D$, respectively. The spanwise dimension of $8D$ was adopted for these meshes. Simulations were performed over periods of at least 900 dimensionless time units, corresponding to about 180 vortex-shedding cycles, with time averaging of results performed over the last 100 shedding cycles, when the flow had reached a "fully developed" state.

Results obtained with the three grids are listed in Table 4.2, and overall show good grid convergence. For example, replacing the coarsest grid G2C with the finest grid

Table 4.2: Mean drag coefficient $\bar{C}_D$, rms lift coefficient C'_L, Strouhal number St, and base pressure coefficient C_{pb} at $Re = 300$ for the 2-D and 3-D grids.

Grid		Re	$\bar{C}_D$	C'_L	St	C_{pb}
G1	2-D	300	1.210	0.551	0.2021	1.0440
G2	2-D	300	1.232	0.559	0.2023	1.0472
G3	2-D	300	1.236	0.562	0.2024	1.0488
G2C	3-D	300	1.157	0.405	0.1915	0.929
G2M	3-D	300	1.167	0.388	0.1967	0.937
G2F	3-D	300	1.172	0.376	0.1989	0.942
G2FF	3-D	300	1.175	0.372	0.1979	0.942
G2FS	3-D	300	1.162	0.365	0.1976	0.926

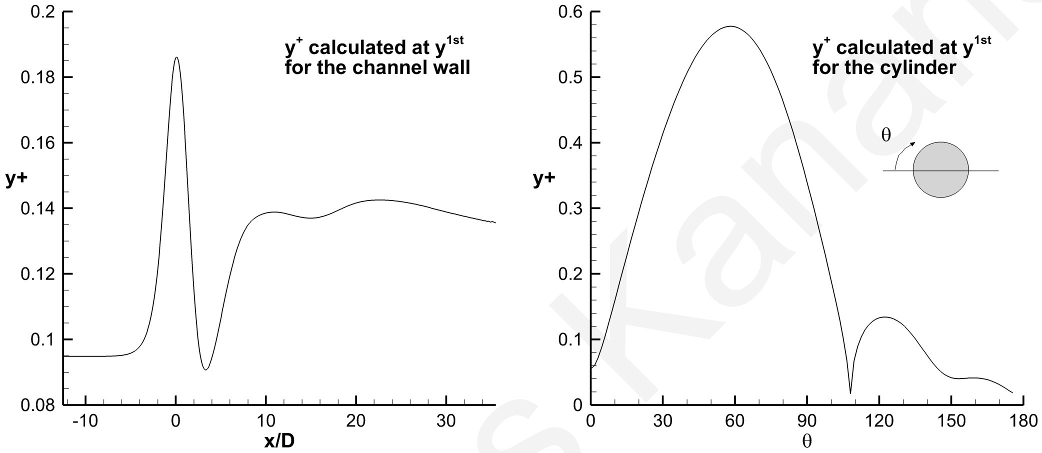

Figure 4.3: y^+ measured around cylinder and at channel walls, using grid G2F.

G2F, resulted in only 3.7% change in St and 1.4% in C_{pb}, whereas the corresponding changes were only 1.1% and 0.6% when replacing the intermediate grid G2M by the finest grid. Based on these results, one could have opted for the intermediate grid G2M. However, because we were particularly interested in capturing the details of the vortical structures downstream of the cylinder, we decided to use the finest grid G2F, despite the increased computational cost. For example, a typical simulation with grid G2F, required a total of 27 days of computation on a 32 node (64 processor) Linux cluster to complete 180 shedding cycles. Each node has dual Opteron 244 (1.8GHz) processors with 4GB of RAM.

Another way to verify adequate grid resolution is to look at the value of y^+ at the cylinder and channel walls. y^+ is a dimensionless wall distance defined as $y^+ = u_* y/\nu$, where u_* is the friction velocity. The value of y^+ in the wall-adjacent cells dictates how the wall shear stress is calculated, and therefore how well resolved the boundary layers are with respect to grid resolution. For accurate simulations with resolved boundary layers the first grid point should have a y^+ which is below 1. Looking at Figure 4.3

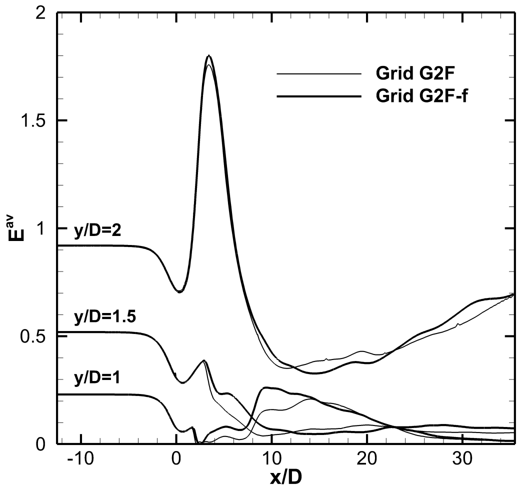

Figure 4.4: Local Enstrophy calculated at different positions for grids G2F and G2FF.

is clear that the flow around the cylinder and close to the channel walls is very well resolved.

We further wanted to explore the effect of the medium-to-far-field resolution on the computed physical characteristics of the flow. Thus, one more grid was generated, namely G2FF. This grid was based on the grid G2F (selected grid for the computations presented in this chapter) differing in the resolution of the mesh in the streamwise direction. In the case of G2FF the grid at the far field was doubled.

Results obtained with grid G2FF are also listed in Table 4.2, and once more show good grid convergence. We also calculated the local and global Enstrophy (based on the averaged vorticity) for grids G2F and G2FF. The difference in global Enstrophy between the two cases, was found to be around 1%. Figure 4.4 displays the local Enstrophy at different positions for the two grids. As seen the differences between the two cases are relatively small, verifying that the resolution of grid G2F is fine enough. However, we believe that this is related to the highly transitional character of the flow, and that the use of longer averaging times would have resulted in better agreement.

Finally, in order to study the natural occurrence of vortex dislocations, a case at $Re = 240$ was computed in a wider domain with a spanwise dimension of $12D$. To accommodate this case, an additional grid (G2W) was generated, which in view of the increased computational requirements, had a spanwise grid spacing of $0.12D$, which is slightly coarser than G2F, but still finer than G2M.

The dimensionless time step was kept constant during each simulation, but was determined independently for each case in order to satisfy the Courand-Friedrichs-Lewy stability criterion, $CFL \leq 1$. This yielded values in the range $7.5 \times 10^{-3} D/U_c$ to $10 \times 10^{-3} D/U_c$.

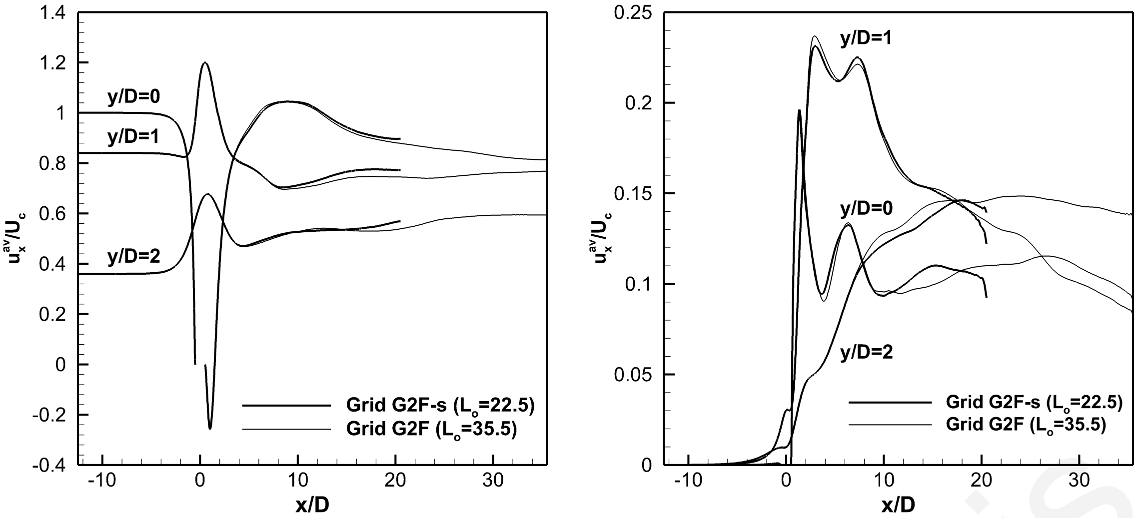

Figure 4.5: Comparison of (a) the time and space averaged streamwise velocity, and (b) the r.m.s. streamwise velocity at different slices using grids G2F ($L_o = 35.5$) and G2F-S ($L_o = 22.5$).

4.2.2 Effect of outlet boundary condition

In order to examine the effect of the convective outlet boundary condition on the computed physical characteristics of the flow, another grid was generated, namely G2F-S. This grid grid was based on grid G2F. However, this time the outlet was positioned closer to the cylinder, at $22.5D$ from the cylinder center (compared to 35.5D in the case of the G2F computations).

Results obtained with the later grid are listed in Table 4.2. When replacing grid G2F by the shortest grid G2F-S, results overall show good agreement with the differences being below 3%. Figure 4.5 displays both the mean and r.m.s. streamwise velocities, averaged over time and along the spanwise direction, at different one-dimensional slices, for grids G2F and G2F-S. From the comparison of the average velocity it can be seen that the effect of the convective outlet is quite small, and maintained in the vicinity of $5D$ from the outlet. In the case of values of the r.m.s. streamwise velocity, the convective outlet seems to affect the flow for a longer distance from the outlet. Again, as already mentioned, we believe that longer averaging times would have yielded better agreement between the two grids.

4.2.3 Comparison against previously reported studies

To the best of our knowledge, the only 3-D results reported in the literature for the case of flow over a confined circular cylinder in a channel are from Rehimi *et al.* [39], who, however, considered a different blockage ratio of $\beta = 1/3$. For the blockage ratio examined in the present paper ($\beta = 1/5$), the only previously available results had been obtained from 2-D simulations. Therefore, 2-D numerical simulations were performed

Table 4.3: Comparison of critical Reynolds number and corresponding Strouhal number with previous two-dimensional numerical studies.

	Present	Sahin and Owens [27]	Zovatto and Pedrizzetti [33]	Chen *et al.* [28]
Re_{cr}	69.5	69.9	68.9	69.3
St_{cr}	0.1567	0.1567	–	0.1559

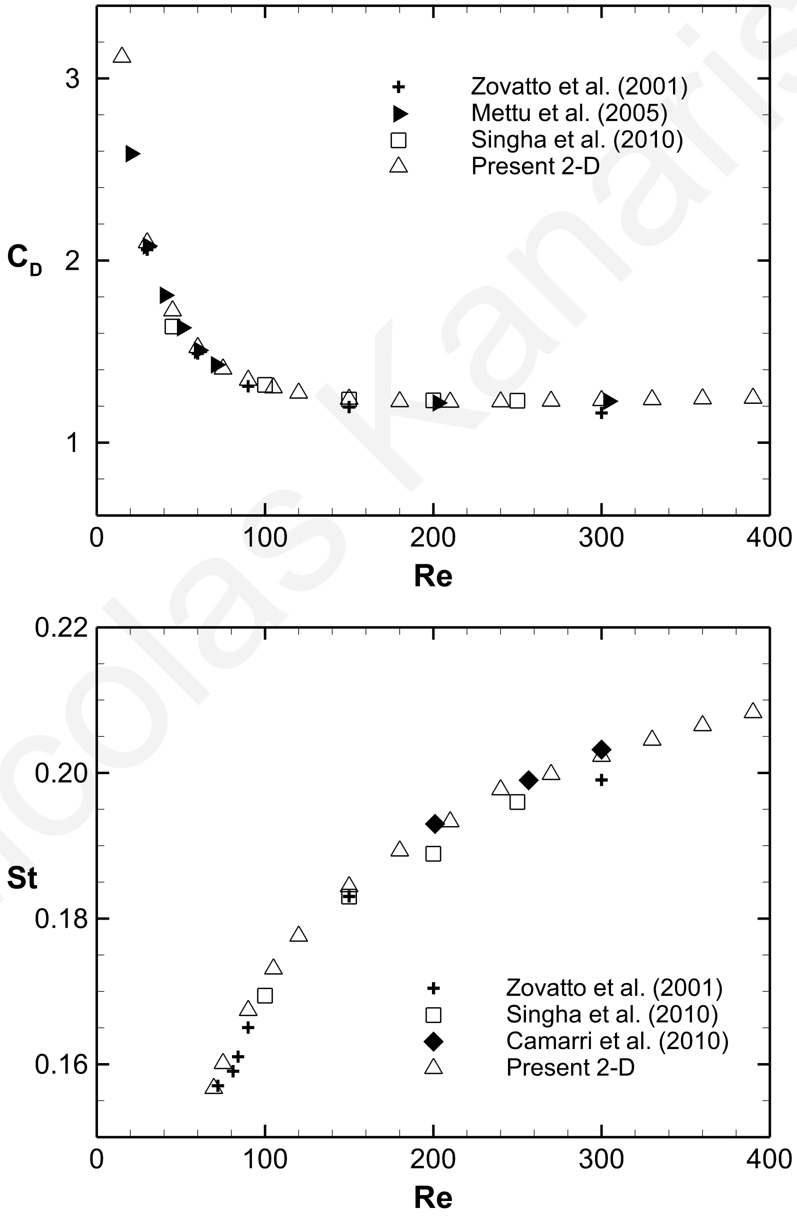

Figure 4.6: Drag coefficient C_D and Strouhal number St versus Reynolds number, numerically obtained from two-dimensional simulations, compared with previous two-dimensional numerical studies (References [33, 34, 29, 40]).

first, allowing the validation of the numerical code and the chosen parameters through comparisons with existing literature.

The critical Reynolds number Re_{cr} for the transition from steady to unsteady flow, the mean drag coefficient $\bar{C}_D$, and the Strouhal number St were computed and compared against previous studies. Our results for Re_{cr}, and the corresponding Strouhal number St_{cr}, are listed in Table 4.3. When compared with the values reported in Refs. [27, 33, 28], these show an excellent agreement. Figure 4.6 displays a comparison of both the drag coefficient and the Strouhal number versus Re. As shown, the agreement is again very satisfactory, confirming the accuracy of the numerical code and the choice of appropriate numerical parameters.

4.3 Three-dimensional effects

4.3.1 Transition to three-dimensionality

In order to carefully investigate transitional effects, a series of nine three-dimensional simulations have been carried out for the range $150 \leq Re \leq 390$, in steps of 30. A summary of the results obtained is listed in Table 4.4.

It is important to note that the vortex shedding in the present 3-D simulations is initiated without imposing or forcing any artificial or external flow-disturbances. Instead, the round-off and truncation errors, which are uniformly distributed over the whole computational domain, were allowed to generate the self-excitation needed for the flow to naturally develop three-dimensionalities. This choice was associated with long computational times that became even longer for the cases that were closer to the transitional regime, as we discuss further below. However, this choice was motivated by the lack of previously reported data on this flow configuration.

The first steps of transition to three-dimensionality are reflected in the amplifica-

Table 4.4: Summary of results from the current three-dimensional numerical simulations.

Case	Re	W	$\bar{C}_D$	C'_L	St	C_{pb}
1	150	8	1.2389	0.271	0.1850	0.8487
2	180	8	1.2253	0.342	0.1893	0.8845
3	210	8	1.166	0.25	0.1852	0.832
4	240	12	1.169	0.30	0.1895	0.880
5	270	8	1.170	0.37	0.1949	0.913
6	300	8	1.172	0.37	0.1989	0.942
7	330	8	1.139	0.33	0.2015	0.918
8	360	8	1.120	0.30	0.2035	0.895
9	390	8	1.099	0.26	0.2053	0.883

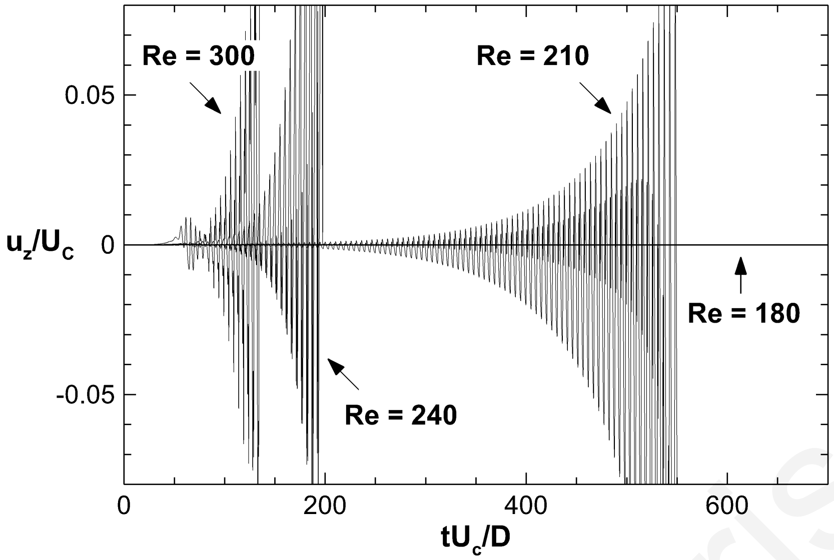

Figure 4.7: Time variation of the spanwise component of velocity, u_z, along the rear axis at x/D=1.5, three-dimensional case.

tion of the spanwise velocity-component, u_z, in the near wake. Figure 4.7 shows the time evolution of u_z in the near-wake, at Reynolds numbers ranging from 180 to 300. For the sake of clarity, each signal is truncated at a different evolution time to avoid overlaps. For the lowest Reynolds numbers considered here, namely $Re = 180$ (and $Re = 150$, which is not shown in Figure 4.7), the flow did not exhibit any sign of spanwise fluctuations, an indication that it remained completely two-dimensional. In contrast, for higher values of the Reynolds number, $Re \geq 210$, the flow showed an exponential growth of u_z, indicating the inception of three-dimensionality. As a general trend, with increasing Reynolds number, the u_z amplification was found to initiate earlier. Thus, the present simulations indicate that the transition in the cylinder's wake occurs within the interval between $Re = 180$ and $Re = 210$. This is consistent with the results of Camarri and Giannetti [40], who carried out a Floquet stability analysis for the same configuration and found a critical value of $Re_{crA} \approx 201$ for the transition to a three-dimensional state.

Transition to three-dimensionality is also depicted on the time history of the lift, C_L, and drag, C_D, coefficients as shown in Figure 4.8. After a transient period, during which the flow remains in a two-dimensional state and periodic vortex shedding is observed, the signal eventually loses its coherence, and a drastic reduction in the lift and drag forces occurs, corresponding to a three-dimensional state of the flow. The flow develops these three-dimensional effects soon after the amplification of the spanwise velocity u_z. The length of the transient period was particularly long for $Re = 210$, approaching 500 time units, but it got shorter as the Reynolds number was further increased. For all other cases up to $Re = 390$, the transient period was ranging between 50 to 200

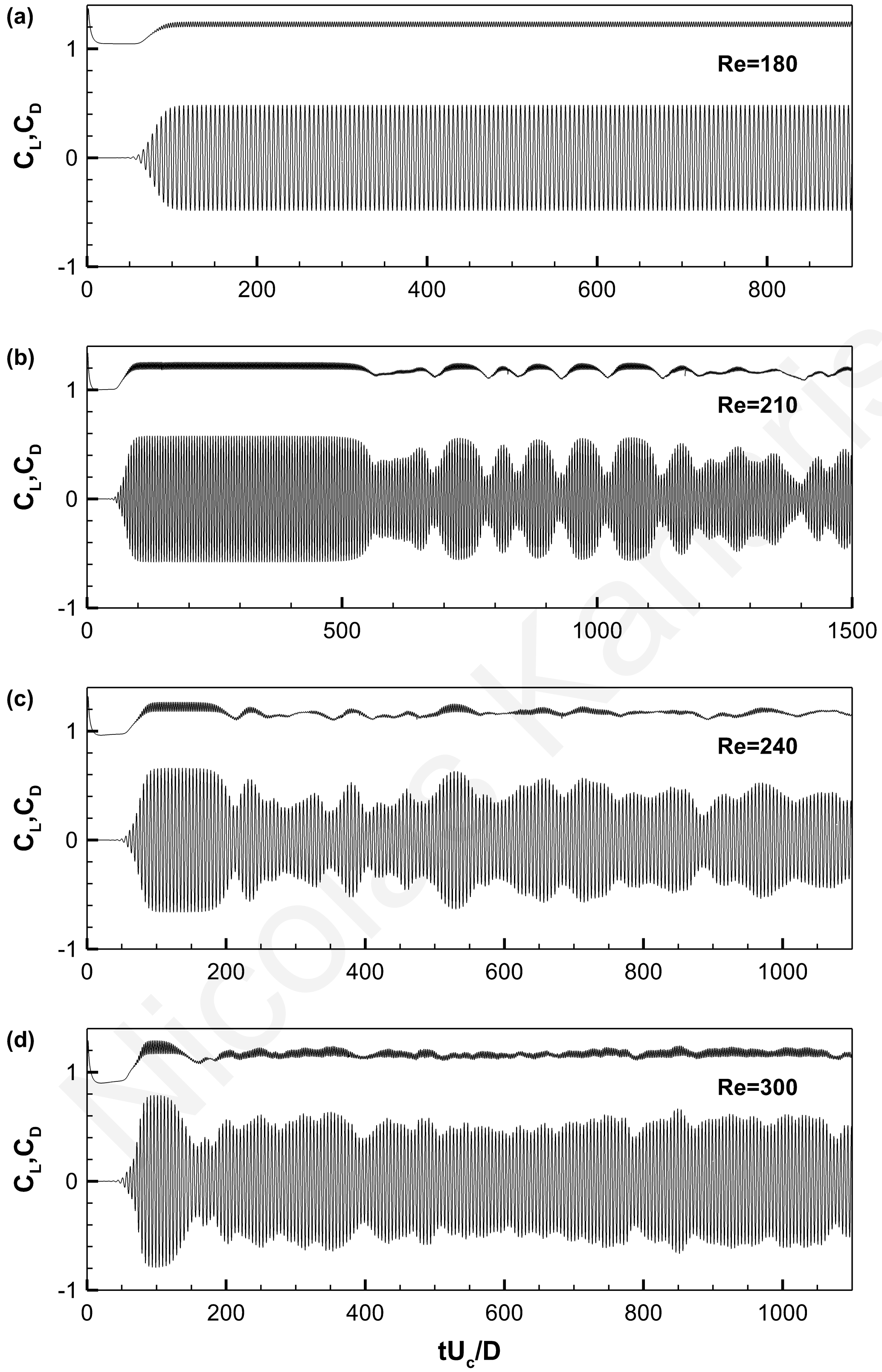

Figure 4.8: Lift C_L and drag coefficient C_D versus time, for the three-dimensional cases: (a) $Re = 180$, (b) $Re = 210$, (c) $Re = 240$, and (d) $Re = 300$.

time units. This behavior bears strong resemblance to the simulations of Mittal and Balachandar [9] for the case of an unconfined circular cylinder.

4.3.2 Effect of Re on Strouhal number St and base pressure coefficient C_{pb}

As the Reynolds number is increased, modifications in the dynamics of the wake structure produce distinct changes in the shedding frequency and the pressure field. The transient nature of the flow necessitates long simulation times before reliable statistics can be collected, especially for *Re* values close to the wake transition critical points. In our case, simulation times were made even longer because of our relyince on self-excitation to trigger transition. Once a statistically stationary state was reached in the computation, the calculation was continued for another 100 to 150 vortex shedding cycles to obtain the time-averaged values. Strouhal numbers have been obtained from the lift coefficient signals using Welch's averaged periodogram method [81]. A Hamming window was applied to each overlapping segment of data.

The variation of the Strouhal number, *St*, as a function of the Reynolds number is shown in Figure 4.9, where results from the present 2-D and 3-D simulations are compared to the experimental results of Williamson [15] for the *unconfined* case. Dashed vertical lines indicate the critical Reynolds numbers, which, according to Camarri and Giannetti [40], mark the onset of different wake instabilities for the case of a confined circular cylinder with the same blockage ratio as used in the present study. As shown in Section 4.3.1, the flow remains completely two-dimensional up to $Re = 180$. Not surprisingly then, results from the 2-D flow simulations are identical to those from the 3-D simulations in this range of *Re* values. However at $Re = 210$, where three-dimensional effects start to develop, a significant difference between the 2-D and 3-D cases is observed. In the 3-D case, *St* undergoes a sudden drop of approximately 4% that persists up to $Re = 240$. As *Re* is further increased, differences are observed to be less significant, and another discontinuity in the *St*–*Re* relationship shows up, which this time is not hysteretic. At $Re = 270$ the difference between 2-D and 3D cases is around 2.5%, while for $Re = 300 - 390$ the difference decreases to 1.5%. Interestingly, results from the three-dimensional simulations compare well to the experimental results of Williamson for the case of an unconfined cylinder, but with a small delay in the critical *Re* values. This offset, towards higher Re in our case, seems to be attributed to the additional confinement from the channel walls, which presumably stabilizes the flow and produces higher transitional Reynolds numbers [82].

Williamson [20] associated these two discontinuous changes in the *St*–*Re* curve, with the development of different instabilities in the wake; mode A instability combined with intermittent vortex dislocations, and mode B instability. In accordance with these observations, current results indicate the existence of two instability regions: the first

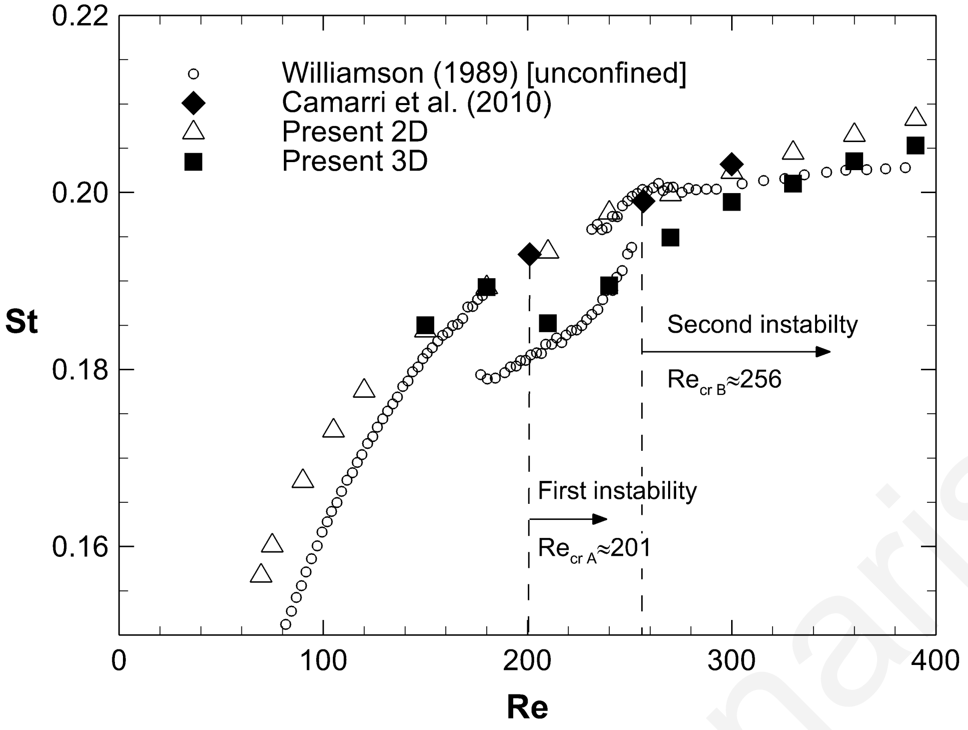

Figure 4.9: Strouhal number St versus Re, compared with the linear stability analysis of Camarri and Giannetti [40], and the experimental study of Williamson [15] for the case of an unconfined circular cylinder. Dashed lines mark the critical Reynolds number indicated by Camarri and Giannetti [40] for the onset of different wake instabilities.

occurs around $Re = 210$ and corresponds to the onset of three-dimensionalities in the flow, while the second occurs around $Re = 270$. We shall discuss these instabilities in greater detail in the following section. These findings are consistent with the results of Camarri and Giannetti [40], who carried out a linear stability analysis for the case of a confined circular cylinder having the same blockage ratio as in the present study and also found the existence of two instability regions. They found the critical value for the onset of the second instability to be $Re_{crB} \approx 256$. According to their work, these instabilities have the same symmetries as the mode A and mode B instabilities found in the unconfined case. However, no drop in the Strouhal number is reported in their study. This is not surprising taking into consideration the limitations of the linear stability approach, and the fact that this transition feature, observed at $Re \approx Re_{crA}$ and above, is not a linear effect of the instability, but is a result of strongly nonlinear phenomena [6, 23].

Despite its value in assessing flow instabilities, the evolution of the base pressure coefficient, C_{pb}, as a function of the Reynolds number has not been previously discussed in the literature for the confined case. Figure 4.10 shows this evolution for the present 2-D and 3-D simulations together with the experimental results of Williamson and Roshko [16], and the data of Dennis and Chang [5] for comparison with the unconfined

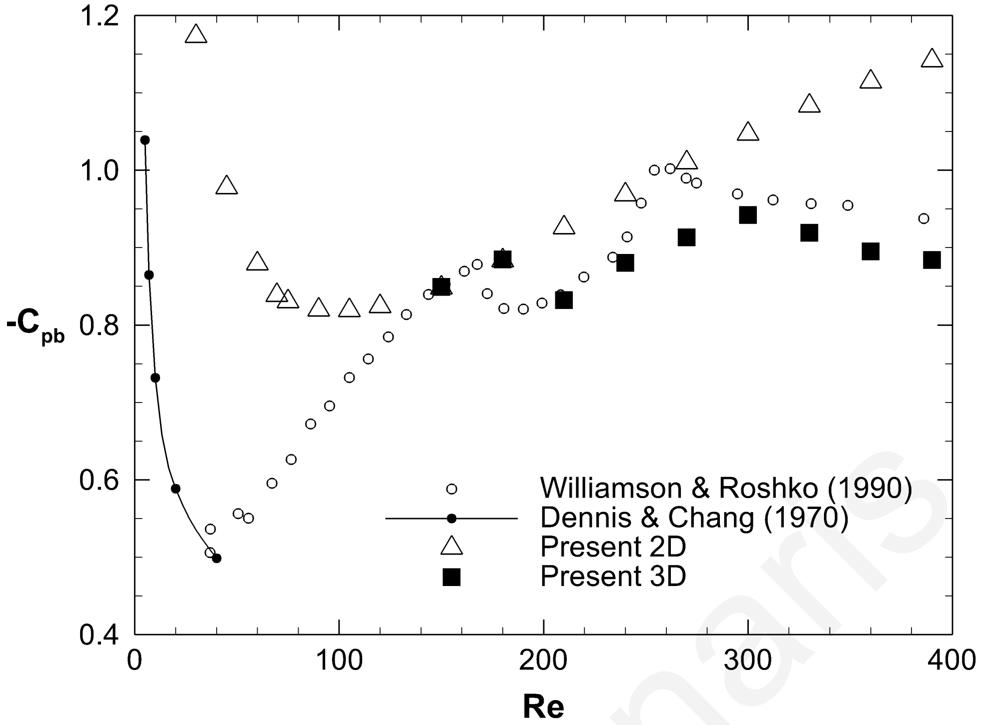

Figure 4.10: Base pressure coefficient C_{pb}, versus Re, compared with the experimental study of Williamson and Roshko [16] and the numerical simulations of Dennis and Chang [5] for the case of an unconfined circular cylinder.

case. Again, as expected, results from the 2-D and 3-D simulated flows are identical up to $Re = 180$, where the flow remains two-dimensional. For $Re > 210$, where three-dimensional effects start to take place, the results from the 3-D simulation show a marked drop in the level of C_{pb}, which remains undetected in the 2-D simulations. Once again, the C_{pb} predictions from the current 3-D simulations exhibit a very similar evolution with Re as found experimentally by Williamson and Roshko [16], for the unconfined case.

According to Williamson [20] and Roshko [26] the variations of the base pressure coefficient correspond to the presence of instabilities in the flow. In the unconfined case, the drop in the base pressure coefficient at $Re = 180$ is thought to be to related to the presence of mode-A instability and vortex dislocations [20]. At $Re = 260$, on the other hand, there is a local maximum that corresponds to a saturation of the primary instability growth [26]. Around that point, the secondary spanwise structure changes to one with smaller scale, mode B instability [20]. As Re is further increased, three-dimensional structures become more disordered and the base suction begins to decrease. Our computations show the same characteristics in the variation of C_{pb} with Re, the only difference being again a small delay in the initiation of 3-D effects in the confined case relative to the unconfined results ($Re = 210$ instead of $Re = 180$), and similar delay in the saturation effects ($Re = 270 - 300$ instead of $Re = 260$), which are attributed to the additional confinement of the channel walls. Based on these results, one would expect the overall structure of the confined wake to be similar to that of the unconfined case. This expectation is confirmed by the findings presented in the following sections.

4.3.3 Instabilities in the wake

In order to identify three-dimensional vortex structures in free shear flows, the vorticity magnitude is usually used. However, in our case due to the existence of vorticity at the channel walls, using the vorticity magnitude to identify vortices would result in deformed vorticity structures and difficulties in visualizing them. The λ_2 criterion is by far more appropriate for boundary layer type of flows and it is defined as the second eigenvalue of $S^2 + X^2$, where S and X denote the symmetric and antisymmetric parts of the velocity gradient tensor respectively [83]. Thus, iso-surfaces of λ_2 were used in order to exclude the wall shear region and focus on the swirling motion of the primary and induced vortices of the cylinder wake. Indeed, through the application of the λ_2 criterion we were able to clearly detect the vortical motions of interest for such a highly three-dimensional wall-bounded shear flow.

A visual impression of the three-dimensional structures related to the different instabilities found in the flow can be obtained from Figure 4.11. There, we show snapshots of iso-surfaces of λ_2 normalized by its absolute minimum, $\lambda_{2,min}$, for different Reynolds numbers with increasing value. Iso-surfaces are colored by the streamwise vorticity component, ω_x, to reveal the streamwise rotation direction of each vortical structure. The spanwise rollers essentially identify the primary vortex cores.

At $Re = 240$ (see Figure 4.11(a)), a Reynolds number corresponding to a regime well after the onset of the first instability, a spanwise waviness of the primary vortex cores is observed in the cylinder's wake, along with the formation of counter-rotating streamwise vortex pairs. Over successive half cycles of vortex shedding, vortex pairs of opposite-sign vorticity are formed. The flow displays a dominant spanwise wavelength of around $4D$, in agreement with the value of $4.65D$ reported by Camarri and Gianneti [40] for a similar configuration. This periodic, out-of-phase, three-dimensional flow pattern is topologically similar to that of mode A [20], at least in the near wake region (as it will be discussed in the next section). Mode A instability appears in the wake of an unconfined circular cylinder with a spanwise wavelength of approximately $4D$ [21, 20, 6].

For $Re = 300$ and above, finer scale streamwise vortex pairs are observed (see Figures 4.11(d) and 4.11(e)), with a distinctly smaller spanwise wavelength of approximately $1D$. This time, successive vortex pairs from one braid layer to the next, have the same orientation, forming an in-phase streamwise vortex pattern. This instability, in contrast to mode A, is restricted to the near wake only and it is not found in the

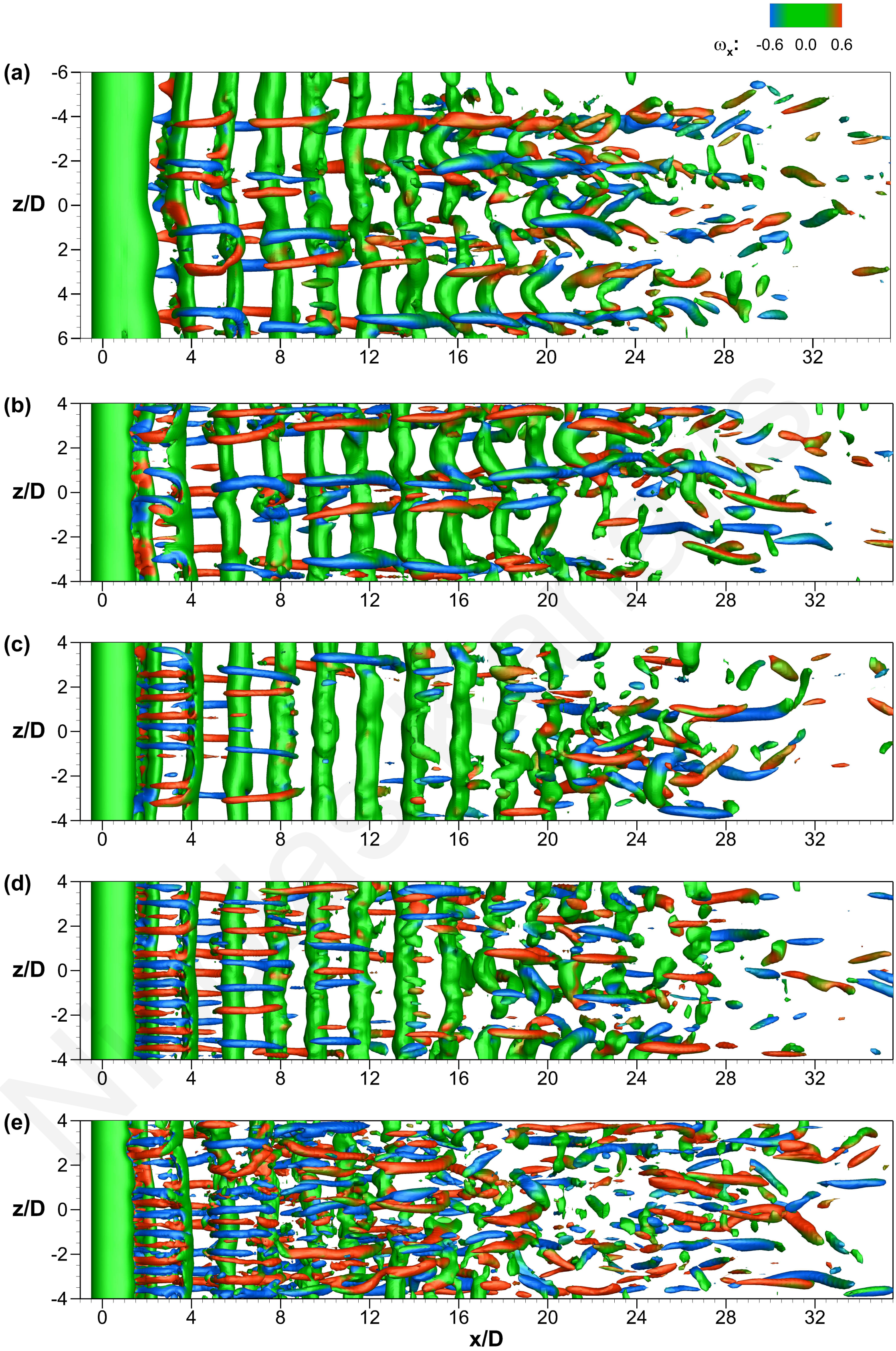

Figure 4.11: Instantaneous plots of iso-surfaces of the λ_2 criterion normalized by its absolute minimum ($\lambda_2/\lambda_{2,min} = 0.5\%$) and rendered by contours of streamwise vorticity, top view. Flow is from left to right. (a) $Re = 240$ at $t = 1116D/U_c$, (b) $Re = 270$ at $t = 1048D/U_c$, (c) $Re = 270$ at $t = 1110D/U_c$, (d) $Re = 300$ at $t = 916D/U_c$, and (e) $Re = 390$ at $t = 694D/U_c$.

far downstream locations. With increasing Re, the number of streamwise vortices is increased, and the flow becomes more distorted. This flow pattern is analogous to that of mode B vortex shedding described by Williamson [20] for the case of an unconfined circular cylinder. It also compares well with the predicted critical wavelength of $0.86D$ found by Camarri and Gianneti [40] for the confined case.

In the case of $Re = 270$, which is close to the instability threshold, $Re_B \simeq 256$, found by Camarri and Gianneti [40], modes of vortex shedding similar to both mode A and mode B were observed at different instances of the flow (see Figures 4.11(b) and Figure 4.11(c), respectively) . This intermittent nature of the flow is in line with the experimental observations of Williamson [20], the direct numerical simulations of Henderson [23], and the stability analysis of Barkley [84] for the unconfined case. They have shown that the transition from mode A to mode B is associated with a gradual transfer of energy from one mode to the other, resulting in a mixed-mode state approximately in the Re range $230-265$. Williamson attributes this to the intermittent swapping between the two modes, rather than the coexistence of both modes. Also, Behara and Mittal [25] in their numerical investigations demonstrated the swapping between modes up to $Re = 275$ for the unconfined case.

The present three-dimensional simulations are the first to reveal the presence of natural vortex dislocations in the confined wake of a circular cylinder. Williamson [17, 20] has shown that large-scale, spot-like, vortex dislocations are an intrinsic phenomenon of wake transition. These irregularities occur spontaneously along the span as a natural feature of the wake flow, and are associated with the presence of mode A instability. However, few three-dimensional simulations have captured them. Zhang *et al.* [21] reproduced numerically Williamson's vortex-dislocations, after applying strong localized spanwise inhomogeneity in the initial conditions. Braza *et al.* [19] were the first to obtain the vortex dislocations naturally by means of a complete Navier-Stokes simulation. In the present work, clear observations of the existence of natural vortex dislocations are presented for the case of a confined circular cylinder.

The occurrence of such dislocations can clearly be seen in Figure 4.12, where snapshots of iso-surfaces of $\lambda_2 = -0.4$ and pressure $p = -0.4$ are presented for $Re = 240$ at $t = 870D/U_c$. Iso-surfaces of λ_2 are colored by streamwise vorticity component, ω_x. At the occurrence of dislocation, in the vicinity of $z/D = -2$, the span-wise coherence of the primary vortex core is lost and a break in the continuity of the vortex tube can be seen. Moreover, during this phase of the flow, dislocations affect the shedding phenomenon, which as a result becomes irregular.

One can identify the occurrence of dislocations through their signature in instantaneous velocity signals and the corresponding spectra at different spanwise positions. Figure 4.13 displays the crossflow velocity component signal from a series of probes spaced in the spanwise direction and placed at the intersection of the horizontal plane y/D=0.5 and the vertical plane x/D=1.5. This a location slightly downstream from

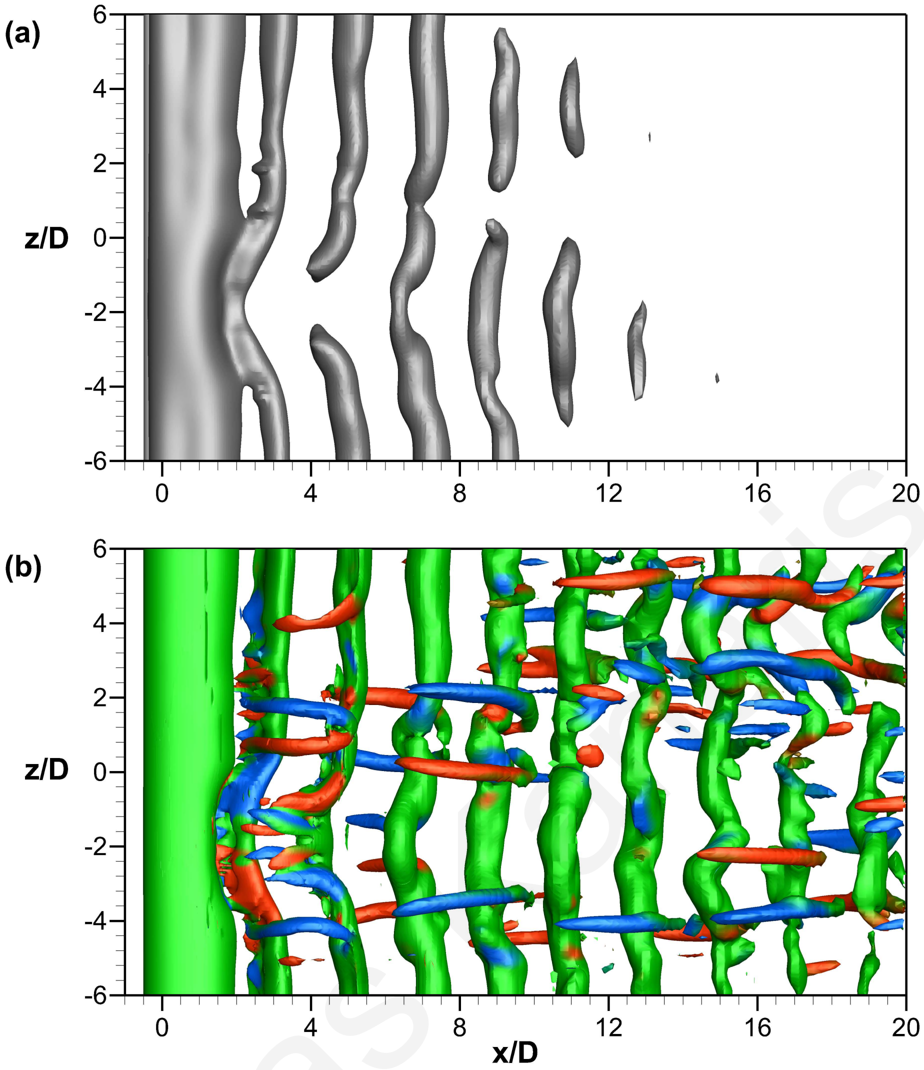

Figure 4.12: Iso-surfaces of (a) pressure ($p = -0.4$) and (b) λ_2-definition ($\lambda_2 = -0.5$), top view, for $Re = 240$ at $t = 870D/U_c$. Iso-surfaces of λ_2 are colored by streamwise vorticity component ω_x.

the cylinder. At certain spanwise positions, the normal Karman vortex shedding gives way to a pronounced modulation in the time history of fluctuating velocities. These can be seen as the marked areas in Figure 4.13(a), or more clearly in Figure 4.13(b), where two samples of velocity signals are displayed in an interval corresponding to the time instant of the snapshot shown in Figure 4.12. These irregularities, or glitches, in the velocity signal correspond directly to the passage of a vortex dislocation structure past the measuring probe [17]. The spontaneous occurrence of such dislocations at different spanwise locations was found to be regular in time.

Another way to visualize dislocations is by looking at the corresponding power spectral density of the velocity signal (see Figure 4.14). Braza *et al.* [19] found that in the regions where a vortex dislocation occurs the spectral energy of the fundamental frequency is reduced considerably. This behavior is clearly seen in Figure 4.14. In the

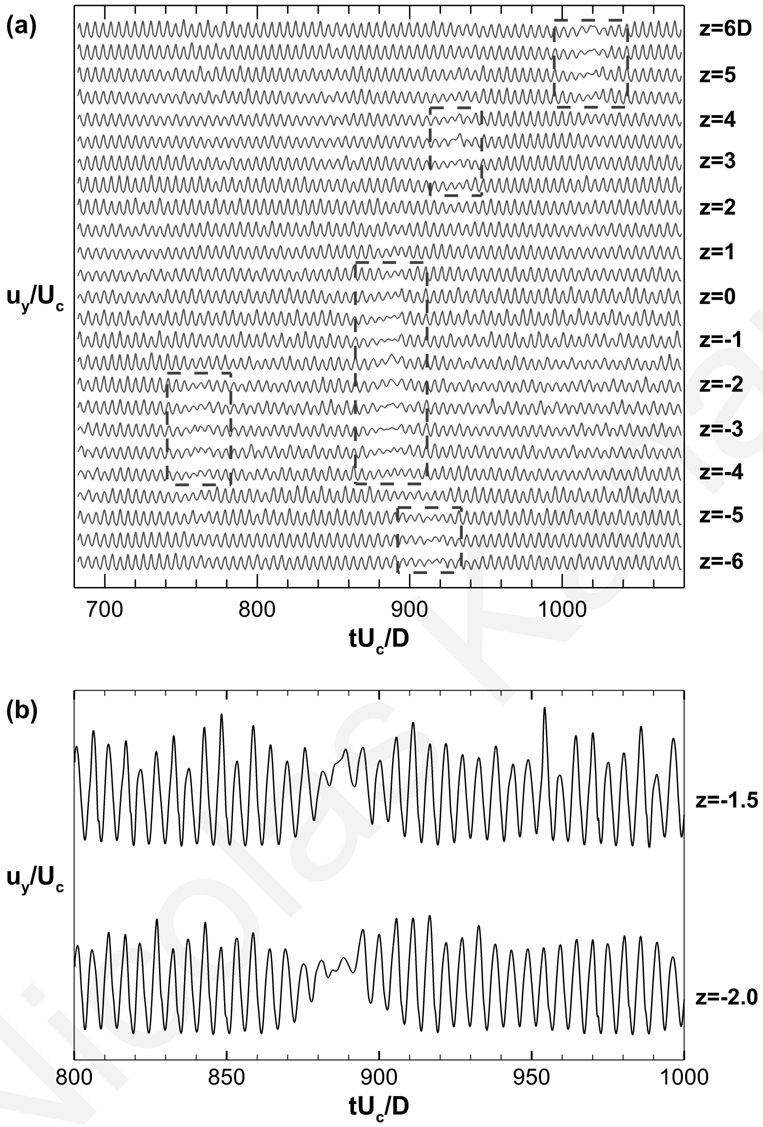

Figure 4.13: (a) Time history of velocity component u_y measured at probes located along the span at the position $x/D = 1.5$, $y/D = 0.5$. Dotted lines mark areas of pronounced modulation of the velocity signal, indicating the presence of vortex dislocations. (b) Expanded view showing two samples of velocity signals in a time interval associated with the snapshot in Figure 4.12.

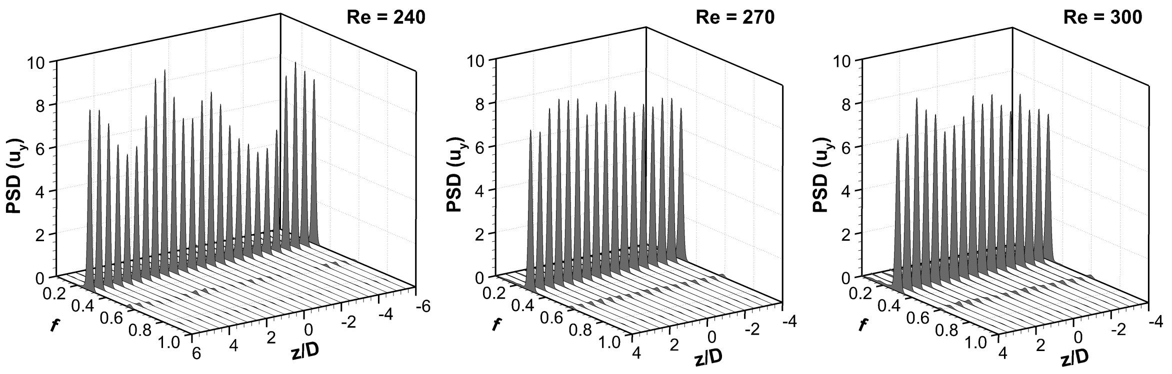

Figure 4.14: Spectra of crossflow velocity component u_y along the span at the position $x/D = 1.5$, $y/D = 0.5$, for $Re = 240, 270$, and 300 from left to right.

case of $Re = 240$, where the flow exhibits mode A vortex shedding, there is a significant decrease in the spectral energy in the vicinity of $z/D = 4$ and $z/D = -3$. The drop, at certain spanwise positions, reaches up to 50% from the maximum value. On the other hand, for the cases of $Re = 270$ and $Re = 300$, which correspond to a mixed or pure mode B vortex shedding, changes in the amplitude of the spectral density are much smaller, approximately 15% and 20% respectively. In these cases, the flow is devoid of vortex dislocations, in agreement with the experiments of Williamson [17] and the numerical simulations of Behara and Mittal [25].

4.3.4 Effects of confinement

In order to identify differences between the wake characteristics of confined and unconfined cylinders, two more simulations were performed, at $Re = 240$ and $Re = 300$, this time for an unconfined cylinder. To accommodate the unconfined simulations, grids G2W and G2F were laterally extended from $5D$ to $50D$, in order to minimize blockage effects [6, 24], while providing a comparable resolution to the corresponding confined cases.

The effects of confinement on mode A flow structures are examined first. A comparison between the confined and the unconfined case is shown in Figure 4.15, where snapshots of iso-surfaces of the λ_2 criterion are plotted at $Re = 240$. Although mode A is identified in the confined case, the downstream evolution of the cylinder wake is strongly affected by confinement. In the near wake region, i.e. for $x/D < 5$, mode A is clearly identifiable in the confined case, and one cannot discern clear differences between the vortical patterns generated by the confined and unconfined cases. Moving further downstream though, one finds that the structure of the confined wake departs from that of a standard unconfined cylinder wake. For example, at $5 < x/D < 17$, the hairpin structures of the braid shear layer that are a standard feature of the unconfined wake, can still be identified in the confined case, but their motion and shape

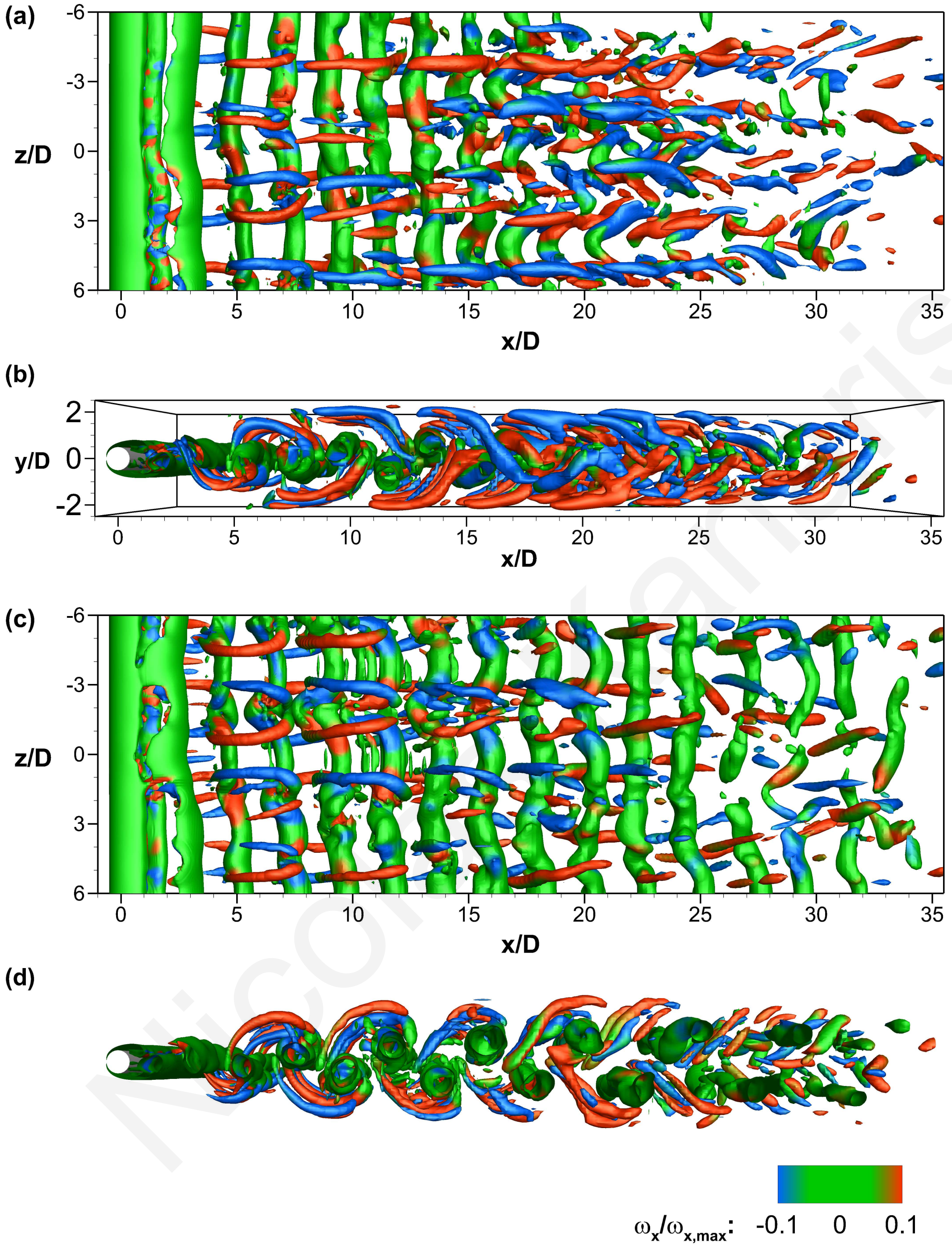

Figure 4.15: Iso-surfaces of λ_2 normalized by its absolute minimum ($\lambda_2/\lambda_{2,min} = 0.35\%$), colored by the streamwise vorticity component, for the case of a confined (a,b) and an unconfined (c,d) circular cylinder at $Re = 240$. $\omega_{x.max}$ is the maximum streamwise vorticity magnitude. Supplementary movie shows an animation of the vortex structures for the confined case (Mode A instability).

is significantly modified. These differences may be attributed to the inversion of the Von Karman vortices caused by wall interactions in the confined case, as described by Camarri and Gianneti [40]. For $x/D > 17$, the confined wake is much more fragmented, without a clear presence of primary vortex cores, which in the unconfined case, are seen to persist this far downstream. In the same region, one finds a stronger streamwise alignment of vortices in the confined case compared to the unconfined case. In the confined case, hairpin vortices sustain their coherency and persist for larger distances, up to $x/D \approx 30$.

The breakdown of the primary vortex cores and the fragmented nature of the flow depicted by iso-surfaces of $\lambda_2 = -0.3$ (0.5% of its absolute minimum) is represented over successive time instants at $Re = 240$ in Figure 4.16. In order to have a more clear view of the spanwise vortex cores, rather than the streamwise vortices, iso-surfaces are colored by the spanwise vorticity component ω_z. At $t = 1111 D/U_c$ one can observe that from approximately $x/D \approx 17$ and above, the primary vortex cores lose their coherence and break into smaller structures that become aligned in the streamwise direction as they are advected further downstream. If we focus our attention on one such a pair of counter-rotating spanwise vortex cores (see Figure 4.16(a) - box A), and follow them in time as they move further downstream, the initial small waviness grows, and they seem to be gradually pulled backwards and towards the channel walls. When they reach the vicinity of $x/D = 17$ (see Figure 4.16(b) - box B), the front counterclockwise vortex roller (top roller, colored red) starts losing its continuity and breaks. At $x/D \approx 22$, eventually both vortices break down and they are transformed to U-shaped vortices (see Figure 4.16(c) - box C). The legs of these structures are later separated and transformed to streamwise rollers as they are advected downstream (see Figure 4.16(d) - box D). Interestingly this pattern of behavior is systematic and all primary vortex cores are stretched and eventually break down in a similar manner and around the same spanwise positions.

Figures 4.17(a) and 4.17(b) show iso-surfaces of the streamwise component of the velocity field, for $u_x = 0.5$ and 1.5 respectively, for $Re = 240$ at $t = 1130 D/U_c$. Looking at Figure 4.17(a), one can observe close to the channel walls “streaks” of low-velocity fluid that protrude towards the center of the channel. These “streaks” are aligned in the streamwise direction and occur on both sides of the channel walls at similar spanwise positions. In between these low-velocity fields, regions of high-velocity fluid are observed that are also aligned in the streamwise direction, as seen in Figures 4.17(b) and 4.17(d).

This organized, “symmetric” mixing of low and high velocity fields results from the interaction of the streamwise vortex pairs, from mode A instability, and the channel walls. Figure 4.17(c) shows a contour plot of u_x in the plane $x/D = 7.2$ (plane A). Contour lines of streamwise vorticity, $\omega_x = \pm 0.6, \pm 0.8$, are superimposed to give information on the location and rotation direction of the streamwise vortex pairs. The

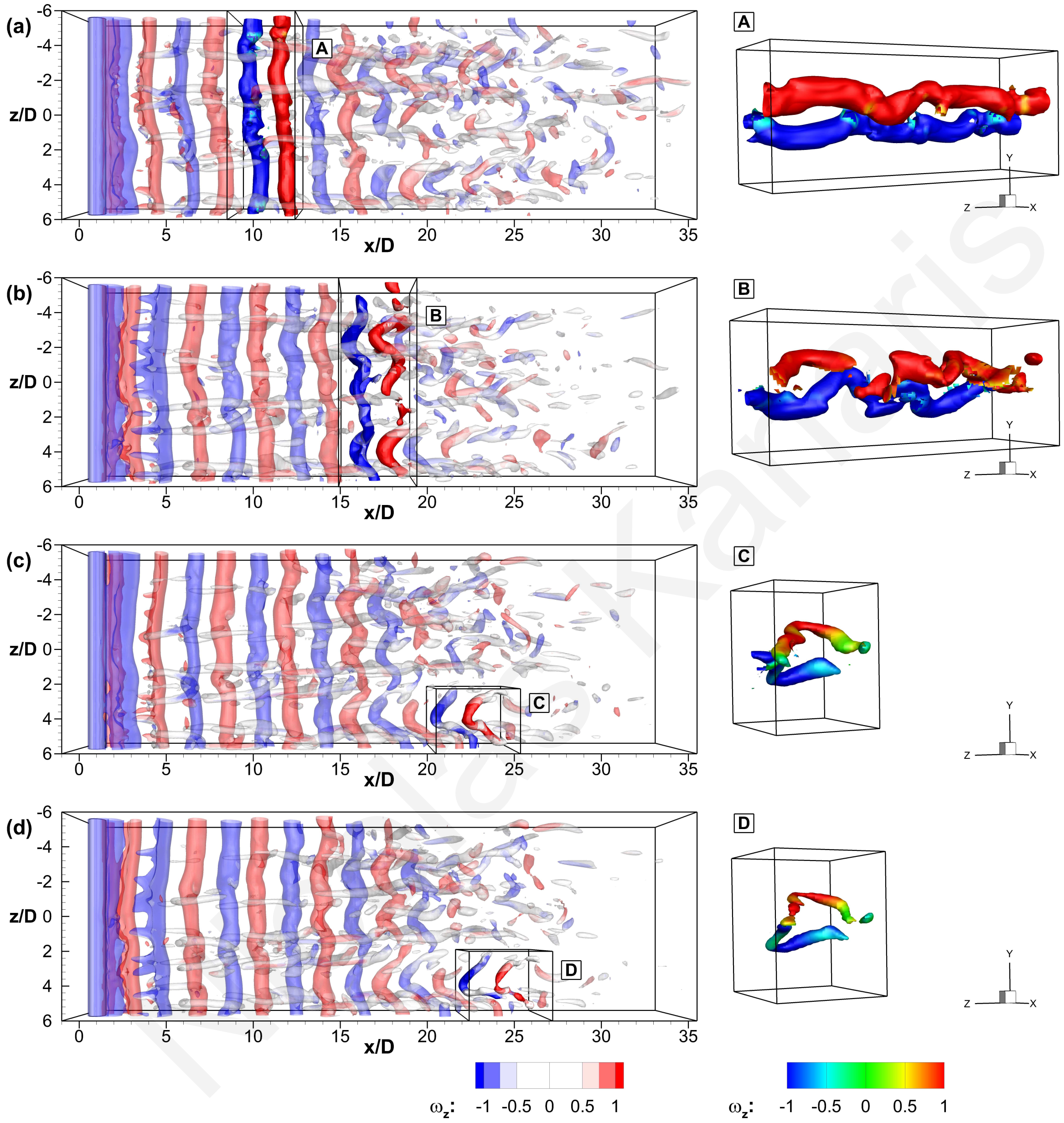

Figure 4.16: Instantaneous visualization of iso-surfaces using $\lambda_2 = -0.3$ over successive time instants at $Re = 240$. Iso-surfaces are colored by the spanwise vorticity, ω_z. (a) $t = 1111D/U_c$, (b) $t = 1120D/U_c$, (c) $t = 1127D/U_c$, (d) $t = 1130D/U_c$.

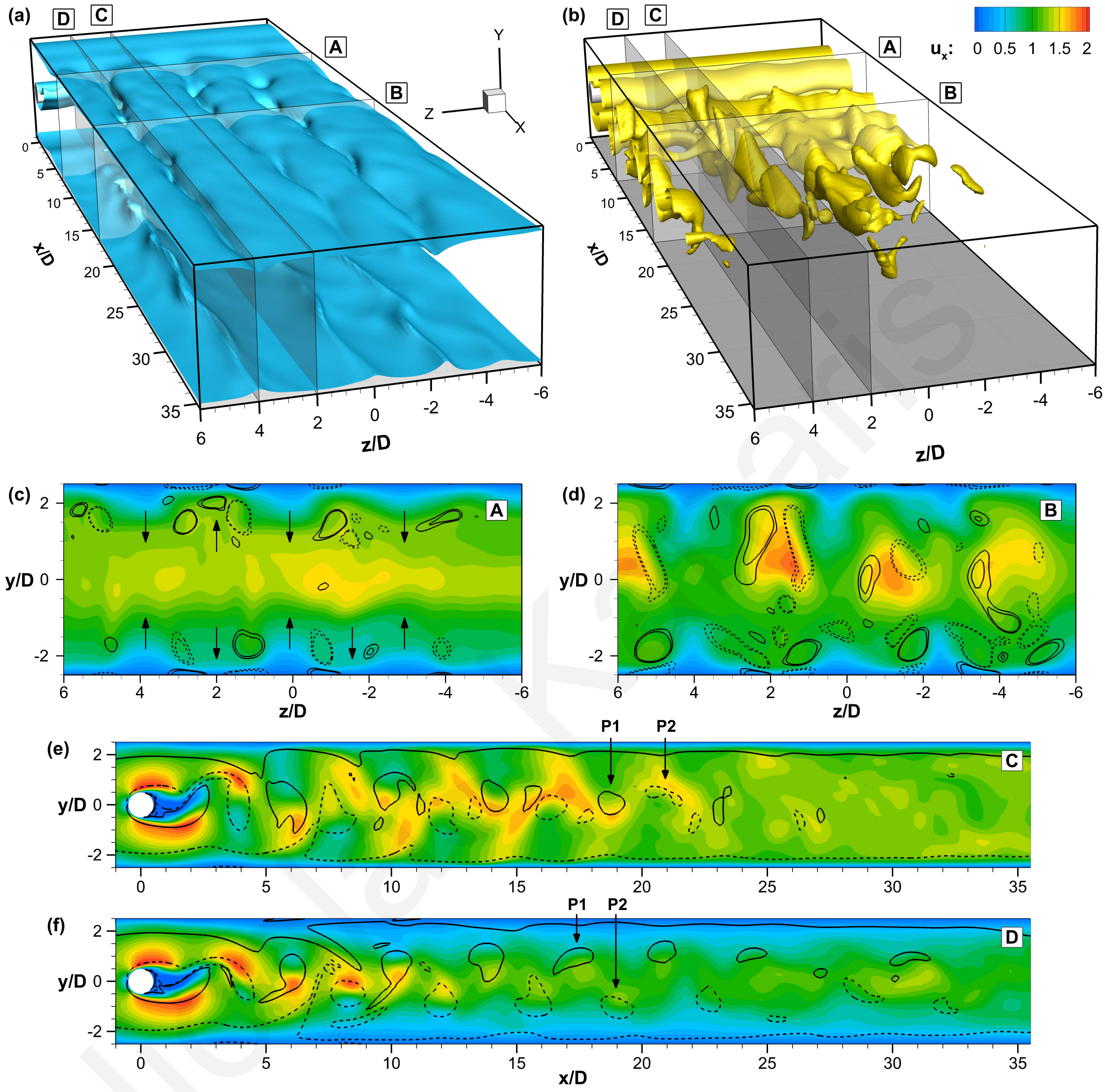

Figure 4.17: Instantaneous visualizations of the streamwise velocity field, u_x, for the case of $Re = 240$ at $t = 1130D/U_c$. (a-b) Iso-surfaces of $u_x = 0.5$ (a), and $u_x = 1.5$ (b). (c-d) Contour plots of u_x in the planes $x/D = 7.2$ (c), and $x/D = 16.8$ (d). Lines represent the values of streamwise vorticity, $\omega_x = \pm 0.6, \pm 0.8$ (dashed lines correspond to negative values of ω_x). Arrows indicate the direction of the velocity induced by the streamwise vortices. (e-f) Contour plots of u_x in the planes $z/D = 2$ (e), and $z/D = 4$ (f). Lines represent the values of spanwise vorticity, $\omega_z = \pm 0.8$ (dashed lines correspond to negative values of ω_z). $P1$ and $P2$ are anticlockwise and clockwise primary vortex cores respectively.

induced velocity due to the streamwise vortex pairs drives low-velocity fluid towards the centreplane of the wake and high-velocity fluid towards the channel walls. Because mode A instability gives an out-of-phase streamwise vortex pattern at particular spanwise locations, streamwise vortex pairs of opposite sign reside on opposing sides of channel walls. As a result, the deformation and stretching of low and high velocity fluid towards and away from the centreplane of the wake occurs at the same spanwise positions on both sides. The self-sustaining nature of mode A, that gives an array of streamwise vortex pairs that travel further downstream at the same spanwise positions, explains why these low and high speed regions are aligned in the streamwise direction.

Figures 4.17(e) and 4.17(f) show contour plots of u_x in the planes $z/D = 2$ (plane C) and $z/D = 4$ (plane D) respectively, which correspond to areas in the wake where high and low velocity fields are more prominent accordingly. In order to investigate the effect of the velocity field on the primary vortex cores, lines representing values of spanwise vorticity, $\omega_z = \pm 0.8$ are displayed on top. As seen in Figure 4.17(e) the primary vortex cores strongly interact with the high-speed velocity field and are forced to follow a trajectory close to the centerline as they shed downstream. On the other hand, in the plane $z/D = 4$ (see Figure 4.17(f)), as segments of the vortex cores are caught in the low-speed region, the primary vortex cores follow an oblique trajectory closer to the channel walls and progressively slow down (see vortex cores $P1$ and $P2$). This accelerating and slowing down of segments of the primary vortex cores at different spanwise locations causes the enhanced waviness observed. Around $x/D = 17$ the stretching of the vortex core become so strong that forces it to break down.

So far, the discussion of confinement effects has been limited to mode A instability. In the case of mode B, when compared with the unconfined case, the downstream evolution of the cylinder wake also seems to be strongly affected by confinement in a similar manner with mode A as shown in Figure 4.18 for $Re = 300$. For higher values of Re, the break down of the primary vortex cores ensues further upstream (up to $x/D = 12$ for $Re = 390$, as shown in Figure 4.11(e)) and the flow becomes more fragmented. However, in the presence of mode B instability, it was not possible to observe a regular pattern of vortex breakdown.

There are mainly two features of the flow responsible for this behavior. Unlike mode A, mode B instability leads to an in-phase streamwise vortex array with a smaller spanwise wavelength (see Figures 4.11 and 4.19(c)). Also, a spanwise wandering of the streamwise vortices from one half-cycle to the next is observed, in line with the experimental visualizations of Williamson [20] for the unconfined case. As a result, induced velocity from the streamwise vortices was found to generate irregular streams of low velocity, as shown in Figure 4.19(a). In contrast with mode A, these slow-moving regions, were neither aligned along the streamwise direction nor observed at symmetric locations on the channel walls. In addition, no clustered regions of high velocity extending in the streamwise direction were identified (see Figure 4.19(b)).

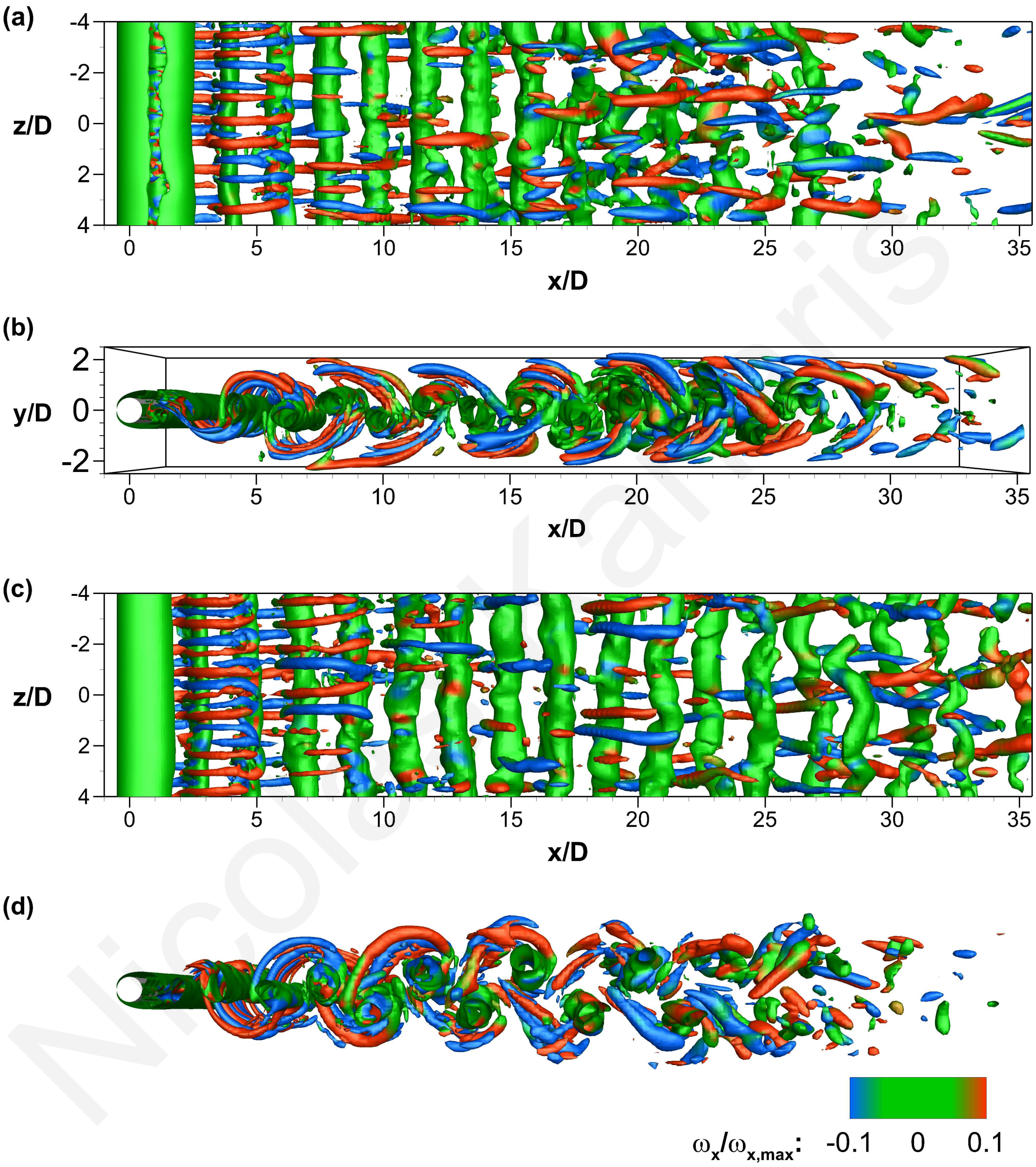

Figure 4.18: Same as Figure 4.15, but for Reynolds number, $Re = 300$. Supplementary movie shows an animation of the vortex structures for the confined case at $Re = 300$ and $Re = 390$ (Mode B instability).

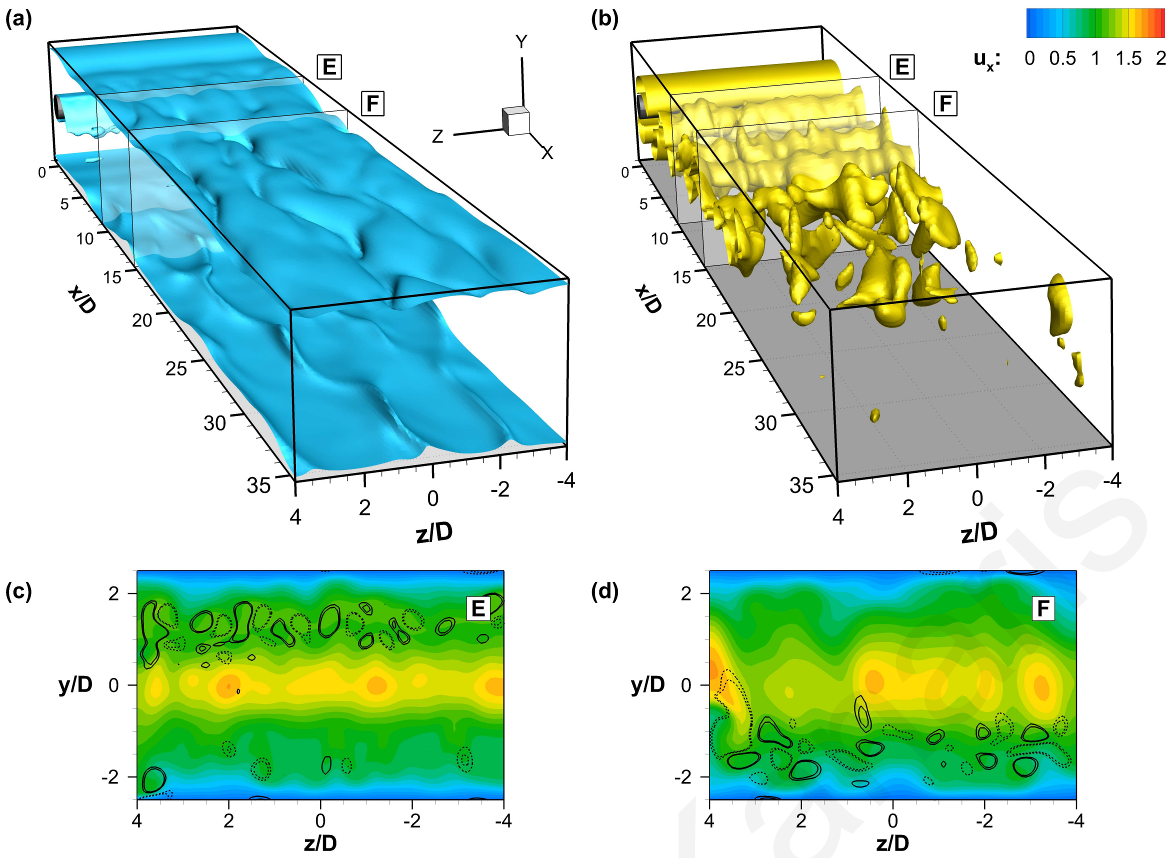

Figure 4.19: Instantaneous visualizations of the streamwise velocity field, u_x, for the case of $Re = 300$ at $t = 916D/U_c$. (a-b) Iso-surfaces of $u_x = 0.5$ (a), and $u_x = 1.5$ (b). (c-d) Contour plots of u_x in the planes $x/D = 8.9$ (a), and $x/D = 14.6$ (b). Lines represent the values of streamwise vorticity, $\omega_x = \pm 0.6, \pm 0.8$ (dashed lines correspond to negative values of ω_x).

These features promote the amplified distortion observed for mode B instability and result to the irregular break down of the primary vortex cores. With increasing Re these effects become even more pronounced leading to the breakdown of the primary vortex cores earlier downstream.

4.4 Conclusions

Direct numerical simulations of the two- and three-dimensional flow around a circular cylinder placed in a plane channel have been performed. The blockage ratio was kept constant at 1/5, and the Reynolds number was varied between 10 and 390.

Present results indicate that up to $Re = 180$ the flow remains two-dimensional. For higher values of the Reynolds number, $Re \geq 210$, the flow develops three-dimensional effects which are depicted on the time history of the lift, C_L, and drag, C_D, coefficients. Two discontinuous changes were detected in the St–Re curve corresponding to different spanwise instabilities in the wake, an effect that is linked to inherently nonlinear mechanisms and which previous studies failed to capture. We have also confirmed for the first time, that the critical points are also reflected in the C_{pb}–Re relationship, as was also found by Williamson for the unconfined case. Similar to the case of an unconfined circular cylinder, mode A 3-D shedding was observed for $Re = 210$ and 240. For $Re \geq 300$, mode B vortex structures were detected. At $Re = 270$ the flow exhibited an intermittent swapping between the two modes. The intermittent presence of naturally occurring vortex dislocations, as a fundamental feature of wake transition, was also demonstrated. This is the first time that the existence of these instabilities, has been confirmed via full 3-D simulations for the confined circular cylinder in a channel.

The present work leads to a clarification of how the shape and evolution of mode A and mode B instabilities are affected downstream by the confinement of the channel walls. In case of mode A, organized, “symmetric" mixing of low and high velocity fields is observed downstream, which eventually forces the primary vortex cores to break in a consistent and systematic way. In the case of mode B, irregular streams of low and high velocity are observed, which result to the irregular breakdown of the vortex cores. Understanding the hydrodynamic field and knowledge of the velocity profiles is important to properly predict local phenomena such as heat transfer and corrosion effects.

Chapter 5

Three-dimensional numerical simulations of MHD flow around a confined circular cylinder under low, moderate and strong magnetic fields

The work in this chapter was motivated by the lack of detailed three-dimensional simulations addressing the case of confined MHD flows with flow-obstructions. In this study, we perform fully three-dimensional direct numerical simulations around a circular cylinder placed symmetrically in a rectangular duct. The Hartmann and Shercliff layers developing along solid surfaces are fully resolved without using any wall model. Results are presented for values of the Hartmann number (based on the duct width) in the range of $0 \leq Ha \leq 1120$, and the Reynolds number (based on the cylinder diameter and centerline velocity) in the range $0 \leq Re_c \leq 5000$. Most of the studies in the literature have been based on the Q2D model, whose validity is restricted to high Ha numbers. Hence a main objective of this study is to fill in the gap in the area of low Ha for this type of flows. Fully three-dimensional direct numerical simulations are used to assess independently the performance and range of validity of simplified models, such as the Q2D model. Leveraging the information provided by the fully 3-D simulations, we attempt to address physical effects, which, as already pointed out by Dousset and Pothérat, [56] are not properly accounted for in the Q2D model due its inherent limitations. For example, we aim to shed light on the effect of the magnetic field intensity on the generated flow regimes. In addition, we describe the evolution of the flow characteristics (force coefficients and recirculation length) with Ha and Re, and discuss their spanwise distribution along the cylinder. Providing the full three-dimensional flow characteristics could also be beneficial to future modelers working towards the construction of advanced near-wall models for these type of flows.

The chapter is organized as follows. In Section 5.1, we define the test case considered and recall the governing equations, along with the proper boundary conditions. Section 5.2 is devoted to the numerical aspects of this study; in particular, we describe the numerical algorithm and the development of the grid design along with its respective validation and verification. In Section 5.3, we present the evolution of the critical Reynolds number for the onset of vortex shedding with respect to Ha, while in Sections 5.4 and 5.5 results under steady and unsteady flow conditions are presented, respectively. Finally, Section 5.6 presents the concluding remarks derived from the numerical experiments.

5.1 Problem statement and formulation

5.1.1 Flow configuration and mathematical formulation

The geometry considered in this study is shown in Figure 5.1. The geometry consists of a circular cylinder of diameter D and length W placed symmetrically in a rectangular duct. The ratio of the cylinder length to its diameter defines the aspect ratio,

$$\alpha = W/D\,, \tag{5.1}$$

while the ratio of the cylinder diameter to the duct height H (distance between the duct walls perpendicular to the cylinder axis) defines the blockage ratio,

$$\beta = D/H\,. \tag{5.2}$$

Results are reported for $\beta = 1/4$ and $\alpha = 4$, allowing for a direct comparison with the numerical simulations of Dousset and Pothérat [56]. The origin of the coordinates axes is placed at the cylinder's geometrical center, with the z direction being aligned with the cylinder axis. The duct inlet is placed at a distance of $L_i = 12.5D$ upstream of the circular cylinder, while the outlet is located at $L_o = 35.5D$ behind the body. This choice of parameters ensures minimal distortion of the flow structures due to the outlet boundary conditions, while maintaining a reasonable computational cost, as will be described further in Section 5.2.3.

The flow of an incompressible, electrically conducting Newtonian fluid, of density ρ, kinematic viscosity ν and electrical conductivity σ, is considered. An external homogeneous magnetic field of amplitude B_0 is applied along the spanwise direction z, aligned with the cylinder axis. The walls of the cylinder and the duct are assumed to be electrically insulating. In most cases of liquid-metal flow encountered in industrial applications, the magnetic Reynolds number is in general very small, and thus the induced magnetic field is found to be negligible when compared to the imposed magnetic field. Hence, in this study it is also assumed that the magnetic Reynolds number, R_m, is much smaller than unity, $R_m \ll 1$, therefore the *quasi-static* approximation is

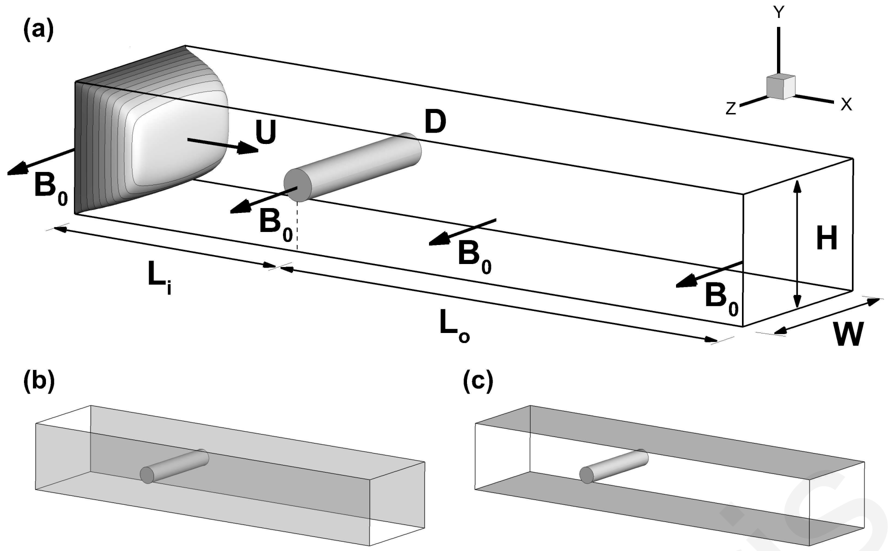

Figure 5.1: (a) Schematic diagram of the flow configuration and related geometrical parameters. (b-c) Shaded areas represents location of the Hartmann layers (b), and Schercliff layers (c).

invoked [85]. Under these assumptions, the non-dimensional magnetohydrodynamic equations governing the flow can be written as:

$$\nabla \cdot \mathbf{u} = 0\,, \tag{5.3}$$

$$\frac{\partial \mathbf{u}}{\partial t} + \mathbf{u} \cdot \nabla \mathbf{u} = -\nabla p + \frac{1}{Re_c} \nabla^2 \mathbf{u} + N(\mathbf{j} \times \mathbf{B}_0)\,, \tag{5.4}$$

$$\mathbf{j} = -\nabla \phi + \mathbf{u} \times \mathbf{B}_0\,, \tag{5.5}$$

$$\nabla \cdot \mathbf{j} = 0\,. \tag{5.6}$$

The dimensionless flow variables appearing in equations (5.3) - (5.6) are obtained from their dimensional counterpart by using the centerline inflow velocity, U_c, as the characteristic velocity scale and the cylinder's diameter, D, as the characteristic length scale. Therefore, the following variables, t, $\mathbf{u}$, p, $\mathbf{j}$, $\mathbf{B}$, ϕ, which denote the dimensionless time, velocity, pressure, current density, imposed magnetic field and electric potential are scaled with D/U_c, U_c, $\rho {U_c}^2$, $\sigma U_c B_0$, B_0, and $D U_c B_0$, respectively. Two dimensionless parameters appear in equation (5.4). The Reynolds number, Re_c, and the interaction parameter, N,

$$Re_c = U_c D/\nu\,, \quad N = \frac{\sigma D B_0^2}{\rho U_c} = \frac{D^2}{W^2} \frac{Ha^2}{Re_c}\,, \tag{5.7}$$

where Ha is the Hartmann number, defined as:

$$Ha = W B_0 \sqrt{\frac{\sigma}{\rho \nu}}\,. \tag{5.8}$$

The drag, C_D, and lift coefficient, C_L, the Strouhal number, St, and the base pressure coefficient, C_{pb}, are defined by equations (4.3)-(4.6) in Chapter 3. The recirculation length, L_r, is defined as the average distance, along the center-plane ($y = 0$), from the rear stagnation point of the cylinder (180 degrees from the front), to the point where the streamwise velocity is zero.

5.1.2 Boundary Conditions

Boundary conditions are given at the domain's inlet by prescribing the analytical solution for an MHD flow in a rectangular duct with insulating walls, in the absence of a cylinder, as described by Müller and Bühler [50]. A no-slip boundary condition is imposed on the cylinder surface and the duct walls, $\mathbf{u}_{wall} = 0$. At the outlet, in order to minimize reflective effects and avoid the distortion of the flow structures leaving the domain, while ensuring mass conservation, a convective boundary condition is applied,

$$\frac{\partial u_i}{\partial t} + U_{conv}\frac{\partial u_i}{\partial n} = 0. \tag{5.9}$$

Here $U_{conv} \equiv \int u_j n_j ds / \int ds$, with the integrals being calculated over the outlet surface.

For the electric potential, the condition $\partial\phi/\partial n = 0$ is imposed at the duct walls to ensure that no current crosses the insulating walls. At the inlet and outlet of the duct, the following boundary condition is used,

$$\frac{\partial \phi}{\partial n} = (\mathbf{u} \times \mathbf{B}) \cdot \mathbf{n}, \tag{5.10}$$

ensuring that no electric currents enter or leave the domain [59]. This boundary condition reduces to the requirement of zero normal component of the current at the inlet and outlet.

5.2 Numerical Aspects

5.2.1 Numerical method

The current computations have been performed using the unstructured collocated nodal-based finite-volume code (CDP). Extensive details of the code, related with the discretization methods and the numerical techniques used, have been described in Chapter 3.

For this study, we have complemented this code with a module to compute the Lorentz force and include it in the momentum balance. A very detailed description of the numerical techniques used by this module is reported in Albets-Chico *et al.* [72]. A consistent and conservative computation of the Lorentz force is used [75]. The implementation and integration of this module in CDP has been validated for several

Table 5.1: Numerical grids used for MHD simulations in a duct with no cylinder. Δy_{min}: grid spacing at Shercliff walls, Δz_{min}: grid spacing at Hartmann walls.

Grid	$N_y \times N_z$	Δy_{min}	Δz_{min}
G1	45×45	0.02	0.02
G2	65×65	0.01	0.01
G3	85×85	0.005	0.005
G4	85×104	0.005	0.002

MHD flows and in various geometries including the MHD channel flow [86] and the MHD pipe flow [87]. In the next subsection, we further validate the code together with the proper grid density and design for fully-developed MHD flow in a rectangular duct, in the absence of a cylinder.

5.2.2 2-D fully-developed MHD duct flow

In order to provide the appropriate grid for the different flow regimes analyzed by this work, and in particular to establish proper resolution criteria regarding the Hartmann and Shercliff layers, a series of preliminary numerical computations are performed in a rectangular duct without the presence of the cylinder. Additionally, this step further validates the numerical code and its ability to deal with basic MHD flow dynamics, as the numerical results can be assessed against the known semi-analytical solution for the duct flow without a cylinder [50].

For this reason, the configuration of Figure 5.1 is first considered without the presence of a cylinder. The flow is assumed to be fully developed, hence a two-dimensional case is addressed, with periodic boundary conditions for the velocity in the streamwise direction, and with a fixed pressure drop (iteratively computed such as to enforce a constant mass flow) that is used in the whole domain as a forcing term. The Reynolds number is fixed at $Re_c = 100$, while Hartmann numbers in the range $Ha = 0 - 1120$ are considered.

Four different grid configurations are tested, differing in the spatial resolution at the Hartmann and Shercliff walls, as summarized in Table 5.1. In the direction normal to these walls, linear grid stretching is applied. The non-dimensional velocity profiles resulting from the respective different grids are shown in Figure 5.2. In this Figure the velocity is scaled by $W^2\nu^{-1}\rho^{-1}(-\partial p/\partial x)$, where $\partial p/\partial x$ is the pressure gradient driving the flow. This scaling relates the velocity profile with the magnitude of the pressure drop required to produce it. This is a strict, but critical way to present results because one could obtain very similar velocity profiles, even with a very coarse mesh, just by fixing the mass flow. However, in such case, the viscous stresses at the walls, and hence the pressure drop, would be overpredicted. Therefore, it is necessary not only to obtain an accurate velocity profile, but also to predict accurately the pressure drop needed to

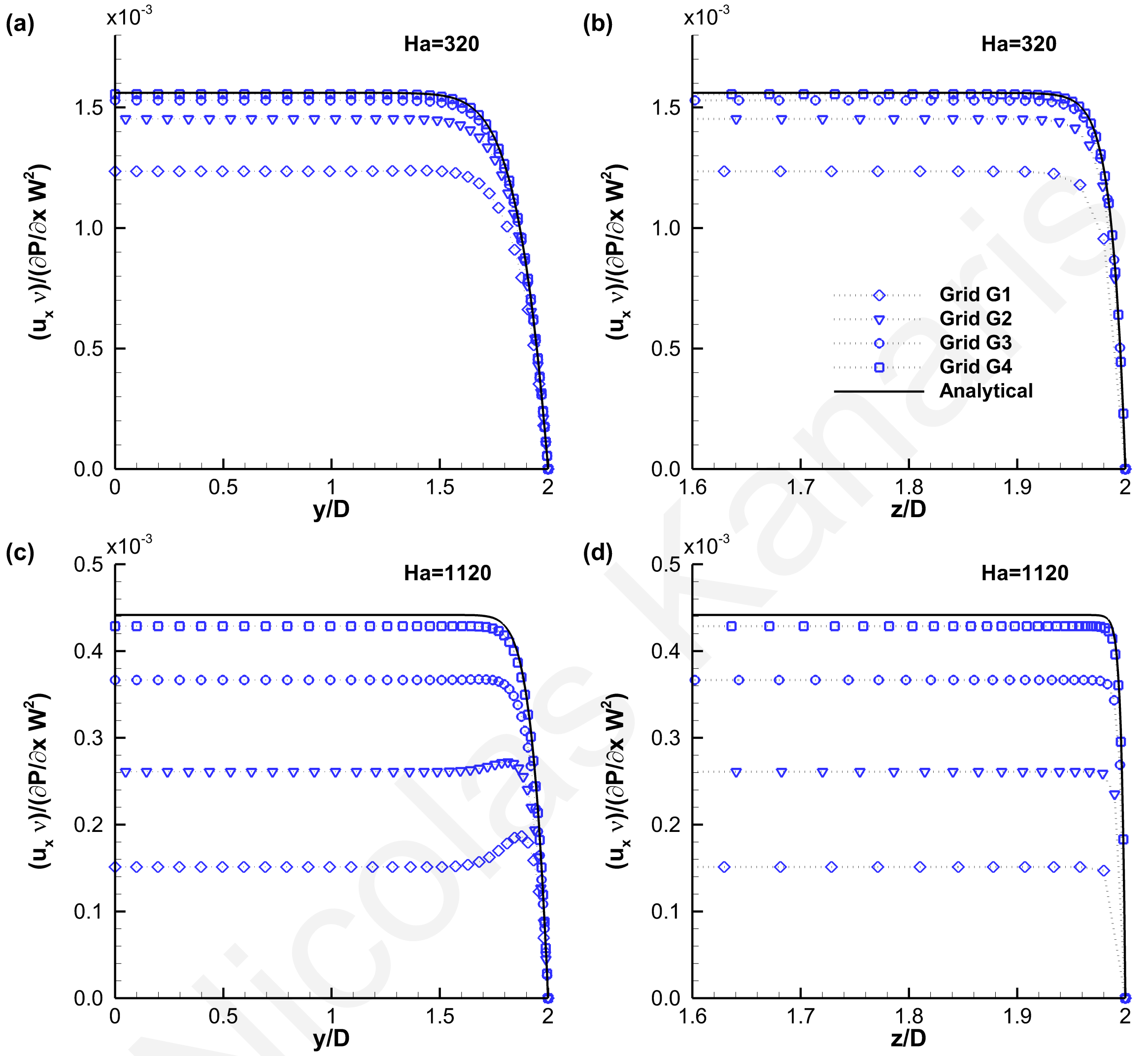

Figure 5.2: Velocity profiles for $Ha = 320$ (a,b) and $Ha = 1120$ (c,d) at Shercliff (a,c), and Hartmann walls (b,d), for the case of a fully developed MHD flow in a rectangular duct, in the absence of the cylinder. Symbols show results from current computations using different grid configurations, while solid lines represent the analytical solution of Müller and Bühler [50].

drive the fluid through the duct.

Results are compared with the analytical solution in terms of a series expansion provided by Müller and Bühler. [50] The solution was obtained for the case of an MHD flow in a rectangular duct with insulating walls and a strong transverse magnetic field. For brevity, only results for $Ha = 320$ and 1120 are shown. For lower Ha numbers even better agreement with the semi-analytical solution is obtained, as the electrodynamic layers are less challenging from a numerical point of view. For $Ha = 320$, the maximum local discrepancy between the velocity profiles predicted numerically on grid G3 with respect to the ones obtained analytically is less than 2%. This percentage difference is further reduced to less than 0.4% when the analytical solution is compared to the results obtained using grid G4. Hence, one can conclude that the intermediate grid G3 is sufficiently fine to resolve the flow for $Ha \leq 320$, as lower Ha numbers present thicker electrodynamic layers. On the other hand, for higher values of Ha, ($Ha = 1120$), the maximum local discrepancy between the analytical velocity profiles with respect to the ones obtained numerically on grid G3 is around 17%, which is unacceptably high. This fact makes imperative the use of the finer grid G4 for this range of Hartmann flows, so as to reduce the numerical error to less than 3%. In general, when using grid G3 for $Ha \leq 320$ and grid G4 for $320 < Ha \leq 1120$ the agreement is very good for all the examined cases, confirming the ability of our numerical code, together with the appropriate grids, to accurately resolve the Hartmann and Shercliff layers.

5.2.3 3-D mesh details and computational domain

In this subsection we present the mesh design for the configuration of interest (see Figure 5.1), that is in the presence of a circular cylinder, together with a domain-dependence analysis.

The influence of the grid resolution on the computed physical characteristics of the purely hydrodynamic flow was examined in detail in a previous paper of ours [79], for the case of a circular cylinder confined in a channel with a slightly smaller blockage ratio. Grid development for the current configuration was based on that study, with a few modifications to compensate for the different blockage ratio and the additional confinement from the walls at the cylinders ends. Furthermore, results related to the grid resolution of the Shercliff and Hartmann layers found in the previous subsection were considered when generating the grid. In view of the exponential decay of the thickness of the Hartmann layers with increasing Ha ($\delta_H \sim O(Ha^{-1})$), and in order to accommodate the wide range of Ha numbers investigated herein, two grids, differing only in the resolution of the Hartmann layers have been used.

Hence, based on the results obtained for the fully-developed case in the previous section, two grids were generated, namely GL-M and GH-M, with a minimum grid spacing along the direction of the magnetic field, of $\Delta z_{min} = 0.005D$ and $0.002D$

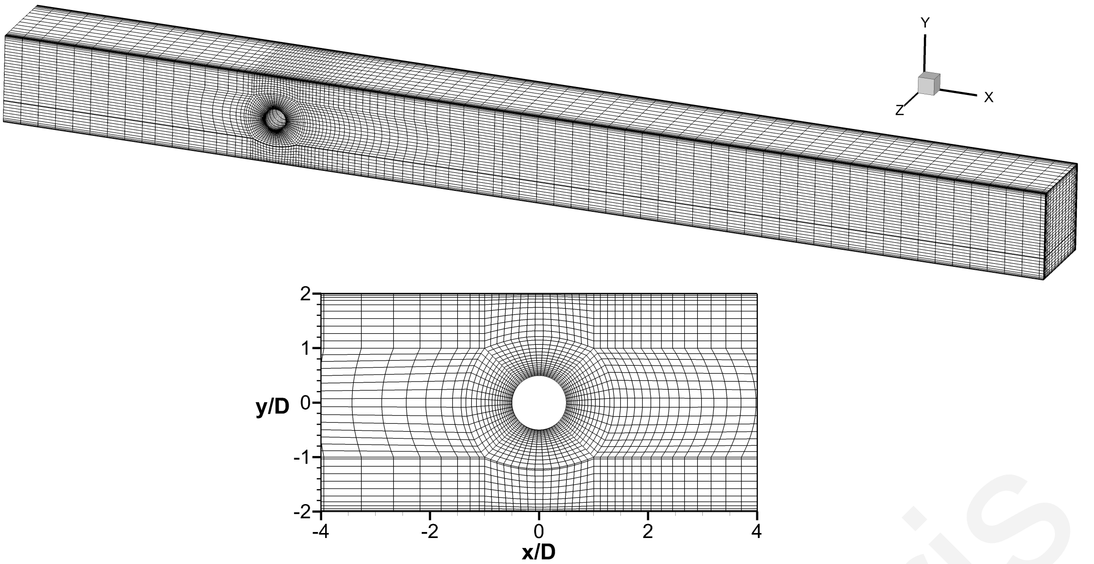

Figure 5.3: Computational grid GL-M. The upper plot shows the whole domain, while the bottom plot shows an expanded view in the vicinity of the cylinder. Only every 4th node is plotted for clarity.

respectively. The grid-naming convention adopted here is as follows. The first segment of the grid name (two letters preceding the hyphen) indicate the the relative grid resolution, i.e. GL- and GH- stand for Lower and Higher grid resolution respectively. The second segment of the grid name (letter following the hyphen) indicates the domain size, i.e. S, M and L stand for Short, Medium and Long domains respectively. The short (-S) and and long (-L) domains were used only during the domain-size independence study, otherwise the medium domain (-M) was used in all other runs. The parameters of the different grid configurations tested are summarized in Table 5.2.

Grid GL-M has been used for the cases where $Ha \leq 320$, and grid GH-M for the last two cases with the higher Hartmann numbers, $Ha = 640$ and $Ha = 1120$. *A posteriori*, we determined that at least 6 mesh nodes were present inside the Hartmann layers and 18 nodes in the Shercliff layers for all the analyzed cases. For both grids, a hyperbolic tangent-based function was used to stretch the cell sizes in a clustered region close to the cylinder, and a linear grid stretching was applied in the direction normal to the duct walls, as shown in Figure 5.3. Further upstream and downstream of the cylinder, a uniform grid was used in the stream-wise direction.

In order to examine the influence of the computational domain on the predicted flow fields, a domain-dependence study is also performed. For this reason, two more grids are tested, namely GL-S and GL-L, with a smaller and larger computational domain respectively. These grids are based on the spacing of grid GL-M. The tests are carried out at $Ha = 320$, and $Re_c = 2000$, which are the highest Hartmann and Reynolds numbers examined for mesh GL-M. Simulations are performed over periods of at least 180 dimensionless time units, corresponding to about 45 vortex shedding

Table 5.2: Grid parameters used for the three-dimensional flow configuration. Δn_H: grid spacing normal to the Hartmann walls; $\Delta n_{S,C}$: grid spacing normal to the Shercliff and cylinder walls; N_z: nodes along spanwise direction.

Grid	Cases		L_i	L_o	Δn_H	$\Delta n_{S,C}$	N_z	Total Nodes
GL-S	$Ha = 320$	$Re = 2000$	8.5	22.5	0.005	0.005	85	4,535,090
GL-M	$Ha \leq 320$	$Re \leq 5000$	12.5	35.5	0.005	0.005	85	5,568,265
GL-L	$Ha = 320$	$Re = 2000$	16.5	45.5	0.005	0.005	85	6,419,115
GH-M	$Ha > 320$	$Re \leq 5000$	12.5	35.5	0.002	0.005	104	6,812,936
GF-M	$Ha = 320$	$Re = 5000$	12.5	35.5	0.005	0.005	85	8,600,000
GX-M	$Ha = 1120$	$Re = 5000$	12.5	35.5	0.002	0.005	104	10,507,120
GR-T	$Ha = 320$	$Re = 5000$	7	14	0.0015	0.0015	129	19,762,978

Table 5.3: Effect of grid design on time-averaged flow characteristics: Mean recirculation length $\bar{L}_r$, pressure coefficient calculated in front and rear staganation point of the cylinder $\bar{C}'_{pb}$, mean drag coefficient $\bar{C}_D$, and Strouhal number St.

Grid	Ha	Re_c	$\bar{L}_r$	$\bar{C}'_{pb}$	$\bar{C}_D$	St
GL-S	320	2000	0.490	3.149	1.715	0.260
GL-M	320	2000	0.488	3.152	1.714	0.260
GL-L	320	2000	0.479	3.159	1.714	0.260
GL-M	320	5000	0.524	3.028	1.627	0.241
GF-M	320	5000	0.514	3.054	1.644	0.248
GR-T	320	5000	0.513	3.063	1.661	0.249
GH-M	1120	5000	-	3.727	2.148	0.265
GX-M	1120	5000	-	3.728	2.152	0.265

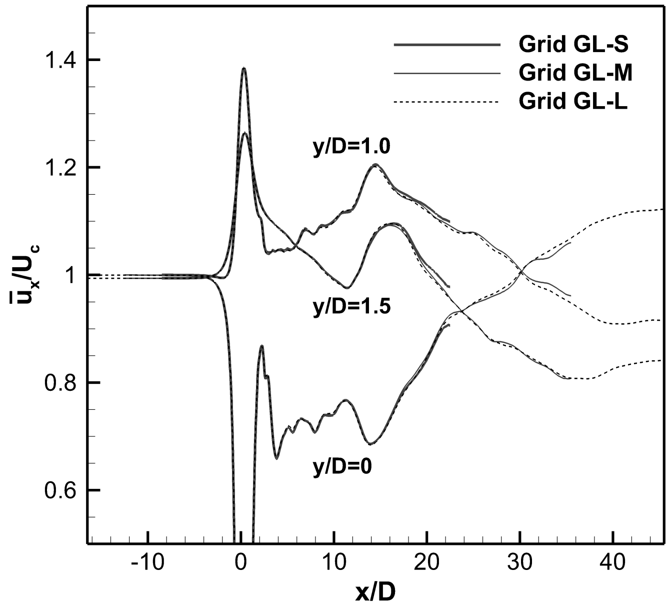

Figure 5.4: Effect of domain size on the average streamwise velocity at three different locations in the mid-plane (z=0) using grids GL-S, GL-M and GL-L at $Ha = 320$ and $Re_c = 1000$.

cycles, with time averaging of results performed over the last 25 shedding cycles, when the flow had reached a statistically steady state.

The discrepancy between the time-averaged values of drag coefficient $\bar{C}_D$, recirculation length $\bar{L}_r$, base pressure coefficient $\bar{C}'_{pb}$, and the Strouhal number St resulting from the use of different domain sizes is shown in Table 5.3. Because, C_{pb} (see equation (4.6)) depends on the distance between the points used to compute the pressure drop, we define a different base pressure coefficient, C'_{pb} in which the reference pressure is at the front stagnation point of the cylinder (0 degrees from the front). Results show that a domain independent solution can be achieved with the domains considered. For example, replacing the shortest domain GL-S with the longest one, GL-L, resulted in only 2.3% change in $\bar{L}_r$, and 0.3% in $\bar{C}'_{pb}$, whereas the corresponding changes were 1.9% and 0.2% when replacing the intermediate domain GL-M with the longest domain. In the case of $\bar{C}_D$ and St almost no variations can be seen. Furthermore, Figure 5.4 displays the mean streamwise velocities at different one-dimensional slices, for domains GL-S, GL-M and GL-L. From this comparison it can be concluded that the effect of the convective outlet is very small, and is isolated within a distance of $2D$ from the outlet. Based on these results, one can conclude that the intermediate domain GL-M is sufficiently long to resolve the flow.

As explained below, it was necessary to design additional grids that would enable us to investigate the presence of the fourth flow regime, which has been reported to come in succession after regular vortex shedding [51, 56]. For this purpose, simulations have been performed for an even higher Reynolds number, $Re_c = 5000$, and for $Ha =$

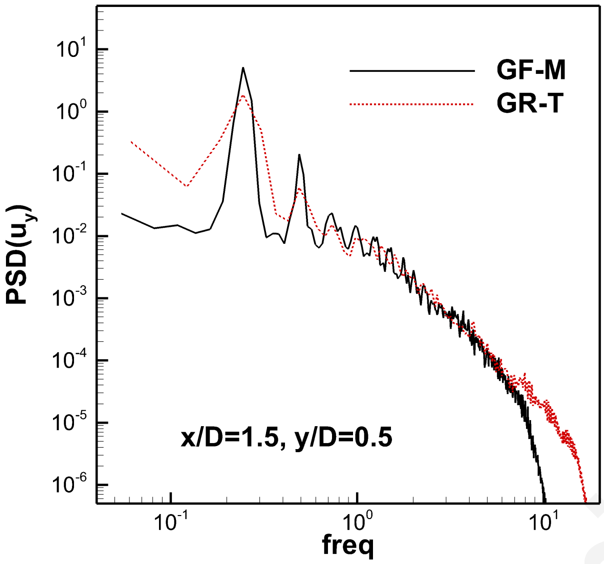

Figure 5.5: Spectra of crossflow component of velocity at the mid-plane ($z = 0$), for $Ha = 320$ and $Re_c = 5000$.

320 and 1120. The high value of the Reynolds number in this regime was found to promote the presence of finer structures, especially at $Ha = 320$ (see Figure 5.18). To capture these fine structures, grids GL-M and GH-M that were used in cases where $Ha = 320$ and $Ha = 1120$, respectively, were refined even further. Grid refinement was performed only in the streamwise direction, in the vicinity of the cylinder and further downstream, decreasing the maximum value of Δx_{max} from $0.2D$ to $0.1D$. As summarized in Table 5.2, this yielded two finer grids, namely GF-M (Fine resolution, Medium domain) and GX-M (eXtra fine resolution, Medium domain), with a total of 8.6 and 10.5 million nodes, respectively. Given the irregular character of the flow in this regime, special care was needed to ensure the validity of statistical quantities. For this purpose, simulations were carried out for longer periods of at least 400 dimensionless time units (100 vortex shedding cycles), while the time-averaging was performed over a minimum period of 300 time units (75 shedding cycles). As we shall discuss in Section 5.5, in the case of $Ha = 320$, $Re = 5000$, the presence of small-scale structures in the near-wake is an inherent and important feature of the flow. In an effort to ensure proper resolution of the smallest scales of motion on grid GF-M, an even finer grid was generated in a shorter domain, namely GR-T (Reference resolution, Truncated domain). The latter grid is up to three times finer in the near-wake region than grid GF-M (see Table 5.2). Because of the extremely high computational cost associated with the use of this grid, only one simulation was performed to provide a reference case at $Ha = 320$, and $Re_c = 5000$.

Overall, as shown in Table 5.3, the agreement between the results obtained with the different grids is very satisfactory, with the discrepancies being below 2.2% at $Ha = 320$, and 0.3% at $Ha = 1120$. Figure 5.5 shows the power spectral density of the crossflow velocity component u_y, obtained at $x = 1.5D$, $y = 0.5D$, $z = 0$ using grids GF-M and GR-T. The observed spectra, as we shall see in Section 5.5, are consistent with the instantaneous visualizations of the flow, where the presence of small scales is clearly observed. The good agreement between the two cases indicates that the mesh resolution of grid GF-M is sufficient to represent correctly the small scales of motion.

5.3 Cririical Re, onset of vortex shedding

We have first investigated the effect of Ha on the laminar flow regime and the transition from steady to unsteady flow. In order to determine $Re_{c,cr}$ for a given value of Ha, a series of independent simulations were performed for different values of Re starting from a zero velocity field in all cases. Figure 5.6(a) shows the critical Reynolds number $Re_{c,cr}$ (based on the centerline velocity) for the onset of vortex shedding as a function of the Hartmann number. Each critical Reynolds number is defined in an interval represented by an error bar. The lower end of the bar corresponds to the simulation with the highest Re that leads to a steady flow-regime, while the higher end corresponds to the simulation with the lowest Re that leads to unsteady flow. Results are compared with those obtained by Dousset and Pothérat [56] using a Q2D model. However, it should be noted that in their study, Re_{cr} was obtained by performing two series of numerical computations, where Re was sequentially increased in small steps till unsteadiness was reached, and then gradually decreased again till steadiness was recovered. Figure 5.6(b) shows an expanded view in the area of low values of Hartmann number, this time showing the critical Reynolds number $Re_{b,cr}$ based on the bulk velocity. Keeping Re_b fixed while varying Ha corresponds to the same mass flow rate, which is important when presenting the transition from steady to unsteady flow.

As seen from these figures, for $Ha > 80$ the critical Reynolds number becomes proportional to the Hartmann number with the linear relation $Re_{cr} \simeq 0.52Ha$. This relation is in very good agreement with the results of Dousset and Pothérat, [56] who report a relation of $Re_{cr} \simeq 0.43Ha$. A similar linear relationship between Re and Ha was also observed by Frank *et al.* [51] ($Re_{cr} \simeq 0.47Ha$) and Hussam *et al.* [57] ($Re_{cr} \simeq 0.5Ha$) for configurations with different blockage and aspect ratio, i.e. $\beta = 0.1$, $\alpha = 5$ and $\beta = 0.2$, $\alpha = 2.5$ respectively. The relative differences between the results obtained by Ref. [56] and the current study (see Table 5.4), may be at least partly attributed to the different methods used for obtaining the critical Reynolds number. Nevertheless, the agreement between the quasi-two-dimensional model and current three-dimensional results gradually improves with increasing Ha. This is expected, due to the enlargement of the quasi-inviscid core flow, which improves the validity of the Q2D model.

Surprisingly, as one decreases the Hartmann number below $Ha = 80$, the critical Reynolds number decreases slightly until it reaches a minimum value, $Re_{b,cr}^{min} \approx 90$, in

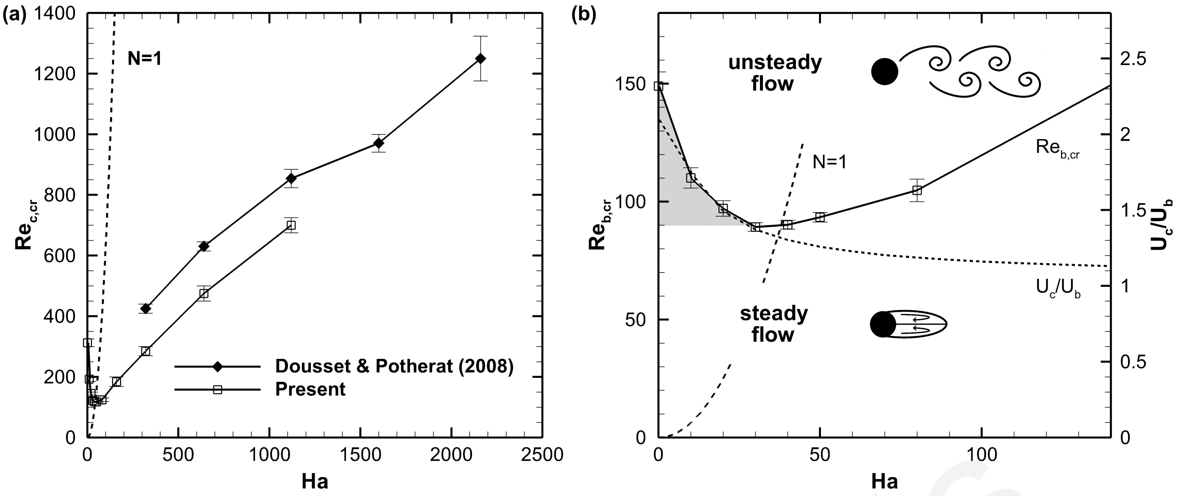

Figure 5.6: (a) Effect of magnetic field intensity on the critical Reynolds number for the onset of vortex shedding. (b) Expanded view in the area of low Ha, for the same bulk flow through the duct.

Table 5.4: Relative differences between the critical Reynolds numbers for the onset of vortex shedding, obtained in the present study and by Dousset and Pothérat. [56]

Ha	320	640	1120
$Re_{c,cr}$	33%	25%	18%

the vicinity of $Ha_{cr} \approx 35$. From that point on, it starts to increase up to $Re_{b,cr} \approx 150$ as Ha is further decreased towards the hydrodynamic case, $Ha = 0$. This counter-intuitive behavior indicates that there is a group of parameters in the range of $Ha < Ha_{cr}$, and $Re_{cr}^{min} < Re < Re_{cr}(Ha)$ [shaded area in Figure 5.6(b)], in which for a fixed value of Re and with increasing Ha, the flow will go from a steady to an unsteady state. To verify the unexpected effect of generating unsteadiness by increasing Ha, we have performed a series of additional numerical simulations for a few selected Re values (within the shaded area), as opposed to the original simulations that were done for fixed Ha values. For each Re value, the new simulations were carried out by increasing Ha in small steps, each time allowing the flow to reach a statistically steady state. By doing so, we have verified that when crossing the original stability boundary, as given in Figure 5.6(b), unsteadiness was obtained. Of course, when Ha is increased significantly steadiness eventually prevails again.

To the best of our knowledge, this is the first time that such a behavior at low Hartmann numbers is observed, at least for the case of a wake flow with the magnetic field aligned with the cylinder axis. Other studies in the literature of similar flow configurations approached the problem by making use of the Q2D model [51, 56, 57], and as a result, were limited to relatively high Hartmann numbers ($Ha \geq 320$), where

Re_{cr} is only found to increase with increasing Ha. Nonetheless, it is important to note that similar non-monotonic scenarios have been demonstrated in the past for other configurations, such as the case of a free cylinder with the magnetic field being parallel to the oncoming flow [88] and the case of a duct flow [55]. For example, Ref. [55], while investigating the case of a shear driven flow in a duct with non-uniform conductance of the Hartmann walls, observed a similar behaviour at moderate values of Ha and attributed that effect to the velocity deficit across the shear layers. Despite the fact that once again a Q2D model was used in his study, results were expected to apply qualitatively. Even though that study was addressing a different configuration, our results are qualitatively similar and follow similar physical explanations, as we shall see in the following paragraphs.

The overall behavior can be explained taking into account two physical aspects of the flow: how laminar vortex shedding is triggered in the wake of a circular cylinder and how the magnetic field affects the stability of the flow.

The first question has been addressed several times in the past and it is well-known: The onset of the von Kármán vortex flow results from a global Hopf bifurcation of the steady flow [11, 12]. The driving mechanism for this self-excited instability is associated with the inception of small disturbances located symmetrically at approximately the end of the separation bubble. In turn, these disturbances generate sinusoidal waves traveling against the basic flow on the sides of the recirculation region [8, 89, 90]. If the blockage and aspect ratio are relatively small and high, respectively, the presence of walls, either at the ends of the cylinder or parallel to the cylinder axis, does not appear to change the bifurcation properties in a dramatic manner. However, as the blockage ratio increases or the aspect ratio becomes smaller, the walls confine the streamlines near the cylinder, and the flow becomes more stable as the propagation of infinitesimal disturbances becomes suppressed [27, 28, 32]. In addition to this effect, the local acceleration of the flow in the vicinity of the cylinder and along the center-line of the duct, presumably stabilizes the flow, leading to a delay of the onset of vortex shedding [32, 33, 58, 82]. In the purely hydrodynamic case, and for the blockage ratio used in this study, namely $\beta = 1/4$, Dousset and Pothérat [56] reported a critical value of $Re_{b,cr} \simeq 55$, without considering any additional confinement from the side walls (channel flow case). In their experimental investigation of the stability of the steady wake, where they considered the effect of confinement due to end plates normal to the cylinder axis, Shair *et al.* [32]. reported a critical value of $Re_{b,cr} \approx 135$ for the case of $\alpha = 5$. Nishioka and Sato [42] showed that, as α is decreased, the standing vortex behind the cylinder is stabilized and vortex shedding does not take place until larger Reynolds numbers. For example, for $\alpha = 4.5$ they found $Re_{b,cr} \approx 140$. Given the smaller aspect ratio used in our study, $\alpha = 4$, along with the additional confinement from the top and bottom walls of the duct, our value of $Re_{b,cr} \approx 150$, is in reasonable agreement with independent results from the literature. From all the aforementioned, it is evident

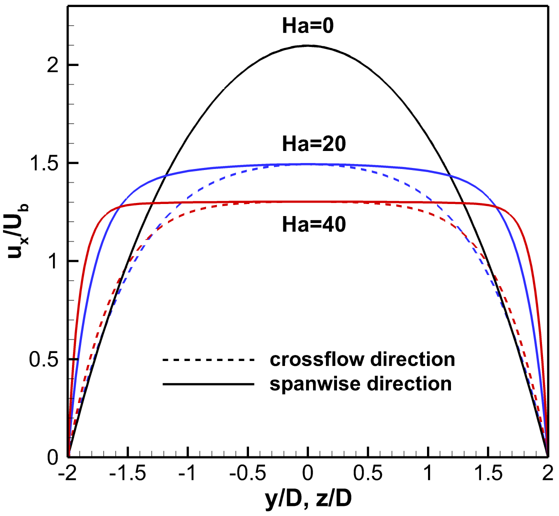

Figure 5.7: Velocity profiles for the same bulk flow rate at the inlet of the rectangular duct along the Shercliff (dashed lines), and Hartmann walls (solid lines) for low Hartmann numbers.

that the rectangular duct aspect and blockage ratios become critical parameters when considering the stability of the flow.

Concerning the second aspect, the magnetic field acts in two ways. On one hand, it increases the damping of the fluctuations of the unstable flow through Joule dissipation, as pointed out by Müller and Bühler [50]. On the other hand, it modifies the velocity distribution of the primary flow, hence also acting on the flow stability through inertia.

For small Hartmann numbers, where $N \sim 1$, viscous and Joule dissipation are of the same order of magnitude and overall dissipation is stronger than in the hydrodynamic case. This would suggest that the stability should increase with increasing Ha, however the current results show the opposite for $Ha < 35$. In fact, what really explains this far from obvious effect is the second action of the Lorentz force, viz. the modification of the velocity distrubution before the cylinder, as shown in Figure 5.7. As already mentioned, the instability mechanism leading to the onset of vortex shedding is affected by local acceleration in the vicinity of the cylinder. Therefore, it is useful to look at the effect of Ha on the fluid velocity on the upstream side of the cylinder. As shown in Figure 5.6(b) (dotted line), with increasing Hartmann number, the centerline velocity U_c decreases rapidly at first, i.e. for low values of Ha, and approaches asymptotically the bulk flow velocity for larger values of Ha. The rapid decrease of the centerline velocity U_c at low Ha can be translated to a deceleration of the flow in the neighborhood of the cylinder, which effectively enhances instabilities and destabilizes the flow. This is in line with the explanation given by Bühler [55]. In other words, with increasing Ha, the action of Lorentz forces leads to a more uniform velocity distribution along the cross-section of the duct (as shown in Figure 5.7), resembling a flow configuration with a higher aspect ratio, and smaller blockage ratio. This action mimics the effect of moving the walls of

Table 5.5: Relative differences between the steady-flow characteristics obtained in the present study and by Dousset and Pothérat.[56]

Ha	L_r	C_{pb}	C_D
320	3%	4%	9%
640	2%	5%	8%
1120	3%	1%	6%

the duct further away from the cylinder. Consequently, having already explained the significance of aspect and blockage ratio on the flow stability, increasing Ha enhances the propagation of disturbances, which eventually destabilizes the flow leading to lower values for the critical Reynolds numbers. This effect becomes clearer when comparing the reduction of the flow stability at fixed bulk flow, and this explains the motivation for using $Re_{b,cr}$ instead of $Re_{c,cr}$ in Figure 5.6(b).

In the case of high Hartmann numbers, where $N \gg 1$, the Lorentz forces become dominant, and the main effect of the magnetic field is the stabilization of the flow, by opposing vortical motions in planes lateral to the direction of the magnetic field. In this case, increasing Ha leads to a significant reduction of the energy amplification of disturbances due to Hartmann damping [58] and the critical Reynolds number becomes proportional to Ha, as already pointed out in our results.

5.4 Steady flow regime

In this section we present and discuss results from numerical simulations with time-independent flow, i.e. under parameters that produce steady mean flow. Results from the present three-dimensional simulations are compared against the numerical results of Dousset and Pothérat [56] obtained using a quasi-two-dimensional model. It should be noted that in their study, they are reporting only results for high Ha, which is necessary for their model to hold, so a direct comparison is only possible for the cases where $Ha \geq 320$. An overview of the relative differences between the results obtained with two studies is given in Table 5.5.

5.4.1 Effect of Ha on the recirculation length L_r

The variation of the spanwise-averaged recirculation length, L_r, as a function of the Reynolds number, Re_c, and Hartmann number, Ha, is shown in Figure 5.8. In Figure 5.8(a), an almost linear evolution of L_r with Re_c, for each Ha, is observed. In the case of low Hartmann numbers, up to $Ha = 80$, the magnetic field seems to have little effect on L_r, and all data collapse onto a single curve that depends only on Re_c. Increasing Ha further causes the data to depart from that curve, while the slope slightly

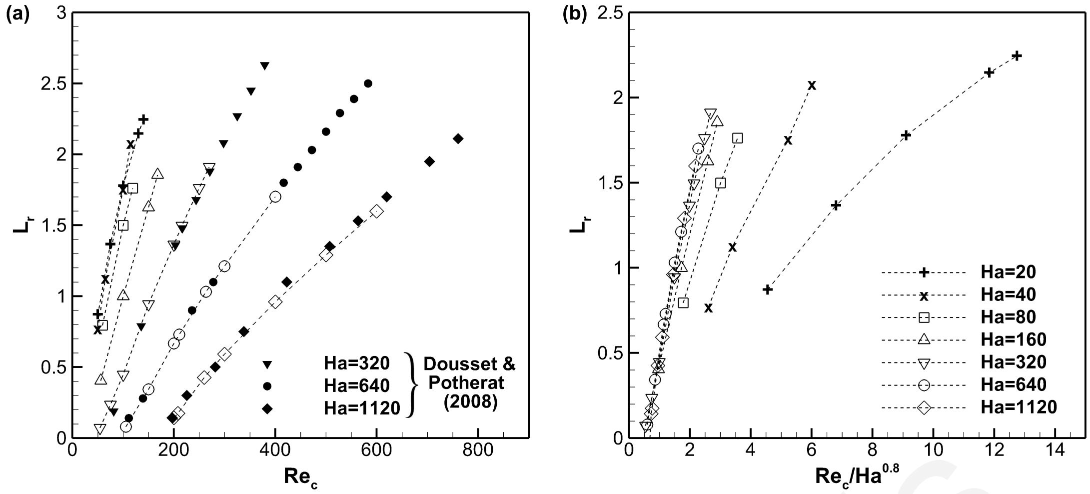

Figure 5.8: Recirculation length averaged along the spanwise direction, versus Re and Ha. Results from present study (open symbols) are compared with the study of Dousset and Pothérat [56] who used a quasi-2D model (closed symbols).

decreases. As shown in Figure 5.8(a), an increase of Ha at a fixed value of Re causes a decrease in L_r. This is attributed to the action of the Lorentz forces as we shall discuss in more detail in the following paragraph. Interestingly, if we plot L_r as a function of $Re_c/Ha^{0.8}$, as shown in Figure 5.8(b), a universal scaling law appears, this time for high Hartmann numbers, $Ha \geq 320$. This collapse for high Ha, was first demonstrated by Dousset and Pothérat, [56] with whom the current results agree very well. As seen from Table 5.5, the relative differences between the two studies are around 3%.

In addition to the spanwise-averaged recirculation length, L_r, it is also useful to look at the distribution of the recirculation length along the span, $L_r(z)$, as shown in Figure 5.9. This allows us to analyze in greater detail the evolution the recirculation length with increasing Ha. In this plot, we compare $L_r(z)$ for different Ha, while keeping the flow rate constant, i.e. Re_b constant. In the case of low Ha values (see Figure 5.9(a)), we can see that, as we move away from the centerline and closer to the Hartmann walls, there is a large discrepancy between the values of $L_r(z)$. Contrary to the previous observation, where the magnetic field was revealed to have little effect on the *average* value of the recirculation length, here we can see that an increasing magnetic field induces significant differences in the distribution of the recirculation length. Particularly at $Ha = 20$, besides the peak reached by $L_r(z)$ at midspan, two local peaks exist near the Hartmann walls. As recently explained by Dousset and Pothérat [91] while considering the case of a *truncated* rectangular cylinder, these two peaks are due to the presence of a pair of counter-rotating streamwise vortices, referred to as base vortices, located in the vicinity of each Hartmann wall downstream of the cylinder. The strength of these vortices is diminished with decreasing boundary layer thickness upstream of the cylinder [92]. Therefore, with the increase of Ha, as the

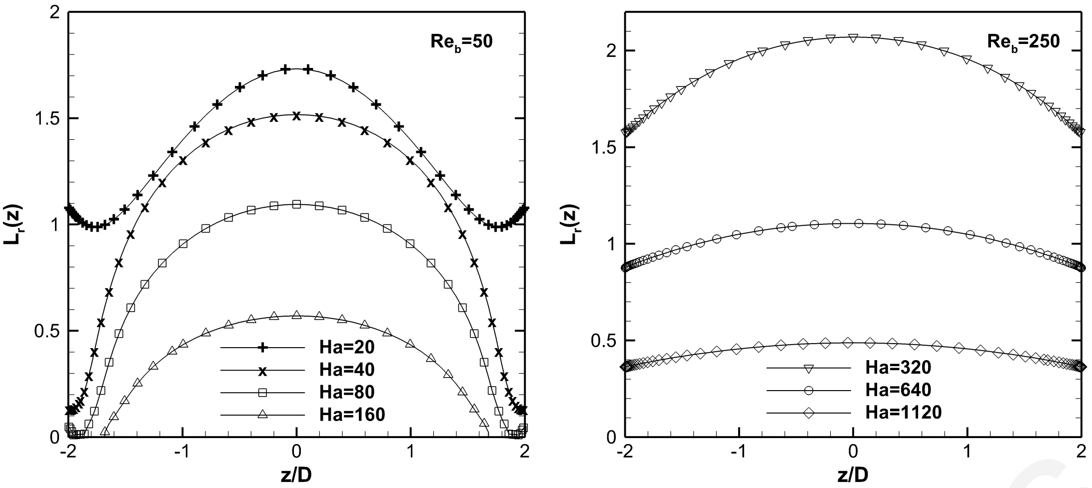

Figure 5.9: Variation of recirculation length along the span for different Ha at the same flow rate. (a) $Ha = 20$, 40, 80, and 160 at $Re_b = 50$. (b) $Ha = 320$, 640 and 1120 at $Re_b = 250$.

Hartmann boundary layer becomes rapidly thinner ($\delta_H \sim 1/Ha$), the base vortices are weakened, which translates into the damping of the peaks near the walls of the duct. In addition to the weakening of the base vortices, Lorentz forces act in the direction opposite to the flow in the core region of the duct, while diffusing vorticity along the magnetic field. These effects explain why increasing the intensity of the magnetic field for a given mass flow rate leads towards lower values of L_r and smaller variations along the span. At higher Hartmann numbers (see Figure 5.9(b)), Lorentz forces are enhanced, and as a result, the recirculation region displays increasingly a relatively flat distribution, i.e. the flow is driven towards a two-dimensional flow.

5.4.2 Evolution of the base pressure coefficient C_{pb}

Figure 5.10, shows the evolution of base pressure coefficient, C_{pb}, with respect to Ha and Re_c. Dousset and Pothérat [56] demonstrated that for high Hartmann numbers, Re/Ha is a governing parameter for which all data collapse on a single curve. In this study, we observe that the Re/Ha universality holds also for all the low values of Ha investigated here for the first time. Even though at low Hartmann numbers a shift towards higher values of Re/Ha is observed, the slope remains the same and Re/Ha can be considered as a governing parameter of C_{pb}, for the entire range of parameters studied here. As shown in Table 5.4, when the current results are compared with the results obtained with the Q2D model, once again, a remarkable agreement between the two studies can be observed. The relative difference between the two studies ranges between 4% and 5% for $Ha = 320$ and 640, and drops to 1% for $Ha = 1120$. This demonstrates that the Q2D model produces a very accurate averaging of the physical phenomena along the spanwise direction, provided that the magnetic field is sufficiently

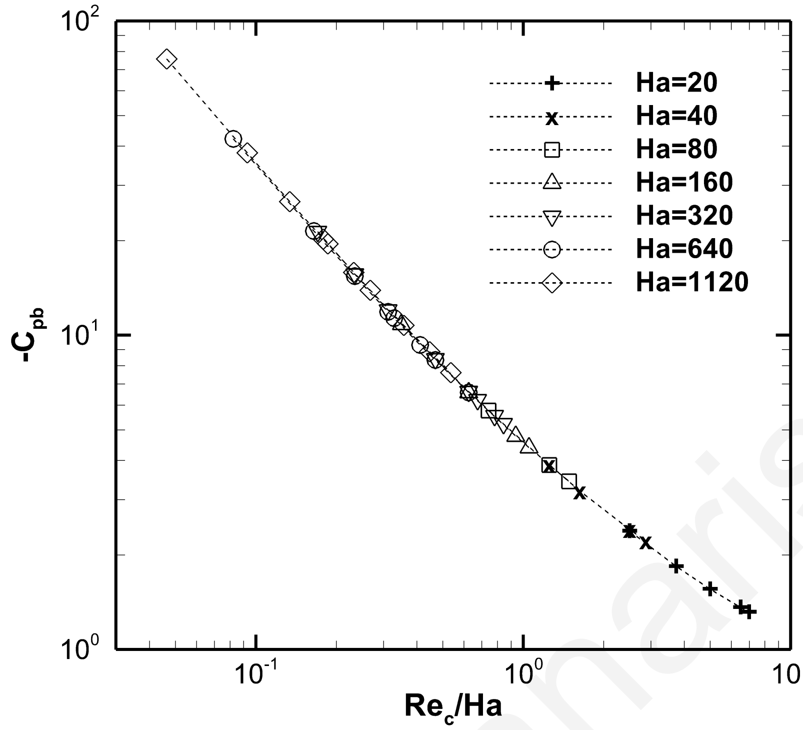

Figure 5.10: Base pressure coefficient versus Re and Ha.

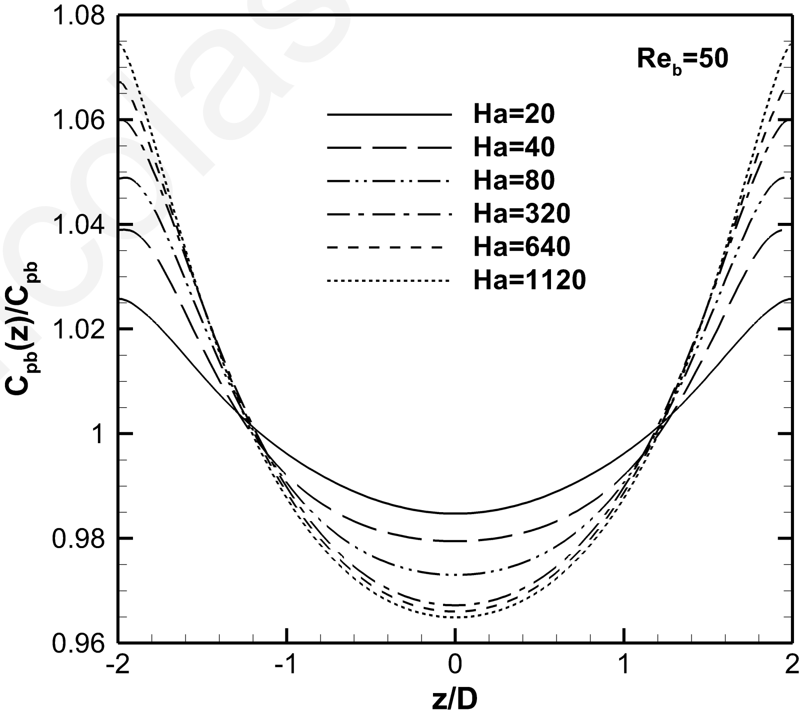

Figure 5.11: Spanwise distribution of the normalised base pressure coefficient for $Re_b = 50$.

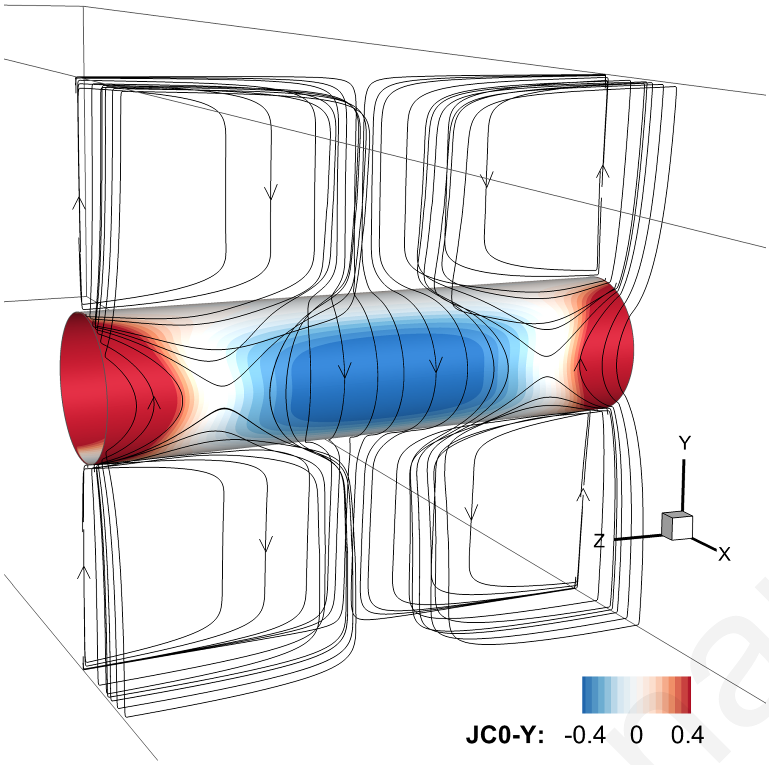

Figure 5.12: Sreamlines of the current density field passing close to the rear part of the cylider surface at $Ha = 1120$ and $Re_b = 50$. Along the cylinder surface, a contour plot of the crossflow component of the current density is shown.

strong for the model to hold.

The spanwise distribution of the base pressure coefficient, $C_{pb}(z)$, normalized with its spanwise average value can be seen in Figure 5.11. In contrast to the spanwise distribution of the recirculation length, where a stronger magnetic field leads to a flatter distribution of $L_r(z)$ (see Figure 5.9), the base pressure coefficient is found to become less uniform for higher values of Ha. As the Hartmann number increases, the pressure progressively drops at the mid span and increases close the side walls. This unexpected trend is linked to the three-dimensional distribution of the Lorentz forces along the surface of the cylinder. For example, Figure 5.12 shows the current density streamlines, passing close to the rear part of the cylinder surface at $Ha = 1120$. The surface of the cylinder is colored by the crossflow component of the current density, J_y. As clearly seen, due to the electrically insulating flow insert, the current density paths are deflected, generating a three-dimensional distribution of currents around the cylinder. Along the rear side of the insert, this current pattern becomes more complex, with a region of negative values of the cross-flow component of current density J_y appearing between regions of positive values. In turn, this non-uniform distribution of the current density field at the rear part, induces Lorentz forces which act in the positive streamwise direction at both ends of the cylinder and towards the upstream direction at the core region of the flow. These non-uniform forces effectively redistribute the pressure field at the rear part of the cylinder leading to the “three-dimensionality" of the base pressure coefficients as shown in Figure 5.12. As the Hartmann number is increased, Lorentz forces become stronger, and the variation of the base pressure coefficient along the spanwise direction is enhanced. Nevertheless, it is important to note that the spanwise variation of $C_{pb}(z)$ is relatively small. Even at the highest Hartmann number considered in this investigation, $Ha = 1120$, the relative difference between the minimum and maximum values of $C_{pb}(z)$ is found to be around 10% with respect to the minimum value.

5.4.3 Influence of Ha on the drag coefficient C_D

Figure 5.13, shows the evolution of the drag coefficient, C_D, as a function of Re_c, and Ha. Focusing at the range of high Ha values in this figure ($Ha \geq 320$), a universal scaling law is found to hold for the drag coefficient as a function of $Re/Ha^{0.8}$, as was the case with L_r. While the same slope is valid for values of $Ha < 320$, results in this case are shifted relative to the curve followed at high Ha. Here again, the agreement between the current three-dimensional simulations and the Q2D model, is very good, as shown in Table 5.5. Nevertheless, the discrepancy between the two studies is found to be larger for C_D values than for C_{pb}, and this difference is explained in the following paragraphs. However, in the present study we have further found that there is a relatively accurate universal scaling, for all Hartmann numbers, if we plot C_D with respect to $Re/Ha^{0.6}$ as shown in Figure 5.13(b). Even though the collapse at high Ha is not that accurate as with the previous scaling, for both high and low Ha numbers results are concentrated in a narrow region. Of course, at low Ha results still shift to lower values of C_D. We have also noticed that if we use the drag coefficient based on the bulk flow velocity, $C_{D,bulk} = C_D U_c^2/U_b^2$, and plot it versus the bulk Reynolds number, Re_b, results at low Hartmann numbers, $Ha \leq 80$, collapse to a single curve (see Figure 5.13(c)). For higher Ha, results are shifted to higher $C_{D,bulk}$.

The distribution along the cylinder span, of the drag coefficient, C_D(z), normalized with its spanwise average is shown in Figure 5.14, where different Hartmann numbers are compared at $Re_b = 50$. Similarly to the base pressure coefficient, an increasing variation of the drag coefficient along the spanwise direction is observed with increasing Ha. Indeed, $C_D(z)$ displays a rather flat distribution at low Hartmann numbers and gradually becomes highly non-uniform as Ha is increased. This evidence shows again how the budget of forces becomes more “three-dimensional” with increasing Ha due to the stronger action of the Lorentz forces. The physical mechanism underlying such a non-uniformity can be better understood by examining the spanwise variations of the pressure and viscous components of the total drag, as shown in Figure 5.15 for selected values of Hartmann numbers. In all cases, the magnitude of the total drag is dominated by the pressure forces around the surface of the cylinder, which on average correspond

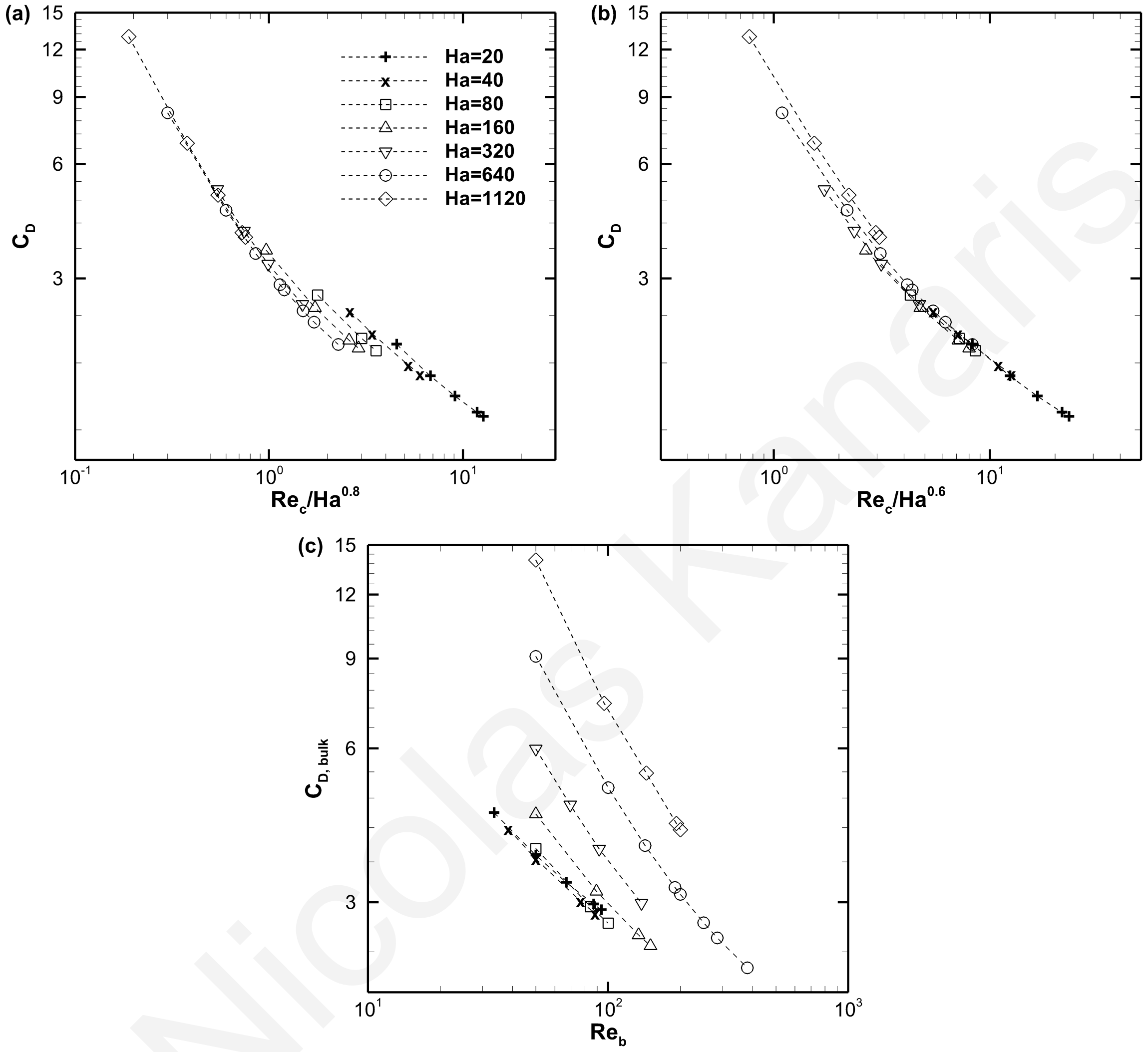

Figure 5.13: Drag Coefficient as a function of Re and Ha. (a) The universal scaling law $C_D = f(Re/Ha^{0.8})$ for high Ha is verified. (b) A new scaling law is proposed for all Ha, $C_D = f(Re/Ha^{0.6})$. (c) Plotting $C_{D,bulk}$ versus Re_b data at low $Ha \leq 80$, collapse to a single curve.

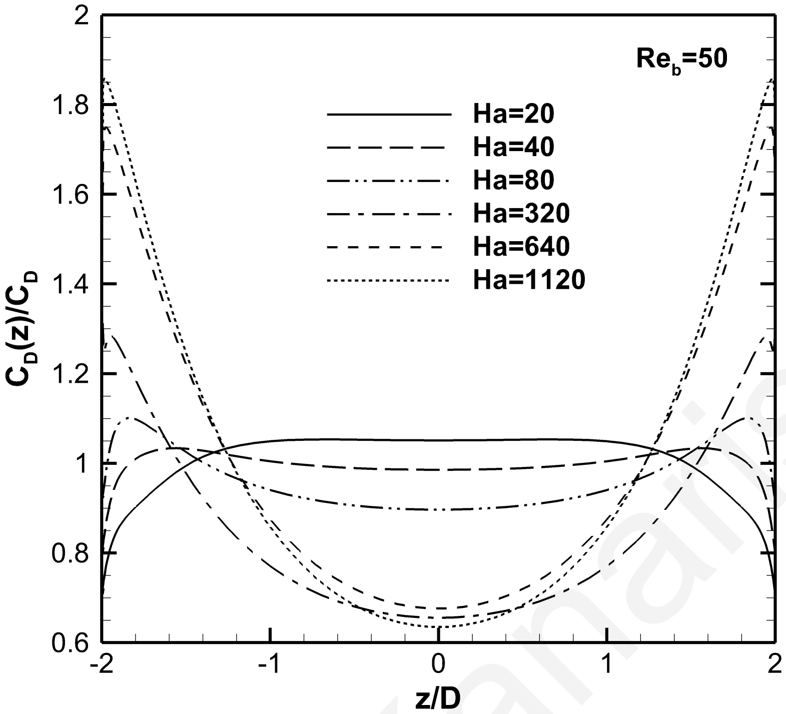

Figure 5.14: Variation of the normalised drag coefficient along the span for different Hartmann numbers at the same flow rate, $Re_b = 50$.

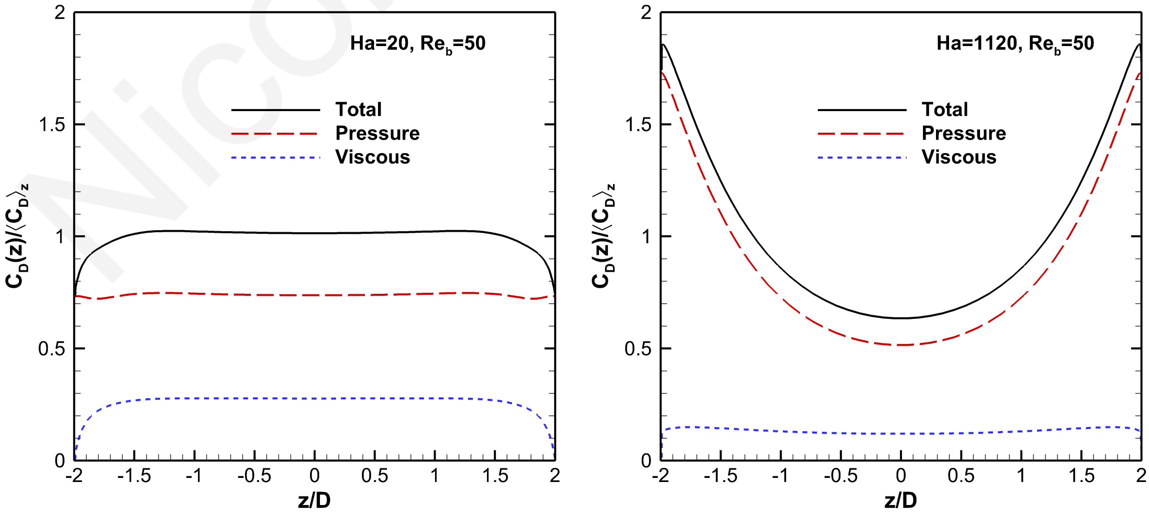

Figure 5.15: Spanwise variation of the drag coefficient and its components, viscous and pressure drag, for $Re_b = 50$, at $Ha = 20$ and 1120.

to about 80% of the total. At $Ha = 20$, the influence of Lorentz forces on the pressure drag is small with the latter displaying a relatively flat profile, therefore the spanwise variation of $C_D(z)$ is due almost entirely to the effect of viscous stresses, that are obviously affected by the wall-boundary layer at both ends of the cylinder. At $Ha = 1120$, owing to the stronger magnetic field, the Lorentz forces affect considerably the distribution of the pressure forces, as previously explained. As a result, the contribution of the pressure drag to the spanwise variation of the total drag, outweighs significantly the viscous forces. Interestingly, unlike $C_{pb}(z)$, the relative difference between the minimum and maximum value of $C_D(z)$ for $Ha = 1120$, is almost 200% with respect to its minimum value. This is attributed to the fact that $C_{pb}(z)$ is simply a point measurement, while $C_D(z)$ is an integral quantity of both the viscous and pressure forces over the surface of the cylinder and therefore more indicative of the Lorentz forces effect. From an engineering point of view, the increased non-uniformity of the spanwise distribution of C_D is important since it can lead to uneven stress distributions. Yet, this unexpected trend could not have been inferred by examining the velocity distribution, which on the contrary becomes more two-dimensional with increasing Ha.

In view of this strikingly "three-dimensional" distribution of the drag coefficient, one would have expected that the Q2D-calculated value for the average C_D would have differed significantly from the result produced by this fully three-dimensional simulation. However, as shown in Table 5.5, the discrepancies between the two studies are quite small, and not significantly larger than those for the C_{pb}. This fact suggests that for steady-flow configurations, the averaging of the three-dimensional governing equations – as done by the Q2D model – can capture the integral effects of the MHD flow, thus producing sensible and reasonably accurate values for the averaged parameters, such as C_D and C_{pb}. Yet, despite providing an accurate prediction for the average C_D, the Q2D model cannot reproduce the details of the pressure distribution along the flow insert that the present three-dimensional study has revealed. While not surprising, this limitation means that the Q2D model should not be used for predicting spanwise force distributions on inserts, even at high Hartmann numbers, where in general the Q2D model is expected to hold.

5.5 Flow characteristics of the unsteady regime

The third and final part of the current study concerns the unsteady flow regime. Within this regime very rich phenomena appear, which are of interest partially due to the antecedents in the literature. As already mentioned in the introduction, the results of Frank *et al.* [51], and Dousset and Pothérat [56], revealed the presence of an additional flow regime that comes in succession after the laminar periodic vortex shedding. This regime is characterized by irregular vortex patterns and by the shedding of secondary vortices from the top and bottom walls, and it does not have a counterpart in the

Table 5.6: Relative differences between the unsteady-flow characteristics obtained in the present study and those by Dousset and Pothérat [56]. It should be noted, that there simualtions were performed at $Ha = 320$, $Re = 2030$, and $Ha = 1120$, $Re = 4790$.

Case	$\bar{C}'_{pb}$	$\bar{C}_D$	St
$U1$	26%	36%	16%
$U3$	2%	8%	7%

purely hydrodynamic case at such moderate blockage ratio [27].

The aim of this section is to verify the presence of this regime and to describe additional flow features that can only be observed using a full three-dimensional analysis. Furthermore, the analysis includes a discussion of unsteady regimes at low interaction parameters, $N \sim 1$, never addressed before.

Due to the increased computational time needed for such three-dimensional flow simulations, and especially the need to integrate to a sufficiently long physical time to achieve a statistically steady-state, only a limited number of simulations are carried out. The choice of simulations is guided by the current results from Section 5.3, which show when regular vortex shedding starts to take place, and by the parametric study of Dousset and Pothérat [56], which indicates when the newly identified flow regime occurs. Therefore, a total of three simulations are carried out, namely cases $U1$, $U2$ and $U3$, using grids GL-M, GF-M and GX-M, respectively. Case $U1$ is performed, at $Ha = 320$, $Re_c = 2000$, $N \simeq 3$, matching the von Kármán vortex flow. The other two simulations are performed for a fixed higher Reynolds number ($Re_c = 5000$) while varying the Hartmann numbers. Thus, case $U2$ corresponds to moderate ($Ha = 320$) and case $U3$ to strong magnetic field intensity ($Ha = 1120$). These sets of parameters correspond to the forth flow regime according to Ref. [56] and yield interaction parameters of $N \simeq 1$ and $N \simeq 16$, respectively for cases $U2$ and $U3$.

The results obtained in the unsteady flow regime are summarized in Table 5.3, while in Table 5.6 they are compared to the data reported in Ref. [56]. For case $U3$, results between the two studies are in good agreement, however for case $U1$ large discrepancies can be observed. These can be attributed to the low interaction parameter associated with case $U1$, as the Q2D model used in Ref. [56] is likely to produce invalid results at this low interaction parameter, as pointed out by the authors [56].

5.5.1 Case $U1$: $Ha = 320$, $Re = 2000$

Figure 5.16 shows snapshots of contour plots of spanwise vorticity, ω_z, in the center-plane $z = 0$, for the case $U1$ ($Ha = 320$, $Re_c = 2000$). In this figure, a typical von Kármán vortex street is observed. Vortices are shed in a regular manner from alternate sides of the cylinder, forming two rows that move alternately clockwise and

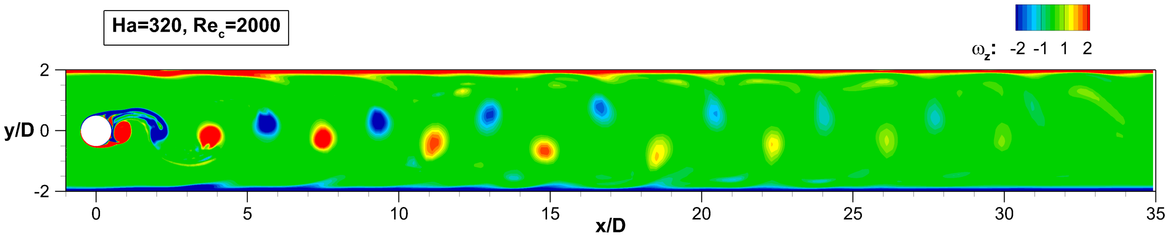

Figure 5.16: Contour plots of spanwise vorticity, ω_z, in the mid-plane ($z = 0$) for the case of $Ha = 320$ and $Re_c = 2000$.

anti-clockwise. Nevertheless, when the vortex trajectories are contrasted to the corresponding confined case of flow over a cylinder in a *channel* [33, 40, 79], a fundamental difference between the two cases can clearly be observed. Unlike the channel flow case, where the trajectories of the two rows of vortices intersect and their position with respect to the symmetry line is inverted [33, 40, 79], in this case no inversion of the shed vortices is observed. As reported in previous studies [50, 51, 93], under the action of the magnetic field the wake of the cylinder is narrowed and the distance between the vortices is reduced. Consequently, shed vortices reach the vicinity of the walls only further downstream. As the inversion of the von Kármán vortices is caused by interactions with the top and bottom walls soon after they are shed [33, 40], no inversion of vortices is observed in this case.

5.5.2 Case $U2$: $Ha = 320$, $Re = 5000$

In case $U2$, inertial effects are amplified with respect to case $U1$, by increasing Re number to $Re_c = 5000$, while keeping the Hartmann number constant at $Ha = 320$. As seen in Figure 5.17(a-b), vortex shedding remains periodic, but appears irregular. Looking at the different instances of the flow, the wake still comprises of an arrangement of vortices shed from the cylinder, however the wake is further narrowed and loses its symmetry. Shed vortices maintain their vorticity for longer distances, follow an irregular path and their paths intersect crossing each other. It is interesting to note that in the near wake region, $x/D < 5$, generated vortices are fragmented and small-scale structures are observed. This can be seen more clearly in Figure 5.17(c), where a closer look into the near wake region of Figure 5.17(a) is presented. Here, the primary vortices appear heavily distorted, and small structures appear in the separated shear layers. Moving further downstream, these smaller structures are eventually damped, and one finds that the structure of the wake returns to a more coherent state.

The visualization of flow structures in this rather complicated three-dimensional wall-bounded shear flow can be facilitated using the λ_2 criterion. The λ_2 is defined as the second eigenvalue of $S^2 + X^2$, where S and X denote the symmetric and antisymmetric parts of the velocity gradient tensor respectively [83]. Plotting iso-surfaces of λ_2

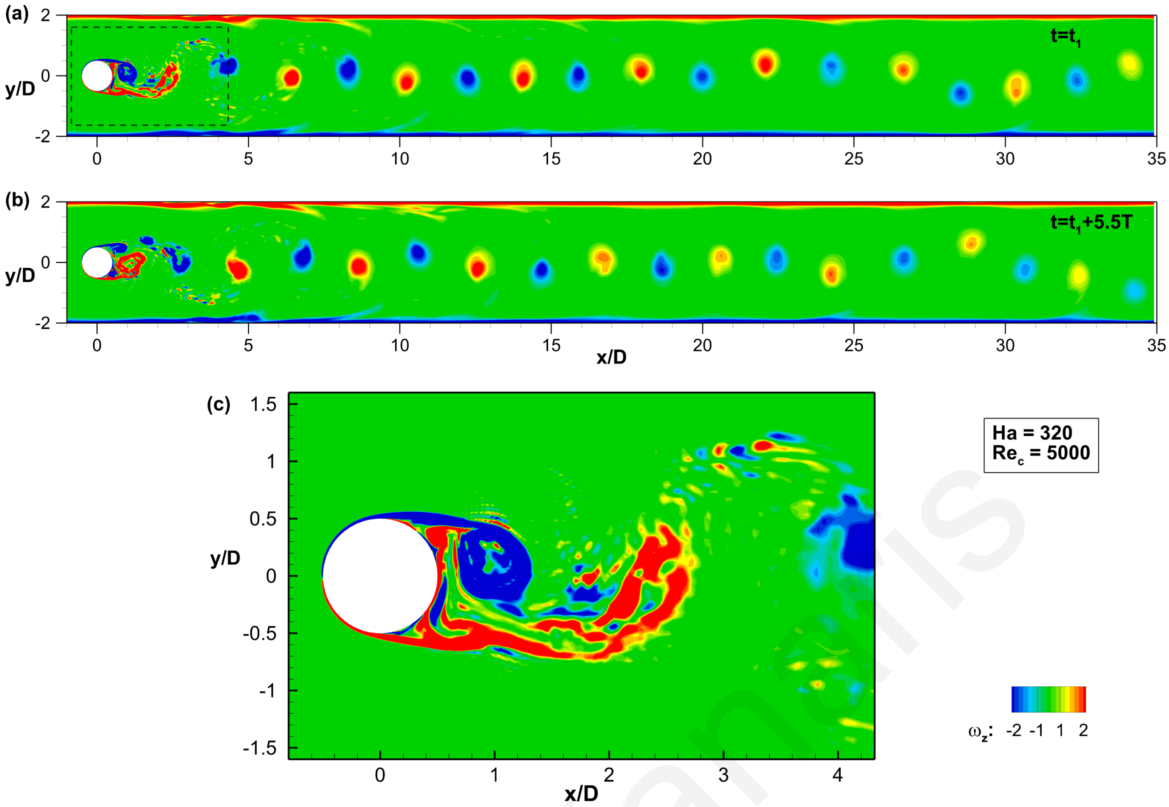

Figure 5.17: Contour plots of spanwise vorticity, ω_z, in the mid-plane ($z = 0$) for the case of $Ha = 320$ and $Re_c = 5000$. (a-b) Different instances of the flow. (c) Expanded view of figure (a) marked by the dashed line.

provides an effective way to visualize the primary and induced vortices of the cylinder wake, while excluding the wall shear region.

Figure 5.18 shows snapshots of iso-surfaces of λ_2 normalized by its absolute minimum, $\lambda_{2,min}$, for the case $U2$. Iso-surfaces are colored by the spanwise vorticity component, ω_z, in order to reveal the spanwise rotation direction of each vortical structure. The spanwise rollers essentially identify the primary vortex cores. At these values of $Ha = 320$ and $Re_c = 5000$, the corresponding interaction parameter is $N \simeq 1$, and the flow is expected to approach a two-dimensional state according to Mück *et al* [59]. This can be verified from Figure 5.18, if we focus our attention further downstream. Indeed, from approximately $x \simeq 5D$ and further downstream, the primary vortex cores are aligned in the spanwise direction, parallel to the magnetic field direction, although they display a slight curvature in the bulk of the flow. Only in the very thin viscous Hartmann layers close to the side walls, three-dimensional effects are visible. This tendency towards a two-dimensional flow is in very good agreement with the observations of Mück *et al* [59]. However, in the near wake region the flow is strikingly more complex and highly three-dimensional. The flow in the separated shear layers is highly fragmented and hosts a plethora of small-scale vortices. Inevitably, as these small turbulent-like structures travel downstream, they become suppressed by the magnetic

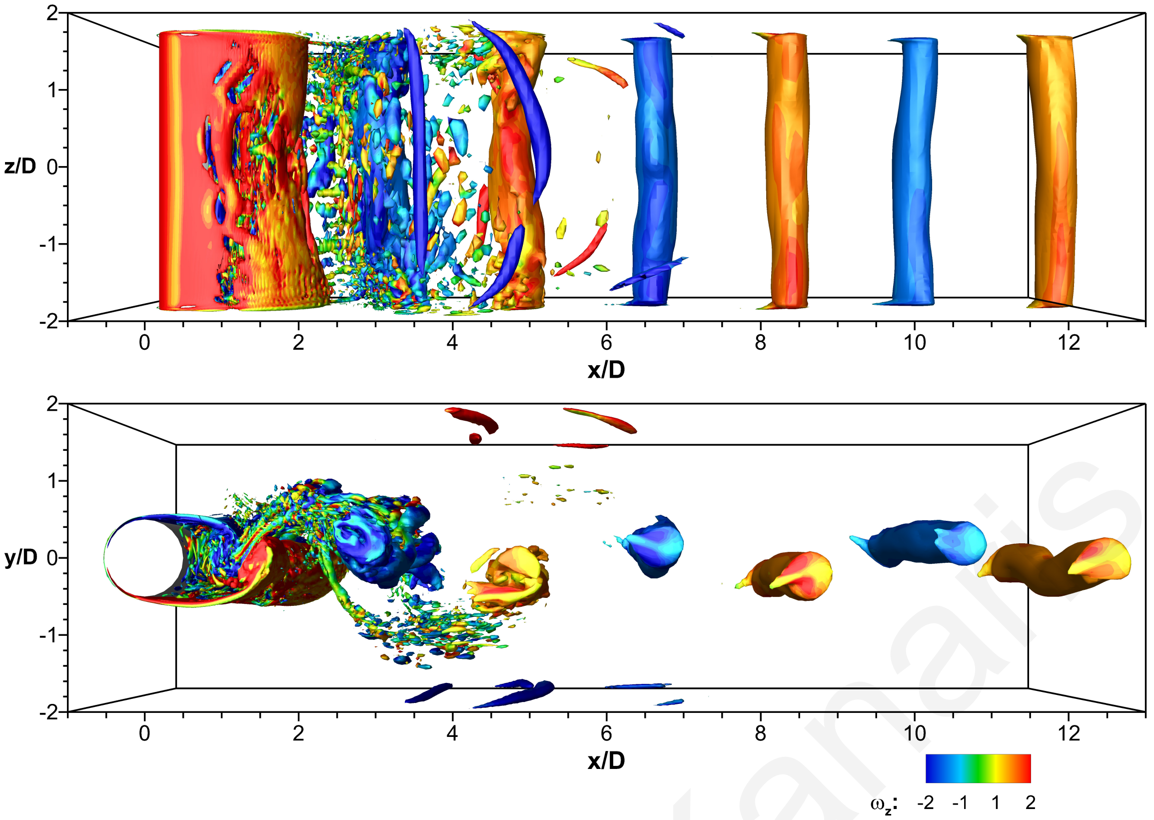

Figure 5.18: Instantaneous plots of iso-surfaces of the λ_2 criterion normalized by its absolute minimum ($\lambda_2/\lambda_{2,min} = 0.2\%$), for $Ha = 320$ and $Re_c = 5000$. Iso-surfaces are colored by spanwise vorticity component.

field and eventually are completely damped.

Figure 5.18 shows snapshots of iso-surfaces of λ_2 normalized by its absolute minimum, $\lambda_{2,min}$, for the case $U2$. Iso-surfaces are colored by the streamwise vorticity component, ω_x, in order to reveal the streamwise rotation direction of each vortical structure. The spanwise rollers essentially identify the primary vortex cores. Here, we recall that values of $Ha = 320$ and $Re_c = 5000$ correspond to an interaction parameter $N \simeq 5$, thus in this case the electrodynamic forces are slightly dominant in the flow, and the flow is expected to approach a two-dimensional state. This can be verified from Figure 5.18, if we focus our attention further downstream. Indeed, from approximately $x/D \simeq 5$ and further downstream, the primary vortex cores are aligned in the spanwise direction, parallel to the magnetic field direction. Only in the very thin viscous Hartmann layers close to the side walls, three-dimensional effects are visible. The slight curvature, of these vortices, observed along the direction of the magnetic field is in line with the observations of Mück *et al* [59]. Nevertheless, in the near wake region the flow is strikingly more complex and highly three-dimensional. The flow in the separated shear layers is highly fragmented and hosts a plethora of small scale vortices. Inevitably, as these small turbulent-like structures travel downstream, they become suppressed by the magnetic field and eventually are completely damped.

The structure of the near wake can be attributed to the presence of the circular cylinder, which acts as a turbulence promoter, thereby facilitating the generation of three-dimensional flow structures (especially at this high Reynolds number). Looking at a collection of various snapshots the small-scale vortices in the near wake seem to arise from instabilities originating at the shear layers, before mixing with the primary Kármán vortices. This development of three-dimensional structures on the scale of the shear layer vortices, bears resemblance to flow characteristics during the initial stages of the shear-layer transition regime, as described in several purely hydrodynamic studies for the case of a free cylinder at similar Reynolds numbers [94, 95, 96]. In hydrodynamic scenarios, the shear layers separating from the sides of the cylinder eventually become turbulent. Of course, this phenomenon can not be seen here due to the damping action of the magnetic field.

One could also argue that the irregular character of vortex shedding resembles the new flow regime reported in previous studies for similar values of Ha and Re_c [51, 56]. For this range of parameters, reference [56] reported irregular shedding of primary vortices that interacted strongly with the boundary layers at the walls leading to shedding of secondary vortices from the top and bottom walls. However, this is not supported by the present results. Despite the irregular shedding of primary vortices also seen in case $U2$, the wake remains narrow and the interaction between the primary vortices and the Shercliff layers at the top and bottom walls of the duct is weak. As a consequence, the flow fails to produce boundary layer separation at the duct walls and, eventually, no shedding of secondary vortices from the top and bottom walls is observed. Secondary vortices shed from the top and bottom walls, represent a primary feature of the reported flow regime in reference [56], and therefore a main difference between the two analyses. It is nevertheless important to underline the fact that Dousset and Pothérat [56] suggested that for such a low interaction parameter, i.e. $N \simeq 1$, three-dimensional effects are likely to appear, therefore rendering the validity of the quasi-2D approximation questionable, which in turn raises questions about their description of the flow regime. Indeed, the current three-dimensional computations show that, for these set of parameters, 3-D structures are a salient feature of the flow. Current results reveal that the quasi-2D model is not able to capture these specific three-dimensional effects, as they are caused by small and turbulent-like events which can not be accurately captured by the averaging of the equations. A more detailed discussion concerning these differences and the respective physical reasons behind them will be addressed in subsection 5.5.5.

5.5.3 Case $U3$: $Ha = 1120$, $Re = 5000$

Case $U3$ corresponds to the same Reynolds number ($Re_c = 5000$) as case $U2$, but at a higher Hartmann number value of $Ha = 1120$. Intuitively, under these conditions

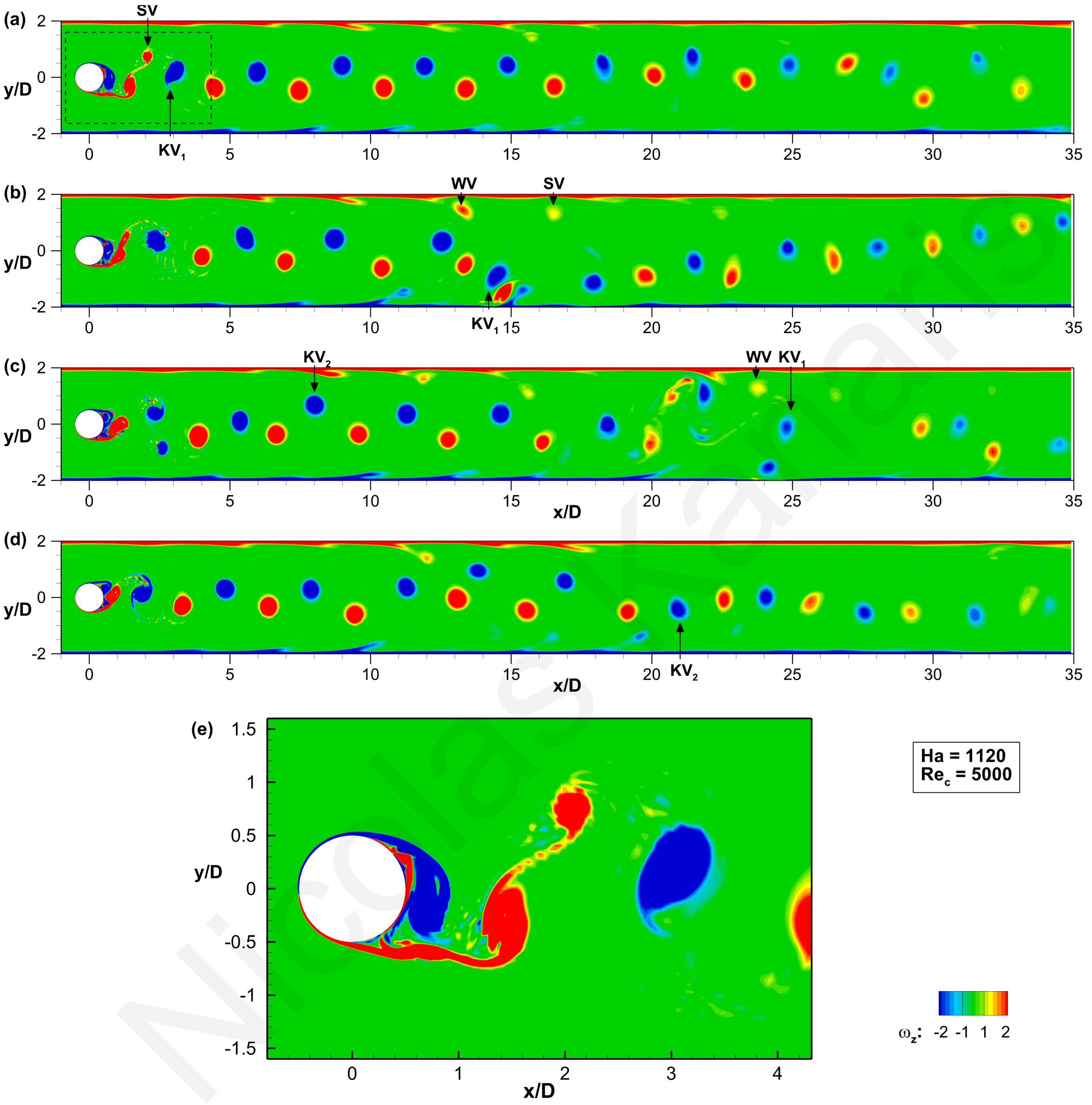

Figure 5.19: Instantaneous visualization of contour plots of streamwise vorticity, ω_z, in the plane $z/D = 0$. (a) $t = 271.4D/U_C$, (b) $t = 284.8D/U_C$, (c) $t = 294.6D/U_C$, (d) $t = 307.7D/U_C$, (e) zoomed area of plot (a) marked by dashed line.

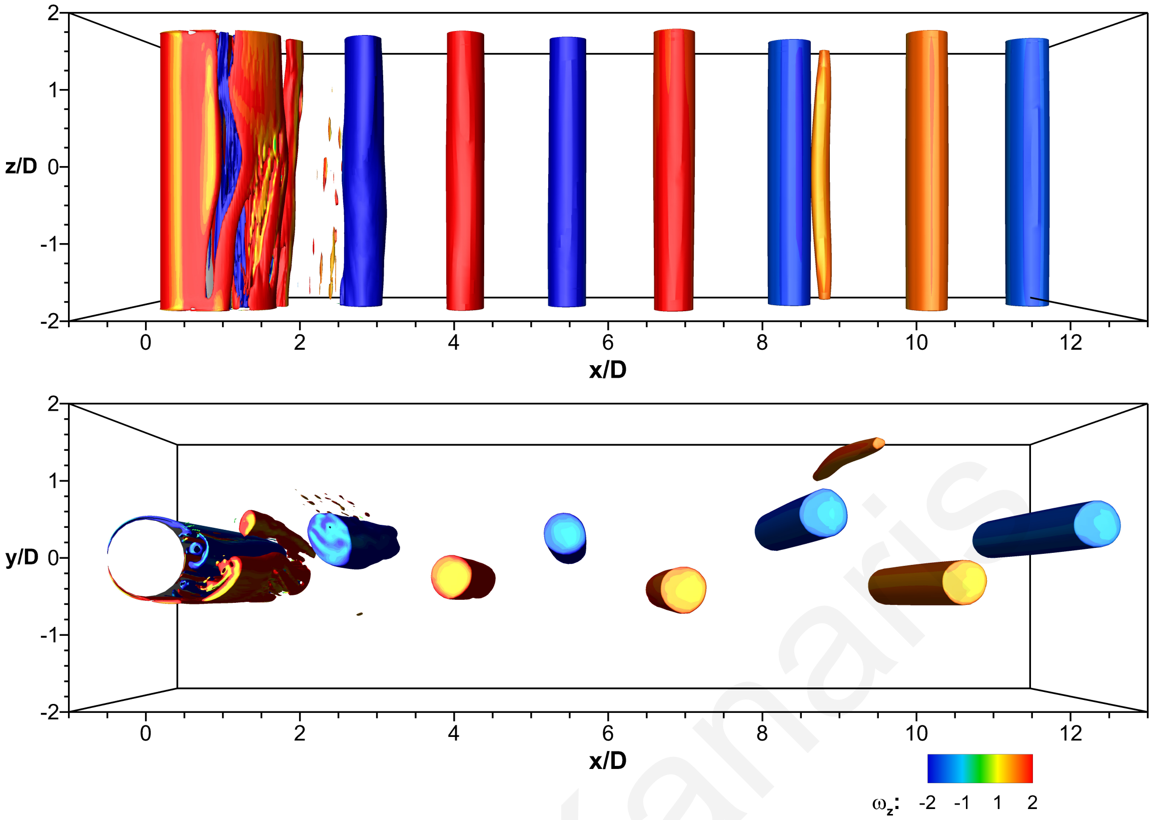

Figure 5.20: Instantaneous plots of iso-surfaces of the λ_2 criterion normalized by its absolute minimum ($\lambda_2/\lambda_{2,min} = 0.2\%$), for $Ha = 1120$ and $Re_c = 5000$. Iso-surfaces are colored by spanwise vorticity component ω_z.

of stronger electrodynamic damping, one would expect the shed vortices to be more suppressed and to diffuse more rapidly as they convect downstream, while reducing the irregularity of the overall vortex shedding pattern. Surprisingly, as seen in Figure 5.19, the current results show that the shedding pattern of the vortices for this set of parameters is actually even more irregular when compared with the previous case (case $U2$) for a lower Hartmann number ($Ha = 320$, Figure 5.17). In the near wake of the cylinder, i.e. $x/D < 10$, the lateral spacing between shed vortices is increased, with the vortices following an irregular oblique trajectory closer to the top and bottom walls. As they are progressively convected further downstream, i.e. $x/D > 10$, they interact with the duct walls inducing secondary vortices from the top and bottom walls (see vortex core WV in Figure 5.19) and inevitably are reflected back in the opposite direction (see vortex cores KV_1, KV_2). The induced *secondary* vortices are, however, weak and are quickly dissipated soon after they are shed. Nevertheless, their influence on the overall phenomenology is significant. Another interesting feature of the flow is the appearance of secondary vortices (see vortex core SV) alongside with the main vortices. At times a primary vortex core, soon after it is shed, deforms and eventually is torn apart, giving birth to a smaller secondary vortex. This intermittent secondary vortex, interacts with its surrounding vortices and eventually disrupts significantly the trajectories of the primary vortex cores. This effect occurs spontaneously from either side of the cylinder in a consistent and systematic way. The formation of the secondary vortex can be clearly seen in Figure 5.19(d), where a close-up view of Figure 5.19(a) in the vicinity of the cylinder is presented. Additionally, the figure displays shed vortices that appear less fragmented and more coherent at the shear layers.

This is also evident in Figure 5.20 where iso-surfaces of λ_2, normalized by its absolute minimum, $\lambda_{2,min}$, are presented for this case. In this figure, the stronger magnetic damping (as compared to the previous case $U2$, shown in Figure 5.18) is obvious. Close to the cylinder for example, the shear layers are devoid of small three-dimensional structures and more coherent vortices are formed. Only a weak undulation of the primary vortices is observed. Vortex rollers are almost perfectly aligned along the spanwise direction further downstream. These effects can clearly be attributed to the flattening of the velocity profiles along the spanwise direction as mentioned before, and as expected due to the high interaction parameter $N \simeq 16$. It is interesting to note that for this Hartmann number the vortex alignment highly resembles that of a flow configuration without side-walls or even unconfined cases. The current flow phenomenology for case $U3$ is in better agreement with the results of reference [56], although the flow is still clearly less irregular. In order to understand the differences and the physical reasons behind them, a detailed spectral analysis is incorporated next in the discussion.

5.5.4 Effect on lift and drag coefficient

The regular or irregular nature of the flow is reflected by the time history of the lift, C_L, and drag, C_D, coefficients as shown in Figure 5.21. For case $U1$, the perfectly time-periodic nature of the flow is displayed in Figure 5.21(a). The irregular vortex shedding observed in cases $U2$ and $U3$, is clearly depicted on the time history of the lift and drag coefficient, as seen in Figures 5.21(b-c). Both signals keep a periodic character, however, lose their coherence.

5.5.5 Spectral analysis

Another powerful way to identify the occurrence of vortex structures, and investigate the presence of irregular flow phenomena, is through a spectral analysis of velocity signals gathered from probes placed at different streamwise positions. Figure 5.22 displays the power spectral density of the crossflow velocity, u_y, obtained from probes positioned at the mid-plane ($z = 0$) at several (x, y) locations: in the vicinity of the cylinder's shear layer ($x = 1.5D$, $y = 0.5D$), at the center downstream ($x = 10D$, $y = 0$) and further downstream ($x = 20D$, $y = 0$). Power spectral densities have been obtained using Welch's averaged periodogram method [81], while a Hamming window was applied to each overlapping segment of data. Results are shown for all cases examined in this subsection, namely cases $U1$, $U2$ and $U3$.

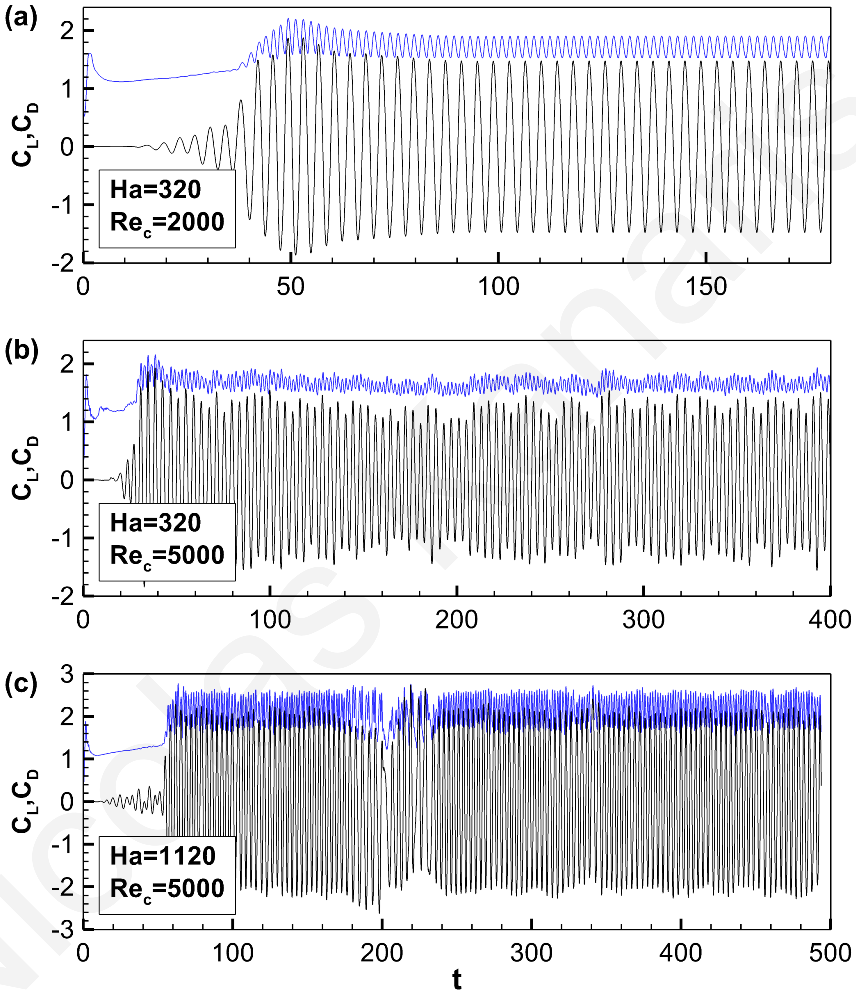

Figure 5.21: Time history of drag and lift coefficient.

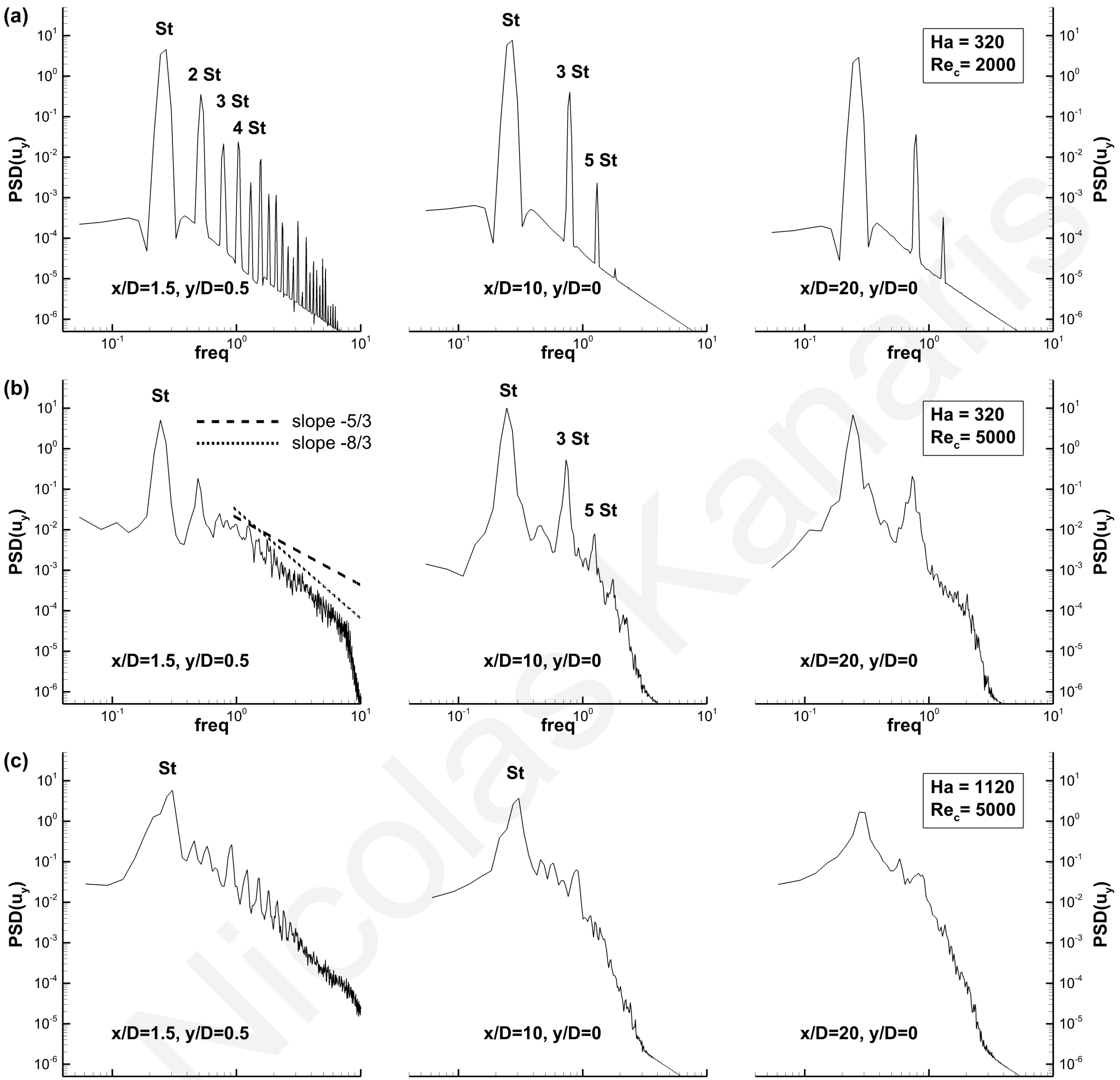

Figure 5.22: Spectra of crossflow velocity component, u_y, along the centerline at the plane $z/D = 0$ at different positions for (a) $Ha = 320$ $Re = 2000$, (b) $Ha = 320$ $Re = 5000$ and (c) $Ha = 1120$ $Re = 5000$.

For the case $U1$ ($Ha = 320$, $Re_c = 2000$), the power spectrum exhibits the expected strong peak at the fundamental frequency of the flow (Strouhal frequency, St), corresponding directly to the passage of a laminar periodic vortex array through the measuring probe. The rest of the peaks observed represent harmonic frequencies (in the centerline only odd harmonics are observed), in line with the observations of Kovasznay [97] for the hydrodynamic flow over an unconfined cylinder in the laminar flow regime.

In the case $U2$ ($Ha = 320$, $Re_c = 5000$), the strong presence of the Strouhal frequency in the spectra can still be observed, suggesting that a vortex street continues to be present. However, the spectrum close to the cylinder, at $x = 1.5D$, is broadened indicating the presence of smaller scales of motion. The scaling of the energy spectrum in the inertial region is of the form f^{-3}, which is characteristic of MHD turbulence [98, 54]. This broad range of frequencies illustrates the development of finer-scale three-dimensional structures in the shear layers, in line with our previous observations (see Figure 5.17). Looking at the spectra obtained from the probes positioned further downstream, at $x = 10D$ and $x = 20D$, it is evident that the small-scale fluctuations are slowly suppressed, and the spectra are dominated by a primary frequency of oscillation and its harmonics. The weakly turbulent behaviour of the flow gives place to larger, regular and smoother vortices that correspond to the primary vortices. Nevertheless, non-harmonic components are also present due to a irregular periodic signal, supporting the idea of the irregular vortex shedding process described before.

Finally, in the case $U3$ ($Ha = 1120$, $Re_c = 5000$) the spectra exhibit different features. Close to the cylinder, at $x = 1.5D$, the spectrum is characterized by fewer high frequencies and harmonics of the primary shedding frequency can clearly be identified. This spectral feature support the visualizations of the flow shown in Figure 5.20, where the cylinder wake was found to be dominated by coherent vortices with shear layers devoid of small-scale three-dimensional structures. More importantly, when compared to case $U2$, the energy content of low frequencies is strongly enhanced (by almost an order of magnitude) indicating the presence of more energetic primary vortices in the flow. This is associated with the irregular character of the flow at this set of parameters, as will be explained in the following paragraph. Irregular vortex shedding is also supported, by looking at the spectra further downstream, at $x = 10D$ and $x = 20D$. Although a strong peak is present indicating periodic vortex shedding, the absence of clearly identifiable harmonic frequencies, together with the broadening of the power spectrum is linked with the presence of irregular vortex flow patterns. Furthermore, the power density contained in the higher frequencies has been greatly reduced, indicating that no turbulent-like phenomena are present. This complete suppression of turbulence is of course not surprising, given the stronger magnetic field.

The presented spectral analysis, in combination with the flow visualizations of cases $U2$ and $U3$ (shown in subsections 5.5.2 and 5.5.3 respectively), allow us to finally propose a mechanism explaining the surprising enhancement of flow irregularity with increasing Hartmann number and the differences observed the between current results and quasi two-dimensional studies. This explanation is based on the MHD modification of small-scale three-dimensional motions. At low interaction parameters, $N \simeq 1$, the combination of strong inertial forces due to the high Reynolds number ($Re_c = 5000$) and of a flow obstruction promotes transitional or even turbulent characteristics near the cylinder. The presence of small scale three-dimensional structures causes very strong Joule dissipation, which eventually extracts energy from the large-scale primary vortex cores. Through this process the primary vortices become less energetic, leading to a more regular vortex shedding pattern. For a given Reynolds number, increasing the Hartmann number suppresses the intensity of the smallest three-dimensional flow structures due to increased Hartmann damping. Consequently, increasing Ha results in more energetic primary vortices, which retain most of their inertia since less energy is transferred to smaller scales of motion. This fact explains why for the higher Ha number considered (case $U3$), the vortex cores start interacting with the top and bottom walls, thus inducing secondary vorticity and leading to a more irregular flow pattern. The Q2D model fails to capture the enhancement of the Joule dissipation due to the presence of highly three-dimensional structures, and as a result, over-predicts the inertia retained in the primary vortex cores, especially at these high Reynolds numbers. This phenomenology explains why the Q2D model yields more irregular flow characteristics than those observed in the current three-dimensional analysis for the same set of parameters.

Nevertheless, additional work would be required in order to clarify the trends at Ha values even higher than those considered here. A further increase of the Hartmann number, could damp even more the three-dimensional effects, yielding a more irregular flow regime, closer to the one identified by the Q2D approach. On the other hand, the increased magnetohydrodynamic damping could be sufficiently strong to suppress vortex shedding, stabilize the flow, and eventually lead to a steady flow regime. These considerations require further extensive simulations that would help understand the complex interaction between the inertial three-dimensional effects, the mechanisms of magnetic dumping, and the way they affect the generated flow patterns.

5.6 Conclusions

Direct numerical simulations of three-dimensional flow of a liquid metal around a circular cylinder placed in a rectangular duct, under a wide range of magnetic field intensities have been performed. The blockage and aspect ratio were kept constant at $\beta = 1/4$, $\alpha = 4$. The Reynolds number was varied between $50 \leq Re_c \leq 5000$ for Hartmann numbers in the range of $0 \leq Ha \leq 1120$.

A non-monotonus behavior of the critical Reynolds number for the onset of vortex shedding with respect to the Hartmann number has been shown. For $Ha > 80$, a linear dependence of the critical Re is observed with respect to Ha. However, when decreasing the Hartmann number below $Ha = 80$, a non-monotonous relation is observed, where initially Re_{cr} decreases slightly until it reaches a minimum value around $Ha \simeq 35$. As Ha is decreased even further, Re_{cr} starts to increase again. This unexpected phenomenon is explained by the effect of the Lorentz forces on the velocity profile, which becomes flatter for increasing Hartmann numbers. A flatter velocity profile implies a reduction of the velocity deficit for a given bulk flow, which essentially mimics the effect of moving the walls further away, therefore, promoting the destabilization of the flow. This effect could be of practical importance in various engineering applications where enhancement of heat and mass transfer or mixing is desired.

Within the steady flow regime, the evolution of the recirculation length and of the drag and base pressure coefficients with respect to Ha and Re was presented. The predictions of the Q2D model for these global flow characteristics are in good agreement with the current three-dimensional numerical results when averaged over the cylinder length. However, the current three-dimensional computations display an increase in the three-dimensionality of the spanwise distribution of forces along the cylinder with increasing Ha, an effect that cannot possibly be captured in the Q2D analysis. Hence, depending on the range of parameters, an accurate stress analysis of the cylinder, and presumably of other flow inserts, could require a fully three-dimensional treatment.

We have also showed that for a high Reynolds number, $Re_c = 5000$, even for relatively high values of the interaction parameter (N up to 16), inertia effects in the near wake play a significant role in the formation and transport of vortices. For $Ha = 320$ ($N \simeq 1$), inertial forces lead to turbulence-like instabilities, which redistribute the energy towards small scales, eventually reducing the energy of the shedding vortex cores. When the Hartmann number is increased to $Ha = 1120$ ($N \simeq 16$), the presence of a stronger magnetic field acts like a turbulent suppressor, hence primary vortices retain most of the inertia and remain more energetic as they move downstream. This phenomenology leads to the surprising new observation of enhanced flow irregularity with increasing Ha. This effect also explains the differences observed between the current three-dimensional results and the Q2D model predictions. The quasi-two-dimensional model can not capture the enhancement of the Joule dissipation due to the presence of highly three-dimensional structures in the flow. As consequence, it overestimates the energy retained in the primary vortex cores and predicts a much more irregular vortex shedding for a given set of parameter values than what has been observed in the present work. Nevertheless, it is reasonable to expect this behavior to be non-monotonic, as for even higher magnetic fields the flow should become steady again, since the energy of the large scales would eventually be also damped by stronger magnetic fields.

Chapter 6

Summary and Future Work

6.1 Summary of present work

As already discussed, fluid flow past a bluff body is a common occurrence associated with many engineering applications and can have a significant impact on design. The alternate shedding of vortices in the near wake, in the classical vortex street configuration, leads to large fluctuating pressure forces in a direction transverse to the flow and may cause structural vibrations, acoustic noise, or resonance, which in some cases can trigger failure. On the other hand, bluff bodies may promote turbulence and in this way enhance mixing and heat transfer in a flow. Therefore, the motivation for studying the wake dynamics of such a flow arises not only from the need to improve our understanding of the fundamental processes that drive the flow, but also from the need to devise methods for effectively controlling vortex shedding in engineering applications.

Disturbed flows around all bluff bodies develop similar flow structures in the wake of the flow, despite differences in shape and the presence or absence of sharp edges. The flow over a circular cylinder represents an idealization of several industrially important processes. In this thesis, we studied and analyzed the effect of *confinement* on the flow characteristics and associated flow regimes in the wake of a *circular* cylinder. Confinement was investigated in the case of a *channel flow* and flow in a *rectangular duct*. In the later case, the fluid was assumed electrically conducting and the action of an externally applied magnetic field was investigated. We addressed these flows, using full three-dimensional direct numerical simulations (DNS). Despite the very large demand in CPU power and memory storage capacity associated with this method of choice, DNS is a very reliable and accurate method, as it does not involve any model nor approximation.

In the purely hydrodynamic case of flow over a circular cylinder in a plane channel, 3-D simulations were carried out in the Reynolds number range $150 \leq Re \leq 390$, for a blockage ratio (ratio of the cylinder diameter to the channel height) of $\beta = 1/5$. Three-dimensional effects were observed for $Re \geq 210$. For the first time, two discontinuous changes were detected in the $St - Re$ and $C_{pb} - Re$ curves, corresponding to different spanwise instabilities in the wake. For $Re = 210$ and 240, *mode A* 3-D shedding was observed, while for $Re > 300$ *mode B* vortex structures were detected. The intermittent presence of naturally occurring vortex dislocations, as a fundamental feature of wake transition, was also demonstrated for the first time. The present work leads to a clarification of how the shape and evolution of *mode A* and *mode B* instabilities are affected downstream by the confinement of the channel walls.

We have then considered the case of a further confined configuration bounded by four impermeable walls, i.e. the case of flow over a cylinder in a rectangular duct. We further considered the flow to be electrically conducting and in the presence of an externally applied magnetic field, under a wide range of magnetic field intensities. The walls of the cylinder and the duct were assumed to be electrically insulating. The blockage and aspect ratio (ratio of the cylinder length to its diameter) was kept constant at $\beta = 1/4$, and $\alpha = 4$ respectively. The Reynolds number was varied between $50 \leq Re \leq 5000$, for Hartmann numbers in the range of $0 \leq Ha \leq 1120$. This work revealed the presence of a non-monotonic behaviour of the critical Reynolds number for the onset of vortex shedding, with respect to the Hartmann number. This unexpected effect of generating unsteadiness by increasing Ha could be of practical importance in various engineering applications where enhancement of heat and mass transfer is desired. For example, controlling the flow this way could be used to stir metal alloys more efficiently in industrial settings. Performing a series of simulations in the unsteady flow regime for high values of Ha and Re numbers, we further showed a new and surprising result, the destabilization of the flow with increasing Ha. This unexpected behavior was attributed to the formation of turbulent characteristics near the cylinder, and the action of an energy-transfer mechanism to the higher frequency range. Due to the presence of such strongly 3-D phenomena, the quasi 2-D model fails to capture this mechanism yielding flow characteristics that significantly more irregular than those observed by the current 3-D analysis.

Overall, this work provides new understanding of the flow characteristics and physical mechanisms in the case of flow over bluff bodies in a confined geometry, and as such it could contribute to efforts to devise improved means of controlling flow characteristics in related configurations.

6.2 Future Work

Following the investigations described in this thesis, several lines of research arising from this work could be pursued.

A main line of research that could be pursued further is the heat transfer characteristics for the investigated configurations for a wide range of Reynolds and Prandtl numbers. Heat transfer characteristics, have so far received even less attention than the purely hydrodynamic part of the problem. Such studies would be particularly interesting in the flow regimes investigated in the current thesis where highly three-dimensional flow patterns were observed, and which are expected to significantly modify the distribution of the heat transfer mechanisms. The proposed research could focus on the development of simple correlations for Nusselt number (ratio of convective heat transfer to conductive heat transfer) as a function of the pertinent dimensionless variables. In addition, to the average Nusselt number, the effects of the Reynolds number, Prandtl number (ratio of momentum diffusivity to thermal diffusivity) and thermal boundary conditions on the temperature field near the cylinder and the walls, and on the local Nusselt number distributions could also be studied. This would help researchers develop a deeper understanding of the underlying physical processes related to heat transfer phenomena.

Another line of research, associated with the heat transfer analysis, is to investigate the effects of geometrical parameters (blockage ratio, aspect ratio, symmetric or off-centre placement of the obstacle) and thermal boundary conditions on the local Nusselt number and on the temperature field near the cylinder and along the confining walls. Using the numerical results, simple heat transfer correlations could be obtained for constant temperature and constant heat flux conditions as a function of the geometrical parameters on the solid circular cylinder. These investigations could be used to fill the gap that exists in the literature by providing parametric relations between the dynamical and geometrical parameters, enhance our understanding on complex fluid flow regimes and heat transfer characteristics, and provide further physical insight into the nature of the flow.

Finally, it would be interesting to investigate the flow characteristics and enhancement of heat transfer, as observed by increased Nusselts, by means of testing new configurations like multiple obstacles with a staggered arrangement within the confined geometry.

Bibliography

[1] M. M. Zdravkovich, *Flow around circular cylinders, vol. 1: Fundamentals*, Oxford University Press, New York, 1997.

[2] M. M. Zdravkovich, *Flow around circular cylinders, vol. 1: Applications*, Oxford University Press, New York, 2003.

[3] C. H. K. Williamson, “Vortex dynamics in the cylinder wake,” *Annu. Rev. Fluid. Mech*, vol. 28, pp. 477–539, 1996.

[4] S. Taneda, “Experimental investigation of the wakes behind cylinders and plates at low Reynolds numbers,” *J. Phys. Soc. Japan*, vol. 11, pp. 302–307, 1956.

[5] S. C. R. Dennis and G.Z. Chang, “Numerical solutions for steady flow past a circular cylinder at Reynolds numbers up to 100,” *J. Fluid Mech.*, vol. 42, pp. 471–4489, 1970.

[6] D. Barkley and R. D. Henderson, “Three-dimensional Floquet stability analysis of the wake of a circular cylinder,” *J. Fluid Mech.*, vol. 322, pp. 215–241, 1996.

[7] A. S. Grove, F. H. Shair, E. E. Petersen, and A. Acrivos, “An experimental investigation of the steady separated flow past a circular cylinder,” *J. Fluid Mech.*, vol. 19, pp. 60–80, 1963.

[8] J. H. Gerrard, “The wakes of cylindrical bluff bodies at low Reynolds number,” *Philos. Trans. R. Soc. London, Ser. A*, vol. 288, pp. 351–382, 1978.

[9] R. Mittal and S. Balachandar, “Effect of three-dimensionality on the lift and drag of nominally two-dimensional cylinders,” *Phys. Fluids*, vol. 8, pp. 1841–1865, 1995.

[10] A. Roshko, “On the drag and shedding frequency of two-dimensional bluff bodies,” NACA Technical Note No. 3169, 1954.

[11] C. P. Jackson, “A finite-element study of the onset of vortex shedding in flow past variously shaped bodies,” *J. Fluid Mech.*, vol. 182, pp. 23–45, 1987.

[12] M. Provansal, C. Mathis, and L. Boyer, "Benard-von Karman instability: transient and forced regimes," *J. Fluid Mech.*, vol. 182, pp. 1–22, 1987.

[13] Th. von Kármán, "Über den Mechanismus des Widerstandes, den ein bewegter Körper in einer Flüssigkeit erfährt. 1 teil," *Nachr. Ges. Wiss. Göttingen. Math. Phys. Klasse*, vol. 29, pp. 509–517, 1911.

[14] Th. von Kármán, "Über den Mechanismus des Widerstandes, den ein bewegter Körper in einer Flüssigkeit erfährt. 2 teil," *Nachr. Ges. Wiss. Göttingen. Math. Phys. Klasse*, pp. 547–556, 1912.

[15] C. H. K. Williamson, "The existence of two stages in the transition to three-dimensionality of a cylinder wake," *Phys. Fluids*, vol. 31, pp. 3165–3168, 1988.

[16] C. H. K. Williamson and A. Roshko, "Measurements of base pressure in the wake of a cylinder at low Reynolds numbers," *Z. Flugwiss Weltraumforsch*, vol. 14, pp. 38–46, 1990.

[17] C. H. K. Williamson, "The natural and forced formation of spot-like vortex dislocations in the transition of a wake," *J. Fluid Mech.*, vol. 243, pp. 393–441, 1992.

[18] G. E. Karniadakis and G. S. Triantafyllou, "Three-dimensional dynamics and transition to turbulence in the wake of bluff objects," *J. Fluid Mech.*, vol. 238, pp. 1–30, 1992.

[19] M. Braza, D. Faghani, and H. Persillon, "Succesive stages and the role of natural vortex dislocations in three-dimensional wake transition," *J. Fluid Mech.*, vol. 439, pp. 1–41, 2001.

[20] C. H. K. Williamson, "Three-dimensional wake transition," *J. Fluid Mech.*, vol. 328, pp. 345–407, 1996.

[21] H. Q. Zhang, U. Fey, B. R. Noack, M. Konig, and H. Eckelmann, "On the transition of the cylinder wake," *Phys. Fluids*, vol. 7, pp. 779–794, 1995.

[22] M. Thompson, K. Hourigan, and J. Sheridan, "Three-dimensional instabilities in the wake of a circular cylinder," *. Exp. Therm. Fluid Sci.*, vol. 12, pp. 190–196, 1996.

[23] R. D. Henderson, "Nonlinear dynamics and pattern formation in turbulent wake transition," *J. Fluid Mech.*, vol. 352, pp. 65–112, 1997.

[24] H. Persillon and M. Braza, "Physical analysis of the transition to turbulence in the wake of a circular cylinder by three-dimensional navier-stokes simulation," *J. Fluid Mech.*, vol. 365, pp. 23–88, 1998.

[25] S. Behara and S. Mittal, “Wake transition in flow past a circular cylinder,” *Phys. Fluids*, vol. 22, pp. 114104, 2010.

[26] A. Roshko, “Perspectives on bluff body aerodynamics,” *J. Wind Eng. Industrial Aerodyn.*, vol. 49, pp. 79–100, 1993.

[27] M. Sahin and R. G. Owens, “A numerical investigation of wall effects up to high blockage ratios on two-dimensional flow past a confined circular cylinder,” *Phys. Fluids*, vol. 16, pp. 1305–1320, 2004.

[28] J. H. Chen, W. G. Pritchard, and S. J. Tavener, “Bifurcation of flow past a cylinder between parallel planes,” *J. Fluid Mech.*, vol. 284, pp. 23–41, 1995.

[29] S. Singha and K. P. Sinhamahapatra, “Flow past a circular cylinder between parallel walls at low Reynolds numbers,” *Ocean Engineering*, vol. 37, pp. 757–769, 2010.

[30] P. Anagnostopoulos, G. Iliadis, and S. Richardson, “Numerical study of the blockage effects on viscous flow past a circular cylinder,” *Int. J. Numer. Meth. Fluids*, vol. 22, 1996.

[31] M. H. Wu, C. Y. Wen, R. H. Yen, M. C Weng, and A. B. Wang, “Experimental and numerical study of the separation angle for flow around a circular cylinder at low Reynolds number,” *J. Fluid Mech.*, vol. 515, pp. 233–260, 2004.

[32] F. H. Shair, A. S. Grove, E.E. Petersen, and A. Acrivos, “The effect of confining walls on the stability of the steady wake behind a circular cylinder,” *J. Fluid Mech.*, vol. 17, pp. 546–550, 1963.

[33] L. Zovatto and G. Pedrizzetti, “Flow about a circular cylinder between parallel walls,” *J. Fluid Mech.*, vol. 440, pp. 1–25, 2001.

[34] S. Mettu, N. Verma, and R. P. Chhabra, “Momentum and heat transfer from an asymmetrically confined circular cylinder in a plane channel,” *Heat Mass Transfer*, vol. 42, pp. 1037–1048, 2006.

[35] P. W. Bearman and M. M. Zdravkovich, “Flow around a circular cylinder near a plane boundary,” *J. Fluid Mech.*, vol. 89, pp. 33–47, 1978.

[36] C. Lei, L. Cheng, and K. Kavanagh, “Re-examination of the effect of a plane boundary on force and vortex shedding of a circular cylinder,” *J. Wind Eng. Industrial Aerodyn.*, vol. 80, pp. 263–286, 1999.

[37] S. J. Price, D. Sumner, J. G. Smith, K. Leong, and M. P. Paidoussis, “Flow visualization around a circular cylinder near to a plane wall,” *J. Fluids Struct.*, vol. 16, pp. 175–191, 2002.

[38] X. K. Wang and S. K. Tan, "Near wake flow characteristics of a circular cylinder close to a wall," *J. Fluids Struct.*, vol. 24, pp. 605–627, 2008.

[39] F. Rehimi, F. Aloui, S. Ben Nasrallah, L. Doubliez, and J. Legrand, "Experimental investigation of a confined flow downstream of a circular cylinder centred between two parallel walls," *J. Fluids Struct.*, vol. 24, pp. 885–882, 2008.

[40] S. Camarri and F. Giannetti, "Effect of confinement on three-dimensional stability in the wake of a circular cylinder," *J. Fluid Mech.*, vol. 642, pp. 447–487, 2010.

[41] C. J. Baker, "The laminar horseshoe vortex," *J. Fluid Mech.*, vol. 95, pp. 347–367, 1979.

[42] M. Nishioka and H. Sato, "Measurements of velocity distributions in the wake of a circular cylinder at low Reynolds numbers," *J. Fluid Mech.*, vol. 65, pp. 97–112, 1974.

[43] E. Berger and R. Wille, "Periodic flow phenomena," *Annu. Rev. Fluid. Mech*, vol. 4, pp. 313–340, 1972.

[44] C. H. K. Williamson, "Oblique and parallel modes of vortex shedding in the wake of a circular cylinder at low Reynolds numbers," *J. Fluid Mech.*, vol. 206, pp. 579–627, 1989.

[45] D. Gerich and H. Eckelmann, "Influence of end plates and free ends on the shedding frequency of circular cylinders," *J. Fluid Mech.*, vol. 122, pp. 109–121, 1982.

[46] M. König, H. Eisenlohr, and H. Eckelmann, "The fine structure in the Strouhal-Reynolds number relationship of the laminar wake of a circular cylinder," *Phys. Fluids A*, vol. 2, pp. 1607–1614, 1990.

[47] M. König, H. Eisenlohr, and H. Eckelmann, "Visualization of the spanwise cellular structure of the laminar wake of wall-bounded circular cylinders," *Phys. Fluids A*, vol. 4, pp. 869–872, 1992.

[48] H. Eisenlohr and H. Eckelmann, "Vortex splitting and its consequences in the vortex street wake of cylinders at low Reynolds number," *Phys. Fluids A*, vol. 1, pp. 189–192, 1989.

[49] P. A. Davidson, *An Introduction to Magnetohydrodynamics*, Cambridge University Press, Cambridge, 2001.

[50] U. Müller and L. Bühler, *Magnetofluiddynamics in Channels and Containers*, Springer, 2001.

[51] M. Frank, L. Barleon, and U. Muller, "Visual analysis of two-dimensional magnetohydrodynamics," *Phys. Fluids*, vol. 13, pp. 2287–2295, 2001.

[52] J. C. R. Hunt, "Magnetohydrodynamic flow in rectangular ducts," *J. Fluid Mech.*, vol. 21, 1965.

[53] B. Knaepen and R. Moreau, "Mahnetohydrodynamic turbulence at low magnetic Reynolds number," *Annu. Rev. Fluid. Mech*, vol. 40, pp. 25–45, 2008.

[54] J. Sommeria and R. Moreau, "Why, how, and when, MHD turbulence becomes two-dimensional," *J. Fluid Mech.*, vol. 118, 1982.

[55] L. Buhler, "Instabilities in quasi-two-dimensional magnetohydrodynamic flows," *J. Fluid Mech.*, vol. 326, pp. 125–150, 1996.

[56] V. Dousset and A. Pothérat, "Numerical simulations of a cylinder wake under a strong axial magnetic field," *Phys. Fluids*, vol. 20, pp. 017104, 2008.

[57] W. K. Hussam, M. C. Thompson, and G. J. Sheard, "Dynamics and heat transfer in a quasi-two-dimensional MHD flow past a circular cylinder in a duct at high hartmann number," *Int. J. Heat Mass Transfer*, vol. 54, pp. 1091–1100, 2011.

[58] W. K. Hussam, M. C. Thompson, and G. J. Sheard, "Optimal transient disturbances behind a circular cylinder in a quasi-two-dimensional magnetohydrodynamic duct flow," *Phys. Fluids*, vol. 24, pp. 024105, 2012.

[59] B. Mück, C. Günther, U. Müller, and L. Bühler, "Three-dimensional MHD flows in rectangular ducts with internal obstacles," *J. Fluid Mech.*, vol. 418, pp. 265–295, 2000.

[60] S. V. Patankar, *Numerical heat transfer and fluid flow*, Hemisphere Pub. Corp., 1980.

[61] H. K. Versteeg and W. Malalasekera, "An introduction to Computational Fluid Dynamics: The Finite Volume Method," *Longman Scientific and Technical, Essex*, 1995.

[62] J. H. Ferziger and M. Peric, *Computational methods for fluid dynamics*, Springer, 2001.

[63] J. Blazek, *Computational Fluid Dynamics: Principles and Applications*, Elsevier, 2001.

[64] M. Spiga and G. L. Morini, "A symmetric solution for velocity profile in laminar flow through rectangular ducts," *International Communications in Heat and Mass Transfer*, vol. 21, pp. 469–475, 1994.

[65] A. Shercliff, "Steady motion of conducting fluids in pipes under transverse magnetic fields," *Proc. Cam. Phil. Soc.*, vol. 49, pp. 136–144, 1953.

[66] L. Dragos, *Magnetofluid dynamics*, Abacus Press, 1975.

[67] F. Ham, K. Mattson, G. Iaccarino, and P. Moin, "Towards time-stable and accurate LES on unstructured grids," *Lect. Notes Comput. Sci. Eng.*, vol. 56, pp. 235–250, 2007.

[68] K. Mahesh, G. Constantinescu, and P. Moin, "A numerical method for large eddy simulation in complex geometries," *J. Comput. Phys.*, vol. 197, pp. 263–286, 215-240.

[69] F. H. Harlow and J. E. Welch, "Numerical calculation of time-dependent viscous incompressible flow of fluids with free surfaces," *Phys. Fluids*, vol. 8, pp. 2182–2189, 1965.

[70] C. M. Rhie and W. L. Chow, "A numerical study of the turbulent flow past an isolated airfoil with trailing edge separation," *J. AIAA*, vol. 21, pp. 1525–1532, 1983.

[71] F. Ham and G. Iaccarino, "Energy conservation in collocated discretization schemes on unstructured meshes," Annual Research Briefs, Center for Turbulence Research, Stanford University/NASA Ames, 2004.

[72] X. Albets-Chico, H. Radhakrishnan, S. Kassinos, and B. Knaepen, "Numerical simulation of a liquid-metal flow in a poorly conducting pipe subjected to a strong fringing magnetic field," *Phys. Fluids*, vol. 23, pp. 047101, 2011.

[73] F. Ham, K. Mattson, and G. Iaccarino, "Accurate and stable finite volume operators for unstructured flow solvers," Annual Research Briefs, Center for Turbulence Research, Stanford University/NASA Ames, 2006.

[74] M.-J. Ni, R. Munipalli, N.B. Morley, P.Y. Huang, and M. Abdou, "A current density conservative scheme for MHD flows at a low magnetic Reynolds number. Part I: On a rectangular collocated grid system," *J. Comput. Phys.*, vol. 227, pp. 174–204, 2007.

[75] M.-J. Ni, R. Munipalli, P.Y. Huang, N.B. Morley, and M. Abdou, "A current density conservative scheme for incompressible MHD flows at a low magnetic Reynolds number. Part II: On an arbitrary collocated mesh," *J. Comput. Phys.*, vol. 227, pp. 205–228, 2007.

[76] R. Courant, K. O. Friedrichs, and H. Lewy, "Uber die partiellen differenzengleichungen der mathematisches physik," *Math. Ann.*, vol. 100, pp. 32–74, 1928.

[77] A. J. Chorin, “A numerical method for solving incompressible viscous flow problems,” *J. Comput. Phys.*, vol. 2, pp. 12–26, 1967.

[78] J. Kim and P. Moin, “Application of a fractional-step method to incompressible Navier-Stokes equations,” *J. Comput. Phys.*, vol. 59, pp. 308–323, 1985.

[79] N. Kanaris, D. Grigoriadis, and S. Kassinos, “Three dimensional flow around a confined circular cylinder,” *Phys. Fluids*, vol. 23, pp. 064106, 2011.

[80] A. Sohankar, C. Norberg, and L. Davidson, “Low-Reynolds-number flow around a square cylinder at incidence: study of blockage, onset of vortex shedding and outlet boundary condition,” *International J. Numer. Meth. Fluids*, vol. 26, pp. 39–56, 1998.

[81] P. D. Welch, “The use of fast Fourier transform for the estimation of power spectra: A method based on time averaging over short, modified periodograms,” *IEEE Trans. Audio Electroacoust.*, vol. 15, pp. 70–73, 1967.

[82] A. Sohankar, C. Norberg, and L. Davidson, “Simulation of three-dimensional flow around a square cylinder at moderate Reynolds numbers,” *Phys. Fluids*, vol. 11, pp. 288–306, 1999.

[83] J. Jeong and F. Hussain, “On the identification of a vortex,” *J. Fluid Mech.*, vol. 285, pp. 69–94, 1995.

[84] D. Barkley, L. S. Tuckerman, and M. S. Golubitsky, “Bifurcation theory for three-dimensional flow in the wake of a circular cylinder,” *Phys. Rev. E*, vol. 61, pp. 5247–5252, 2000.

[85] U. Schumann, “Numerical simulation of the transition from three- to two-dimensional turbulence under a uniform magnetic field,” *J. Fluid Mech.*, vol. 74, pp. 31–58, 1976.

[86] A. Viré, D. Krasnov, T. Boeck, and B. Knaepen, “Modeling and discretization errors in large eddy simulations of hydrodynamic and magnetohydrodynamic channel flows,” *J. Comput. Phys.*, vol. 230, pp. 1903–1922, 2011.

[87] S. Vantieghem, X. Albets-Chico, and B. Knaepen, “The velocity profile of laminar MHD flows in circular conducting pipes,” *Theor. Comput. Fluid Dyn.*, vol. 23, pp. 525–533, 2009.

[88] G. Mutschke, G. Gerbeth, V. Shatrov, and A. Tomboulides, “The scenario of three-dimensional instabilities of the cylinder wake in an external magnetic field:A linear stability analysis,” *Phys. Fluids*, vol. 13, 2001.

[89] B. Pier, “On the frequency selection of finite-amplitude vortex shedding in the cylinder wake,” *J. Fluid Mech.*, vol. 458, pp. 407–417, 2002.

[90] F. Giannetti and P. Luchini, “Structural sensitivity of the first instability of the cylinder wake,” *J. Fluid Mech.*, vol. 581, pp. 167–197, 2007.

[91] V. Dousset and A. Pothérat, “Characterization of the flow past a truncated square cylinder in a duct under a spanwise magnetic field,” *J. Fluid Mech.*, vol. 691, pp. 341–367, 2012.

[92] H. F. Wang, Y. Zhou, C. K. Chan, and K. S. Lam, “Effect of initial conditions on interaction between a boundary layer and a wall-mounted finite-lenght-cylinder wake,” *Phys. Fluids*, vol. 18, pp. 065106, 2006.

[93] D. D. Papailiou, “Magneto-fluid-mechanic turbulent vortex streets,” in *Fourth Beer-Sheva Seminar on MHD Flows and Turbulence*, 1984, pp. 152–173.

[94] C. H. Chyu and D. Rockwell, “Near-wake structure of an oscillating cylinder: Effect of controlled shear-layer vortices,” *J. Fluid Mech.*, vol. 322, pp. 21–49, 1996.

[95] A. Prasad and C. H. K. Williamson, “The instability of the shear layer separating from a bluff body,” *J. Fluid Mech.*, vol. 333, pp. 375–402, 1997.

[96] A. G. Kravchenko and P. Moin, “Numerical studies of flow over a circular cylinder at Re_D=3900,” *Phys. Fluids*, vol. 12, pp. 403–417, 2000.

[97] L. S. G. Kovasznay, “Hot-wire investigation of the wake behind cylinders at low Reynolds numbers,” *Proc. R. Soc. Lond. A*, vol. 198, pp. 174–190, 1949.

[98] A. Alemany, R. Moreau, P. L. Sulem, and U. Frisch, “Influence of an external magnetic field on homogeneous MHD turbulence,” *J. Méc.*, vol. 18, pp. 273–313, 1979.

Appendix A

Software Development

Although CDP has the potential to deal with the problems under consideration in this thesis, it had to be further developed in order to simulate and analyze in detail the flows of interest. For this reason we additionally developed routines and modules, which allowed simulations and analysis of flow around a confined cylinder in a channel and a rectangular duct. The implemented modules can produce quantities and parameters characterizing the flow such as the lift/drag coefficients, wall shear stresses etc.

In order to meet the objectives of this thesis a parallel implementation of the developed software is required. All the modules were designed and developed for parallel execution using Fortran 90/95 and the Message Passing Interface (MPI), a library specification for message passing. The developed routines and modules used in this thesis are shown below.

A.1 Modified hooks file

```
subroutine register_hook(if2)

  use if2_defs_m
  use misc_tools_m ! for VORT, CFL - see below
  use param_m
  use if_qs_m          ! MHD

  implicit none

  type(if2_t), intent(inout) :: if2

  ! ------------------------------------

  real(WP),dimension(:),pointer :: wall_shear,tke
```

```
  logical :: solve_mhd

  ! ------------------------------------------------

  if (myrank == 0) &
       write(*,*) 'register_hook...'

  ! add your own data here...
  if (get_logical_param('CALCULATE_WALL_SHEAR_TKE',default=.FALSE.)) then
    NULLIFY(wall_shear); call register_r1(wall_shear,'WALL_SHEAR',NO_DATA
         ,if2%gp,readwrite_flag=.TRUE.)
    NULLIFY(tke); call register_r1(tke,'TKE',NO_DATA,if2%gp,
         readwrite_flag=.TRUE.)
  end if

  ! if using misc_tools_m...
  if (get_logical_param('CALCULATE_VORT',default=.FALSE.)) &
       call register_VORT(if2%gp)
  if (get_logical_param('CALCULATE_LAMBDA2',default=.FALSE.)) &
       call register_LAMBDA2(if2%gp)

  ! get the step interval for dumping profiles
  ! quasi-static initialization...
  if (get_logical_param('SOLVE_MHD',default=.FALSE.)) then
    call init_qs(if2)
  end if

end subroutine register_hook

subroutine initial_hook(if2)

  use if2_defs_m
  use gp_func_m
  use param_m
  use global_m              ! to use pi
  use cdp_if2_hooks_m       ! calc_max_velocity_volume

  implicit none

  type(if2_t), intent(inout), target :: if2

  ! ------------------------------------------------

  type(gp_t), pointer :: gp
  real(WP) :: x(3),u(3),&
       HEIGHT,WIDTH,RADIUS,          &
       B0Z,SIGMA_REF,Ha,TOL,         &          ! parameters for MHD profile
       lambda_n,p1_n,p2_n,k_n,       &          ! coefficients for MHD profile
```

```
       y_star,z_star,                 &
       f_n,f1_n,u_n,                  &              ! MHD profile
       u_add,my_max_u_add,max_u_add,        &        ! MHD profile
       mean_velocity(3),max_velocity(3), &           ! scaling
       U_TARGET,U_scaling_coeff                      ! scaling
logical :: adjust_bulk_velocity
!real(WP), pointer :: phi(:)
integer :: ino,n,ierr,          &
       INITIAL_BULK_PROFILE
real(WP) :: HARVEST

! ---------------------------------------

if (myrank == 0) &
     write(*,*) 'initial_hook...'

gp => if2%gp
! phi => get_r1('PHI',gp)

if (if2%step == 0) then
  ! get parameters of geometry
  HEIGHT = get_real_param('HEIGHT',default=1.0_WP)
  WIDTH = get_real_param('WIDTH',default=1.0_WP)
  RADIUS = get_real_param('RADIUS',default=1.0_WP)
  ! get initial conditions for bulk flow
  INITIAL_BULK_PROFILE = get_integer_param('INITIAL_BULK_PROFILE',
      default=0)

  select case(INITIAL_BULK_PROFILE)
  ! ...for plug flow
  case(1)
    if (myrank == 0) &
         write(*,*) '␣>␣applying␣initial␣velocity␣in␣x␣direction'
    do ino = 1,gp%nno_ib
      if2%u(1,ino) = 1.0_WP
      if2%u(2:3,ino) = 0.0_WP
      if2%p(ino) = 0.0_WP
    end do
  ! ..for channel (poiseuille flow)
  case(2)
    if (myrank == 0) &
         write(*,*) '␣>␣applying␣initial␣parabolic␣velocity␣profile␣
             along␣channel'
    do ino = 1,gp%nno_ib
      if2%u(1,ino) = (3.0_WP/2.0_WP)*( 1.0_WP-( gp%node_cc(2,ino)/(
          HEIGHT/2.0_WP) )**2 )
      if2%u(2:3,ino) = 0.0_WP
      if2%p(ino) = 0.0_WP
```

```
    end do
  ! ..for channel (poiseuille flow) with SPANWISE NOISE
  case(3)
    if (myrank == 0) &
          write(*,*) '␣>␣applying␣initial␣parabolic␣velocity␣profile␣
              along␣channel␣with␣SPANWISE␣NOISE'
    do ino = 1,gp%nno_ib
      if2%u(1,ino) = (3.0_WP/2.0_WP)*( 1.0_WP-( gp%node_cc(2,ino)/(
          HEIGHT/2.0_WP) )**2 )
      if2%u(2,ino) = 0.0_WP
      call random_number(HARVEST)
      if2%u(3,ino) = HARVEST*0.0001_WP
      if2%p(ino) = 0.0_WP
    end do
  ! ...for duct (two parabolas)
  case(4)
    if (myrank == 0) &
          write(*,*) '␣>␣applying␣initial␣parabolic␣velocity␣profile␣
              along␣duct'
    do ino = 1,gp%nno_ib
      if2%u(1,ino) = (9.0_WP/4.0_WP)*( 1.0_WP-( gp%node_cc(2,ino)/(
          HEIGHT/2.0_WP) )**2 )*  &
            ( 1.0_WP-( gp%node_cc(3,ino)/(WIDTH/2.0_WP) )**2 )
      if2%u(2:3,ino) = 0.0_WP
      if2%p(ino) = 0.0_WP
    end do
  ! ...MHD Duct flow,
  case(5)
    if (myrank == 0) &
          write(*,*) '␣>␣applying␣initial␣velocity␣profile␣along␣duct␣
              for␣MHD␣flow'
    do ino = 1,gp%nno_ib
      if2%u(1:3,ino) = 0.0_WP
      if2%p(ino) = 0.0_WP
    end do
    ! calculate Hartman number...
    ! ...characteristic length is along B direction / 2
    B0Z = get_real_param('B0Z',default=0.0_WP)
    SIGMA_REF = get_real_param('SIGMA_REF',default=0.0_WP)
    Ha = (WIDTH/2.0_WP)*B0Z*sqrt(SIGMA_REF/if2%constant_nu)

    TOL = 2e-7
    my_max_u_add = 1.0_WP       !
    max_u_add    = 1.0_WP       ! to enter loop
    n = -1                      ! to start with n=1 when enter the loop

    do while (( max_u_add>TOL ).AND.( n<20000 ))
      n = n+2                 ! n corresponds to 1,3,5,... for Sum
```

```
      ! calculate coefficients
      lambda_n = REAL(n)*pi/( 2.0_WP*(HEIGHT/WIDTH) )
      p1_n = 0.5_WP*( Ha -sqrt( Ha**2 +4.0_WP*lambda_n**2 ) )
      p2_n = 0.5_WP*( Ha +sqrt( Ha**2 +4.0_WP*lambda_n**2 ) )
      k_n  = 2.0_WP*sin( lambda_n*HEIGHT/WIDTH  )/( lambda_n*HEIGHT/
           WIDTH )

      my_max_u_add = 0.0_WP  ! reset max value to zero

      do ino = 1,gp%nno_ib
         ! create non-dimensional dimensions of duct
         ! NOTE: y is normal to B, and z is aligned with B
         y_star = gp%node_cc(2,ino)/(WIDTH/2)    ! -H/W < y* < H/W
         z_star = gp%node_cc(3,ino)/(WIDTH/2)    ! -1   < z* < 1

         f_n  = sinh( p2_n )*cosh( p1_n*z_star ) -sinh( p1_n )*cosh(
               p2_n*z_star )
         f1_n = sinh( p2_n-p1_n )
         !!f1_ii = alpha2_ii*cosh( p1_ii*WIDTH/2.0_WP ) - alpha1_ii*cosh
               ( p2_ii*WIDTH/2.0_WP )
         u_n = ( k_n/(lambda_n**2) )*( 1.0_WP - f_n/f1_n )

         u_add = u_n*cos( lambda_n*y_star )
         ! analytical value of velocity = sum of all parts of expansion
         if2%u(1,ino) = if2%u(1,ino)+u_add
         ! check convergence
         my_max_u_add = max( u_add,my_max_u_add )
      end do

      call MPI_ALLREDUCE(my_max_u_add,max_u_add,1,MPI_REAL_WP,MPI_MAX,
           mycomm,ierr)

      if (myrank == 0) &
              write(*,*) '␣>␣loop',n,'␣max_u_add',max_u_add
   end do
! ..for pipe (Hagen-Poiseuille flow)
case(6)
   if (myrank == 0) &
           write(*,*) '␣>␣applying␣initial␣parabolic␣velocity␣profile␣
                along␣pipe'
   do ino = 1,gp%nno_ib
      if2%u(1,ino) = 2.0_WP*( 1.0_WP -(gp%node_cc(2,ino)**2+gp%node_cc
          (3,ino)**2)/(RADIUS**2) )
      if2%u(2:3,ino) = 0.0_WP
      if2%p(ino) = 0.0_WP
   end do
! ..for pipe (Hagen-Poiseuille flow) with SPANWISE NOISE
```

```
! NOISE = 20% of streamwise velocity
case(7)
  if (myrank == 0) &
       write(*,*) '␣>␣applying␣initial␣parabolic␣velocity␣profile␣along␣pipe␣with␣SPANWISE␣NOISE'
  do ino = 1,gp%nno_ib
    if2%u(1,ino) = 2.0_WP*( 1.0_WP -(gp%node_cc(2,ino)**2+gp%node_cc(3,ino)**2)/(RADIUS**2) )
    if2%u(2,ino) = 0.0_WP
    call random_number(HARVEST)
    if2%u(3,ino) = HARVEST*0.20_WP*if2%u(1,ino)
    if2%p(ino) = 0.0_WP
  end do
! ...zero everywhere
case default
  if (myrank == 0) &
       write(*,*) '␣>␣starting␣with␣ZERO␣velocity␣everywhere'
  do ino = 1,gp%nno_ib
    if2%u(1:3,ino) = 0.0_WP
    if2%p(ino) = 0.0_WP
  end do
end select

! ——— SCALING ———
!
! Calculate coefficient for VELOCITY scaling
call calc_mean_max_axial_velocity_volume(mean_velocity,max_velocity,if2)

if (get_logical_param('ADJUST_MEAN_VELOCITY',default=.FALSE.)) then
  adjust_bulk_velocity = .TRUE.
  U_TARGET = get_real_param('U_MEAN_TARGET',default=1.0_WP)
  U_scaling_coeff = U_TARGET/mean_velocity(1)
  if (myrank == 0) &
       write(*,*) '␣␣␣>␣adjust␣mean␣velocity...␣scaling␣coeff.:␣', U_scaling_coeff
else if (get_logical_param('ADJUST_MAX_VELOCITY',default=.FALSE.)) then
  adjust_bulk_velocity = .TRUE.
  U_TARGET = get_real_param('U_MAX_TARGET',default=1.0_WP)
  U_scaling_coeff = U_TARGET/max_velocity(1)
  if (myrank == 0) &
       write(*,*) '␣␣␣>␣adjust␣max␣velocity...␣scaling␣coeff.:␣', U_scaling_coeff
else
  adjust_bulk_velocity = .FALSE.
  if (myrank == 0) &
       write(*,*) '␣␣␣>␣NOTE:␣No␣scaling␣of␣velocity'
```

```
    end if

    ! SCALE VELOCITY profile
    if (adjust_bulk_velocity) then
      do ino = 1,gp%nno_ib
        if2%u(1,ino) = if2%u(1,ino)*U_scaling_coeff
        if2%u(3,ino) = if2%u(3,ino)*U_scaling_coeff
      end do

      call calc_mean_max_axial_velocity_volume(mean_velocity,max_velocity
          ,if2)
    end if

  end if

end subroutine initial_hook

subroutine scalar_bc_hook(phi_bc,bc_type,scalar,zone,if2)

  use if2_defs_m

  implicit none

  real(WP), pointer :: phi_bc(:)
  integer, intent(out) :: bc_type
  type(scalar_t), intent(in) :: scalar
  type(zone_t), intent(in) :: zone
  type(if2_t), intent(inout), target :: if2

  ! ---------------------------------------

  ! ---------------------------------------

  write(*,*) 'Error:␣called␣scalar_bc_hook␣for␣scalar:␣', &
       trim(scalar%name),'␣zone:␣',trim(zone%name)
  call graceful_exit(0)

end subroutine scalar_bc_hook

subroutine scalar_source_hook(Ap,bp,scalar,if2)

  ! -----------------------------------------------------------------
  ! modify the scalar system with a source if you want to:
  ! [Ap]{phi} = {bp}
  ! NOTE that bp is now a RHS vector
  ! -----------------------------------------------------------------

  use if2_defs_m
```

```fortran
  implicit none

  real(WP), intent(inout) :: Ap(:),bp(:)
  type(scalar_t), intent(in) :: scalar
  type(if2_t), intent(inout) :: if2

  ! ----------------------------------------

  if (myrank == 0) &
       write(*,'(3a)') '␣␣>␣scalar_source_hook:␣"',trim(scalar%name),'
          "...'

end subroutine scalar_source_hook

subroutine momentum_bc_hook(u_bc,bc_type,zone,if2)

  use if2_defs_m
  use param_m
  use cdp_if2_hooks_m      ! read_velocity_profile
  use global_m             ! to use pi

  implicit none

  real(WP), pointer :: u_bc(:,:)
  integer, intent(out) :: bc_type
  type(zone_t), intent(in) :: zone
  type(if2_t), intent(inout), target :: if2

  ! ----------------------------------------

  type(gp_t), pointer :: gp
  integer :: i,ino,ierr,      &
       INLET_PROFILE,          &
       TRANC_EXP,p,q,m,n
  real(WP) :: x(3),tmp,u(3),nu,                  &
       U_MEAN_TARGET,HEIGHT,WIDTH,RADIUS,       &
       factor1,factor2,y_shifted,z_shifted,     &
       sin_my,sin_nz, &
       HARVEST, &
       B0Z,SIGMA_REF,Ha,TOL,        &       ! parameters for MHD profile
       lambda_n,p1_n,p2_n,k_n,      &       ! coefficients for MHD profile
       y_star,z_star,               &
       f_n,f1_n,u_n,                &       ! MHD profile
       u_add,my_max_u_add,max_u_add         ! MHD profile
  real(WP), allocatable, save :: ux_bc_stored(:)
  logical, save :: first = .TRUE.
```

```
! ------------------------------------------

gp => if2%gp

if ((zone%name == 'inlet').OR.(zone%name == 'INLET')) then

   ! READ INLET FROM FILE...
   if (get_logical_param('READ_PROFILE',default=.FALSE.)) then

      call read_velocity_profile(u_bc,zone,if2)

   ! OR DEFINE EQUATION...
   else

      ! get parameters of geometry and mean velocity at inlet
      HEIGHT = get_real_param('HEIGHT',default=1.0_WP)
      WIDTH = get_real_param('WIDTH',default=1.0_WP)
      RADIUS = get_real_param('RADIUS',default=1.0_WP)
      U_MEAN_TARGET = get_real_param('U_MEAN_TARGET',default=1.0_WP)

      ! get desired inlet velocity profile
      INLET_PROFILE = get_integer_param('INLET_PROFILE',default=0)

      select case(INLET_PROFILE)
      ! Plug flow
      case(1)
         do i = 1,zone%n_nodelist
            ino = zone%nodelist(i)
            u_bc(1:3,ino) = (/ 1.0_WP, 0.0_WP, 0.0_WP /)
         end do

      ! Plane Poiseuille flow
      case(2)
         do i = 1,zone%n_nodelist
            ino = zone%nodelist(i)
            u_bc(1,ino) = (3.0_WP/2.0_WP)*U_MEAN_TARGET* &
                  ( 1.0_WP-( gp%node_cc(2,ino)/(HEIGHT/2.0_WP) )**2 )
            u_bc(2:3,ino) = 0.0_WP
         end do

      ! Plane Poiseuille flow with Spanwise Disturbances (order e-4)
      case(3)
         do i = 1,zone%n_nodelist
            ino = zone%nodelist(i)
            u_bc(1,ino) = (3.0_WP/2.0_WP)*U_MEAN_TARGET* &
                  ( 1.0_WP-( gp%node_cc(2,ino)/(HEIGHT/2.0_WP) )**2 )
            u_bc(2,ino) = 0.0_WP
            call random_number(HARVEST)
```

```
    u_bc(3,ino) = HARVEST*0.0001_WP
  end do

! Duct flow,
case(4)
  if (first .EQV. .TRUE. ) then

    ! create dummy array to store velocity after reading
    if (.NOT. allocated (ux_bc_stored) ) allocate (ux_bc_stored(
       zone%n_nodelist))

    ux_bc_stored(:) = 0.0_WP

    do i = 1,zone%n_nodelist
      ino = zone%nodelist(i)

      ! set truncation error for the expansion
      TRANC_EXP = 10

      ! sum over the order of the expansion
      factor1 = 16.0_WP/if2%constant_nu/(pi**4.0_WP)
      do p = 0,TRANC_EXP
        m = 2*p+1
        do q = 0,TRANC_EXP
          n = 2*q+1
          factor2 = factor1/( 1.0_WP*m*n*((m**2/WIDTH**2) + (n**2/
             HEIGHT**2)) )
          ! analytical solution is for y,z at corner of duct
          ! ...so if coordinates are at center must be moved
          y_shifted = gp%node_cc(2,ino)+(HEIGHT/2.0_WP)
          z_shifted = gp%node_cc(3,ino)+(WIDTH/2.0_WP)
          sin_my = sin( m*pi*y_shifted/HEIGHT )
          sin_nz = sin( n*pi*z_shifted/WIDTH )
          ux_bc_stored(i) = ux_bc_stored(i) + factor2*sin_my*sin_nz
        end do
      end do

    end do   ! loop over inlet nodes

    first = .FALSE.
  end if

  ! define u_bc for inlet
  do i=1,zone%n_nodelist
    ino = zone%nodelist(i)
    u_bc(1,ino) = ux_bc_stored(i)
    u_bc(2:3,ino) = 0.0_WP
  end do
```

```
! MHD Duct flow,
case(5)

  ! calculate Hartman number...
  ! ...characteristic length is along B direction / 2
  B0Z = get_real_param('B0Z',default=0.0_WP)
  SIGMA_REF = get_real_param('SIGMA_REF',default=0.0_WP)
  Ha = (WIDTH/2.0_WP)*B0Z*sqrt(SIGMA_REF/if2%constant_nu)
  if (myrank == 0) &
       write(*,*) '␣>␣Ha␣number␣based␣on␣half␣width␣=', Ha

  ! compute analytic profile only for first iteration
  if (first .EQV. .TRUE.) then

    ! create dummy array to store velocity after reading
    if (.NOT. allocated (ux_bc_stored) ) allocate (ux_bc_stored(zone%n_nodelist))

    ux_bc_stored(:) = 0.0_WP
    !TOL = 10e-8
    TOL = get_real_param('TOL',default=5.0E-8_WP)
    my_max_u_add = 1.0_WP      !
    max_u_add    = 1.0_WP      ! to enter loop
    n = -1                     ! to start with n=1 when enter the loop

    do while (( max_u_add>TOL ).AND.( n<20000 ))

      n = n+2                  ! n corresponds to 1,3,5,... for Sum

      ! calculate coefficients
      lambda_n = REAL(n)*pi/( 2.0_WP*(HEIGHT/WIDTH) )
      p1_n = 0.5_WP*( Ha -sqrt( Ha**2 +4.0_WP*lambda_n**2 ) )
      p2_n = 0.5_WP*( Ha +sqrt( Ha**2 +4.0_WP*lambda_n**2 ) )
      k_n  = 2.0_WP*sin( lambda_n*HEIGHT/WIDTH )/( lambda_n*HEIGHT/WIDTH )

      my_max_u_add = 0.0_WP  ! reset max value to zero

      do i = 1,zone%n_nodelist
        ino = zone%nodelist(i)

        ! create non-dimensional dimensions of duct
        ! NOTE: y is normal to B, and z is aligned with B
        y_star = gp%node_cc(2,ino)/(WIDTH/2)    ! -H/W < y* < H/W
        z_star = gp%node_cc(3,ino)/(WIDTH/2)    ! -1   < z* < 1
```

```
        f_n  = sinh( p2_n )*cosh( p1_n*z_star ) -sinh( p1_n )*cosh(
             p2_n*z_star )
        f1_n = sinh( p2_n-p1_n )
        !!f1_ii = alpha2_ii*cosh( p1_ii*WIDTH/2.0_WP ) - alpha1_ii*
            cosh( p2_ii*WIDTH/2.0_WP )
        u_n = ( k_n/(lambda_n**2) )*( 1.0_WP - f_n/f1_n )

        u_add = u_n*cos( lambda_n*y_star )
        ! analytical value of velocity = sum of all parts of
            expansion
        ux_bc_stored(i) = ux_bc_stored(i)+u_add
        ! check convergence
        my_max_u_add = max( u_add,my_max_u_add )
      end do

      call MPI_ALLREDUCE(my_max_u_add,max_u_add,1,MPI_REAL_WP,
         MPI_MAX,mycomm,ierr)

      if (myrank == 0) &
           write(*,*) '␣>␣loop',n,'␣max_u_add',max_u_add

    end do   ! loop over inlet nodes

    first = .FALSE.
  end if

  ! define u_bc for inlet
  do i=1,zone%n_nodelist
    ino = zone%nodelist(i)
    u_bc(1,ino) = ux_bc_stored(i)
    u_bc(2:3,ino) = 0.0_WP
  end do

! Laminar Pipe (Hagen-Poiseuille flow)
case(6)
  do i = 1,zone%n_nodelist
    ino = zone%nodelist(i)
    u_bc(1,ino) = 2.0_WP*U_MEAN_TARGET* &
         ( 1.0_WP -(gp%node_cc(2,ino)**2+gp%node_cc(3,ino)**2)/(
            RADIUS**2) )
    u_bc(2:3,ino) = 0.0_WP
  end do

case default
  write(*,*) 'Error:␣momentum_bc_hook␣equation␣not␣set␣up␣for␣zone:
      ␣', &
       trim(zone%name)
  call graceful_exit(0)
```

```
      end select

    end if
    bc_type = INJECT_BC

    ! scale velocity at inlet profile
    call inlet_velocity_scaling(u_bc,zone,if2)

  else
     write(*,*) 'Error:␣momentum_bc_hook␣not␣set␣up␣for␣zone:␣', &
          trim(zone%name)
     call graceful_exit(0)
  end if

end subroutine momentum_bc_hook

subroutine momentum_source_hook(Au,bu,if2)

  ! -------------------------------------------------------------
  ! modify the momentum system with a source if you want to:
  ! [Au]{u} = {bu}
  ! NOTE that bu is now a RHS vector
  ! -------------------------------------------------------------

  use if2_defs_m
  use param_m
  use cdp_if2_hooks_m      ! inlet_convergence
  use if_qs_m              ! MHD
 ! use my_data_m

  implicit none

  real(WP), intent(inout) :: Au(:,:),bu(:,:)
  type(if2_t), intent(inout) :: if2

  ! -------------------------------------

  if (myrank == 0) &
       write(*,*) '␣>␣momentum_source_hook...'

  ! for channel, apply a negative pressure gradient - so on the
  ! RHS this is a positive source of momentum...
  if (get_logical_param('FORCE_FLOW',default=.FALSE.)) then
    if (myrank == 0) &
         write(*,*) 'applying␣turbulent␣channel␣forcing...'

    call pressure_gradient_controller(bu,if2)
```

```
    call check_inlet_convergence(bu,if2)

  end if

  ! Add Lorentz force (MHD)
  if (get_logical_param('SOLVE_MHD',default=.FALSE.)) then
    call coulomb_source(if2, bu)
  end if

end subroutine momentum_source_hook

subroutine temporal_hook(if2)

  use cdp_if2_hooks_m       ! output_velocity_profile / calc_drag
  use if2_defs_m
  use param_m
  use misc_tools_m
  !use gp_io_new_m
  !use gp_func_m

  implicit none

  type(if2_t), intent(inout) :: if2

  ! ------------------------------------------

  !character(len=64) :: filename
  real(WP) :: gwss,gtke,xcut
  logical, save :: first = .TRUE.

  ! ------------------------------------------

  if (myrank == 0) &
       write(*,*) 'temporal_hook...'

  ! ------------------------------------------------------------
  ! get parameters from file 'cdp_if2.in'...
  ! ...to decide what subroutines to use
  ! ------------------------------------------------------------
  if (get_logical_param('EXTRACT_PROFILE',default=.FALSE.)) then
    if (MOD(if2%step,20000) == 0) &
         call extract_velocity_profile(if2)
  end if

  if (get_logical_param('CALCULATE_DRAG',default=.FALSE.)) &
       call calc_drag(if2)

  if (get_logical_param('CALCULATE_DRAG_SLICES',default=.FALSE.)) &
```

```
       call calc_drag_slices(if2)

  if (get_logical_param('CALCULATE_WALL_SHEAR_TKE',default=.FALSE.)) then
    xcut = 60.0_WP ! For the aneurysm geometry

    !call get_dump_bounds(if2,xmin,xmax)
    call calc_shear_wall(if2,gwss)
    call calc_global_total_ke(if2,xcut,gtke)

    ! Write data to file
    if (myrank == 0) then
      write(*,*) '␣>␣global␣wall␣shear␣stress␣', gwss
      write(*,*) '␣>␣global␣total␣kinetic␣energy␣', gtke

      ! only first time write header to file
      if (first) then
        open (145,FILE="stationary.dat",STATUS='unknown',ACTION='
            readwrite',POSITION='append')
        write (145,*) 'var␣=␣"ite","time","gWSS",␣"gTKE"'
        close (145)
        first = .FALSE.
      end if

      open(145,FILE="stationary.dat",STATUS='UNKNOWN',ACTION='READWRITE',
         POSITION='APPEND')
      write(145,'(i8,2x,e12.6,2x,e12.6,2x,e12.6)'),if2%step,if2%time,gwss
         ,gtke
      close(145)
    end if
  end if

  ! if using misc_tools_m...
  if (get_logical_param('CALCULATE_VORT',default=.FALSE.)) &
       call update_VORT(if2%u,if2%gp)
  if (get_logical_param('CALCULATE_LAMBDA2',default=.FALSE.)) &
       call update_LAMBDA2(if2%u,if2%gp)

end subroutine temporal_hook

subroutine final_hook(if2)

  use if2_defs_m

  implicit none

  type(if2_t), intent(inout) :: if2

  ! ------------------------------------
```

```
  ! ------------------------------------------------------------

  if (myrank == 0) &
       write(*,*) 'final_hook...'

end subroutine final_hook

subroutine init_b0_hook(if2)
  ! MHD
  use global_m ! for main_ts_loop_index
  use if2_defs_m
  use iqs_defs_m
  use if_qs_m
  use param_m

  implicit none

  ! ------------------------------------------------------------

  type(if2_t), intent(inout), target :: if2
  real(WP) :: &
       x(3),set_position,  &
       b0x,b0y,b0z,        &
       SIGMA,WIDTH,Haw
  integer :: ino

  ! ------------------------------------------------------------

  if (myrank == 0) &
         write(*,*) 'hook,␣setting␣up␣the␣magnetic␣field...CNT'

  b0x = get_real_param('B0X',default=0.0_WP)
  b0y = get_real_param('B0Y',default=0.0_WP)
  b0z = get_real_param('B0Z',default=0.0_WP)

  if (myrank == 0) &
          write(*,*) 'setting␣up␣the␣magnetic␣field...'

  do ino = 1,if2%gp%nno_ib

    x(1:3) = if2%gp%node_cc(1:3,ino)

    set_position=(x(1)-0.0_WP)

    bc0(1,ino) = b0x
    bc0(2,ino) = b0y
    bc0(3,ino) = b0z
```

```
  end do

  if (myrank == 0) then
    SIGMA     = get_real_param('SIGMA_REF',default=0.0_WP)
    WIDTH = get_real_param('WIDTH',default=0.0_WP)
    Haw = 1.0_WP*WIDTH*b0z*sqrt( SIGMA/if2%constant_nu )

    open (50,FILE='INFO-flow_params.dat',status='unknown',action='write',
        position='APPEND')
    write(50,*)
    write(50,*) '␣>␣MHD_PARAMETERS...'
    write(50,'(␣5(2X,A16)␣)') 'B0X', 'BOY', 'BOZ' ,'SIGMA','Ha_w'
    write(50,'(␣5(2X,G16.8)␣)') b0x, b0y, b0z, SIGMA, Haw
    close (50)
  end if

end subroutine init_b0_hook
```

A.2 Developed module

```
module cdp_if2_hooks_m

  use if2_defs_m          ! type if2_t

contains

  subroutine calc_mean_max_velocity_face(mean_velocity,max_velocity,if2)

    use gp_defs_m

    implicit none

    real(WP), intent(out) :: mean_velocity(1:3),max_velocity(1:3)
    type(if2_t), intent(inout), target :: if2

    ! ------------------------------------------

    type(gp_t), pointer :: gp
    type(zone_t), pointer :: zone
    real(WP) :: &
      area_of_node_at_face, &    ! area of node at face
      my_face_area,         &    ! area of face for each processor (local)
      my_mass_flow(3),      &    ! q = v.dA , for each proseccor (local)
      face_area,            &    ! area of all face (global)
```

```
    mass_flow(3),          &    ! Q = Sum{q} , over the whole face (
        global)
    my_max_velocity(3)
  integer :: i, ino, ierr, &
    ino_first,ino_last

  ! ----------------------------------------

  if (myrank == 0) &
        write(*,*) '␣␣>␣calc_mean_and_max_velocity␣for␣face␣inlet...'

  !
     -------------------------------------------------------------------------------

  ! loop through zones until zone is INLET
  !
     -------------------------------------------------------------------------------

  zone => if2%gp%first_zone_ptr

  do while (associated(zone))
    if ((zone%name == 'inlet').OR.(zone%name == 'INLET')) then

      ! ---------------------------------
      ! calculate mean velocity
       my_face_area       = 0.0_WP
       my_mass_flow(1:3)  = 0.0_WP
       face_area          = 0.0_WP
       mass_flow(1:3)     = 0.0_WP

       ! find "mass flow" and "area of face" locally
       do i = 1,zone%n_nodelist
         ino = zone%nodelist(i)

         my_mass_flow(1:3) = my_mass_flow(1:3) +  &
              dot_product( if2%u_bc(1:3,ino),-zone%no_local_normal(1:3,i
                  ) )

         area_of_node_at_face = sqrt( zone%no_local_normal(1,i)**2 +  &
              zone%no_local_normal(2,i)**2 + zone%no_local_normal(3,i)
                  **2 )
         my_face_area = my_face_area + area_of_node_at_face

       end do

       ! SUM "mass flow" and "face volume" from all processors
       ! 'AllReduce' sends back the result to all processors
```

```
      call MPI_AllReduce(my_face_area,face_area,1,MPI_REAL_WP,MPI_SUM,
         mycomm,ierr)
      call MPI_AllReduce(my_mass_flow,mass_flow,3,MPI_REAL_WP,MPI_SUM,
         mycomm,ierr)

      mean_velocity(1:3) = mass_flow(1:3) / face_area

      ! ----------------------------
      ! calc max velocity
      my_max_velocity(1:3) = 0.0_WP
      max_velocity(1:3)    = 0.0_WP
      if (.NOT.(zone%n_nodelist==0)) then
        ino_first = zone%nodelist(1)
        ino_last  = zone%nodelist(zone%n_nodelist)
        do i = 1,3
          my_max_velocity(i) = maxval( if2%u_bc(i,ino_first:ino_last) )
        end do
      end if
      call MPI_AllReduce(my_max_velocity,max_velocity,3,MPI_REAL_WP,
         MPI_MAX,mycomm,ierr)

      if (myrank == 0) &
        write(*,'(a,2g18.8)') '␣inlet␣mean,␣max␣x-velocity:␣',
           mean_velocity(1), max_velocity(1)

    end if      ! if zone is INLET
    zone => zone%next
  end do

end subroutine calc_mean_max_velocity_face

! ##########################################################

subroutine calc_mean_max_axial_velocity_volume(mean_velocity,
   max_velocity,if2)

  use gp_defs_m

  implicit none

  real(WP), intent(out) :: mean_velocity(1:3),max_velocity(1:3)
  type(if2_t), intent(inout), target :: if2

  ! ----------------------------------

  type(gp_t), pointer :: gp
  real(WP) :: &
```

```
      my_volume,             &    ! volume of geometry for each processor (
          local)
      my_mass_flow(3),       &    ! q = v.dA , for each proseccor (local)
      volume,                &    ! hole volume of geomtery (global)
      mass_flow(3),          &    ! Q = Sum{q} , over the whole face (
          global)
      coeff,                 &
      my_max_velocity(3)
integer :: i,ino,ierr

! ----------------------------------------

gp => if2%gp

if (myrank == 0) &
      write(*,*) '␣␣>␣calc_mean_axial_velocity␣for␣volume...'

! ---------------------------------
! calculate mean velocity of geometry
my_volume          = 0.0_WP
my_mass_flow(1:3)  = 0.0_WP
volume             = 0.0_WP
mass_flow(1:3)  = 0.0_WP

! find "mass flow" locally
do ino = 1,gp%nno_ib
   coeff = gp%no_local_volume(ino)
   my_mass_flow(1:3) = my_mass_flow(1:3) + if2%u(1:3,ino)*coeff
   my_volume = my_volume + coeff
end do

! SUM "mass flow" and "face volume" from all processors
! 'AllReduce' sends back the result to all processors
call MPI_AllReduce(my_mass_flow,mass_flow,3,MPI_REAL_WP,MPI_SUM,
    mycomm,ierr)
call MPI_AllReduce(my_volume,volume,1,MPI_REAL_WP,MPI_SUM,mycomm,ierr
    )

mean_velocity(1:3) = mass_flow(1:3) / volume

! ---------------------------------
! calc max velocity
my_max_velocity(1:3) = 0.0_WP
max_velocity(1:3)    = 0.0_WP
do i = 1,3
   my_max_velocity(i) = maxval( if2%u(i,1:gp%nno_ib) )
end do
```

```
  call MPI_AllReduce(my_max_velocity,max_velocity,3,MPI_REAL_WP,MPI_MAX
      ,mycomm,ierr)

  if (myrank == 0) &
       write(*,'(a,2g18.8)') '␣volume␣mean,␣max␣x-velocity:␣',
           mean_velocity(1), max_velocity(1)

end subroutine calc_mean_max_axial_velocity_volume

! ############################################################################

subroutine pressure_gradient_controller(bu,if2)

  use param_m

  implicit none

  real(WP), intent(inout) :: bu(:,:)
  type(if2_t), intent(inout) :: if2

  ! ----------------------------------------------------------------

  real(WP), save, allocatable :: &
       dPdx(:),dPdx_old(:)       ! p gradient at t^{n}, t^{n-1}
  real(WP) :: &
       mean_velocity(3),    &  ! mean velocity of domain at t^{n}
       max_velocity(3),     &
       mean_ux_REFERENCE,   &  ! reference mean x velocity
       e0,e1,               &  ! error = u_REF-u_mean --> at t^{n}, t^{
           n-1}
       Kp,Ki,Kd                ! proportional, integral and derivative
           gain
  real(WP), save :: &
       mean_ux_old             ! mean x velocity of domain at t^{n-1}
  integer :: ino
  logical, save :: first = .TRUE.

  ! ----------------------------------------------------------------

  ! get controller gain parameters
  Kp = get_real_param('Kp',default=1.0_WP)
  Ki = get_real_param('Ki',default=1.0_WP)
  Kd = get_real_param('Kd',default=1.0_WP)
  mean_ux_REFERENCE = get_real_param('U_REF',default=1.0_WP)

  ! create arrays - size varies according to partitioning
  if (.NOT. allocated (dPdx) ) allocate ( dPdx(if2%gp%nno_ib) )
  if (.NOT. allocated (dPdx_old) ) allocate ( dPdx_old(if2%gp%nno_ib) )
```

```
call calc_mean_max_axial_velocity_volume(mean_velocity,max_velocity,
    if2)

if (first .EQV. .TRUE.) then
  ! set t^{n-1} values to zero for first iteration
  dPdx_old = 0.0_WP
  mean_ux_old = mean_velocity(1)

  ! write header to file
  if (myrank == 0) then
    open (80,FILE='controller_output.dat',status='unknown',action='
        write',position='append')
    write(80,*) '␣variables␣=␣"ite",␣"time",␣"Ux␣mean",␣"error(k)",␣"
        Ux␣mean␣(REFERENCE)"'
    close(80)

    open (81,FILE='controller_parameters.dat',status='unknown',action
        ='write',position='append')
    write(81,'(␣4(2x,A,F6.3)␣)') 'Kp␣=',Kp, 'Ki␣=',Ki, 'Kd␣=',Kd
    write(81,'(␣2x,A,F6.3␣)') 'U␣mean␣REF␣=␣',mean_ux_REFERENCE
    close(81)
  end if

  first = .FALSE.
end if

! calculate errors
e0 = mean_ux_REFERENCE - mean_velocity(1)
e1 = mean_ux_REFERENCE - mean_ux_old

do ino = 1,if2%gp%nno_ib
  ! adjust p gradient using a PID controler
  dPdx(ino) = &
       Kp*e0 +                          &  ! proportional controller
       dPdx_old(ino) + Ki*e0/if2%dt +   &  ! integral controller
       Kd*(e0-e1)/if2%dt                   ! derivative controller

  bu(1,ino) = if2%gp%no_local_volume(ino)*dPdx(ino)

  ! new gradient value goes to old var for next iteration
  dPdx_old(ino) = dPdx(ino)
end do

! new mean x velocity value goes to old var for next iteration
mean_ux_old = mean_velocity(1)

if (myrank == 0) then
```

```
    open (80,FILE='controller_output.dat',status='unknown',action='
        write',position='append')
    write(80,'(I6,2X,G12.4,6(2X,G16.8))') &
          if2%step, if2%time, mean_velocity(1), e0, mean_ux_REFERENCE
    close(80)
  end if

end subroutine pressure_gradient_controller

! ########################################################################

subroutine check_inlet_convergence(bu,if2)

  implicit none

  type(if2_t), intent(inout), target :: if2
      real(WP), intent(in) :: bu(:,:)

  ! ----------------------------------------------------------

  real(WP) :: &
       dU, dUdt, dPdx, mean_dPdx,            &
       my_total_volume, total_volume,        &
       my_sum_dPdx_dV, sum_dPdx_dV,          &
       my_sum_dUdt_over_dPdx_dV,sum_dUdt_over_dPdx_dV,  &
       mean_dUdt_over_dPdx,                  &
       my_max_dU_abs, max_dU_abs,            &
       my_max_dUdt_over_dPdx, max_dUdt_over_dPdx
  integer :: ino
  integer :: ierr,irank,status(MPI_STATUS_SIZE)   ! these are for
     MPI_Send,MPI_Recv
  logical, save :: first = .TRUE.

  ! ----------------------------------------------------------

  ! initialize arrays
  my_total_volume = 0.0_WP
  total_volume    = 0.0_WP
  my_sum_dPdx_dV = 0.0_WP
  sum_dPdx_dV    = 0.0_WP
  my_sum_dUdt_over_dPdx_dV = 0.0_WP
  sum_dUdt_over_dPdx_dV    = 0.0_WP
  my_max_dU_ABS = 0.00000000001_WP          ! (to compare against
     residuals of the solver)
  max_dU_ABS    = 0.0_WP
  my_max_dUdt_over_dPdx = 0.00000000001_WP  ! (to compare against
     residuals of the solver)
  max_dUdt_over_dPdx    = 0.0_WP
```

```
! All processors calculate their part of variables
do ino = 1,if2%gp%nno_ib
   my_total_volume = my_total_volume + if2%gp%no_local_volume(ino)
   ! difference between u - u0
   dU = ( if2%u(1,ino)-if2%u0(1,ino) )       !+&
          !( if2%u(2,ino)-if2%u0(2,ino) )**2.0_WP        +&
          !( if2%u(3,ino)-if2%u0(3,ino) )**2.0_WP)
   ! calc derivatives
   dUdt = dU/if2%dt
   dPdx = bu(1,ino)/if2%gp%no_local_volume(ino)

   ! sum derivatives and dpdx volume integral
   my_sum_dUdt_over_dPdx_dV = my_sum_dUdt_over_dPdx_dV +  if2%gp%
       no_local_volume(ino)*abs( dUdt )/dpdx
   my_sum_dPdx_dV = my_sum_dPdx_dV + bu(1,ino)             ! Sum { volume
       *dP/dx    }

   ! absolut max velocity increment
   my_max_dU_ABS = max( my_max_dU_ABS,abs(dU) )
   ! percentage of the transient term respect the pressure drop per
       node
   my_max_dUdt_over_dPdx = max( my_max_dUdt_over_dPdx,(100.0_WP*dUdt/
       dPdx) )
end do

! SUM DERIVATIVES from ALL processors
call MPI_Reduce(my_sum_dUdt_over_dPdx_dV,sum_dUdt_over_dPdx_dV,1,
     MPI_REAL_WP,MPI_SUM,0,mycomm,ierr)
call MPI_Reduce(my_sum_dPdx_dV,sum_dPdx_dV,1,MPI_REAL_WP,MPI_SUM,0,
     mycomm,ierr)
call MPI_Reduce(my_total_volume,total_volume,1,MPI_REAL_WP,MPI_SUM,0,
     mycomm,ierr)

! -------------------------------------
!  RANK 0 RECIEVE's
! -------------------------------------
if (myrank == 0) then
   ! first collect data from rank 0,
   ! swap local maximum value with global maximum value (nothing yet
       to compare with)
   max_dU_ABS = my_max_dU_ABS
   max_dUdt_over_dPdx = my_max_dUdt_over_dPdx

   ! then collect data from other processes
   do irank = 1,nprocs-1
      call MPI_RECV(my_max_dU_ABS,1,MPI_REAL_WP,irank,50002,mycomm,
          status,ierr)
```

```
      call MPI_RECV(my_max_dUdt_over_dPdx,1,MPI_REAL_WP,irank,50002+1,
         mycomm,status,ierr)

      ! compare global with every local value to find maximum value
      max_dU_ABS = max( max_dU_ABS, my_max_dU_ABS)
      max_dUdt_over_dPdx = max( max_dUdt_over_dPdx,
         my_max_dUdt_over_dPdx )
    end do
  ! ----------------------------------------
  !  OTHER PROCESSES SEND
  ! ----------------------------------------
  else
    call MPI_SEND(my_max_dU_ABS,1,MPI_REAL_WP,0,50002,mycomm,ierr)
    call MPI_SEND(my_max_dUdt_over_dPdx,1,MPI_REAL_WP,0,50002+1,mycomm,
       ierr)
  end if

  ! Write data to file
  if (myrank == 0) then
    ! only first time write header to file
    if (first) then
      open (10,FILE='time_convergence.dat',status='unknown',action='
         write',position='append')
      write (10,*) 'var␣=␣"ite","time","MEAN␣dPdx","MEAN␣dUdt/dPdx","
         MAX␣dUdt/dPdx␣[%]","MAX␣|delta␣U|"'
      close (10)
      first = .FALSE.
    end if

    mean_dUdt_over_dPdx = sum_dUdt_over_dPdx_dV/total_volume
    mean_dpdx = sum_dPdx_dV/total_volume

    write(*,*) 'checking␣steady␣state␣in␣PRESSURE␣FIELD␣IMPOSED␣ALONG␣X
       !'
    write(*,*) 'MEAN␣dUdt/dPdx␣[%]␣=', mean_dUdt_over_dPdx
    write(*,*) 'MAX␣|delta␣U|␣=', max_dU_ABS

    open(10,FILE='time_convergence.dat',status='unknown',action='write'
       ,position='append')
    write(10,'(I6,5G14.6)') if2%step, if2%time, mean_dPdx,
       mean_dUdt_over_dPdx, max_dUdt_over_dPdx, max_dU_ABS
    close(10)
  end if

end subroutine check_inlet_convergence

! ############################################################################
```

```
subroutine extract_velocity_profile(if2)

  use gp_defs_m           ! type zone_t,gp_t
  use bc_parsing_m        ! function zone_is_wall

  implicit none

  type(if2_t), intent(inout), target :: if2

  ! ———————————————————————————————

  type(gp_t), pointer :: gp
  type(zone_t), pointer :: zone
  real(WP), pointer :: u(:,:)
  real(WP) ::    &
       accuracy,x_intersection_plane,x_node,   &
       x_left_plane,x_right_plane
  real(WP), allocatable ::          &
       my_y_of_point_on_plane(:), &
       my_z_of_point_on_plane(:), &
       my_u_of_point_on_plane(:), &
       y_of_point_on_plane(:),     &
       z_of_point_on_plane(:),     &
       u_of_point_on_plane(:)
  integer ::                 &
       i,j,ino,icounter,   &
       my_array_size,array_size,      &    ! will be the size of my
           allocatable arrays
       ierr,status(MPI_STATUS_SIZE), &    ! these are for MPI_Send,
           MPI_Recv
       TAG0,TAG1,TAG2,TAG3                 !
  logical :: done
  character(30) :: filename

  ! ———————————————————————————————

  gp => if2%gp
  u  => if2%u

  ! parameters for plane for intersection
  x_intersection_plane = 0.0_WP                          ! ...define
      position
  accuracy = 0.01_WP                                     ! ...set
      accuracy
  x_right_plane = x_intersection_plane + accuracy        ! ...set upper
      limit
  x_left_plane = x_intersection_plane - accuracy         ! ...set lower
      limit
```

```
! ————————————————————————————————————
!  RANK 0 RECIEVE's
! ————————————————————————————————————
if (myrank == 0) then
  write(*,*) '␣␣>␣output␣velocity␣profile␣in␣file...'

  write(filename,'(a,i6.6,a)') 'velocity_profile.',if2%step,'.dat'
  open (30,FILE=filename)

  do i = 1,nprocs-1
    ! redifine ID's for sending requests for each process
    TAG0 = i*1000
    TAG1 = i*1000 + 1
    TAG2 = i*1000 + 2
    TAG3 = i*1000 + 3

    ! first recieve size of array's
    call MPI_Recv(array_size,1,MPI_INTEGER,i,TAG0,mycomm,status,ierr)

    ! if size not zero then recieve rest of data's
    if (array_size .NE. 0) then

      ! size of arrays need to be known precise for MPI_Recv
      allocate (y_of_point_on_plane(array_size))
      allocate (z_of_point_on_plane(array_size))
      allocate (u_of_point_on_plane(array_size))

      call MPI_Recv(y_of_point_on_plane,array_size,MPI_REAL_WP,i,TAG1
          ,mycomm,status,ierr)
      call MPI_Recv(z_of_point_on_plane,array_size,MPI_REAL_WP,i,TAG2
          ,mycomm,status,ierr)
      call MPI_Recv(u_of_point_on_plane,array_size,MPI_REAL_WP,i,TAG3
          ,mycomm,status,ierr)

      ! write data from each process to file
      do j = 1,array_size
        write(30,*) y_of_point_on_plane(j),z_of_point_on_plane(j),
            u_of_point_on_plane(j)
      end do

      deallocate (y_of_point_on_plane,z_of_point_on_plane,
          u_of_point_on_plane)
    end if

  end do        ! end loop from all procs

  ! write to file also points from rank 0
```

```
      do ino = 1,gp%nno_ib
        x_node = gp%node_cc(1,ino)
        if ((x_node < x_right_plane).AND.(x_node > x_left_plane))   &
            write(30,*) gp%node_cc(2,ino),gp%node_cc(3,ino),u(1,ino)
      end do

      close (30)

    ! ---------------------------------------------------
    !  OTHER PROCESSES SEND
    ! ---------------------------------------------------
    else

      ! first count number of points on plane of intersection for each
         process
      ! in order to allocate size of array to be SEND and be able to
         RECIEVE
      my_array_size = 0
      do ino = 1,gp%nno_ib
        x_node = gp%node_cc(1,ino)
        if ((x_node < x_right_plane).AND.(x_node > x_left_plane))   &
          my_array_size = my_array_size + 1
      end do

      ! ID for send functions
      TAG0 = myrank*1000
      TAG1 = myrank*1000 + 1
      TAG2 = myrank*1000 + 2
      TAG3 = myrank*1000 + 3

      ! first SEND SIZE of array's
      call MPI_Send(my_array_size,1,MPI_INTEGER,0,TAG0,mycomm,ierr)

      ! if size of array's not zero then SEND ARRAY's
      if (my_array_size .NE. 0) then

        ! size of arrays need to be known precise for MPI_Recv
        allocate (my_y_of_point_on_plane(my_array_size))
        allocate (my_z_of_point_on_plane(my_array_size))
        allocate (my_u_of_point_on_plane(my_array_size))

        ! extract and store data from each process to arrays
        icounter = 0
        do ino = 1,gp%nno_ib
          x_node = gp%node_cc(1,ino)
          if ((x_node < x_right_plane).AND.(x_node > x_left_plane)) then
                ! if point on plane
            icounter = icounter + 1
```

```
          my_y_of_point_on_plane(icounter) = gp%node_cc(2,ino)      ! y
          my_z_of_point_on_plane(icounter) = gp%node_cc(3,ino)      ! z
          my_u_of_point_on_plane(icounter) = u(1,ino)               ! u
        end if
      end do

      ! SEND the array's
      call MPI_Send(my_y_of_point_on_plane,my_array_size,MPI_REAL_WP,0,
         TAG1,mycomm,ierr)
      call MPI_Send(my_z_of_point_on_plane,my_array_size,MPI_REAL_WP,0,
         TAG2,mycomm,ierr)
      call MPI_Send(my_u_of_point_on_plane,my_array_size,MPI_REAL_WP,0,
         TAG3,mycomm,ierr)

      deallocate(my_y_of_point_on_plane,my_z_of_point_on_plane,
         my_u_of_point_on_plane)
    end if

  end if   ! end SEND-RECIEVE

end subroutine extract_velocity_profile

! ############################################################

subroutine read_velocity_profile(u_bc_tmp,zone,if2)

  ! ------------------------------------------------------------
  ! NOTE: THIS SUBROUTINE IS CALLED IF ZONE IS INLET
  ! ------------------------------------------------------------

  use param_m

  implicit none

  real(WP), pointer :: u_bc_tmp(:,:)
  type(zone_t), intent(in) :: zone
  type(if2_t), intent(inout), target :: if2

  ! ----------------------------------

  type(gp_t), pointer :: gp
  real(WP), save, allocatable :: u_bc_stored(:,:)
  real(WP), allocatable :: &
       y_inp(:),z_inp(:),ux_inp(:), &    ! data of input nodes
       dist(:,:)                         ! distance between input and
           inlet nodes
  real(WP) :: &
       y,z,              &  ! cartesian coordinates of input nodes
```

```
      y_ref,z_ref,         &  ! cartesian coordinates of inlet nodes
      closest_dist(4),     &  ! closest distance in each quadrant from
          reference node
      sum_weights,         &  ! sum weight of input nodes used to
          calculate inlet velocity
      mean_velocity(3)
  integer :: &
      i,j,ino,ierr,        &
      num_nodes_file,      &  ! number of nodes in file '
          inlet_velocity_profile.dat'
      index_mn,            &  ! location of node in array if matching
          nodes
      index_cn(4)             ! location of closest node in array
  real(WP), parameter :: MAX_DISTANCE = 1000.0_WP
  real(WP) :: &
      CHAR_LENGTH, Re_TARGET, U_MEAN_TARGET, &
      Re, Re_scaling_coeff, U_mean_scaling_coeff
  logical, save :: first = .TRUE.
  logical :: nodes_match  !, done

  ! ------------------------------------------

  gp => if2%gp

  if (myrank == 0) &
      write(*,*) '␣␣>␣read␣velocity␣profile␣from␣file...'

  if (first .EQV. .TRUE.) then

    ! ------------------------------------------
    ! READ FILE FOR EXTRAPOLATION...
    ! ------------------------------------------

    open (31,FILE='inlet_velocity_profile.dat',STATUS='OLD')

    ! find what is the size of the file (read until End-Of-File)
    ierr = 0                    ! if ierr=-1 then EOF
    num_nodes_file = 0          ! number of records in file
    do while (ierr == 0)
      num_nodes_file = num_nodes_file + 1
      read (31,*,iostat=ierr)
    end do
    num_nodes_file = num_nodes_file - 1
    rewind(31)

    ! create arrays on-the-fly -> use size of file
    if (.NOT. allocated (y_inp) ) allocate (y_inp(num_nodes_file))
    if (.NOT. allocated (z_inp) ) allocate (z_inp(num_nodes_file))
```

```
if (.NOT. allocated (ux_inp) ) allocate (ux_inp(num_nodes_file))
if (.NOT. allocated (dist) ) allocate (dist(zone%n_nodelist,
   num_nodes_file))
! create dummy array to store velocity after reading
if (.NOT. allocated (u_bc_stored) ) allocate (u_bc_stored(3,zone%
   n_nodelist))

u_bc_stored(:,:) = 0.0_WP

! read data from file
do i = 1,num_nodes_file
  read (31,*) y_inp(i),z_inp(i),ux_inp(i)
end do

! calculate distance between inlet and input nodes
do i = 1,zone%n_nodelist
  ino = zone%nodelist(i)
  do j = 1,num_nodes_file
    dist(i,j) = sqrt( ( gp%node_cc(2,ino)-y_inp(j) )**2 + &
                      ( gp%node_cc(3,ino)-z_inp(j) )**2 )
  end do
end do

! ---------------------------------------------------------------------
!   find 4 closest nodes
! ---------------------------------------------------------------------

! loop over all inlet nodes
do i = 1,zone%n_nodelist
  ino = zone%nodelist(i)

  closest_dist(1:4) = MAX_DISTANCE     ! distance from closest point
     at all directions

  ! For comparisson we use 'ino' as an argument { e.g. y_ref = gp%
     node_cc(2,ino) } ...
  ! BUT for storage we use 'i' { u_bc_stored(1,i) }  ...
  ! otherwise we would had a big array like if2%u_bc { allocate
     u_bc_stored(3,gp%nno_ib) } ...
  ! we lots of zeros at places for all other zones.

  ! cartesian coordinates of node of reference
  y_ref = gp%node_cc(2,ino)
  z_ref = gp%node_cc(3,ino)

  ! loop over all input nodes
  j = 1
  nodes_match = .FALSE.      ! assume nodes don't match
```

```
do while ((j <= num_nodes_file).AND.(nodes_match .EQV. .FALSE.))
  ! cartesian coordinates of input node
  y = y_inp(j)
  z = z_inp(j)

  ! check first if refernce node match any inlet node
  if ((y == y_ref).AND.(z == z_ref)) then
    nodes_match=.TRUE.
    index_mn = j

  ! if not then locate nodes around reference node...
  ! ...at four quadrants of a cartesian coordinate system
  else

    ! ...check above the node of reference - fisrt 2 quadrants
    if (y >= y_ref) then
      ! check 1st quadrant
      if (z >= z_ref) then
        if (dist(i,j) < closest_dist(1)) then
          index_cn(1) = j                    ! index of closest node
               in array
          closest_dist(1) = dist(i,j)
        end if
      end if
      ! check 2nd quadrant
      if (z <= z_ref) then
        if ( dist(i,j)<closest_dist(2)) then
          index_cn(2) = j                    ! index of closest node
               in array
          closest_dist(2) = dist(i,j)
         end if
      end if
    end if

    ! ...check below the node of reference - last 2 quadrants
    if (y <= y_ref) then
      ! check 3rd quadrant
      if (z <= z_ref) then
        if ( dist(i,j)<closest_dist(3)) then
          index_cn(3) = j                    ! index of closest node
               in array
          closest_dist(3) = dist(i,j)
        end if
      end if
      ! check 4th quadrant
      if (z >= z_ref) then
        if ( dist(i,j)<closest_dist(4)) then
```

```
              index_cn(4) = j                 ! index of closest node
                  in array
              closest_dist(4) = dist(i,j)
            end if
          end if
        end if

      end if

      j = j + 1
    end do  ! loop over input nodes

    ! calculate inlet velocity at nodes
    if (nodes_match .EQV. .TRUE.) then
      u_bc_stored(1,i) = ux_inp(index_mn)
    else
      ! Equation: u = sum{ weight(i)*ux(i)/sum[weight(i)] }
      sum_weights = ( 1.0_WP/closest_dist(1) ) + &
                    ( 1.0_WP/closest_dist(2) ) + &
                    ( 1.0_WP/closest_dist(3) ) + &
                    ( 1.0_WP/closest_dist(4) )

      u_bc_stored(1,i) = ( ( 1.0_WP/closest_dist(1) )*ux_inp(index_cn
          (1)) +   &
                           ( 1.0_WP/closest_dist(2) )*ux_inp(index_cn
                              (2)) +   &
                           ( 1.0_WP/closest_dist(3) )*ux_inp(index_cn
                              (3)) +   &
                           ( 1.0_WP/closest_dist(4) )*ux_inp(index_cn
                              (4)) )/  &
                           sum_weights
    end if

  end do    ! loop over inlet nodes

  deallocate( y_inp,z_inp,ux_inp,dist )
  close(31)

  first = .FALSE.
end if

! define u_bc for inlet
do i=1,zone%n_nodelist
  ino = zone%nodelist(i)
  u_bc_tmp(1,ino) = u_bc_stored(1,i)
  u_bc_tmp(2:3,ino) = 0.0_WP
end do
```

```
end subroutine read_velocity_profile

! ##########################################################################

subroutine inlet_velocity_scaling(u_bc_tmp,zone,if2)

   ! --------------------------------------------------------------------------
   ! NOTE: THIS SUBROUTINE IS CALLED IF ZONE IS INLET
   ! --------------------------------------------------------------------------

   use param_m

   implicit none

   real(WP), pointer :: u_bc_tmp(:,:)
   type(zone_t), intent(in) :: zone
   type(if2_t), intent(inout), target :: if2

   ! ------------------------------------------

   real(WP) :: mean_velocity(3),max_velocity(3)
   integer :: i,ino
   real(WP) :: &
         CHAR_LENGTH,Re_TARGET,U_TARGET, &
         Re_bulk, Re_cent
   real(WP), save :: &
         Re_scaling_coeff, U_scaling_coeff
   logical, save :: first = .TRUE.
   logical :: adjust_inlet_velocity

   ! ------------------------------------------

   if (myrank == 0) &
         write(*,*) '␣␣>␣adjust␣velocity␣at␣inlet␣by␣scaling␣velocity␣and
            ␣viscosity...'

   if (first .EQV. .TRUE.) then
      ! ------ BEFORE SCALING ------
      !
      ! Calculate Re and velocities before any scaling
      Re_TARGET = get_real_param('Re_TARGET',default=100.0_WP)
      CHAR_LENGTH = get_real_param('CHAR_LENGTH',default=1.0_WP)

      ! define if2%u_bc for inlet to be able to use subroutine
         calc_mean_Velocity
      ! ...until now if2%u_bc is not defined
      do i=1,zone%n_nodelist
         ino = zone%nodelist(i)
```

```
  if2%u_bc(1,ino) = u_bc_tmp(1,ino)
  if2%u_bc(2:3,ino) = 0.0_WP
end do

call calc_mean_max_velocity_face(mean_velocity,max_velocity,if2)

Re_bulk = mean_velocity(1)*CHAR_LENGTH/if2%constant_nu
Re_cent = max_velocity(1)*CHAR_LENGTH/if2%constant_nu

open (50,FILE='INFO–flow_params.dat')
write(50,*) '␣>␣INLET␣VELOCITY␣SCALING...'
write(50,*) '␣␣␣<␣Before␣Scaling␣>'
write(50,'(␣6(2X,A16)␣)') 'Re␣target', 'Re_bulk', 'Re_cent', 'mean␣
   velocity', 'max␣velocity', 'viscosity'
write(50,'(␣6(2X,G16.8)␣)') Re_TARGET, Re_bulk, Re_cent,
   mean_velocity(1), max_velocity(1), if2%constant_nu
!
! ———— SCALING ————
!
! Calculate coefficient for VELOCITY scaling
if (get_logical_param('ADJUST_MEAN_VELOCITY',default=.FALSE.)) then
  if (myrank == 0) &
       write(*,*) '␣␣␣>␣adjust␣mean␣velocity...'
  U_TARGET = get_real_param('U_MEAN_TARGET',default=1.0_WP)
  U_scaling_coeff = U_TARGET/mean_velocity(1)
  adjust_inlet_velocity = .TRUE.
else if (get_logical_param('ADJUST_MAX_VELOCITY',default=.FALSE.))
   then
  if (myrank == 0) &
       write(*,*) '␣␣␣>␣adjust␣max␣velocity...'
  U_TARGET = get_real_param('U_MAX_TARGET',default=1.0_WP)
  U_scaling_coeff = U_TARGET/max_velocity(1)
  adjust_inlet_velocity = .TRUE.
else
  if (myrank == 0) &
       write(*,*) '␣␣␣>␣NOTE:␣No␣adjustment␣of␣flow␣parameters'
  adjust_inlet_velocity = .FALSE.
end if

! SCALE VELOCITY profile
if (adjust_inlet_velocity) then


  do i=1,zone%n_nodelist
    ino = zone%nodelist(i)
    if2%u_bc(1,ino) = u_bc_tmp(1,ino)*U_scaling_coeff
    if2%u_bc(2:3,ino) = 0.0_WP
  end do
  call calc_mean_max_velocity_face(mean_velocity,max_velocity,if2)
```

```
      ! Reynolds number after mean velocity correction
      Re_bulk = mean_velocity(1)*CHAR_LENGTH/if2%constant_nu
      Re_cent = max_velocity(1)*CHAR_LENGTH/if2%constant_nu

      ! Viscosity is also adjusted by default, but this is optional...
      ! ...it can be deactivated using 'ADJUST_VISCOSITY=.FALSE.' in
         input file
      if (get_logical_param('ADJUST_VISCOSITY',default=.TRUE.)) then
        ! Calculate COEFFICIENT for VISCOSITY scaling
        if (get_logical_param('ADJUST_MEAN_VELOCITY',default=.FALSE.))
           then
          Re_scaling_coeff = Re_TARGET/Re_bulk
        else if (get_logical_param('ADJUST_MAX_VELOCITY',default=.FALSE
           .)) then
          Re_scaling_coeff = Re_TARGET/Re_cent
        end if
        ! SCALE VISCOSITY
        if2%constant_nu = if2%constant_nu/Re_scaling_coeff

        if (myrank == 0) &
             write(*,*) '␣␣␣>␣viscosity␣adjusted:␣', if2%constant_nu

        ! Reynolds number after viscosity correction
        Re_bulk = mean_velocity(1)*CHAR_LENGTH/if2%constant_nu
        Re_cent = max_velocity(1)*CHAR_LENGTH/if2%constant_nu
      end if
    end if
    !
    ! —— AFTER SCALING ——
    !
    write(50,*) '␣␣␣<␣After␣Scaling␣>'
    write(50,'(␣6(2X,A16)␣)') 'Re␣target', 'Re_bulk', 'Re_cent', 'mean␣
       velocity', 'max␣velocity', 'viscosity'
    write(50,'(␣6(2X,G16.8)␣)') Re_TARGET, Re_bulk, Re_cent,
       mean_velocity(1), max_velocity(1), if2%constant_nu
    close (50)
    !
    ! ————————————————
    first = .FALSE.
  end if

  ! scale inlet velocity profile
  ! ...velocity scaling coeff. is stored to save time
  u_bc_tmp = u_bc_tmp*U_scaling_coeff

end subroutine inlet_velocity_scaling
```

```
! ####################################################################

subroutine calc_drag(if2)

  ! DRAG AND LIFT IS CALCULATED BASED ON REFERENCE VELOCITY (either
     mean or max U)

  use bc_parsing_m          ! function zone_is_wall
  use gp_func_m             ! subroutine calc_duidxj()
  use buffer_m              ! subroutine use_r3_buffer(),var r3_buffer
  use param_m               ! function get_real_param
  use gp_defs_m             ! type zone_t,gp_t

  implicit none

  type(if2_t), intent(inout), target :: if2

  ! ----------------------------------------

  type(gp_t), pointer :: gp
  type(zone_t), pointer :: zone
  real(WP), pointer :: u(:,:),p(:),nu(:)
  real(WP) :: &
       my_drag_form(3),drag_form(3),               &
       my_drag_friction(3),drag_friction(3),       &
       drag(3),        &
       drag_coeff(3),drag_coeff_cyl(3),             &
       HEIGHT,DIAMETER,WIDTH,                       &  ! parameters of flow
       DENSITY,CHAR_LENGTH,                         &  ! parameters of flow
       mean_velocity(3),max_velocity(3),U_cyl,      &  ! mean max Vel. in
          channel & in front of cylinder
       Re,Re_cyl,                                   &  ! Reynolds number and
           cylinder based Re
       time_star,                                   &  ! dimensionless time
       b_ratio,aspect_ratio
  real(WP), save :: U_ref
  integer :: i,ino,j,ierr
  character(35), save :: filename1,filename2
  !!logical :: POISEUILLE_FLOW
  logical, save :: first = .TRUE.

  ! ----------------------------------------

  if (myrank == 0) &
       write(*,*) '␣␣>␣calculate␣drag...'

  gp => if2%gp
  u  => if2%u
```

```
p  => if2%p
nu => if2%nu

! ---------------------------------------------------------------------
!  Calculate characteristic numbers of the flow
! ---------------------------------------------------------------------
! first time calc reference velocity and store it
if (first .EQV. .TRUE.) then

  call calc_mean_max_velocity_face(mean_velocity,max_velocity,if2)

  if (get_logical_param('ADJUST_MEAN_VELOCITY',default=.FALSE.)) then
    U_ref = mean_velocity(1)
  else if (get_logical_param('ADJUST_MAX_VELOCITY',default=.FALSE.))
     then
    U_ref = max_velocity(1)
  else
    U_ref = 1.0_WP
  end if
end if

if (myrank == 0) then
  ! get parameters of geometry and velocity profile
  HEIGHT    = get_real_param('HEIGHT',default=1.0_WP)
  DIAMETER = get_real_param('DIAMETER',default=1.0_WP)
  WIDTH     = get_real_param('WIDTH',default=1.0_WP)
  DENSITY   = get_real_param('DENSITY',default=1.0_WP)
  CHAR_LENGTH = get_real_param('CHAR_LENGTH',default=1.0_WP)

 ! characteristic numbers
  b_ratio      = DIAMETER/HEIGHT
  aspect_ratio = WIDTH/DIAMETER
  Re = U_ref*CHAR_LENGTH/if2%constant_nu
  time_star = if2%time*U_ref/CHAR_LENGTH
  ! Cylinder based Re
  ! ...WORKS ONLY FOR CHANNEL FLOW
  ! ...NEED MORE WORK FOR OTHER FLOWS
  U_cyl  = 1.5_WP*U_ref*(1.0_WP-(DIAMETER**2)/(3.0_WP*HEIGHT**2))
  Re_cyl = Re*U_cyl

  if (first .EQV. .TRUE.) then
    open (50,FILE='INFO-flow_params.dat',status='unknown',action='
        write',position='APPEND')
    write(50,*)
    write(50,*) '␣>␣CALCULATE␣DRAG...'
    write(50,'(␣4(2X,A16)␣)') 'Re_ref', 'ref␣velocity', 'mean␣
        velocity', 'max␣velocity'
```

```
    write(50,'(␣4(2X,G16.8)␣)') Re, U_ref, mean_velocity(1),
       max_velocity(1)
    close (50)
  end if
end if

! ----------------------------------------------------------------------
! Loop through zones until zone is WALL .AND. zone%name=cylinder
! ----------------------------------------------------------------------
zone => gp%first_zone_ptr
do while (associated(zone))
  if ( zone_is_wall(zone%name) .AND. &
       ((zone%name == 'cylinder').OR.(zone%name == 'CYLINDER')) )
          then

    ! ------------------------------------------------------------
    !  calculate FORM DRAG and FRICTION DRAG for all nodes on
       cylinder
    ! ------------------------------------------------------------
    !initialize arrays
    my_drag_form(1:3)     = 0.0_WP
    my_drag_friction(1:3) = 0.0_WP
    drag_form(1:3)     = 0.0_WP
    drag_friction(1:3) = 0.0_WP
    drag(1:3)          = 0.0_WP

    ! the explicit velocity gradients are required for some terms...
    call use_r3_buffer(3,3,gp%nno_ib)
    r3_buffer(1:3,1:3,1:gp%nno_ib) = 0.0_WP
    call calc_duidxj(r3_buffer,u,gp)

    do i = 1,zone%n_nodelist
      ino = zone%nodelist(i)

      ! FORM DRAG
      ! i.e. Fx = Area*Pressure*normal
      my_drag_form(1:3) = my_drag_form(1:3) + &
           p(ino)*( -zone%no_local_normal(1:3,i) )

      ! FRICTION DRAG
      ! i.e. Fx = Area*viscosity*dot_product( grad(u),normal )
      do j= 1,3
        my_drag_friction(j) = my_drag_friction(j) + nu(ino)* &
            ( dot_product( r3_buffer(1:3,j,ino),-zone%
                no_local_normal(1:3,i) ) + &
              dot_product( r3_buffer(j,1:3,ino),-zone%
                  no_local_normal(1:3,i) ) )
      end do
```

```
    end do

    ! SUM DRAG from all processors
    call MPI_Reduce(my_drag_form,drag_form,3,MPI_REAL_WP,MPI_SUM,0,
        mycomm,ierr)
    call MPI_Reduce(my_drag_friction,drag_friction,3,MPI_REAL_WP,
        MPI_SUM,0,mycomm,ierr)

    ! ---------------------------------------------------------------
    !   calculate DRAG-COEFF
    ! ---------------------------------------------------------------
    if (myrank == 0) then
      ! TOTAL DRAG
      drag(1:3) = -drag_form(1:3) + drag_friction(1:3)

      ! DRAG COEFFICIENT
      drag_coeff(1:3) = drag(1:3)/ &
            ( 0.5_WP*DENSITY*(U_ref**2)*DIAMETER*WIDTH )
      ! ...cylinder based
      drag_coeff_cyl(1:3) = drag_coeff(1:3)/(U_cyl**2)

      ! ----------------
      !   output results
      ! ----------------
      write(filename1,'(A,F3.1,A,F4.2,A,I4.4,A)') &
            'CDrag-AR',aspect_ratio,'-b',b_ratio,'-Re',nint(Re),'.dat'
      write(filename2,'(A,F3.1,A,F4.2,A,I4.4,A)') &
            'CLift-AR',aspect_ratio,'-b',b_ratio,'-Re',nint(Re),'.dat'

      open (31,FILE=filename1,status='unknown',action='write',
          position='APPEND')
      open (32,FILE=filename2,status='unknown',action='write',
          position='APPEND')

      if (first .EQV. .TRUE.) then
        write(31,*) 'variables␣=␣"ite",␣"time*",␣"Cd",␣"%form",␣"%
            friction"'
        write(32,*) 'variables␣=␣"ite",␣"time*",␣"Cl",␣"%form",␣"%
            friction"'
      end if

      write(31,'(␣I6,4(2X,G18.10)␣)') if2%step, time_star, drag_coeff
          (1), &
                -drag_form(1)*100.0_WP/drag(1), drag_friction(1)*100.0
                    _WP/drag(1)
      write(32,'(␣I6,4(2X,G18.10)␣)') if2%step, time_star, drag_coeff
          (2), &
```

```
                  -drag_form(1)*100.0_WP/drag(1), drag_friction(1)*100.0
                     _WP/drag(1)

         close (31); close (32)
       end if
       ! ---------------------------------------------------------------

     end if      ! if zone is wall
     zone => zone%next
   end do

   ! no longer needed
   call free_r3_buffer()

   first = .FALSE.
 end subroutine calc_drag

 ! ####################################################################

 subroutine calc_drag_slices(if2)
                               ! BELOW: WHAT IS DEFINED AND WHERE
   use bc_parsing_m            ! function zone_is_wall
   use gp_func_m               ! subroutine calc_duidxj()
   use buffer_m                ! subroutine use_r3_buffer(),var r3_buffer
   use param_m                 ! function get_real_param
   use gp_defs_m               ! type zone_t,gp_t
   use global_m                ! for pi

   implicit none

   type(if2_t), intent(inout), target :: if2

   ! ----------------------------------------

   type(gp_t), pointer :: gp
   type(zone_t), pointer :: zone
   real(WP), pointer :: u(:,:),p(:),nu(:)
   real(WP) :: &
        my_drag_form(3),drag_form(3),               &
        my_drag_friction(3),drag_friction(3),       &
        drag(3),        &
        drag_coeff(3),drag_coeff_cyl(3),             &
        HEIGHT,DIAMETER,WIDTH,                       &  ! parameters of flow
        DENSITY,CHAR_LENGTH,                         &  ! parameters of flow
        mean_velocity(3),max_velocity(3),U_cyl,      &  ! mean Vel. in
           channel & in front of cylinder
        Re,Re_cyl,                                   &  ! Reynolds number and
            cylinder based Re
```

```
     time_star,                                   &  ! dimensionless time
     b_ratio,aspect_ratio
real(WP), save :: U_ref
integer :: i,ino,j,k,ierr
character(35) :: filename1,filename2
!!logical :: POISEUILLE_FLOW
logical, save :: first = .TRUE.

real(WP), save, allocatable :: slice_z_cc_list(:)
real(WP), allocatable :: &
     slice_my_drag(:,:),slice_drag(:,:),               &
     slice_drag_coeff(:,:),                            &
     slice_my_1D_buffer(:),slice_1D_buffer(:),         &
     slice_my_area(:),slice_area(:),slice_length(:)
real(WP) :: &
     my_drag_form_1node(3),my_drag_friction_1node(3),  &
     node_z,slice_z,slice_z_width,                     &
     slice_z_ubound,slice_z_lbound
integer, save :: inno_along_cylinder
integer :: islice_index,ibuffer_size
logical :: node_in_slice
character(40) :: slice_filename

! ------------------------------------

if (myrank == 0) &
     write(*,*) '␣␣>␣calculate␣drag...'

gp => if2%gp
u  => if2%u
p  => if2%p
nu => if2%nu

! ------------------------------------------------------------------
! Calculate characteristic numbers of the flow
! ------------------------------------------------------------------
! first time calc reference velocity and store it
if (first .EQV. .TRUE.) then

  call calc_mean_max_velocity_face(mean_velocity,max_velocity,if2)

  if (get_logical_param('ADJUST_MEAN_VELOCITY',default=.FALSE.)) then
    U_ref = mean_velocity(1)
  else if (get_logical_param('ADJUST_MAX_VELOCITY',default=.FALSE.))
     then
    U_ref = max_velocity(1)
  else
    U_ref = 1.0_WP
```

```
    end if
  end if

  if (myrank == 0) then
    ! get parameters of geometry and velocity profile from input file
    HEIGHT     = get_real_param('HEIGHT',default=1.0_WP)
    DIAMETER = get_real_param('DIAMETER',default=1.0_WP)
    WIDTH      = get_real_param('WIDTH',default=1.0_WP)
    DENSITY   = get_real_param('DENSITY',default=1.0_WP)
    CHAR_LENGTH = get_real_param('CHAR_LENGTH',default=1.0_WP)

    ! characteristic numbers
    b_ratio         = DIAMETER/HEIGHT
    aspect_ratio  = WIDTH/DIAMETER
    Re = U_ref*CHAR_LENGTH/if2%constant_nu
    time_star = if2%time*U_ref/CHAR_LENGTH
    ! ...cylinder based Re
    ! (!?! --> WORKS ONLY FOR CHANNEL FLOW    <-- ?!?)
    ! (!?! --> NEED MORE WORK FOR OTHER FLOWS <-- ?!?)
    U_cyl   = 1.5_WP*U_ref*(1.0_WP-(DIAMETER**2)/(3.0_WP*HEIGHT**2))
    Re_cyl  = Re*U_cyl

    if (first .EQV. .TRUE.) then
      open (50,FILE='INFO-flow_params.dat',status='unknown',action='
          write',position='APPEND')
      write(50,*)
      write(50,*) '␣>␣CALCULATE␣DRAG... '
      write(50,'(␣4(2X,A16)␣)') 'Re_ref', 'ref␣velocity', 'mean␣
          velocity', 'max␣velocity'
      write(50,'(␣4(2X,G16.8)␣)') Re, U_ref, mean_velocity(1),
          max_velocity(1)
      close (50)
    end if
  end if

  ! ---------------------------------------------------------------------
  ! Loop through zones until zone is WALL .AND. zone%name=cylinder
  ! ---------------------------------------------------------------------
  zone => gp%first_zone_ptr
  do while (associated(zone))
    if ( zone_is_wall(zone%name) .AND. &
          ((zone%name == 'cylinder').OR.(zone%name == 'CYLINDER')) )
              then

      ! -----------------------------------------------------------------
      ! first time read position of nodes spanwise for SLICE_DRAG
      ! -----------------------------------------------------------------
      if (first .EQV. .TRUE.) then
```

```
  open (77,FILE='zPosConstXY.dat',STATUS='OLD')

  ! find what is the size of the file (read until End-Of-File)
  ierr = 0
  inno_along_cylinder = 0          ! number of records in file
  do while (ierr == 0)
    inno_along_cylinder = inno_along_cylinder + 1
    read (77,*,iostat=ierr)
  end do
  inno_along_cylinder = inno_along_cylinder - 1
  rewind(77)

  ! create arrays on-the-fly -> use size of file
  if (.NOT. allocated (slice_z_cc_list)) allocate (
      slice_z_cc_list(inno_along_cylinder))

  ! read data from file
  do i = 1,inno_along_cylinder
    read (77,*) slice_z_cc_list(i)
  end do
  close (77)
end if ! first == .TRUE.

! ----------------------------------------------------------------------
!  calculate form drag and friction drag for each node on
   cylinder
! ----------------------------------------------------------------------
! allocate variables
if (.NOT. allocated (slice_my_drag)) allocate ( slice_my_drag(3,
   inno_along_cylinder) )
if (.NOT. allocated (slice_drag)    ) allocate ( slice_drag(3,
   inno_along_cylinder)  )
if (.NOT. allocated (slice_my_area)) allocate ( slice_my_area(
   inno_along_cylinder) )
if (.NOT. allocated (slice_area)    ) allocate ( slice_area(
   inno_along_cylinder)     )
if (.NOT. allocated (slice_length) ) allocate ( slice_length(
   inno_along_cylinder)  )
if (.NOT. allocated (slice_drag_coeff)  ) allocate (
   slice_drag_coeff(3,inno_along_cylinder) )
ibuffer_size = 3*inno_along_cylinder
if (.NOT. allocated (slice_my_1D_buffer)) allocate (
   slice_my_1D_buffer(ibuffer_size) )
if (.NOT. allocated (slice_1D_buffer)    ) allocate (
   slice_1D_buffer(ibuffer_size) )

slice_my_drag(:,:)      = 0.0_WP
slice_my_area(:)        = 0.0_WP
```

```
my_drag_form(1:3)       = 0.0_WP
my_drag_friction(1:3) = 0.0_WP

! the explicit velocity gradients are required for some terms...
call use_r3_buffer(3,3,gp%nno_ib)
r3_buffer(1:3,1:3,1:gp%nno_ib) = 0.0_WP
call calc_duidxj(r3_buffer,u,gp)

do i = 1,zone%n_nodelist
  ino = zone%nodelist(i)

  ! FORM-DRAG:
  ! [ Fx = Area*Pressure*normal ]
  my_drag_form_1node(1:3) = p(ino)*( -zone%no_local_normal(1:3,i)
      )

  ! FRICTION-DRAG:
  ! [ Fx = Area*viscosity*dot_product( grad(u),normal ) ]
  do j = 1,3
    my_drag_friction_1node(j) = nu(ino)* &
         ( dot_product( r3_buffer(1:3,j,ino),-zone%
             no_local_normal(1:3,i) ) + &
           dot_product( r3_buffer(j,1:3,ino),-zone%
               no_local_normal(1:3,i) ) )
  end do

  ! find in which slice this node belongs to
  ! ...this is for SLICE-DRAG
  islice_index = 0
  node_in_slice = .FALSE.
  do while ((node_in_slice .EQV. .FALSE.).OR.(islice_index <
      inno_along_cylinder))
    islice_index = islice_index + 1    ! node position is given
        using this index

    node_z   = gp%node_cc(3,ino)                ! node spanwise
        position
    slice_z = slice_z_cc_list(islice_index)   ! slice spanwise
        position
    slice_z_width   = 0.0001_WP                  !
    slice_z_ubound = slice_z + slice_z_width    ! upper bound
    slice_z_lbound = slice_z - slice_z_width    ! lower bound

    ! if node in slice then add friction and form drag to reduce
        number of arrays,
    ! and just pass the sum for each slice
    if ((node_z < slice_z_ubound).AND.(node_z > slice_z_lbound))
        then
```

```
        slice_my_drag(1:3,islice_index) = slice_my_drag(1:3,
            islice_index) &
              - my_drag_form_1node(1:3) + my_drag_friction_1node
                  (1:3)
        slice_my_area(islice_index) = slice_my_area(islice_index) +
              zone%no_local_area(i)
        node_in_slice = .TRUE.
      end if
    end do   ! do while

    ! sum form and friction drag seperatly for all nodes on zone
    ! ...this is for DRAG
    my_drag_form(1:3)       = my_drag_form(1:3) + my_drag_form_1node
        (1:3)
    my_drag_friction(1:3) = my_drag_friction(1:3) +
        my_drag_friction_1node(1:3)

  end do     ! loop over nodes in zone "cylinder"

  ! ---------------------------------------------------------
  !  distribute the answers to the root node
  ! ---------------------------------------------------------
  ! reshape array "slice_my_drag" to 1D in order to use MPI_Reduce
  do j = 1,inno_along_cylinder
  do i = 1,3
    slice_my_1D_buffer(3*(j-1)+i) = slice_my_drag(i,j)
  end do
  end do

  call MPI_Reduce( my_drag_form,drag_form,3,MPI_REAL_WP,MPI_SUM,0,
      mycomm,ierr  )
  call MPI_Reduce( my_drag_friction,drag_friction,3,MPI_REAL_WP,
      MPI_SUM,0,mycomm,ierr  )
  call MPI_Reduce( slice_my_area,slice_area,inno_along_cylinder,
      MPI_REAL_WP,MPI_SUM,0,mycomm,ierr  )
  call MPI_Reduce( slice_my_1D_buffer,slice_1D_buffer,ibuffer_size,
       &
        MPI_REAL_WP,MPI_SUM,0,mycomm,ierr  )

  ! ---------------------------------------------------------
  !  calculate DRAG-COEFF and SLICE-DRAG-COEFF
  ! ---------------------------------------------------------
  if (myrank == 0) then
    ! unpack array from sum_buffer to "slice_drag"
    slice_drag = RESHAPE( slice_1D_buffer,(/ 3,inno_along_cylinder
        /) )

    ! DRAG
```

```
drag(1:3) = -drag_form(1:3) + drag_friction(1:3)

! DRAG-COEFF (also cylinder based)
drag_coeff(1:3) = drag(1:3)/ &
     ( 0.5_WP*DENSITY*(U_ref**2)*DIAMETER*WIDTH )
drag_coeff_cyl(1:3) = drag_coeff(1:3)/(U_cyl**2)

! SLICE-DRAG_COEFF
do i = 1,inno_along_cylinder
  slice_length(i) = slice_area(i)/( pi*DIAMETER )

  slice_drag_coeff(1:3,i) = slice_drag(1:3,i)/ &
       ( 0.5_WP*DENSITY*(U_ref**2)*DIAMETER*slice_length(i) )
end do

! ------------------------
!  output results
! ------------------------
! for drag-coeff...
write(filename1,'(A,F3.1,A,F4.2,A,I4.4,A)') &
     'CDrag-AR',aspect_ratio,'-b',b_ratio,'-Re',nint(Re),'.dat'
write(filename2,'(A,F3.1,A,F4.2,A,I4.4,A)') &
     'CLift-AR',aspect_ratio,'-b',b_ratio,'-Re',nint(Re),'.dat'

open (31,FILE=filename1,status='unknown',action='write',
    position='APPEND')
open (32,FILE=filename2,status='unknown',action='write',
    position='APPEND')

if (first .EQV. .TRUE.) then
  write(31,*) 'variables␣=␣"ite",␣"time*",␣"Cd",␣"%form",␣"%
     friction"'
  write(32,*) 'variables␣=␣"ite",␣"time*",␣"Cl",␣"%form",␣"%
     friction"'
end if

write(31,'(␣I6,4(2X,G18.10)␣)') if2%step, time_star, drag_coeff
    (1), &
         -drag_form(1)*100.0_WP/drag(1), drag_friction(1)*100.0
            _WP/drag(1)
write(32,'(␣I6,4(2X,G18.10)␣)') if2%step, time_star, drag_coeff
    (2), &
         -drag_form(1)*100.0_WP/drag(1), drag_friction(1)*100.0
            _WP/drag(1)

close (31); close (32)

! for slice-drag-coeff...
```

```
        do i = 1,inno_along_cylinder
          write(slice_filename,'(A,F3.1,A,F4.2,A,I4.4,A,F5.3,A)') &
             'DragLiftC-AR',aspect_ratio,'-b',b_ratio,'-Re',nint(Re),'-
                z',slice_z_cc_list(i)+2,'.dat'

          open (UNIT=i+1000,FILE=slice_filename,status='unknown',action
             ='write',position='APPEND')

          if (first .EQV. .TRUE.) write(i+1000,*) 'variables␣=␣"ite",␣"
             time*",␣"Cd",␣"Cl"'

          write(i+1000,'(␣I6,3(2X,G18.10)␣)') if2%step, time_star,
             slice_drag_coeff(1,i), slice_drag_coeff(2,i)

          close (i+1000)
        end do
      end if
      ! -------------------------------------------------------

    end if        ! if zone is wall
    zone => zone%next
  end do

  ! no longer needed
  call free_r3_buffer()

  first = .FALSE.
end subroutine calc_drag_slices

! ############################################################

subroutine calc_shear_wall(if2,gwss)

  use bc_parsing_m        ! function zone_is_wall
  use gp_func_m           ! subroutine calc_duidxj()
  use buffer_m            ! subroutine use_r3_buffer(),var r3_buffer
  use param_m             ! function get_real_param
  use gp_defs_m           ! type zone_t,gp_t
  use if2_func_m

  implicit none

  type(if2_t), intent(inout), target :: if2
  real(WP),intent(out) :: gwss

  ! -----------------------------------

  type(gp_t), pointer :: gp
```

```
type(zone_t), pointer :: zone
real(WP), pointer :: u(:,:),p(:),nu(:),wall_shear(:)
real(WP) :: &
     wall_normal_grad(3),wall_normal_normal,wall_normal_tang(3),  &
     area,nn(3),ss(3),my_wss,global_wss,my_area,global_area
integer :: i,ino,j,ierr

! ---------------------------------------

if (myrank == 0) &
     write(*,*) '␣>␣calculate␣shear␣stress␣at␣all␣wall␣zones␣...'

gp => if2%gp
u => if2%u
p => if2%p
nu => if2%nu
wall_shear => get_r1('WALL_SHEAR',gp)

!initialize arrays
my_wss      = 0.0_WP
global_wss  = 0.0_WP
my_area      = 0.0_WP
global_area = 0.0_WP

! the explicit velocity gradients are required for some terms...
call use_r3_buffer(3,3,gp%nno_ib)
r3_buffer(1:3,1:3,1:gp%nno_ib) = 0.0_WP
call calc_duidxj(r3_buffer,u,gp)

! ---------------------------------------------------------------------------
! loop through zones until zone name matches input variable
! ---------------------------------------------------------------------------
zone => gp%first_zone_ptr
zone_loop: do while (associated(zone))
  !print *,len(zone%name),len(zone_name)
  !if (trim(zone%name) == trim(zone_name)) then
  if (zone_is_wall(zone%name) .and. (zone%name .ne. 'DUMP')) then

    ! ---------------------------------------------------------------
    !   calculate wall shear stress for all nodes on zone
    ! ---------------------------------------------------------------
    do i = 1,zone%n_nodelist
      ino = zone%nodelist(i)

      area = sqrt(dot_product(zone%no_normal(1:3,i),zone%no_normal
          (1:3,i)))
      nn(1:3) = zone%no_normal(1:3,i)/area
      ! in CDP faces on the boundary are always outward pointing
```

```
        ! ...be carefoul in what direction you want the normal to be facing
        nn(1:3) = -nn(1:3)

        ! WALL SHEAR STRESS (in general coordinates)
        ! i.e. wall_shear_stress = viscosity*du_tangential/dn_normal
        ! ...we need to calc the tangential velocity
        ! ...then we need the gradient in the wall normal direction
        do j = 1,3
          wall_normal_grad(j) = dot_product( r3_buffer(1:3,j,ino),nn(1:3) )
        end do
        wall_normal_normal = dot_product( wall_normal_grad(1:3),nn(1:3) )
        wall_normal_tang(1:3) = wall_normal_grad(1:3) -nn(1:3)*wall_normal_normal

        ! add constant factors
        ss(1:3) = nu(ino)*wall_normal_tang(1:3)

        ! magnitude of the shear stress
        wall_shear(ino) = sqrt(dot_product(ss(1:3),ss(1:3)))

        ! these are for averaging the global wall shear stress
        my_wss = my_wss + wall_shear(ino)*area
        my_area = my_area + area
      end do
      ! ---------------------------------------------------------------

    end if      ! if zone is wall
    zone => zone%next
  end do zone_loop

  ! SUM DRAG from all processors
  call MPI_Reduce(my_wss,global_wss,1,MPI_REAL_WP,MPI_SUM,0,mycomm,ierr)
  call MPI_Reduce(my_area,global_area,1,MPI_REAL_WP,MPI_SUM,0,mycomm,ierr)

  gwss = global_wss/global_area

  call free_r3_buffer()

end subroutine calc_shear_wall

! ##################################################################

subroutine calc_global_total_ke(if2,xcut,gtke)
```

```
use gp_defs_m           ! type zone_t,gp_t
use buffer_m            ! subroutine use_r3_buffer(),var r3_buffer
use if2_func_m          ! subroutine done_cdp_if2(if2)
use param_m             ! function get_real_param

implicit none

type(if2_t), intent(inout), target :: if2
real(WP),intent(in) :: xcut
real(WP),intent(out) :: gtke

! ----------------------------------------

type(gp_t), pointer :: gp
real(WP), pointer :: tke(:),u(:,:)
real(WP) :: xx(3),my_tke,my_volume,gvol
integer :: ino,ierr

! ----------------------------------------

if (myrank == 0) &
   write(*,*) '␣>␣calculate␣total␣kinetic␣energy␣in␣all␣volumes␣where
      ␣z␣<␣60.0␣...'

gp => if2%gp
tke => get_r1('TKE',gp)
u => if2%u

my_tke = 0.0_WP
gtke = 0.0_WP
my_volume = 0.0_WP
gvol = 0.0_WP

node_loop: do ino = 1,gp%nno_ib
xx  = gp%node_cc(1:3,ino)
if (xx(3) .ge. xcut) cycle node_loop
  tke(ino) = 0.5_WP*dot_product(u(:,ino),u(:,ino))
  my_tke = my_tke + tke(ino)*gp%no_volume(ino)
  my_volume = my_volume + gp%no_volume(ino)
end do node_loop

call MPI_REDUCE(my_tke,gtke,1,MPI_REAL_WP,MPI_SUM,0,mycomm,ierr)
call MPI_REDUCE(my_volume,gvol,1,MPI_REAL_WP,MPI_SUM,0,mycomm,ierr)

if (myrank == 0) print *, gtke,gvol, gtke/gvol

gtke = gtke/gvol
```

```
  end subroutine calc_global_total_ke

end module cdp_if2_hooks_m
```